Engineering Peripheral Structure in Polycyclic Aromatic Hydrocarbons and Graphene Nanoribbons

Dissertation

zur Erlangung des Grades

„Doktor der Naturwissenschaften“

im Fachbereich Chemie, Pharmazie, und Geowissenschaften
der Johannes Gutenberg-Universität Mainz und in Kooperation
mit dem Max-Planck-Institut für Polymerforschung Mainz

vorgelegt von

Xuelin Yao

Geboren in Hunan / China

Mainz, 2019

Dekan:

1. Berichterstatter:

2. Berichterstatter:

Tag der mündlichen Prüfung:

Die vorliegende Arbeit wurde in der Zeit von Oktober 2015 bis November 2019 im Max-Planck-Institut für Polymerforschung Mainz unter der Betreuung von [redacted] durchgeführt.

Ich danke [redacted] für seine wissenschaftliche und persönliche Unterstützung sowie für seine ständige Diskussionsbereitschaft.

To my family

Contents

Index of Abbreviations

1D	one dimension
2D	two dimension
3D	three dimemsion
9-BBN	9-borabicyclo[3.3.1]nonane
Abs.	absorption
AGNR	armchair graphene nanoribbon
BBr_3	boron tribromide
BS	band structure
CB	conduction band
c-HBC	contorted-hexabenzocoronene
cis-PA	*cis*-polyacetylene
CNT	carbon nanotube
COSY	correlation spectroscopy
c-OBCB	octabenzocircumbiphenyl
CV	cyclic voltammetry
CVD	chemical vapor deposition
d	doublet (NMR)
DBBA	dibromo-bianthryl
DFT	density functional theory
DPA	9,10-diphenylanthracene
Et_2O	diethyl ether
FET	field effect transistor
Fluor.	fluorescence
FTIR	Fourier transform infrared
GNR	graphene nanoribbon
HOMO	highest occupied molecular orbital
HRMS	high-resolution mass spectrometry
HSQC	heteronuclear single quantum coherence
LDOS	local density of state
LUMO	lowest unoccupied molecular orbital
m	multiplet (NMR)
MALDI	matrix-assisted laser desorption/ionization

MFH-TB	mean-field-Hubbard tight-binding
nc-AFM	non-contact atomic force microscopy
n-Bu_4NPF_6	tetrabutylammonium hexafluorophosphate
NaCl	sodium chloride
NIR	near infrared
NMR	nuclear magnetic resonance
NOSEY	nuclear Overhauser enhancement spectroscopy
ODCB	*ortho*-dichlorobenzene
OFET	organic field effect transistor
OLED	organic light-emitting diode
p-HBC	hexa-*peri*-benzocoronene
PA	photoinducded absorption
PAH	polycyclic aromatic hydrocarbon
PB	photobleaching
PDI	Perylene diimide
PMMA	poly(methyl methacrylate)
RBLM	radial breathing like mode
s	singlet (NMR)
SE	stimulated emission
SSH	Su–Schrieffer–Heeger
STM	scanning tunneling microscopy
STS	scanning tunneling spectroscopy
t	triplet (NMR)
t_m	inter-cell coupling
t_n	intra-cell coupling
TA	transient absorption
TB	tight binding
TCNQ	7,7,8,8-tetracyanoquinodimethane
THF	tetrahydrofuran
TLC	thin layer chromatography
TOF	time of flight
trans-PA	*trans*-polyacetylene
UHV	ultrahigh vacuum

UV-vis	ultraviolet–visible (absorption spectroscopy)
VB	valence band
ZGNR	zigzag graphene nanoribbon

Chapter 1. Introduction

Carbon allotropes and carbon based materials have played an indispensable role in all aspects of our life, from healthcare, energy, electronics to aerospace, we are, indeed, living in a “carbon world”. As one of the abundant elements in Earth’s crust that constitute the basis of all known organisms, carbon has several allotropes which can occur as either bulk materials like graphite or discrete particles like fullerene, their structures can be either amorphous or crystalline (Figure 1). Interestingly, allotropes of carbon possess physical properties that span a wide range: diamond is one of the hardest natural substances known, while graphite is the one of the softest and slipperiest. When taking a single sheet out of the multilayered graphite, a giant two-dimensional (2D) material consists of sp^2 carbons tightly bound in a hexagonal honeycomb lattice can be produced, this is named graphene. Although graphene has been predicted to be thermodynamically unstable in early theoretical studies,[1-3] the ground-breaking work by Geim and Novoselov, after peeling off separate graphene layers from graphite, has profoundly changed the world of materials science.[4] Graphene has a tremendous relevance for various applications, including electronics, optical sensing, biological labelling and energy conversion and storage. These are based on its extraordinary electronic, optical, thermal, biological and mechanical properties.[5] For their pioneering work, Geim and Novoselov together won the Nobel Prize in Physics in 2010 "for ground-breaking experiments regarding the two-dimensional material graphene."

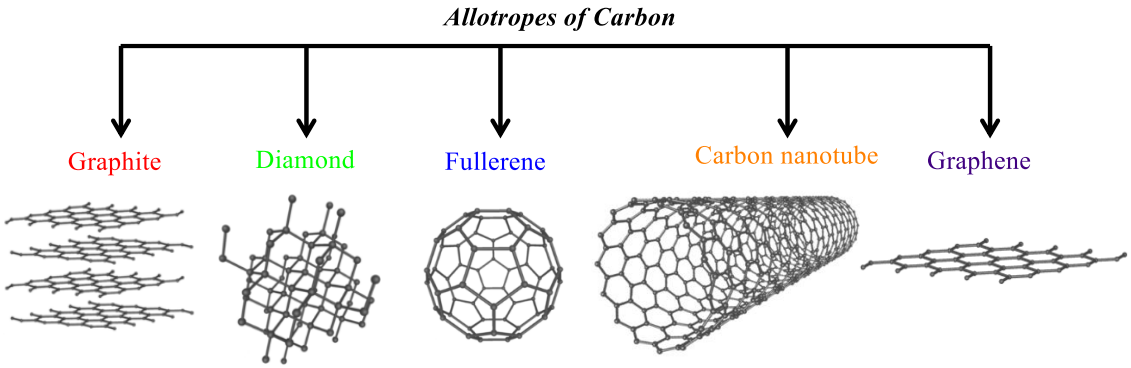

Figure 1. Different allotropes of carbon.

The outstanding properties of graphene, along with variable preparation methods have catalysed the development of science and technology in chemistry, materials and physics related to graphene. According to the crystallographic orientation, there are two basic

peripheral structures in graphene, namely, armchair and zigzag (Figure 2a). When the size of graphene reaches nano level, zigzag periphery exhibits nonbonding edge states while it is absent in armchair periphery.[6] Clearly, hundreds of research groups and institutes around the world are exploring, explaining and extending the different phenomena and results within graphene since the Nobel Prize of graphene. An important recent discovery on graphene has surprised the solid-state physics field, two graphene sheets stacked together, but with a rotation angle of 1.1° (Figure 2b), which called "magic angle", turns the normally metallic graphene into a superconductor.[7,8] The finding of magic twist angles in graphene has opened a window to design tailor-made and atomically thin materials with appealing properties that could be invaluable for future electronics. The discovery of superconductivity in twisted bilayer graphene has already ignited a frenzied race in "twistronics" based on a large class of 2D materials, including graphene, boron nitride, and molybdenum disulfide.

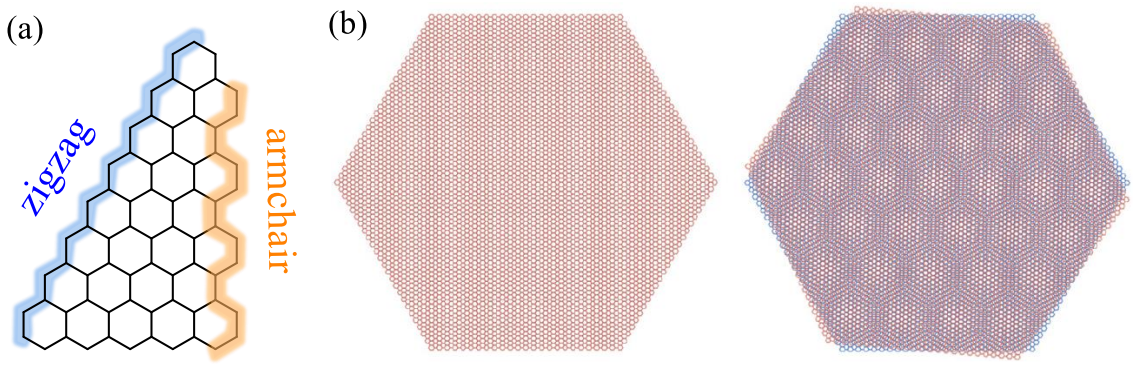

Figure 2. (a) Peripheral structures of graphene; (b) illustration of magic-angled graphene bilayer.

Graphene nanoribbons (GNRs) are quasi-one-dimensional (1D) graphene cutouts, typically with widths in the range of 1–100 nm and length/width ratio larger than 10.[9] Notably, graphene is a kind of semimetal with zero-bandgap.[10] Comparing the electronic characters of the quasi-1D GNRs with those of 2D graphene sheets reveals interesting differences. In particular, the fascinating properties of graphene exhibit various relevant potential applications, ultrahigh charge-carrier mobility (>2 × 10^5 cm^2 V^{-1} s^{-1} at room temperature with the electron density of 2 x 10^{11} cm^{-2}) for example,[11] however, its vanished electronic bandgap makes it non-applicable for field-effect transistors (FETs) and optoelectronic devices as an active component, since a current always flows between source and drain electrodes. An opening of the bandgap and thus a significant on-off ratio could be achieved by a geometric confinement in GNRs, leading to huge potential applications of GNRs in future nanoelectronics.[12-14]

Polycyclic aromatic hydrocarbons (PAHs), consisting of periodically annelated benzene rings, feature the same basic unit with graphene. Nowadays, when we talk about PAHs, we should not ignore the names of pioneers such as Robinson, who first introduced the aromatic π-sextet in 1925[15]. This was further refined in the theory of molecular orbitals by Hückel in 1931.[16] Clar proposed his famous sextet rules in 1964 which offers an easier and predictable approach of the stability of larger aromatic systems;[17,18] Clar and Scholl also laid the groundwork for fundamental aspects of PAH chemistry which lead to the various bottom-up methodologies to numerous PAHs.[17,19-21] Looking back into the past, since its first discovery in coal tar and fossil fuels in the 19th century, PAHs have played an indispensable role in the evolution of modern organic chemistry and materials science.

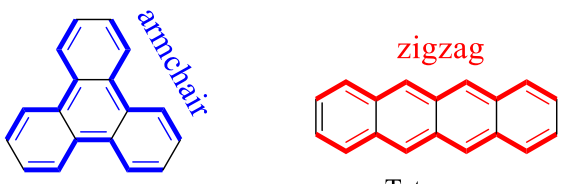

Triphenylene
1

Tetracene
2

Figure 3. Periodical annelation of four benzene rings to triphenylene **1** and tetracene **2** with different edge peripheries.

With intriguing electronic and optoelectronic properties, resulting from the delocalized electrons over its large π-domains, PAHs have attracted attention from different fields of science.[22-28] Typically, when PAH disks substituted with peripheral alkyl chains, the nanophase separation between soft alkyl chains and hard aromatic cores leads to the existence of discotic mesophases, which promotes their applications in solar cells, light-emitting diodes, photo-and-electroluminescent devices as well as field-effect transistors.[29] Actually, for various applications, one of the most appealing properties of PAHs is the tuneable electronic properties through molecular design. PAHs with different peripheries, such as armchair, zigzag and heteroatom-doped exhibit considerably different physical and chemical properties. Taking triphenylene **1** and tetracene **2** as examples (Figure 3), four benzene rings can be arranged in different fashions. Triphenylene with armchair periphery is extremely stable against oxidation and maintains a relatively large optical energy gap while tetracene with zigzag edge can be easily oxidized and displays an optical absorption at longer wavelengths.[30]

PAHs and GNRs with armchair edge structures, usually exhibit larger energy gaps and higher stability, which makes them promising candidates for electronic applications, FET

devices for example.[29] Contrarily, PAHs and GNRs with zigzag peripheries always suffer from issues of stabilization because of the low highest occupied molecular orbital (HOMO)-lowest unoccupied molecular orbital (LUMO) gaps and inherently contain unpaired electron as a result of unsatisfied atomic valences, respectively.[31-33] Electronic properties and chemical reactivity, accordingly, are related to the peripheral structures of PAHs and GNRs. Nowadays, it is widely known that doping of silicon-based semiconductors by group III (p-doing) or group V (n-doping) elements has played a pivotal role in the semiconductor industry. Similarly, in molecular electronics based on carbon-rich materials, heteroatom doping, such as boron (B) and nitrogen (N), is of high importance, as it offers additional opportunities in modulating the electronic, magnetic, and catalytic properties.[34] Modifying the peripheral structure of the π-conjugated system thus provides a viable approach to control the electronic structure.

The great advances in synthetic methods, which have largely avoided harsh reaction conditions, have greatly facilitated the extensive research on PAHs and GNRs from both chemical and physical perspectives. Nonetheless, other developments have further stimulated PAHs and GNRs research. Among these are the ingenious invention of scanning probe techniques (e.g., scanning tunnelling microscopy (STM), scanning tunnelling spectroscopy (STS) and non-contact atomic force microscopy (nc-AFM)) that have enabled the visualization of PAHs and GNRs in real space and with atomic resolution.[35-37] These developments have culminated in a unique combination of surface science, synthetic chemistry, and scanning probe techniques. Specifically, if suitable molecular precursors are deposited on metal surfaces followed by thermally induced intra- or intermolecular reactions, PAHs or GNRs with different sizes and edge structures are obtained and in-situ visualized by STM. It provides a feasible way which allows one to achieve structural information on PAHs or GNRs with high resolution as well as electronic properties. Further, a reliable structure-property relationship can be derived.

The discovery of graphene has provided an extra impetus for the research on PAHs. At the same time, the electronic features and applications of graphene in molecular electronics have catalysed the development of GNRs. Researches based on PAHs and GNRs have expanded rapidly over the past decade. Both PAHs and GNRs have been the subject of interdisciplinary research in the field of chemistry, physics, biology and materials science. Regarding the application of PAHs and GNRs in electronics, more emphasis has been put on the physical properties and device behaviour. However, the “reliability” of the materials is always derived from the intrinsic structural features. For those carbon-based materials with low dimensionality, PAHs and GNRs as typical examples, this structure-property relationship is of

particular significance. Therefore, this introduction will focus on the engineering of peripheries in PAHs and GNRs, including i) the different synthetic strategies, ii) the relationship between the peripheral structure and electronic properties and iii) potential applications.

1.1 Synthetic strategies for PAHs

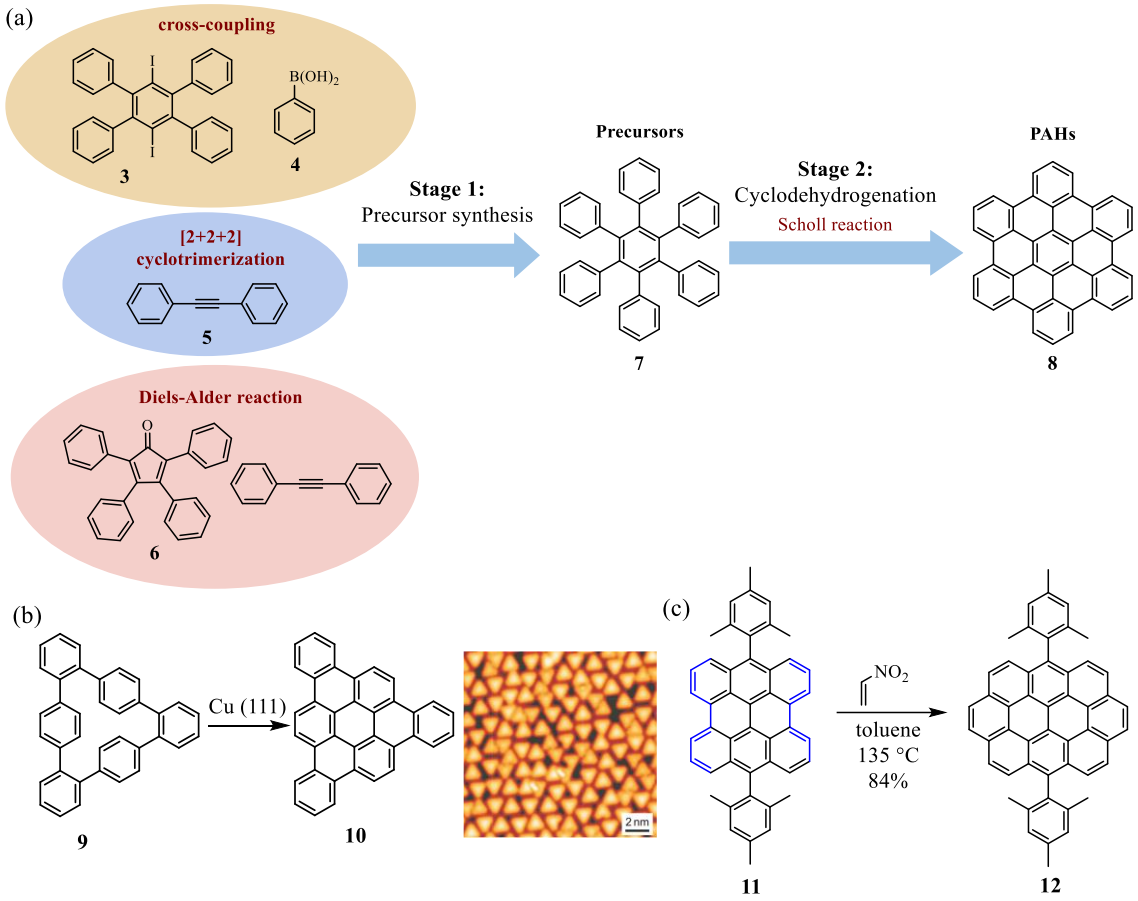

Figure 4. (a) Illustration of the two-stage synthetic protocol ("precursor route") to *p*-HBC; (b) on-surface synthesis of tribenzo[*a*,*g*,*m*]coronene and STM image of PAH 10 on Au(111) surface. Reprinted with permission from Ref.[38], copyright (2010) Springer Nature; (c) synthesis of ovalene via π-extension strategy.

At the early stage of the development of PAHs, distillates directly from coal tar and catalytic hydrocracking of petroleum provided a straightforward approach to smaller PAHs, like naphthalene, anthracene, pyrene and triphenylene. Those smaller PAHs gradually adopted an important role in many fields of science. Along with social progress and industrial development, however, a more defined preparation of PAHs, i.e. organic synthesis, was urgently needed. Fundamental contributions to the synthesis and characterization of PAHs go

back to the pioneering works of Scholl, Clar and Zander. During that time, the synthesis of PAHs always required vigorous reaction conditions, as well high temperature and pressure. The development of modern synthetic methods has furnished milder synthetic methods with high regioselectivity to the chemistry of PAHs.

In general, the synthetic routes to PAHs can be separated into two categories: two-stage synthesis and aromatic core extension. Specifically, two-stage synthesis consists of formation of precursors and further cyclodehydrogenation to generate the ring-fused systems. Taking hexa-*peri*-hexabenzocoronene (*p*-HBC) for instance (Figure 4a), hexaphenylbenzene as precursor is first synthesized via different ways, such as metal catalyzed cross-coupling,[39] cobalt-mediated [2 + 2 + 2] cyclotrimerization[40] and Diels-Alder reaction,[41] and then cyclodehydrogenation by subjecting the precursor hexaphenylbenzene to Scholl reaction provides the fully planarized *p*-HBC. As a newly developing field of research, on-surface synthesis aims at making use of defines solid surfaces, mostly single-crystal metal surfaces, as confinement templates to initiate chemical reactions. On-surface synthesis of planar PAHs from polyphenylene precursors can also proceed as two-stage synthesis (Figure 4b). As exemplified by the synthesis of a triangular nanographene molecule, cyclohexa-*o*-*p*-*o*-*p*-*o*-*p*-phenylene as precursor was first synthesized in solution, followed by cyclodehydrogenation on a Cu(111) surface, resulting in tribenzo[*a*,*g*,*m*]coronene as a triangular PAH which was directly visualized by STM.[38] So far, a majority of PAHs have been fabricated through this two-stage (precursor) protocol.[42]

The second synthetic strategy toward PAHs based on the π-extension of existing aromatic cores plays an important role in the further diversification of PAHs. One typical example is the Diels-Alder cycloaddition in the bay regions (concave armchair edge) of PAHs, which have a diene-like feature and thus can react with dienophiles, such as alkenes, alkynes, arynes and quinones, to make PAHs with extended π-domains.[43] Based on this concept, Scott et al. demonstrated a synthesis of ovalene through the Diels-Alder reaction of bisanthene with the dienophile nitroethylene (Figure 4c).[44] Moreover, different approaches for aromatic core extension have been reported, resulting in various PAHs with larger π-systems in past decades.[45-53]

1.2 Peripheral structure makes difference in PAHs

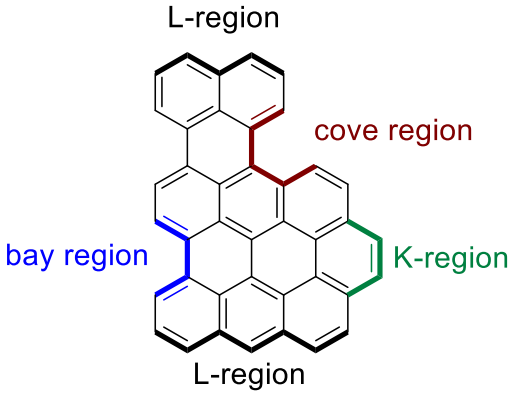

Figure 5. Schematic of typical periphery of PAHs.

The electronic nature of PAHs can be dramatically altered by changing the size of π-conjugation and edge structure. Figure 5 illustrates typical edge structures of PAHs. According to Clar's aromatic sextet rules, PAHs with only armchair (also known as bay regions) peripheral structuries often possess high stability since their chemical structures can be drawn in an all-benzenoid fashion, thus more synthetically accessible. When benzene rings are fused at peri-positions in a triangular manner, one obtains a full zigzag periphery (also known as L region) which make it not possible to draw the whole molecule in Kekulé-style resonant structures, resulting in one or more unpaired electrons.[54] The K-region of PAHs, an isolated carbon–carbon double bonds not being part of a Clar sextet, can be used for further reaction.[51,55] Consequently, PAHs with K-regions offer regioselectivity during the synthesis of PAHs with extended π-domains.[51] PAHs with cove regions normally have non-planar configurations due to steric congestions between the hydrogen atoms in the cove regions. Noteworthy, the edge structures of PAHs make impact on their chemical and physical properties, while peripheral heteroatom doping of PAHs offers tremendous opportunities to modulate the key electronic, magnetic and catalytic properties.[34]

1.2.1 PAHs with armchair-edged structure

As one of the most extensively investigated PAHs, *p*-HBC **8** has fully armchair-edged structure with seven aromatic-sextets. Pioneering works on the synthesis of HBC under mild conditions and with high efficiency were reported by Müllen et al.[56] After that, different PAHs with armchair edge structures have been synthesized (Figure 6).[57-62] The attachment of flexible aliphatic chains to the PAHs' periphery not only provides sufficient solubility and solution processability, but also favors self-assembly into columnar liquid-crystalline phases.[29] Owing

to the symmetrical disk-like shape and large π-skeleton, *p*-HBC with substituents has often been employed as a building block for the formation of discotic liquid crystals.

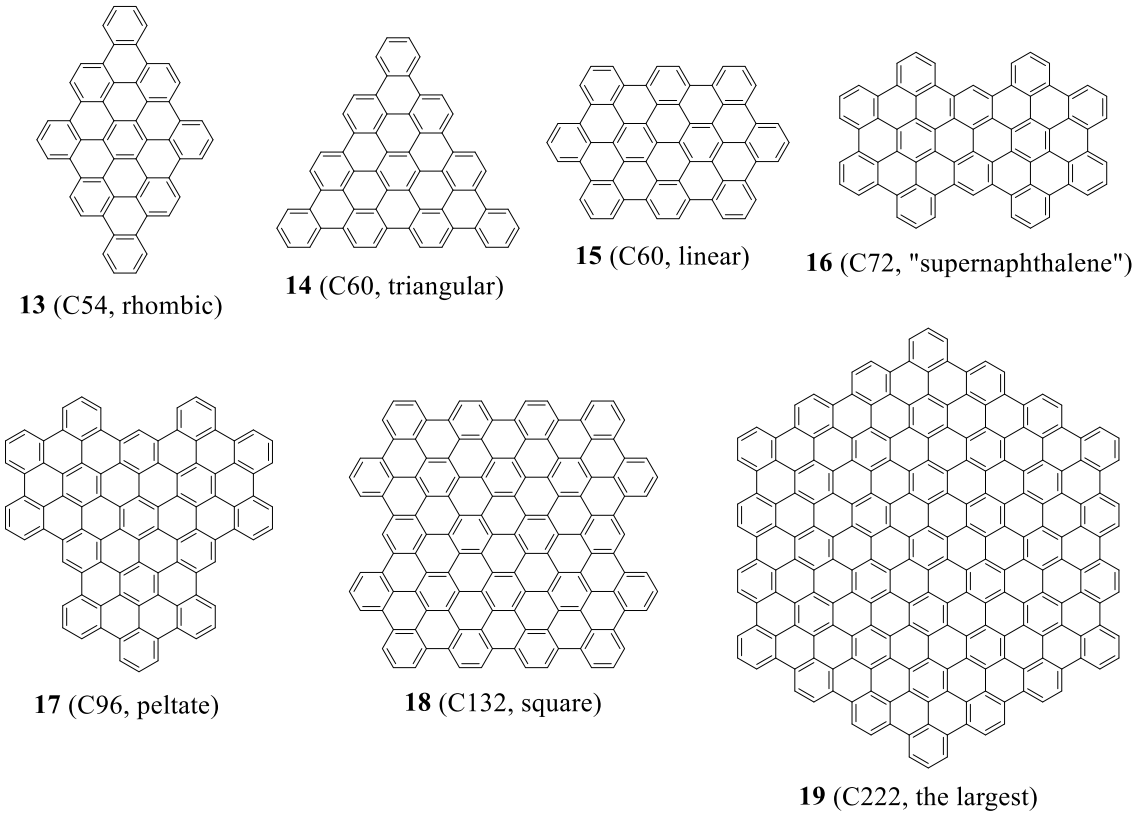

Figure 6. Some examples of PAHs.

Specifically, HBC can assemble into columnar structures in solution due to π-stacking interactions between the aromatic cores. The follow organization process, nanophase separation take place between the highly ordered, rigid aromatic cores and the distorted aliphatic chains offers final superstructures (Figure 7). The ordered and oriented columns intrinsically enable transport of charge carriers. It is obvious that organic materials which exhibit a high intermolecular charge carrier mobility are particularly favourable for the implementation in devices, such as field effect transistors (FETs) and photovoltaic devices. In 2005, FET devices based on a highly ordered layer of HBC with six dodecyl chains have been fabricated by Müllen et al.[63] A zone-casting technique was applied to prompt HBCs to adopt an edge-on arrangement on surfaces. The transfer and output characteristics of the devices, which are measured along the columnar alignment, revealed a good on-off ratio of 10^4 and a field-effect mobility of 5×10^{-3} $cm^2/(Vs)$.

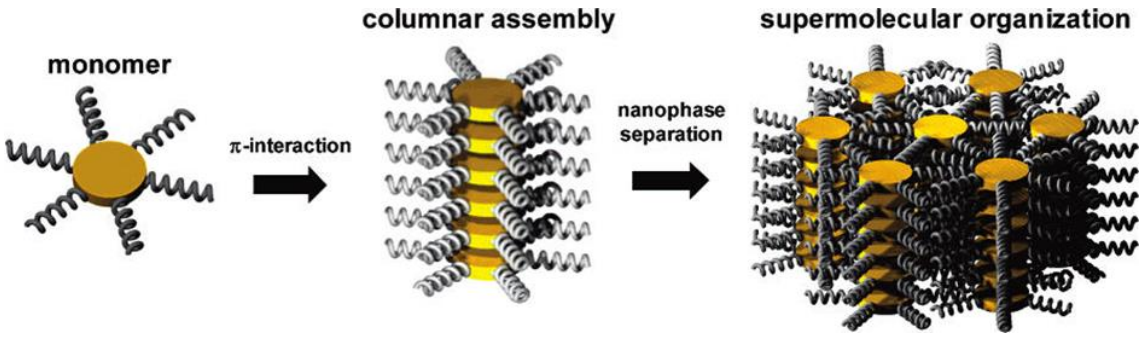

Figure 7. Schematic of the organization of alkyl-substituted PAHs in solution. Reprinted with permission from Ref.[29], copyright (2007) American Chemical Society.

With regard to the molecular structure of *p*-HBC **8**, the hexagonal symmetry suggests its description of "superbenzene", in which each peripheral benzene rings can be depicted as one sp^2 carbon in benzene. The UV-vis study of HBC revealed a weak α-band at 463 nm which could be ascribed to 0–0 transition forbidden because of its perfect mirror symmetry. The absorption maxima of HBC is located at 360 nm.[64] For PAHs with armchair edge but different size, as illustrated in Figure **6**, their optical energy gap displays a size-dependence, namely, larger size leads to smaller energy gap. The reason lies in the fact that larger PAHs possess more delocalized π-electrons. PAH **17** with 96 sp^2 carbons showed an absorption at 460 nm with a low-energy tail extending to roughly 700 nm.[60] When compared with that of **8**, a large red shifted feature can be easily figured out, corresponding to a smaller optical energy gap for **17**. Until now, the largest armchair-edged PAHs is **19** with 222 sp^2 carbons which was reported by Müllen et al.,[62] possessing an optical energy gap as low as 1.6 eV.

1.2.2 PAHs with zigzag-edged structure

PAHs with either partial or full zigzag edge structures were synthesized in solution or on-surface. Appealing electronic phenomena have been revealed by modulating the zigzag edge. An exemplary case to illustrate the essence of edge engineering of PAHs is the edge extension of HBC (Figure 8). By adding extra π-centers (K-regions) onto the bay-region of fully benzenoid *p*-HBC, PAHs with partial zigzag edge structures can be obtained. Simultaneously, significant influences on electronic properties can be observed. The optical absorption of **20** with only one K-region appears at 380 nm, exhibiting a red shift with respect to the corresponding band of *p*-HBC **8**.[65] As the number of K-region increases, drastic changes in photophysical characteristics were observed, as evidenced by prominent red shift of the

absorption maxima when going from **20** to π-annelated derivatives **21** and **22** with two and three K-regions, respectively. A further increase of K-regions, which means more zigzag moieties is not easy, resulting from the lack of sufficient synthetic methods. Recently, HBC with four additional K-regions **23** was synthesized by Feng and Müllen et al.,[66] in which four relatively short zigzag edges were generated. **23** displayed a significantly lowered optical gap when compared with that of **8** and its derivatives with one to three K-regions. By adding six K-regions to *p*-HBC, compound **24** with a full zigzag edge has attracted much theoretical interest, but its synthesis remains challenging and unachieved. More importantly, the K-region provides further options for functionalization, thus unlocking a wide range of PAH chemistry. For example, Müllen et al. demonstrated the selective oxidation of the K-region of a derivative of **20**, leading to the formation of a α-diketone moiety, which was used as a building block to synthesize large heteroatom-containing PAHs.

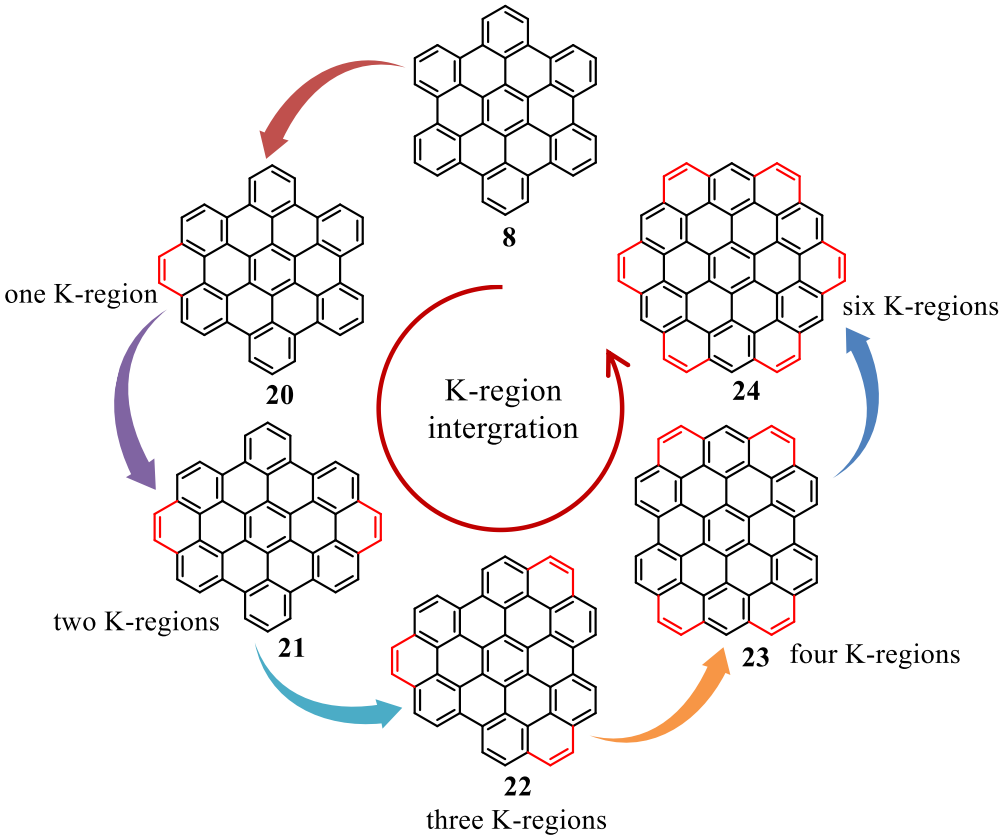

Figure 8. Modulation of electronic properties of *p*-HBC by K-region integration.

Acenes composed of benzene rings fused in a linear fashion are a unique class of PAHs featuring long zigzag edges. As a prototype of organic semiconductors, pentacene has been studied broadly, but its practical applications were seriously hindered by its high chemical reactivity, being particularly vulnerable to oxygen and light. Higher acenes are generally less

stable. The instability issues have obstructed both their syntheses and applications. In pursuing the goal of higher acene fabrications, Müllen et al. developed an ingenious strategy, in which pentacene **26** was synthesized in the solid state via the retro Diels-Alder reactions (Figure 9a).[67] Later, Neckers and Bettinger et al. achieved a serious of higher aecenes up to nonacene **28** through photochemical extrusion of bridging α-diketones in polymer matrices which function as inert atmosphere (Figure 9b).[68-70] Currently, the highest acene is undecacene **30** which was synthesized by Godlewski and Echavarren et al. on a metal surface under ultrahigh vacuum (UHV) which protects the sensitive product from oxygen efficiently (Figure 9c).[71]

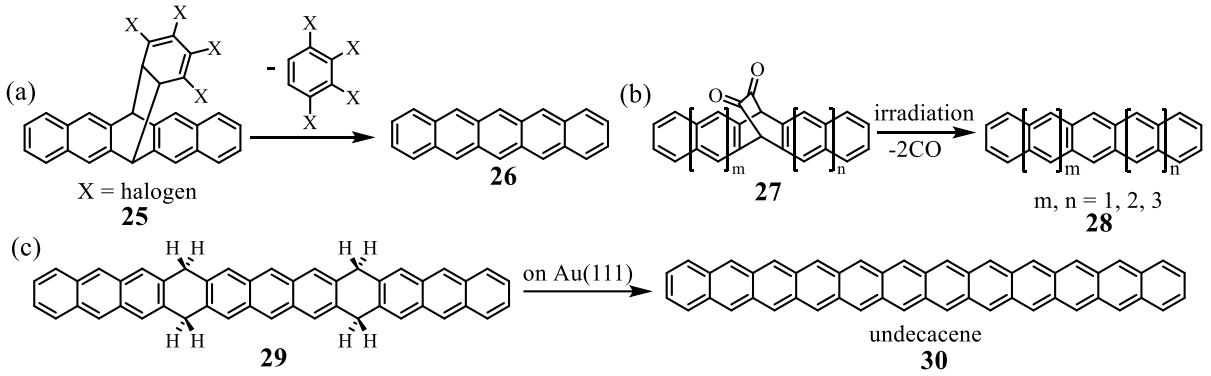

Figure 9. Synthesis of different acenes with zigzag periphery: (a) pentacene; (b) higher acenes up to nonacene; (c) undecacene.

There is another kind of PAHs, featuring paralleled zigzag and armchair edges (Figure 10a), among them peri-acenes, comprising two row of linear acenes, are typical examples. In the large family of peri-acenes, perylene **31** represents the smallest one (Figure 10b). Lateral extension based on perylene leads to bisanthene **32**, which is a well-known closed-shell structure. However, further extension creates higher homologues of peri-tetracene **33** and peri-pentacene **34** which both exhibit open-shell diradical features, thereby posing challenges for syntheses. In 2018, in-solution syntheses of peri-tetracene derivatives were reported independently by Liu and Feng et al. and Wu et al,[72,73] which revealed a singlet biradical character and narrow optical/electrochemical energy gap (around 1.1 eV). Although the synthesis of peri-pentacene in solution remains challenging, Crommie and Fisher et al. demonstrated a surface-assisted approach to the desired product through cyclodehydrogenation of 6,6'-bispentacene on Au(111) surface under UHV.[74] Further extension along the longitudinal direction of perylene and bisanthene provided opportunities for new PAHs, rylenes and anthenes. For example, Kubo et al. reported teranthene **35** and quateranthene **36** via expanding bisanthene into a longitudinal direction (Figure 10c).[75,76] Electrons strongly

delocalized at the zigzag peripheries and biradical characters of these two anthenes have been revealed by the analyses of their crystal structures together with simulation.

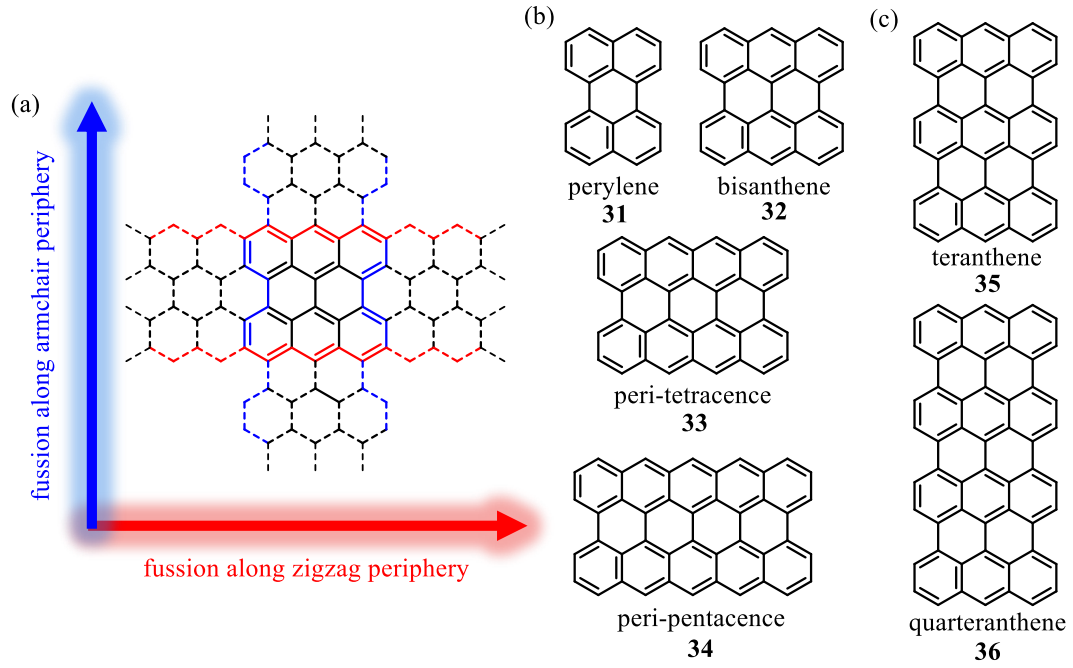

Figure 10. (a) General classification of PAHs with zigzag periphery; (b) examples of different peri-acenes; (c) teranthene and quarteranthene.

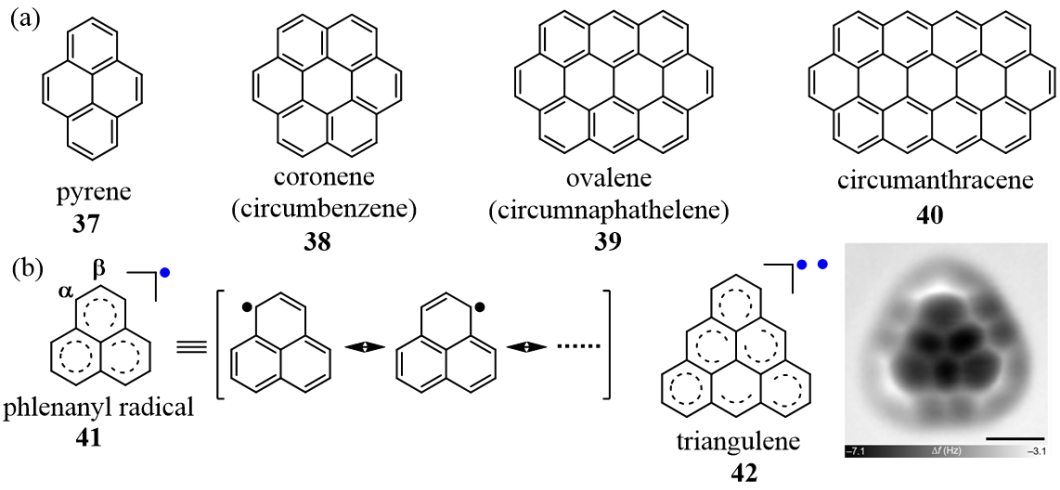

Figure 11. PAHs with full zigzag-edged structures.

PAHs with only zigzag periphery can be divided into two different categories (Figure 11), as their smallest member represented by pyrene **37** and the phenalenyl radical **41**, respectively. As shown in Figure 11a, being one of the full zigzag PAHs, pyrene is quite stable which can be interpret by its photophysical property, whose α-band was located at 372 nm.[77]

Coronene **38**, also called circumbenzene, displaying D_{6h} symmetry is another PAH with full zigzag edges. Its α-band located at 375 nm is identical to that of pyrene in spite of a larger molecular size and more extended conjugation.[78] As two more sextet benzenoid rings can be drawn for ovalene **39** compared to bisanthene, ovalene with full zigzag-edged structure, showing a larger HOMO-LUMO gap, is more stable than bisanthene. Notably, ovalene sometimes named as circumnaphtalene. In 1991, Diederich et al. reported the first synthesis of a higher generation of circumacenes, namely circumanthracene.[79] The other category of fully zigzag-edged PAHs has a in triangular shape (Figure 11b). The phenalenyl radical **41**, in which three benzene rings are fused in a triangular manner with a spin delocalized over the completely molecular skeleton, represents the most fundamental and widely explored member of this family.[80] The first study of phenalenyl radical dates back to the 1950s and it was found to be so reactive that it can be only handled in degassed solution under inert atmosphere.[81] For applications of phenalenyl radical, kinetically stabilizing the reactive sites by bulky substitutes is necessary. Accordingly, the synthesis of higher homologues of phenalenyl radical is much more challenging. π-Extension of phenalenyl radical in a triangular way leads to triangulene **42** which keeps two unpaired electrons. Synthesis and characterization of pristine triangulene has not been achieved because of its extreme reactivity. Only recently, Pavliček et al. reported the on-surface synthesis of it under UHV.[82] The planar structure with high-spin ground states were revealed by STM, which makes it potentially useful in organic spintronic devices.

1.2.3 PAHs with cove-edged structure

Armchair and zigzag edges are the most appealing peripheral structures in PAHs, however, when overlooking the development of PAH chemistry, PAHs with contorted structures have gained more and more attentions.[83,84] One direct molecular feature integrated into the design of this contorted configuration is benzophenanthrene **43** (Figure 12), which is also known as [4]helicene (the number indicating how many benzene rings are *ortho*-fused together). The four *ortho*-fused benzene rings construct the cove periphery. The steric congestion caused by the two hydrogen atoms in the cove region results in a non-planar π-skeleton of [4]helicene. The cove structure has been widely used for the fabrication of PAHs with non-planarity, yielding novel electronic and supramolecular properties.[85,86]

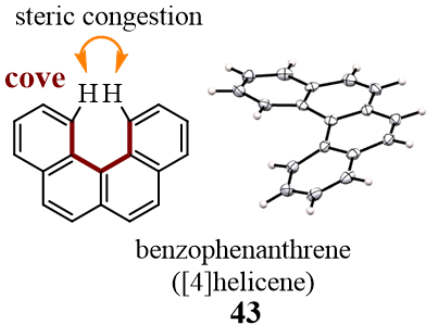

Figure 12. [4]Helicene with cove-edged structure.

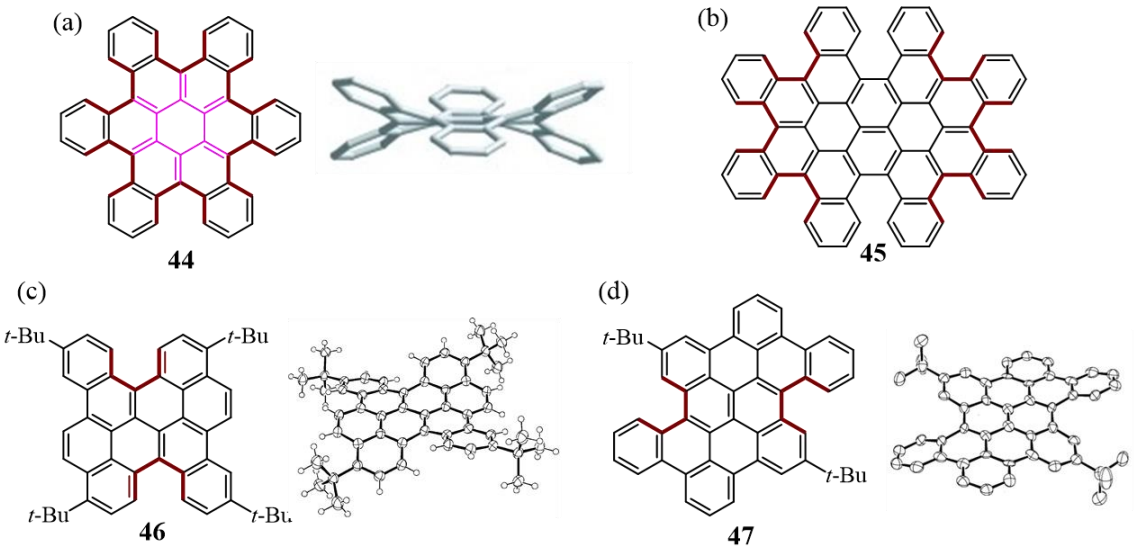

Figure 13. Cove-edged PAHs featured with contorted configurations.

A representative example is contorted HBC (*c*-HBC) **44** featuring six cove regions which was first reported by Clar in 1965 et al.[87] and later by Nuckolls et al.[88] (Figure 13a) with a more efficient synthesis. Single-crystal X-ray diffraction data reveals the nonplanarity of *c*-HBC with the exterior benzo-groups at the cove regions folding alternatively above or below the π-plane. When compared with the fully planar benzenoid *p*-HBC, *c*-HBC displays reasonable solubility in chloroform or xylene with an intense red fluorescence with emission bands at 616 and 627 nm. In spite of a large π-electron number of 48, the absorption spectrum of *c*-HBC displays a blue shifted feature when compared to that of *c*-HBC. FET devices based on *c*-HBC with four dodecycloxy chains exhibit a charge-carrier mobility of 0.02 $cm^2v^{-1}s^{-1}$ and high on-off current ratio of 10^6.[88] Moreover, a larger contorted PAH, octabenzocircumbiphenyl (*c*-OBCB) **45**, with six cove-edged regions was reported by Nuckolls et al[89] in 2013 (Figure 13b). Tetradodecyloxy-substituted *c*-OBCB exhibits a good solubility in solvents like

chloroform and *o*-xylene. Strong absorbances at 411 nm, 433 nm and 493 nm are found, which is red shifted by about 65 nm when compared to that of *c*-HBC. Besides, organic photovoltaic devices based on tetradodecyloxy-substituted *c*-OBCB give power conversion efficiencies of 2.9 % under 100 mW cm^2 illumination. Another two PAHs with cove-edge region were reported by Liu et al. in 2011,[90,91] as shown in Figure 13c and d. By far, PAHs with cove periphery are still less explored.

1.2.4 PAHs with heteroatom-doped peripheral structure

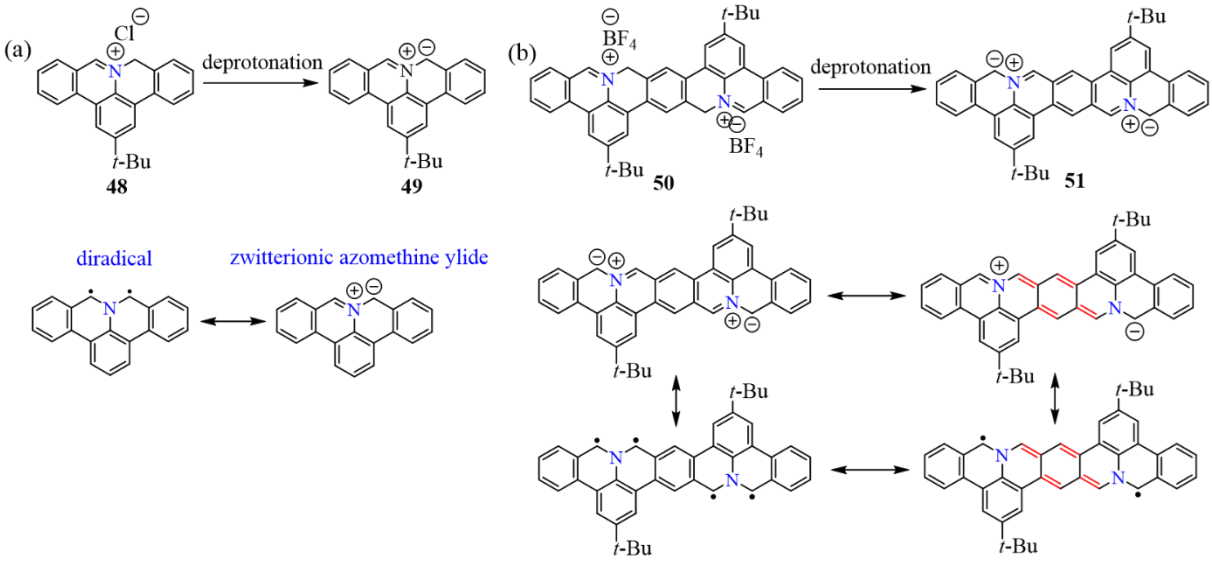

Figure 14. PAHs with N-doped zigzag periphery.

PAHs with zigzag periphery, for example peri-acenes, are particularly appealing for their localized edge states that are spin-polarizable, making them promising for the implementation of magnetic and spintronic applications. However, their syntheses and characterizations are largely hampered by the issue of stability. Edge heteroatom-doping provides a solution for stable PAHs with zigzag edge. In 2014, Beljonne, Feng, and Müllen et al.[92] announced the synthesis of N-doped zigzag peripheries with dibenzo-9*a*-azaphenalene as a basic unit (Figure 14). Monomer **49** (Figure 14a) and dimer **51** (Figure 14b) were successfully obtained. The dibenzo-9*a*-azaphenalene is highly reactive when taking a look at its diradical and zwitterionic azomethine ylide resonance structures. The UV-vis absorption spectra of **49** and **51** recorded in situ under inert conditions exhibit broad absorptions at 580 nm and an absorption maximum at 751 nm, respectively. This large red shifted absorption of **51** compared

to that of **49** stems from not only the extended conjugation but also an additional quinoid resonance, stabilizing the two nitrogen centers (Figure 14b).

In addition to mono-heteroatom doping, Zhang and Feng et al. demonstrated multiple heteroatoms doped zigzag edges.[93] Nitrogen-boron-nitrogen (NBN)-doped zigzag peripheries **52** and **53** (Figure 15) based on the 1,9-diaza-9a-boraphenalene structural motif were synthesized. Alternatively arranged nitrogen and boron atoms impart high chemical stability to the zigzag-edged periphery. The UV-vis absorption maxima for **52** appear around 350 nm, while shifted further to 435 nm for dimer **53**. 4.5,12.13-Dibenzoheptazethrene **54** reported by Clar et al.[94] is an all-carbon analogue of **53**, displaying an absorption at 572 nm which is by 137 nm greater than that of **53**. A larger optical energy bandgap of **53** (2.74 eV) can be deduced, thus a higher stability can be demonstrated just by incorporating multi-heteroatoms at the periphery.

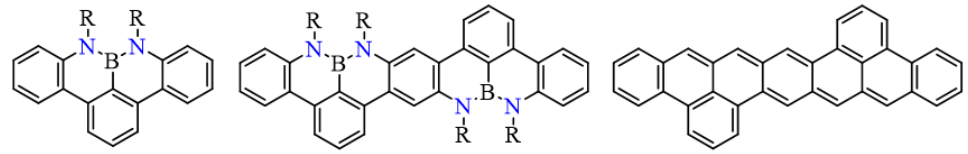

52 **53** **54**

Figure 15. PAHs with NBN-doped zigzag periphery and all carbon zigzag periphery.

As mentioned previously, peri-acenes are an important family of PAHs with zigzag-edged structure but are highly instable under ambient conditions, especially those larger than bisanthene. To overcome the issue of instability, Müllen's group reported an efficient approach for the synthesis of peri-tetracene and peri-hexacene analogues through OBO-doping at the zigzag sites (Figure 16). In solution, OBO-doped peri-tetracenes were obtained via a tandem demethylation-aryl borylation strategy (Figure 16a).[95] An intense absorption at 430 nm was found for **56b**, displaying a large blue-shifted absorption pattern when compared to that of its all-carbon analogue **57**.[72,73] The optical bandgap estimated from the lowest energy absorption onset is 2.84 eV for **56b**, while 1.11 eV for **57**, indicating that the OBO-doped bistetracene analogue exhibits excellent stability in contrast to the unstable all-carbon bistetracene. Moreover, by utilizing the the on-surface synthesis, OBO-doped peri-hexacene **59** was successfully formed on Au(111) surface by applying a precursor with helical feature under visualization with scanning probe techniques (Figure 16c,d).[96] To date, this OBO-doped peri-hexacene turns out to be the longest peri-acene analogue. In the meantime, the success in

obtaining such peri-acence anologues highlights the importance of combining in-solution and on-surface chemistry to pursue a further variety of PAHs with different peripheral structures.

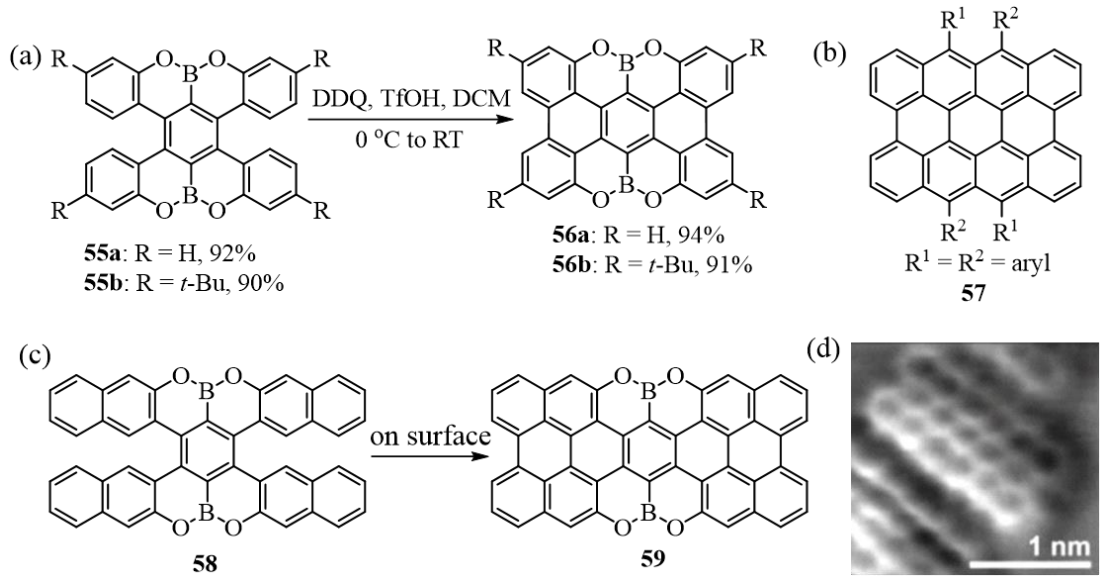

Figure 16. (a) Synthesis of OBO-doped peri-tetracene **56**; (b) all-carbon peri-tetracene; (c) surface-assisted synthesis of OBO-doped peri-hexacene **59**; (d) nc-AFM images of **59** on Au(111) surface. Reprinted with permission from Ref.[96], copyright (2017) American Chemical Society.

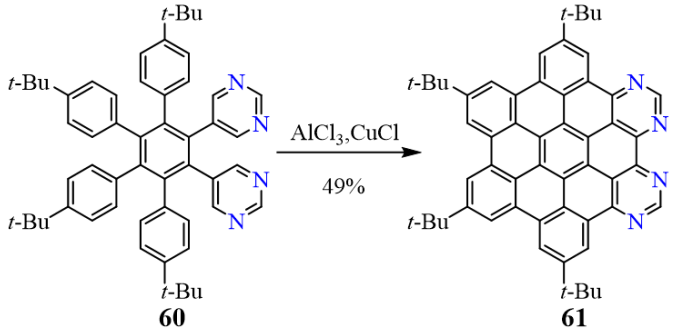

Figure 17. Synthesis of N-doped HBC **61** incorporating pyrimidine rings.

Inspired by the synthetic method for *p*-HBCs, incorporating heteroatoms into the *p*-HBC skeleton just by replacing phenyl groups with other heteroaromatic rings in the hexaarylbenzene precursor appears straighforward. Indeed, Draper et al. synthesized the first N-doped HBC **61** in 2002 through cyclodehydrogenation of the corresponding pyrimidine-substituted precursor (Figure 17).[97] The UV-vis spectrum of N-doped HBC exhibits the characteristic bands of *p*-HBC but a new band at 372 nm and reduced extinction coefficient.

The incorporation of pyrimidine rings endows PAH with electron-accepting properties as compared with the parent HBC. Furthermore, the N atoms in the bay region serve as a coordinating site with transition metals (e.g., Pd(II) and Ru(II)). Such metal complexes display profoundly changed absorption and emission properties.

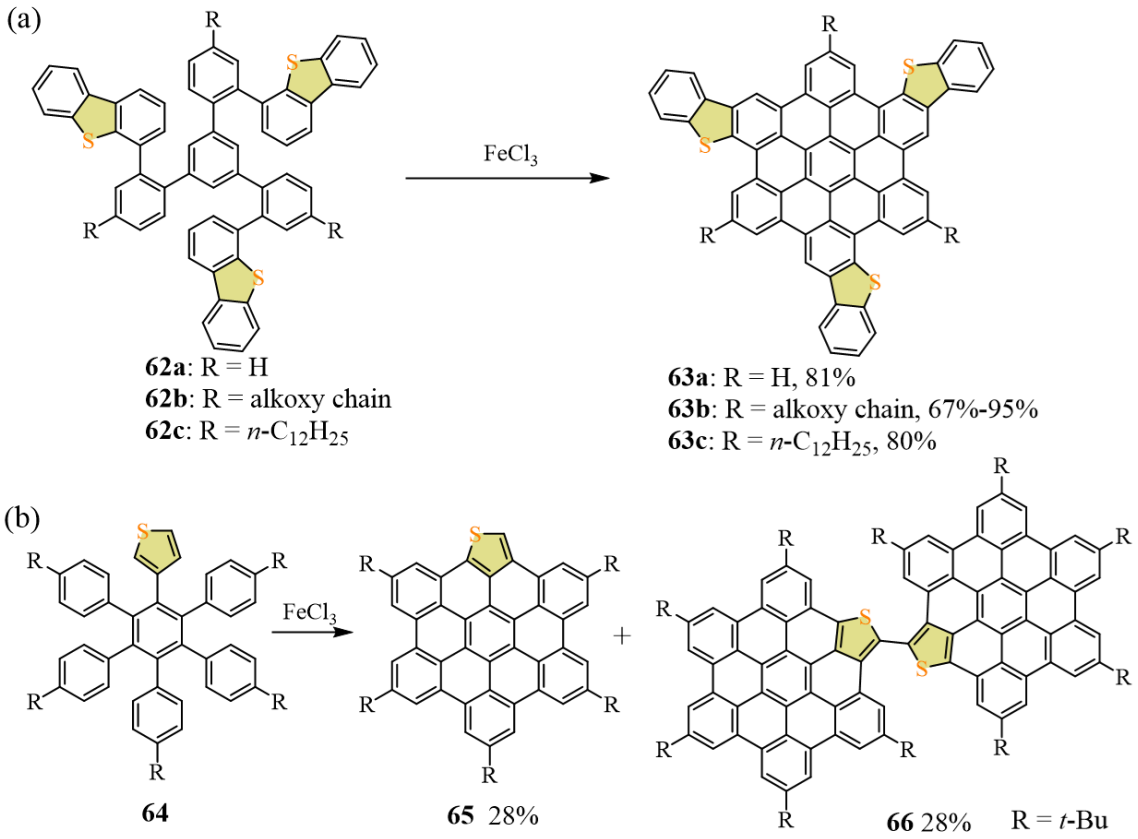

Figure 18. Syntheses of PAHs with S-doped periphery.

Fusing or embedding thiophene rings at the periphery leads to PAHs with S-doped edge structure. In 2007, Müllen et al.[57] synthesized tribenzothiophene HBC **63a** through cyclodehydrogenation of tailor-made precursor **62** as the first example of PAHs with S-doped periphery (Figure 18a). UV-vis and fluorescence spectra of **63a** exhibit a blue shift of 10 nm and about 30 nm, respectively, as compared to that of HBC. Besides, a series of derivatives **63b**,**c** with alkoxyl and alkyl chain were also reported by the same group, in which an obvious variation of HOMO and LUMO levels was observed. In 2011, Draper et al.[98] figured out another strategy to directly embed thiophene ring into S-doped HBC analogue **65** (Figure 18b). Notably, a dimerized product of **65** was also found during the cyclodehydrogenation process. The UV-vis absorption spectrum of **65** displays two intense peaks at 358 and 369 nm, respectively, similar to that of HBC, but a longer wavelength absorption.

1.2.5 PAHs with functionalized periphery

Halogenation, which has been used as reliable technique in graphene research for bandgap opening,[99,100] also serves as powerful tool for the engineering of physical and electronic properties of PAHs. An efficient edge chlorination protocol for large PAHs with an excess amount of iodine monochloride and a catalytic amount of aluminum chloride have been developed by Feng and Müllen et al. in 2013.[101] PAHs with different size, featuring chlorinated edge have been synthesized (Figure 19). Significantly, a greatly enhanced solubility has been observed for the chlorinated products. More interestingly, the absorption bands of those edge chlorinated compounds displayed a significant red shift with respect to their pristine molecules, leading to a decreased optical bandgap. Furthermore, due to the electron-withdrawing effect, chlorine atoms have an obvious consequence of lowering the energetic position of the frontier molecular orbitals. Most importantly, chlorine atoms at the edge provide a new window to the further functionalization of large PAHs.[102-104]

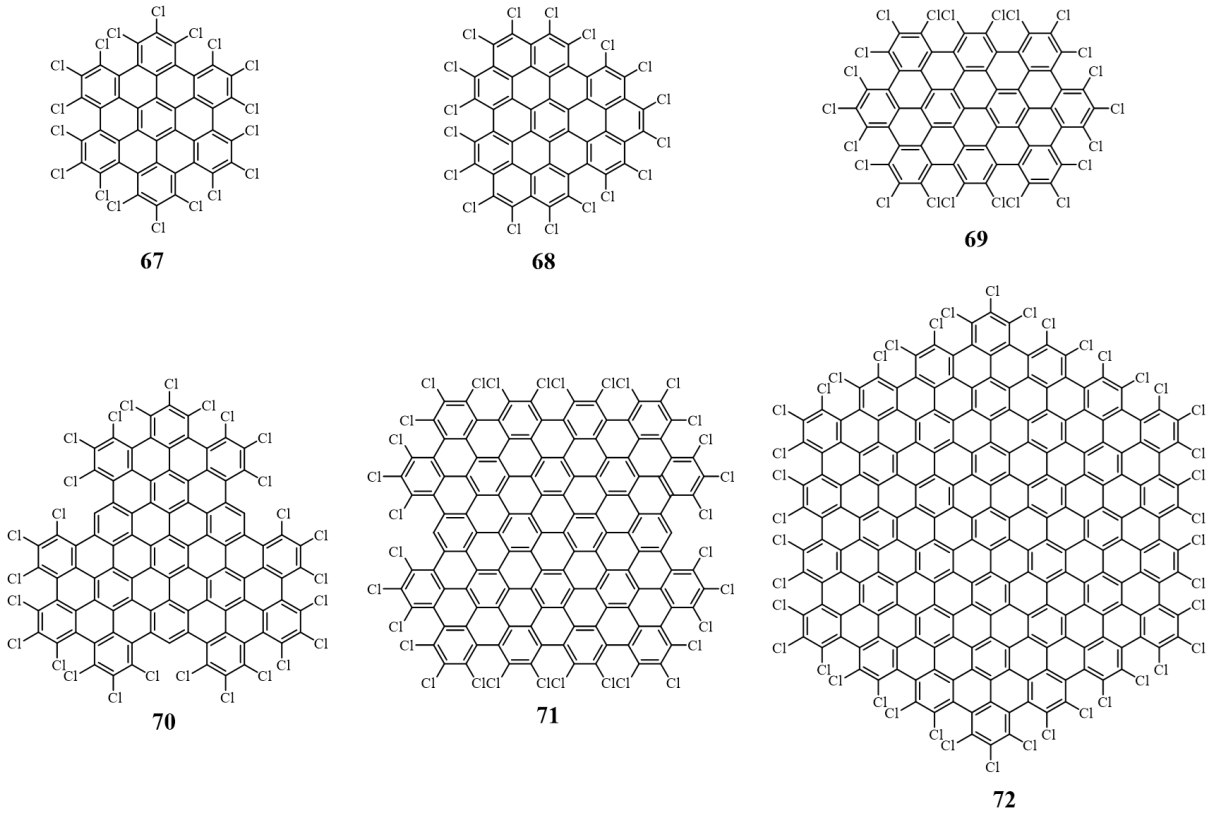

Figure 19. Examples of PAHs with edge chlorinated periphery.

As an approach toward graphene functionalization, hydrogenation can break C=C bonds, generating randomly distributed sp^3-hybridized carbon centers and dramatically change

graphene from semimetal (pristine) to bandgap opened semiconductor (partially hydrogenated), and then to insulator (fully hydrogenated, graphane). Similarly, hydrogenation of PAHs possesses great advantages for electronic property modulation. Unlike the use of techniques such as a hydrogen plasma for graphene hydrogenation, Müllen et al.[105] reported hydrogenation of *p*-HBC derivatives **73** under a moderate hydrogen pressure with the presence of commercially available palladium on activated carbon as catalyst, resulting in stereoselective generation of peralkylated coronenes (Figure 20a). As indicated by the profile of absorption spectra, the new substituted coronene exhibits a red shift by approximately 25 nm to that of pristine coronene (Figure 20b). It is worth noting that a different aromatic core featuring alkylated periphery was obtained efficiently via a totally opposite fashion of π-extension. Altogether, these enlightening results offer a great promise and this is, not more and not less than a completely different strategy to fabricate PAHs with unique π-skeletons.

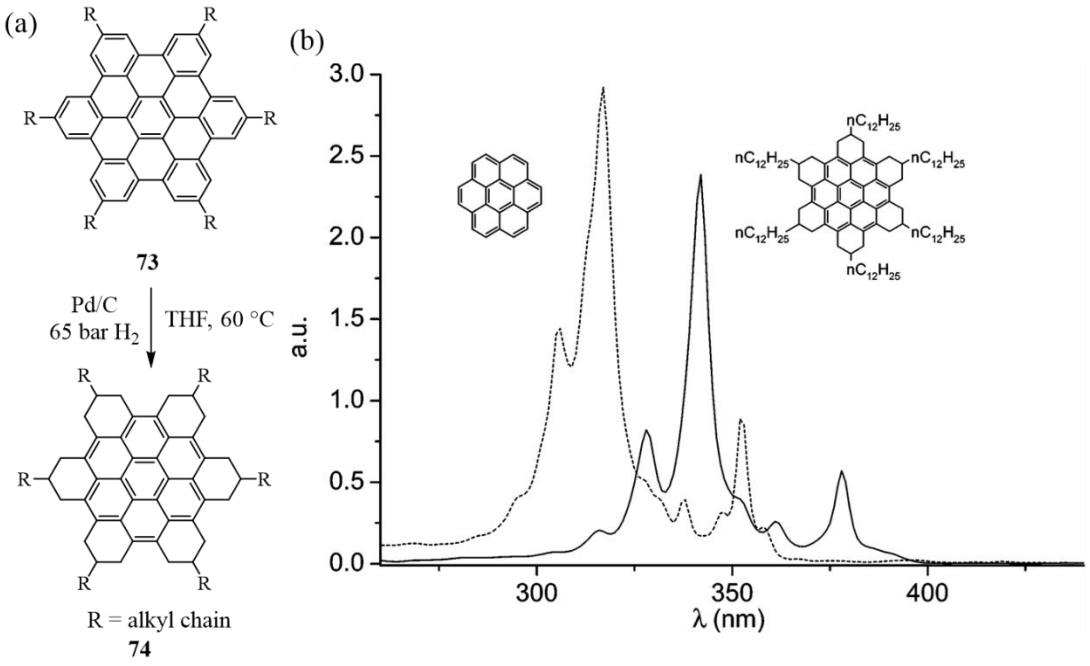

Figure 20. (a) Regioselective hydrogenation of *p*-HBC derivatives **73** toward peralkylated coronenes **74**; (b) UV-vis spectrum of coronene and **74**. Reprinted with permission from Ref.[105], copyright (2004), American Chemical Society.

1.2 Synthetic strategies for GNRs

Generally, GNRs can be fabricated via either "top-down" or "bottom-up" approaches. The former involves the use of some other carbon allotropes such as graphene sheets and carbon

nanotubes as starting materials (Figure 21). Specifically, lithography techniques which are frequently used in semiconductor industry have been applied to the fabrication of GNRs through graphene "cutting".[106] Besides, unzipping CNTs along the longitudinal direction via solution-based oxidative treatment[107] or exploiting transition metal particles (e.g. Co, Ni, or Cu) as chemical scissors to cut CNTs[108] or polymer-protected plasma etching has also turned out be effective way.[109] A wide range of GNRs with width differing from over 500 nm down to sub 5 nm thus have been fabricated through the "top-down" protocol.[110] However, drawbacks cannot be avoided for "top-down", entailing unidentified structural disorder and defects as well as imprecise edge structure, which are unfavourable for the performance of the resulting GNRs. Besides, when GNRs with sub-2-nm width, a practical energy bandgap can be achieved, however, it still remains challenging to achieve widths as narrow as 1–3 nm by means of top-down methods, not to mention the limited control over the edge structure.

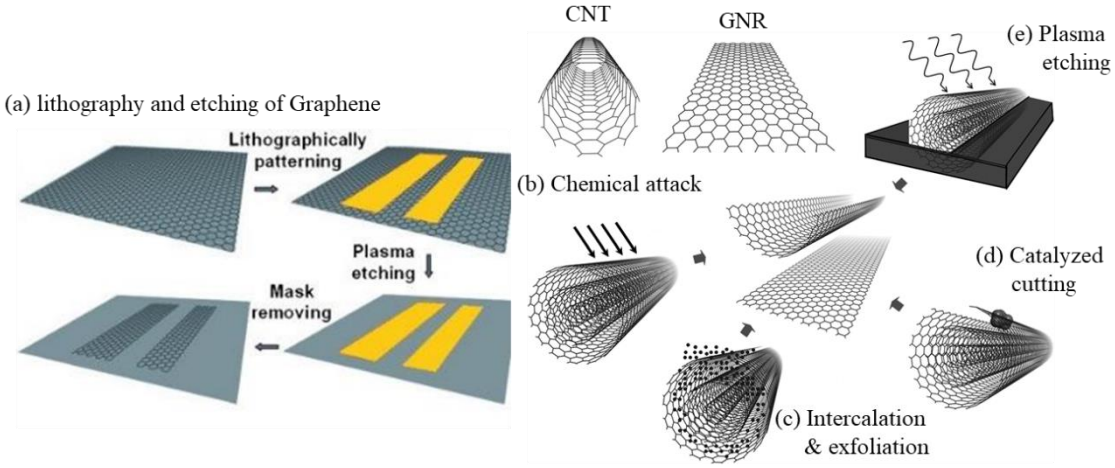

Figure 21. Top-down synthesis of GNRs. Reprinted with permission from Ref.[110], copyright (2012) WILEY-VCH Verlag GmbH & Co. KGaA, Weinheim.

Bottom-up synthesis including solution-mediated and surface-assisted protocols appears more promising for atomically precise GNRs (Figure 22). Based on rational design and synthesis of molecular precursors, GNRs with well-defined width and atomically precise edge structure can be obtained. The most representative work on in-solution synthesis of GNRs was reported by Muellen et al.[111] in 2014 via AB-type Diels–Alder polymerization followed by cyclodehydrogentaion, leading to GNRs with much longer length than that of through AA-type Yamamoto[112] or A_2B_2-type Suzuki polymerization[113] methods (Figure 22a). Pioneering work of on-surface synthesis was developed by Müllen and Fasel et al[114] through direct growth of GNRs on metal surfaces under UHV conditions (Figure 22b). Simultaneously, the atomically precise structures of resulting GNRs can be clearly visualized in situ by using state-

of-the-art high-resolution STM and nc-AFM. On-surface synthesis of GNRs has become a popular approach in the field of GNR research nowadays.

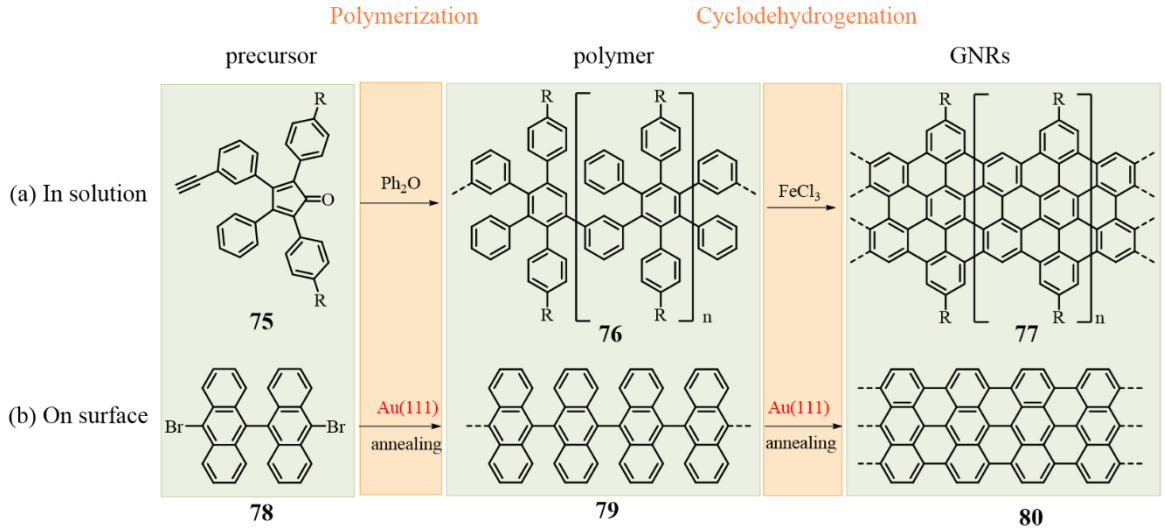

Figure 22. Bottom-up synthesis of GNRs: (a) In solution synthesis; (b) on surface synthesis.

1.3 Peripheral structure makes difference in GNRs

Until now, armchair GNR and zigzag GNR are two representative cases that have attracted the greatest interest in the GNR field (Figure 23a, b). The number of carbon atoms across the ribbon has been used to distinguish ribbons with different widths. For example, the armchair GNR shown in Figure 24a, N = 9 is typically referred to 9-AGNR, whereas for the zigzag GNR shown in Figure 24b, N = 6 is 6-ZGNR. In 1996, Nakada et al.[116] first revealed that the electronic properties of armchair and zigzag GNRs are quite different through tight-bonding calculations. AGNRs can be divided into three families with N = 3n, 3n + 1, and 3n + 2, where n is a positive integer. Compared to AGNRs from N = 3n and 3n + 1, GNRs from N = 3n + 2 have much lower bandgaps.[115,117] While the bandgaps of each family decrease as the ribbon widths increase, suggesting that the bandgap is inversely proportional to the ribbon's width (Figure 23c). Nevertheless, unlike AGNRs, ZGNRs are predicted to have nonbonding edge states that can be manipulated via an external electric field, promising for the application of spintronics.[115,118] Besides, bandgaps of ZGNRs display smaller width dependence than that of AGNRs. Moreover, as demonstrated in Figure 23d, ZGNRs with width narrower than 7 nm and an electronic bandgap of about 0.2–0.3 eV are semiconductors. Further increasing the ZGNRs width, a semiconductor-to-metal transition is observed.[115]

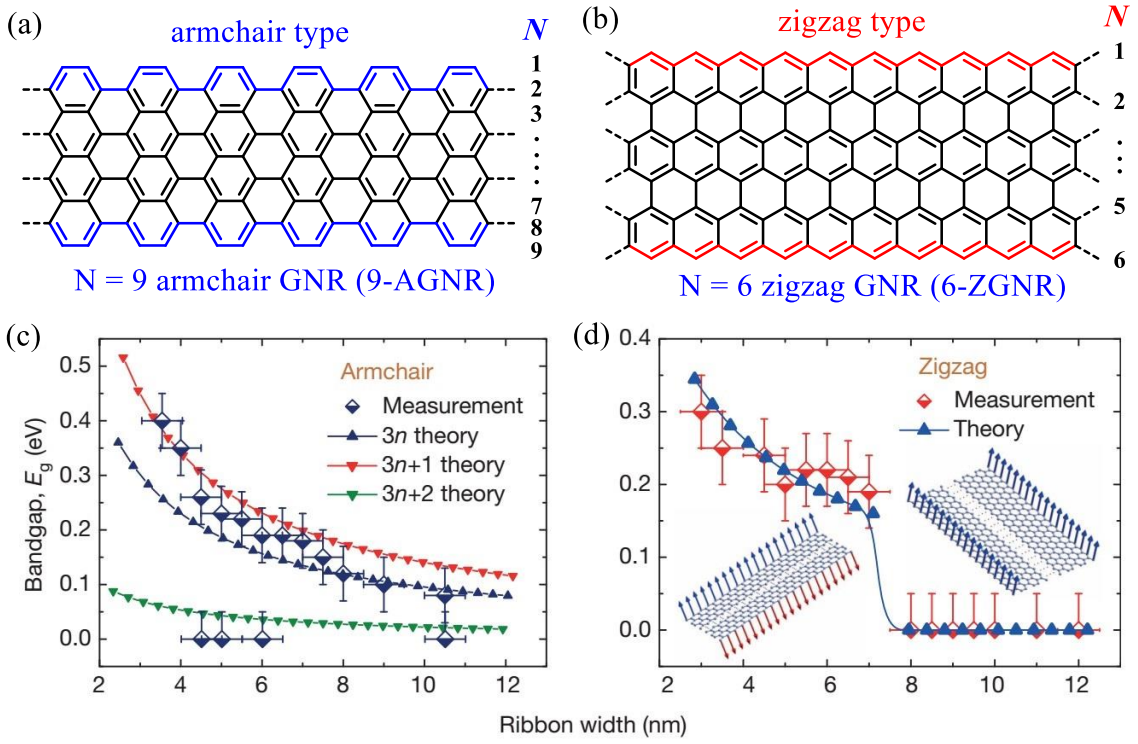

Figure 23. (a, b) Chemical structures of N = 9 armchair GNRs (9-AGNRs) and N = 6 zigzag GNRs (6-ZGNRs) with illustration of width N; (c, d) bandgaps in AGNRs and ZGNRs as a function of ribbon widths. Reprinted with permission from Ref.[115], copyright (2014), Springer Nature.

1.4.1 GNRs with armchair-edged structure

In 2008, Müllen et al.[113] first established a pioneering method for the solution synthesis of N = 9 GNRs with armchair-edged structure (9-AGNRs) through A_2B_2-type Suzuki polymerization, followed by cyclodehydrogenation of the polyphenylene precursor (Figure 24a). Notably, the introduction of alkyl chains to **84** brings about sufficient solubility in common solvents such as dichloromethane and tetrahydrofuran, which is promising for solution processing. The UV-vis spectrum of **84** shows an intense absorption at 485 nm but a significant red shift of around 200 nm compared to that of **83**, confirming the extended aromatic system of **84**. While synthetically remarkable, A_2B_2-Suzuki polymerization is challenging to approach GNRs with high molecular weight due to the difficulties of avoiding stoichiometric imbalances between two monomers. An improved AB-type Suzuki polymerization was reported by Dong's group[119] in 2016 via the designed monomer of 2,3-bisarylated 4-

bromophenylboric acid ester **85** (Figure 24b). The polyphenylene precursor **86** with a molecular weight of 30.6 KDa was synthesized and a polydispersity index of 1.40. Upon cyclodehydrogenation, the resulting N = 9 armchair GNR **87** exhibits semiconducting properties with a bandgap of approximately 1.1 eV as characterized by U-vis-NIR spectroscopy as well as cyclic voltammetry. Besides, the absorption band founded at 900 nm indicates the largely extended π-skeleton of 9-AGNRs. Besides, the feasibility of large-scale production makes this kind of armchair-edge GNRs promising for electronic applications, logic transistors for example.

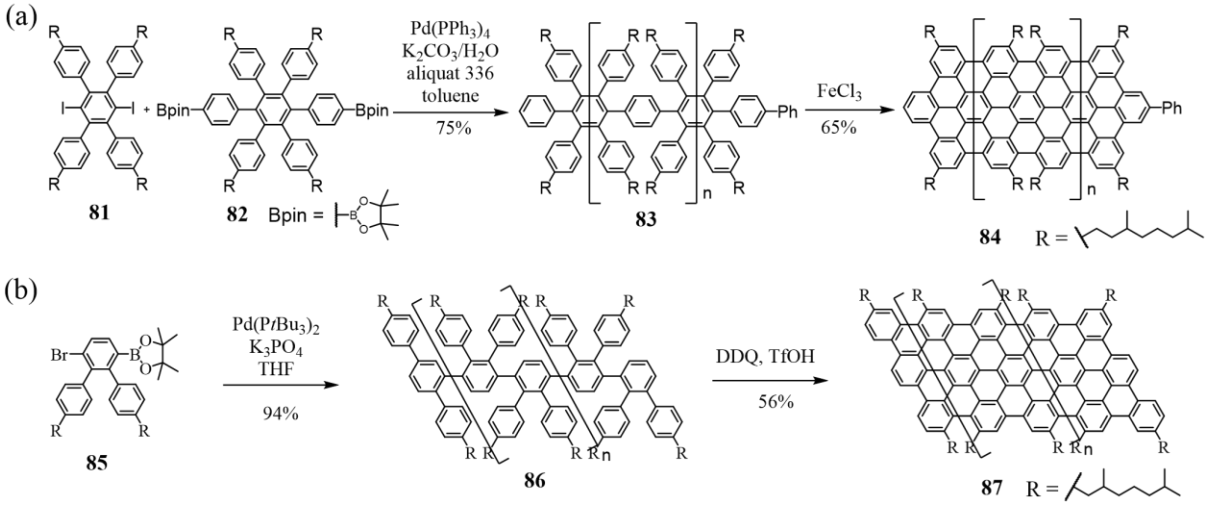

Figure 24. In-solution synthesis of GNRs with armchair periphery: (a) A_2B_2-type Suzuki polymerization; (b) AB-type Suzuki polymerization.

Proving the structural characteristics of such AGNRs synthesized in solution at the atomic level remains a challenge task. Therefore, on-surface synthesis combining with the state-of-the-art of scanning probe techniques is valuable, which enabled an in situ visualization of the obtained GNRs and further detection of its electronic property. In 2010, the seminal work of Müllen and Fasel et al.[114] demonstrated the on-surface synthesis of N = 7 GNR with atomically smooth armchair edges. 10,10'-Dibromo-9,9'-bianthryl **78** was used as precursor, which underwent metal-surface-assisted homocoupling to form linear polymer. Subsequent thermal-induced cyclodehydrogenation directly furnished GNR **80** on a metal surface (Figure 25). The metal surface serves as not only substrate for supporting, but also catalyst for biradical formation and coupling. High-resolution STM unambiguously revealed the well-defined structure of 7-AGNRs at an atomic level. Besides, STS characterization gives a bandgap of 2.3 eV for this 7-AGNR supported on Au(111). This work has become a game changer in the field of GNRs fabrication and opened up a new field of on-surface synthesis of atomically precise

GNRs. Since 2010, the surface-assisted synthesis has become a popular and reliable strategy for the preparation of atomically precise GNRs. Various GNRs with different widths, featuring armchair-edged structure have been made, such as 5-AGNRs,[120,121] 9-AGNRs[122] and 13-AGNRs,[123] intriguing electronic properties have been revealed.

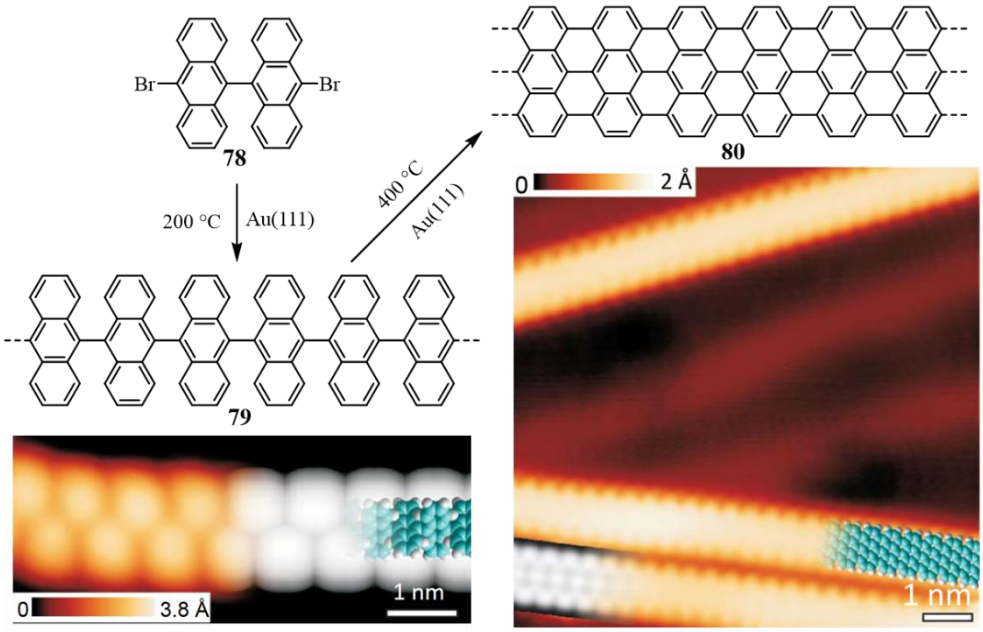

Figure 25. Surface-assisted synthesis of 7-AGNRs. High-resolution STM images were reprinted with permission from Ref.[114], copyright (2010), Springer Nature.

1.4.2 GNRs with zigzag-edged structure

Unlike armchair GNRs, the research in bottom-up synthesis of GNRs with zigzag periphery is remaining largely underdeveloped. Considering the model compound of ZGNRs, i.e. peri-acenes, either the difficulty of precursor synthesis or the intrinsic instability explain the difficult access to ZGNRs in solution. Nevertheless, the problem can be eliminated by surface-assisted synthesis under UHV, which prevents side reactions of oxidation and stabilizes the resulted conjugated structure by interaction with the metal surface. Although on-surface synthesis provides a feasible approach, ZGNR' syntheses are beyond the strength of conventional surface-assisted linear benzene-benzene coupling, which is efficient for AGNRs. Thus, a new precursor design concept is particularly needed and pivotal.

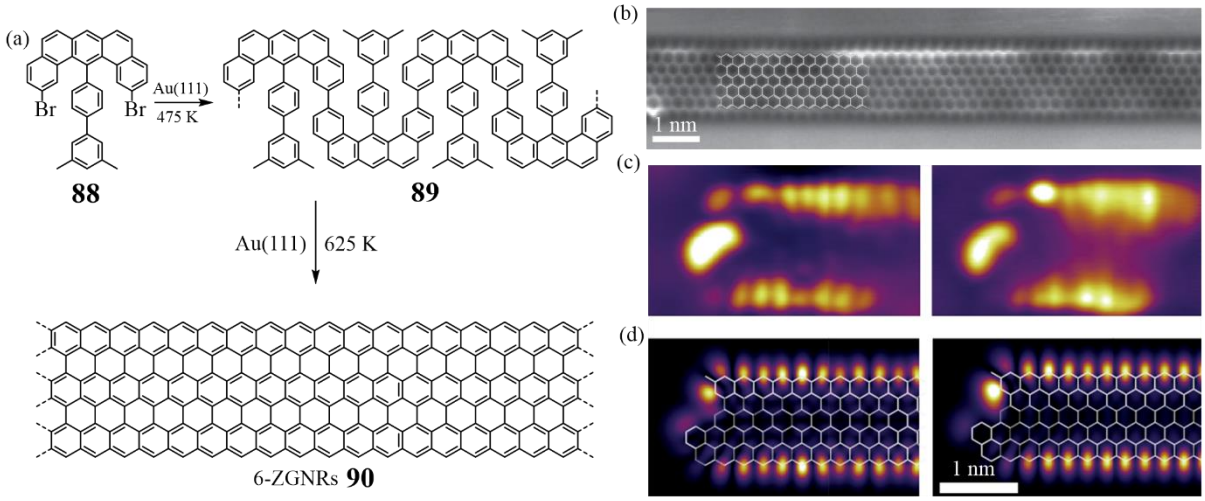

Figure 26. (a) Surface-assisted synthesis of 6-ZGNRs; (b) nc-AFM image of 85; (c) experimental d*I*/d*V* map of **90** on sodium chloride substrate; (d) theoretical d*I*/d*V* map of **90** .(c) and (d) were reprinted with permission from Ref.[33], copyright (2016), Springer Nature.

A landmark breakthrough has been made by Müllen and Fasel et al.[33] in 2016. In their work, the atomically precise 6-ZGNRs was achieved from a rationally designed umbrella-shaped monomer **88** possessing a short zigzag edge intrinsically and methyl groups (Figure 26a). Those two protruding methyl groups underwent oxidative cyclization with the neighbouring benzene rings to form full zigzag edges on Au (111) surface under UHV. It is worth to mention that only the synthesis of **88** took 14 steps, highlighting the indispensable role of demanding chemistry in the bottom-up fabrication of GNRs. nc-AFM imaging with a CO-functionalized tip enables the direct observation of local bond formation, which clearly proves the edge morphology of 6-ZGNRs **90** (Figure 26b). Because of the strong electronic coupling between the ribbons and metal surface, the detection of the electronic edge states of 6-ZGNRs on Au(111) surface becomes difficult. However, by manipulation with the STM tip, 6-AGNR can be directly dragged onto post-deposited insulating sodium chloride island, the effect of metal substrate thus is excluded and local electronic edge state is observed which is well consistent with theoretical predictions (Figure 26c,d). Up to now, the synthesis of atomically precise GNRs with zigzag periphery has been rarely reported. To investigate the width-dependent properties, ZGNRs with a variety of width should be explored. This remains a long-term goal in GNR research.

1.4.3 GNRs with heteroatom-doped edge structure

Doping of GNRs is a key aspect to fully develop the possibilities of these nanostructures as alternative material for semiconductor applications, since heteroatoms have been expected to modify either electronic properties or assembly behaviour of GNRs. In 2013, N-doped chevron-type GNR was reported by Bronner, Hecht, and Tegeder et al.[124] through applying 4,4'-(6,11-dibromo-1,4-diphenyltriphenylene-2,3-diyl)dipyridine **91** as precursor on Au(111) surface synthesis (Figure 27a). Later, the precise structure of N-doped GNR **92** was revealed by high-resolution STM.[125] Interestingly, due to the attractive N···H interactions, N-doped GNRs took a side-by-side alignment (Figure 27b). Furthermore, the N-doping makes no significant changes in the bandgap, while simultaneously lowering the energy levels of the valence and conduction bands of peripheral N-doped GNRs. In 2014, Müllen and Fasel et al.[126] reported the on-surface synthesis of a GNR composed of alternating N-doped and pristine chevron-type ribbon segments (Figure 27c), which represents the first example of a molecular p-n junction in a single-GNR **95** (Figure 27d,e). Significantly, this N-doped GNR heterojunction represents the first example of a molecular p–n junction in single-GNR, exhibiting a band offset of approximately 0.5 eV and and an electric field of 2×10^8 V m^{-1}.

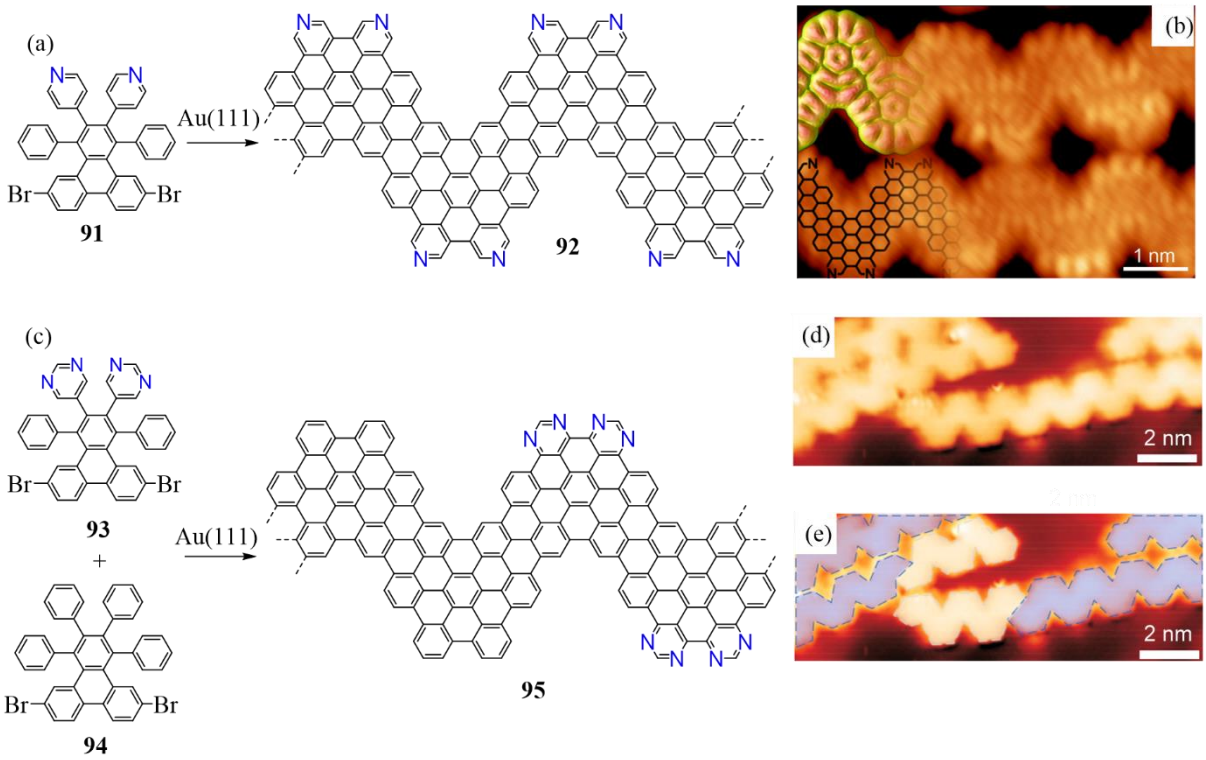

Figure27. (a) Surface-assisted synthesis of N-doped chevron-type GNR **92**. (b) High-resolution STM image of GNR **92**, displaying a side-by-side alignment via the inter-ribbon

N···H interactions. Reprinted with permission from Ref.[125], copyright (2014) AIP Publishing LLC. (c) Surface-assisted synthesis of GNR heterojunction **95**. (d,e) STM images of GNR heterojunction **95**, with N-doped and pristine GNR segments highlighted in blue and light gray dash lines, respectively. Reprinted with permission from Ref.[126], copyright (2014) Macmillan Publishers Ltd.

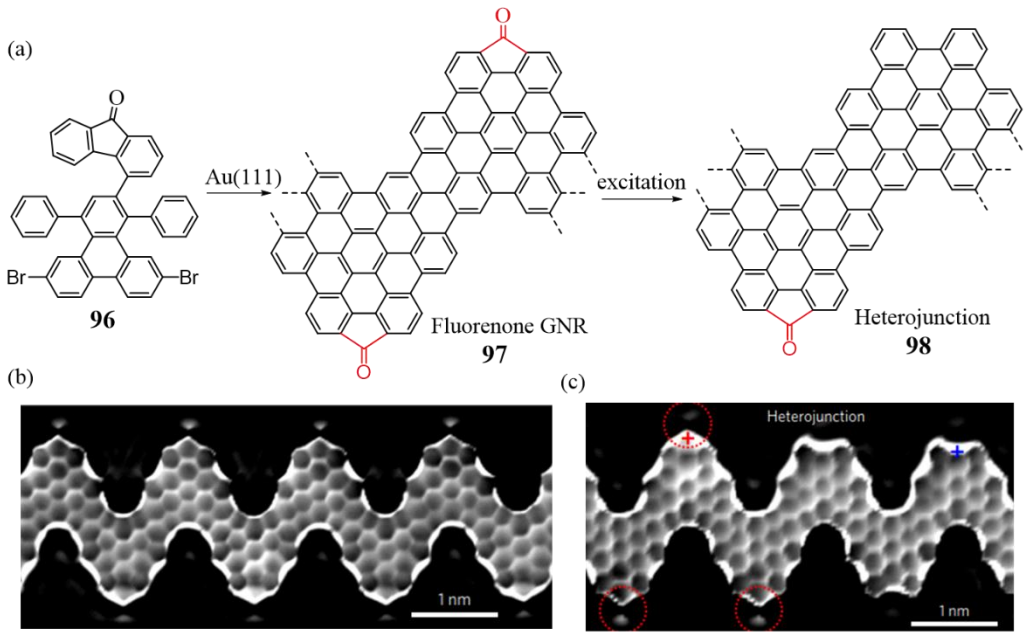

Figure 28. (a) Surface-assisted synthesis of Chevron-type GNRs featuring O-doped periphery; (b) bond-resolved STM image of **97**; (c) bond-resolved image of heterojunction **98**. (b) and (c) were reprinted with permission from Ref.[127], copyright (2017), Springer Nature.

Later on, another type of GNR heterojunction was described by Louie, Fischer and Crommie et al.[127] Starting from a single precursor molecule **96**, which contains sacrificial carbonyl groups, chevron-type GNRs featuring a regular pattern of 9*H*-fluoren-9-one substituents along their convex edges were prepared on Au(111) surfaces (Figure 28a). Bond-resolved STM clearly proves the chevron-type GNR backbone as well as the cyclopentadienone groups derived from fluorenone substituents (Figure 28b). The resulting bandgap for fuorenone GNR **97** is 2.33 eV, smaller than that of the pristine chevron-type GNR by 0.20 eV. Upon further thermal annealing, all of the carbonyl groups were cleaved within localized segments of fluorenone GNRs, thus a heterojunction consisting of a segment of decarbonylated chevron GNR and a segment of fluorenone GNR was formed (Figure 28c). STS measurements revealed that the bandgap of functionalized and unfunctionalized nanoribbons is quite different, thus an effective field of 5×10^8 V m^{-1} across the GNR **98** heterojunction interface is generated, which are of considerable interest for future application

in nanoelectronics. Through molecular engineering of the triphenylene-based monomers, Louie and Fischer et al. further succeeded in making heteroatom-doped chevron-type GNRs with trigonal planar S-, N-, and O-dopant atoms.[128] A characteristic shift of valence band and conduction band as well as reduced bandgap were observed for the doped GNRs.

In 2017, two independent works on S-doped GNRs were reported. One describes the on-surface synthesis of S-doped GNR **100** by employing 6,11-dibromo-1,4-diphenyl-2,3-di-(thien-3-yl)-triphenylene **99** as the monomer (Figure 29a).[129] Because of the rotation of the single bonds connecting thienyl rings and the triphenylene core, different isomers are obtained when deposited onto the Au(111) surface. Further polymerization and cyclodehydrogenation on Au(111) surface result in different S-doped GNR segments (Figure 29b), giving rise to a sequence of tunable bandgaps, as confirmed by experimental STM and STS as well as theoretical DFT calculations. The other study demonstrated a S-doped 13-AGNR **102** by applying a precursor of 10,10'-dibromo-9,9'-bisanthracene **101** featuring (2-phenyl)thiophene substituents followed by the on surface protocol (Figure 29c,d).[130]

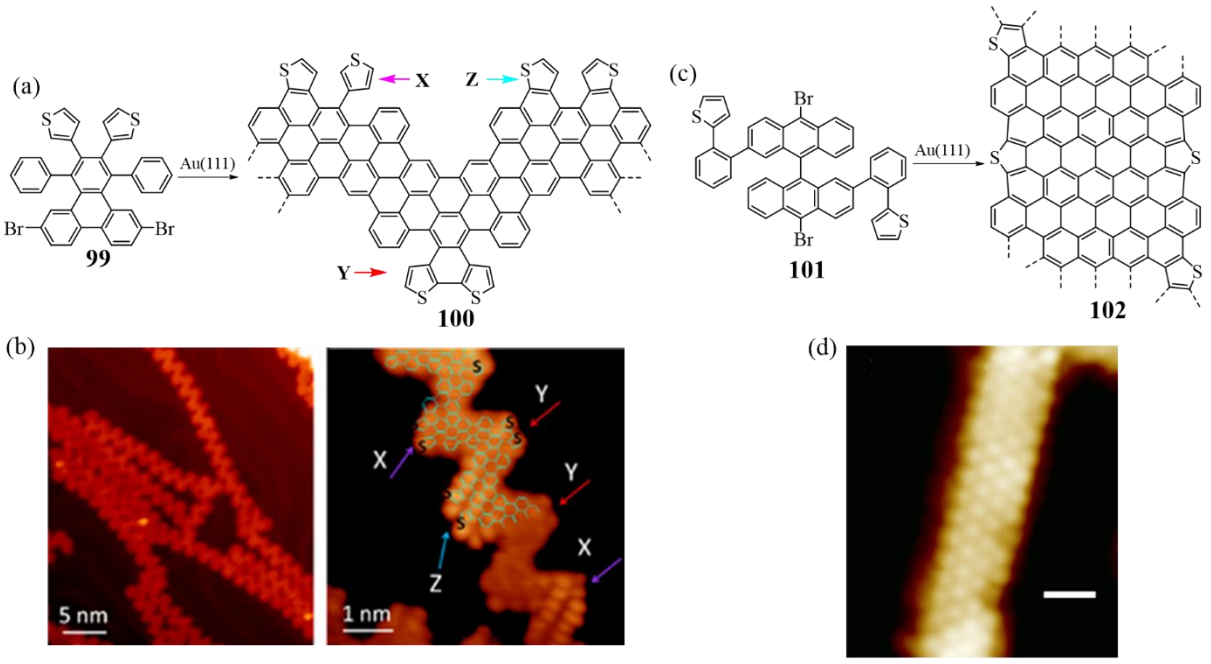

Figure 29. (a) Surface-assisted synthesis of S-doped GNR **100**; (b) STM images of GNR **100**; (c) surface-assisted synthesis of S-doped GNR **102**; (d) STM image of GNR **102**. (b) was reprinted with permission from Ref.[129], copyright (2017) Tsinghua University Press and Springer-Verlag GmbH Germany. (d) was reprinted with permission from Ref., copyright (2016) American Chemical Society.

The bottom-up synthesis of GNRs with multiple heteroatom-doped edge structure is much less described compared to that of single heteroatom-doped. However, the study and understanding of the doping effects of multiple heteroatoms on electronic properties is of particular significance. Thus, in 2018, Fasel, Müllen and Narita et al.[131] claimed the surface-assisted synthesis of the first oxygen–boron–oxygen (OBO)-doped chiral (4,1)-GNR **104** from the rationally designed precursor 6,16-dibromo-9,10,19,20-tetraoxa-9a,19a-diboratetrabenzo[*a*,*f*,*j*,*o*]perylene **103** (Figure 30a). The structure of the OBO-doped chiral GNRs is corroborated by STM and nc-AFM (Figure 30b-d). STS study demonstrates that this OBO-doped GNR has a larger bandgap of 3.33 eV when compared to that of all-carbon chiral (4,1)-GNR, which can be ascribed to the weak conjugation of the p_z orbitals of the OBO segments with the extended π-system of the carbon backbone of the GNR. Furthermore, the OBO-doped GNRs are found to laterally align on the Au(111) substrate, arising from interribbon O···H interactions. This unique self-assembly property of this kind of OBO-doped GNRs could hold great promises for the application in GNR-based devices since a good connection between electrodes could be achieved.

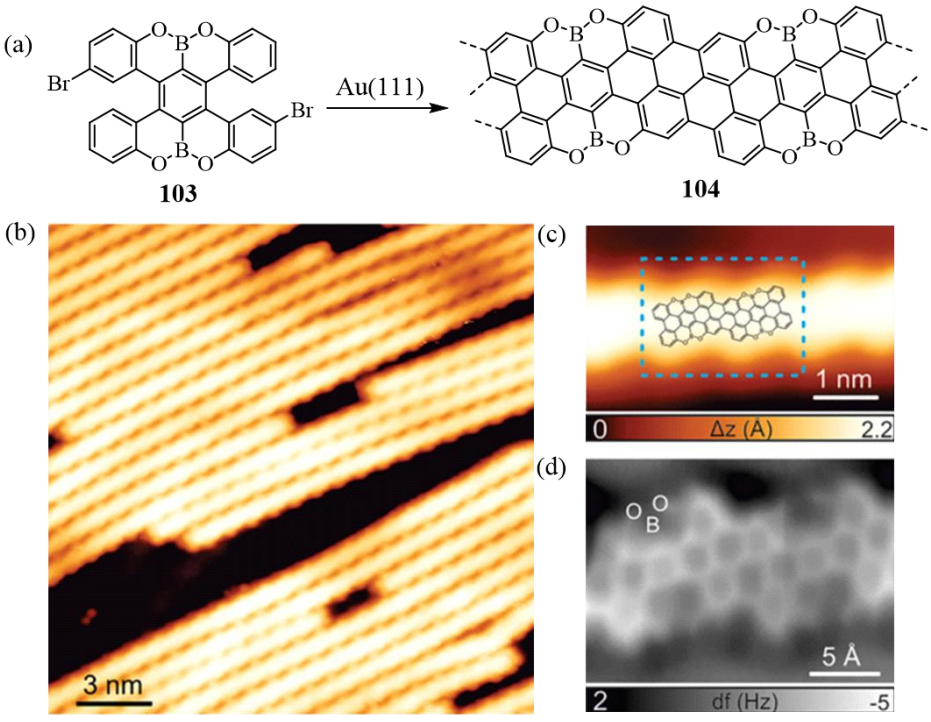

Figure 30. (a) Surface-assisted synthesis of the OBO-doped (4,1)-GNR **104**. (b) Large-area STM image and (c) high-resolution STM image of GNR **104** on Au(111). (d) nc-AFM of GNR **104**. Images were reprinted with permission from Ref., copyright (2018) American Chemical Society.

1.4 GNR theory: topological phase

Materials in nature can be basically divided into three categories: conductor, semiconductor and insulator, based on their electric transport property. In a conductor, such as a metal, there is no energy gap between the valence band (VB) and conduction band (CB), and electrons can flow from VB to CB easily, realizing electric conduction (Figure 31a). For an insulator, the energy gap lies between VB and CB is quite large, and makes electrons hard to jump from VB to CB, thus disallowing electrical conduction (Figure 31c). For a semiconductor, the energy gap can be covered by an appropriate external excitation, like an electrical field, thus generating conductivity (Figure 31b).

In 2016 the Noble Prize in physics has brought a new member into the classification of materials, the topological insulator. Comparing with normal insulator which keeps a totally opened energy gap, topological insulator behaves as insulator in its interior but whose surface or edge contains a gapless state (Figure 31d). The zero energy boundary state is protected by the intrinsic topological property of materials, thus defects or impurities in topological insulators cannot impose any influence on it. Simultaneously, electrons with different spin only move along within different edge of topological insulators. These unique properties of a topological insulator could bring promising applications in electronics. It has attracted enormous attention from scientists and engineers which seem to be confused and frustrated by "the ending of Moore's law is approaching".

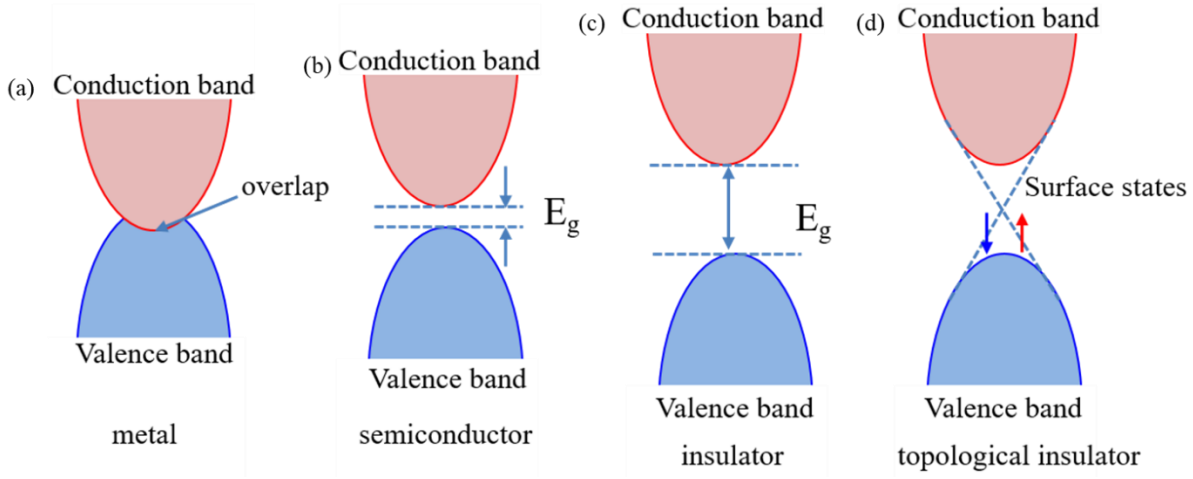

Figure 31. Band structures of (a) metal; (b) semiconductor; (c) insulator; and (d) topological insulator.

The more and more shrunken size in semiconductor devices has caused vast energy losses and heat production. When looked upon from classic thermodynamics, this is because of the chaotic motion of electrons, and concomitant collisions, like cars in a traffic jam (Figure 32a). However, in a topological insulator this kind of situation can be totally avoided, electrons can move smoothly and rapidly, just analogous to cars drives in two-lane highway (Figure 32b). The advent of topological insulators will greatly promote the development of the electronics and semiconductor industry. As an achievement great significance, Zhang et al.[132,133] have initially brought the topological insulator, HgTe, into reality.

Figure 32. Illustration of (a) traffic jam in chips today; (b) info highways for the chips in the future.

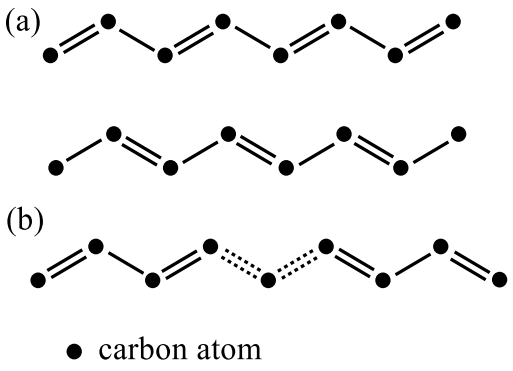

Figure 33. (a) The two degenerate structures in *trans*-polyacetylene based on SSH model; (b) a soliton separates the two degenerate structures.

The theoretical and experimental study of topological phases is nowadays concentrating on either 2D or 3D inorganic materials, like HgTe, Bi_2Te_3 and Sb_2Te_3, but topological phases in 1D materials have remained a matter of theory, while there is no experimental evidence. The earliest theoretical research into 1D materials with topological phase can be traced to the introduction of the SSH model by Su, Schrieffer and Heeger[134,135] in which the concept of solitons in conducting polymers has been raised to explain the conductivity of trans-

polyacetylene. The thermodynamically stable configuration of polyacetylene is a sequence of alternating single and double bonds, thus, there are two different states in linear conjugated polyacetylene, as shown in Figure 33a. When those two modes of bond arrangement coexist in one polyacetylene chain, a structural "defect" is created at the interface, which is soliton (Figure 33b). Intriguingly, interfaces between these two states are related to zero energy boundary states. A soliton can propagate along within a polyacytylene chain, leading to conductivity. In particular, as described by the SSH model, for a finite chain of polyacetylene there are gapless topological states localized at its ends. The key component in the SSH model is an alternation of weak and strong coupling strength between neighbouring orbitals of carbons.

Recently, Louie et al.[136] introduced the classification of topological phase in AGNRs. According to their theoretical works, AGNRs can be classified into a topological trivial category and a topological non-trivial category based on its width and terminating unit cell. An integer 0 or 1, called Z_2 topological invariant, is introduced to describe the difference. $Z_2 = 0$ indicates a trivial topological insulator, whereas $Z_2 = 1$ demonstrates a nontrivial topological insulator. Topology is the mathematical study of global properties of an object preserved under continuous deformations and characterized by invariants. The global properties are stable and only change in integer steps. For example, a bun has zero hole, while a donut keeps one and a pretzel has two holes, thus, the number of holes is topologically invariant that is always an integer but never anything between. Interestingly, when two kinds of AGNRs possessing different topological invariants combine together, a zero energy state can be produced at the interface. There are two possible junctions which can be formed when 7-AGNRs connect with 9-AGNRs, as shown in Figure 34. For the nonsymmetric junction, both the 7-and 9-segments have $Z_2 = 1$, which is topologically equivalent, therefore, there is no interface state. While for the symmetric junction, 7-AGNRs shift laterally with 9-AGNRs, leading to topological inequivalence between these two segments, and one localized interface state emerges as a result.

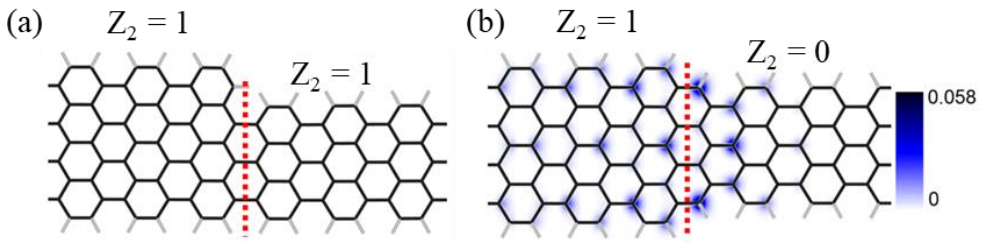

Figure 34. Heterojunctions formed with N = 9 and N = 7 armchair graphene nanoribbons (9-AGNR/7-AGNR) between two (a) topologically equivalent segments and (b) topologically inequivalent segments.

Theoreticians have predicted such topological phases in 1D systems, however, it is desirable to rationally engineer topological phases into materials with stability and processibility to exploit the corresponding properties. The above described chemical approach has offered absolute structure control of 1D materials at the atomic level, on-surface synthesis for example, and thus can serve as an enabling strategy to develop unprecedented topological phases featuring exceptional properties.

1.5 Objectives and motivation

Heteroatom-doped PAHs have long been used as chromophores and semiconducting materials. The rise of graphene at the turn of 21st has created a new impetus for research into atomically precise heteroatom-doped PAHs, which serve as model systems to establish concise structure-property relationships on graphene. Much beyond their role as model systems, heteroatom-doped PAHs with different sizes and edge structures, already in their own right, facilitate the development of material science extensively by their intriguing photophysical properties, being explored as NIR-active dyes, two-photon absorbers and fluorescence sensors. Noteworthy, except the size and peripheral structure of PAHs, attention should also be paid to the type and position of heteroatom doping. Heteroatom-doping of PAHs also promotes the synthesis of stable π-systems with charges or spins.

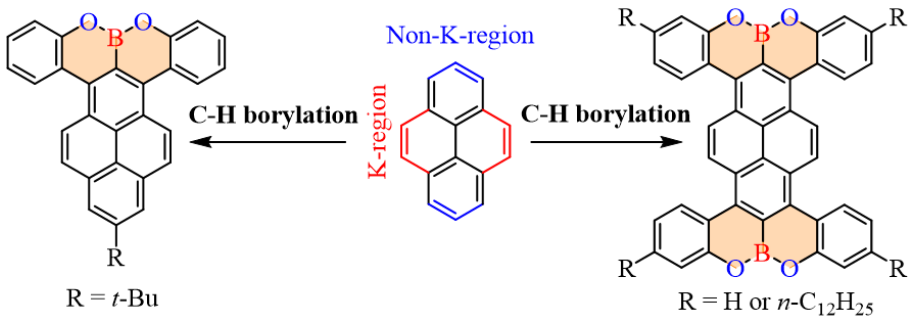

Figure 35. Structure of oxaborin-annelated pyrene derivatives.

As depicted in previous sections, PAHs with zigzag periphery exhibit unique electronic properties thanks to the spin-polarized states at zigzag sites. Despite such appealing characteristics, their syntheses and characterizations are hindered by the low stability. Heteroatom doping of all-carbon zigzag edges provides an opportunity to stabilize PAHs featuring zigzag periphery. Extending π-conjugated cores by fusing heteroatoms has uncovered not only intriguing electronic properties, but is also of particular interest for self-assembly,

showing promising applications in photonics and optoelectronics. Nevertheless, examples of PAHs with heteroatom-doped edges are still scarce, which is ascribed to the lack of efficient synthetic protocols. This, in turn, is an obstacle for developing new types of functional materials with unique properties. In chapter 2, a new kind of oxaborin-annelated pyrene-based chromophores featuring zigzag peripheral structure was synthesized via tandem demethylation-borylation reaction (Figure 35). The direct π-extension at chemically inert non-K-region of pyrene with multiple heteroatoms provides a new access to photonic and optoelectronic materials.

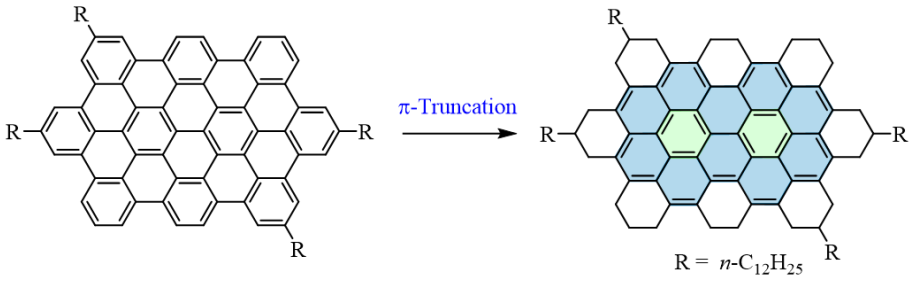

Figure 36. π-Truncation towards peralkylated circumbiphenyl.

As mentioned before, the synthesis of large PAHs is mainly dominated by either the two-stage strategy or the π-extension approach. Indeed, exciting PAHs featuring different shapes, sizes and edge structures have been targeted. However, for the synthesis of some PAHs with unique π-skeleton and periphery, such as circumbiphenyl, those two approaches can only play a limited role. Noteworthy, the properties of PAHs are primarily dependent on its aromatic core structure and thus the synthesis of different aromatic structures is essential. The aforementioned protocols towards PAHs are the "expansion" of the aromatic cores. Nevertheless, there are only very limited examples to obtain certain PAH structures starting from larger PAHs, namely by "shrinking" the aromatic cores. Inspired by the hydrogenation of HBC, in chapter 3, a π-truncation strategy was first developed to acquire a circumbiphenyl core with alkylated edge structure. Distinguished from the aforementioned ways, in this π-truncation motif, a large PAHs consisting of 60 sp^2 carbons featuring armchair edges served as starting material for PAHs with unique aromatic core and edge (Figure 36). Remarkably, hydrogenation only restricted to the peripheral sites, displaying high regioselectivity. Characterizations on the resulted peralkylated circumbiphenyl revealed interesting optoelectronic properties, offering promising applications in future nanoelectronics as optical gain materials.

Since the seminal work of Müllen and Fasel et al on atomically precise GNRs, researches into GNRs field have attracted tremendous attentions. Intriguing properties of GNRs

with different widths and peripheral structures have been uncovered, especially related to spin-localized state in GNRs with full zigzag-edge structure. Recently, devices based on bottom-up synthesized GNRs have been realized, which takes a step further towards the promising applications of GNRs in future electronics, such as transistors and spintronics. It is noticeable that interdisciplinary collaborations among chemists, physicists and material scientists have played an indispensable role in the achievements of GNRs. Curiosity has always pushed human beings to unceasingly explore new domains. Is there any unexplored aspect about GNRs? As discussed above, topological insulators have become one of the hottest research fields of condensed physics, and until now 2D and 3D materials with topological phase have been studied, but 1D materials with topological phases is still in the dark. GNRs with atomically precise structures are typical 1D materials, without doubt, they are ideal candidates to verify the existence of topological phases. Even though, computational works have predicted such topological phases, experimental evidence is missing due to the great difficulty encountered in material fabrication. Chemistry-wise, in chapter 4, two kinds of GNRs with partially hybridized armchair and zigzag edge peripheral structures have been successfully produced via rational precursor design combined with surface-assisted synthesis (Figure 37). By varying precursor molecules though careful design, the topological phase in GNRs can be precisely tuned from trivial to non-trivial, to finally offer an experimental realization of the SSH model.

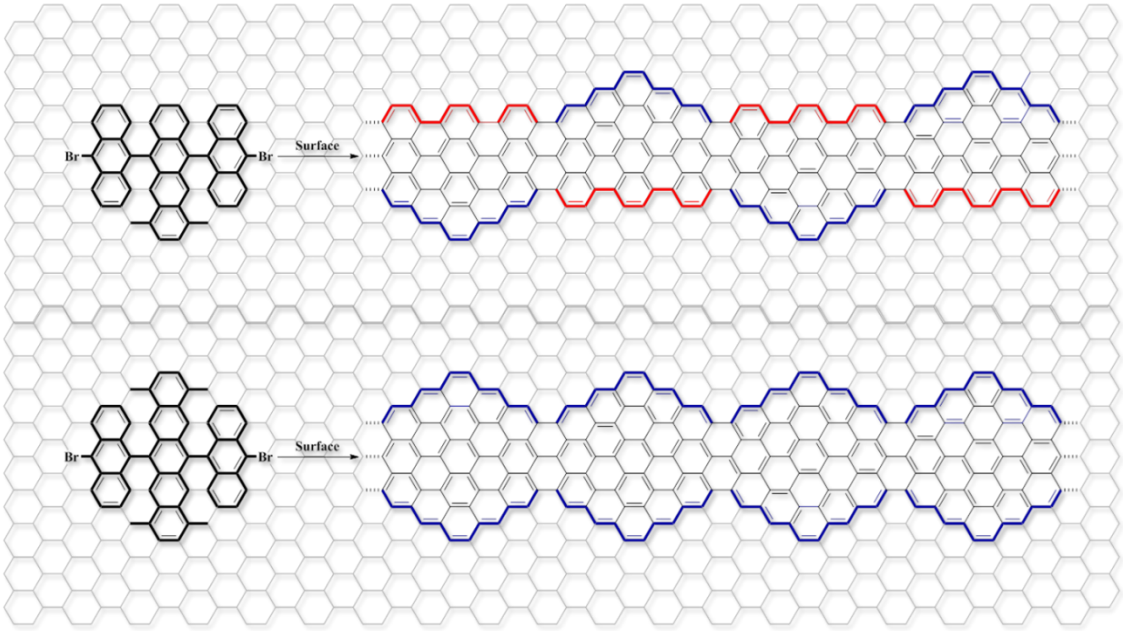

Figure 37. Structure of GNRs with topological phase.

1.7 References:

[1] R. E. Peierls. *Ann. Inst. Henri Poincare* **1935**, *5*, 177-222.

[2] L. D. Landau. *Phys. Z. Sowjetunion* **1937**, *11*, 26-35.

[3] N. D. Mermin. *Phys. Rev.* **1968**, *176*, 250-254.

[4] K. S. Novoselov; A. K. Geim; S. V. Morozov; D. Jiang; Y. Zhang; S. V. Dubonos; I. V. Grigorieva; A. A. Firsov. *Science* **2004**, *306*, 666.

[5] K. S. Novoselov; V. I. Falko; L. Colombo; P. R. Gellert; M. G. Schwab; K. Kim. *Nature* **2012**, *490*, 192-200.

[6] K. A. Ritter; J. W. Lyding. *Nat. Mater.* **2009**, *8*, 235.

[7] Y. Cao; V. Fatemi; A. Demir; S. Fang; S. L. Tomarken; J. Y. Luo; J. D. Sanchez-Yamagishi; K. Watanabe; T. Taniguchi; E. Kaxiras; R. C. Ashoori; P. Jarillo-Herrero. *Nature* **2018**, *556*, 80.

[8] Y. Cao; V. Fatemi; S. Fang; K. Watanabe; T. Taniguchi; E. Kaxiras; P. Jarillo-Herrero. *Nature* **2018**, *556*, 43.

[9] A. Narita; X.-Y. Wang; X. Feng; K. Mullen. *Chem. Soc. Rev.* **2015**, *44*, 6616-6643.

[10] A. H. Castro Neto; F. Guinea; N. M. R. Peres; K. S. Novoselov; A. K. Geim. *Reviews of Modern Physics* **2009**, *81*, 109-162.

[11] K. I. Bolotin; K. J. Sikes; Z. Jiang; M. Klima; G. Fudenberg; J. Hone; P. Kim; H. L. Stormer. *Solid State Commun.* **2008**, *146*, 351-355.

[12] X. Li; X. Wang; L. Zhang; S. Lee; H. Dai. *Science* **2008**, *319*, 1229.

[13] X. Wang; Y. Ouyang; X. Li; H. Wang; J. Guo; H. Dai. *Phys. Rev. Lett.* **2008**, *100*, 206803.

[14] L. Jiao; X. Wang; G. Diankov; H. Wang; H. Dai. *Nat Nano* **2010**, *5*, 321-325.

[15] J. W. Armit; R. Robinson. *J. Chem. Soc., Trans.* **1925**, *127*, 1604-1618.

[16] E. Hückel. *Z. Phys.* **1931**, *70*, 204-286.

[17] E. Clar; R. Schoental: *Polycyclic Hydrocarbons*; Springer, 1964; Vol. 2.

[18] E. Clar. *John Wiley & Sons LTD, London,* **1972**.

[19] R. Scholl; J. Mansfeld. *Ber. Dtsch. Chem. Ges.* **1910**, *43*, 1734-1746.

[20] R. Scholl; C. Seer; R. Weitzenböck. *Ber. Dtsch. Chem. Ges.* **1910**, *43*, 2202-2209.

[21] R. Scholl; C. Seer. *Justus Liebigs Ann. Chem.* **1912**, *394*, 111-177.

[22] F. Würthner; C. R. Saha-Möller; B. Fimmel; S. Ogi; P. Leowanawat; D. Schmidt. *Chem. Rev.* **2016**, *116*, 962-1052.

[23] L. Chen; C. Li; K. Müllen. *J. Mater. Chem. C* **2014**, *2*, 1938-1956.

[24] J. Fabian; H. Nakazumi; M. Matsuoka. *Chem. Rev.* **1992**, *92*, 1197-1226.

[25] J. E. Anthony. *Chem. Rev.* **2006**, *106*, 5028-5048.

[26] T. M. Figueira-Duarte; K. Müllen. *Chem. Rev.* **2011**, *111*, 7260-7314.

[27] M. Sun; K. Müllen; M. Yin. *Chem. Soc. Rev.* **2016**, *45*, 1513-1528.

[28] C. Wang; H. Dong; W. Hu; Y. Liu; D. Zhu. *Chem. Rev.* **2012**, *112*, 2208-2267.

[29] J. Wu; W. Pisula; K. Müllen. *Chem. Rev.* **2007**, *107*, 718-747.

[30] E. Clar; R. Schoental: *Polycyclic Hydrocarbons*; Springer, 1964; Vol. 1.

[31] Z. Sun; Q. Ye; C. Chi; J. Wu. *Chem. Soc. Rev.* **2012**, *41*, 7857-7889.

[32] Z. Sun; Z. Zeng; J. Wu. *Acc. Chem. Res.* **2014**, *47*, 2582-2591.

[33] P. Ruffieux; S. Wang; B. Yang; C. Sánchez-Sánchez; J. Liu; T. Dienel; L. Talirz; P. Shinde; C. A. Pignedoli; D. Passerone; T. Dumslaff; X. Feng; K. Müllen; R. Fasel. *Nature* **2016**, *531*, 489-492.

[34] M. Stępień; E. Gońka; M. Żyła; N. Sprutta. *Chem. Rev.* **2017**, *117*, 3479-3716.

[35] Q. Sun; R. Zhang; J. Qiu; R. Liu; W. Xu. *Adv. Mater.* **2018**, *30*, 1705630.

[36] L. Talirz; P. Ruffieux; R. Fasel. *Adv. Mater.* **2016**, *28*, 6222-6231.

[37] **2016**.

[38] M. Treier; C. A. Pignedoli; T. Laino; R. Rieger; K. Müllen; D. Passerone; R. Fasel. *Nat. Chem.* **2010**, *3*, 61-67.

[39] X. Yang; X. Dou; K. Müllen. *Chem. Asian J.* **2008**, *3*, 759-766.

[40] J. García-Lacuna; G. Domínguez; J. Blanco-Urgoiti; J. Pérez-Castells. *Org. Lett.* **2018**, *20*, 5219-5223.

[41] W. Dilthey; G. Hurtig. *Ber. dtsch. Chem. Ges. A/B* **1934**, *67*, 2004-2007.

[42] X. Feng; W. Pisula; K. Müllen: Large Polycyclic Aromatic Hydrocarbons: Synthesis and Discotic Organization. In *Pure Appl. Chem.*, 2009; Vol. 81; pp 2203–2224.

[43] H. Ito; K. Ozaki; K. Itami. *Angew. Chem. Int. Ed.* **2017**, *56*, 11144-11164.

[44] E. H. Fort; P. M. Donovan; L. T. Scott. *J. Am. Chem. Soc.* **2009**, *131*, 16006-16007.

[45] B. Schuler; S. Collazos; L. Gross; G. Meyer; D. Pérez; E. Guitián; D. Peña. *Angew. Chem. Int. Ed.* **2014**, *53*, 9004-9006.

[46] E. C. Rüdiger; M. Porz; M. Schaffroth; F. Rominger; U. H. F. Bunz. *Chem. Eur. J.* **2014**, *20*, 12725-12728.

[47] I. Nagao; M. Shimizu; T. Hiyama. *Angew. Chem. Int. Ed.* **2009**, *48*, 7573-7576.

[48] W. Yue; J. Gao; Y. Li; W. Jiang; S. Di Motta; F. Negri; Z. Wang. *J. Am. Chem. Soc.* **2011**, *133*, 18054-18057.

[49] H. Dang; M. A. Garcia-Garibay. *J. Am. Chem. Soc.* **2001**, *123*, 355-356.

[50] C. Lütke Eversloh; Y. Avlasevich; C. Li; K. Müllen. *Chem. Eur. J.* **2011**, *17*, 12756-12762.

[51] K. Ozaki; K. Kawasumi; M. Shibata; H. Ito; K. Itami. *Nat. Commun.* **2015**, *6*, 6251.

[52] K. Kato; Y. Segawa; K. Itami. *Can. J. Chem.* **2016**, *95*, 329-333.

[53] A. Konishi; Y. Hirao; K. Matsumoto; H. Kurata; T. Kubo. *Chem. Lett.* **2013**, *42*, 592-594.

[54] Y. Morita; S. Suzuki; K. Sato; T. Takui. *Nat. Chem.* **2011**, *3*, 197-204.

[55] Y. Fogel; M. Kastler; Z. Wang; D. Andrienko; G. J. Bodwell; K. Müllen. *J. Am. Chem. Soc.* **2007**, *129*, 11743-11749.

[56] A. Stabel; P. Herwig; K. Müllen; J. P. Rabe. *Angew. Chem. Int. Ed.* **1995**, *34*, 1609-1611.

[57] X. Feng; J. Wu; M. Ai; W. Pisula; L. Zhi; J. P. Rabe; K. Müllen. *Angew. Chem. Int. Ed.* **2007**, *46*, 3033-3036.

[58] V. S. Iyer; K. Yoshimura; V. Enkelmann; R. Epsch; J. P. Rabe; K. Müllen. *Angew. Chem. Int. Ed.* **1998**, *37*, 2696-2699.

[59] M. Müller; J. Petersen; R. Strohmaier; C. Günther; N. Karl; K. Müllen. *Angew. Chem. Int. Ed.* **1996**, *35*, 886-888.

[60] Ž. Tomović; M. D. Watson; K. Müllen. *Angew. Chem. Int. Ed.* **2004**, *43*, 755-758.

[61] V. Palermo; S. Morelli; C. Simpson; K. Müllen; P. Samorì. *J. Mater. Chem.* **2006**, *16*, 266-271.

[62] C. D. Simpson; J. D. Brand; A. J. Berresheim; L. Przybilla; H. J. Räder; K. Müllen. *Chem. Eur. J.* **2002**, *8*, 1424-1429.

[63] W. Pisula; A. Menon; M. Stepputat; I. Lieberwirth; U. Kolb; A. Tracz; H. Sirringhaus; T. Pakula; K. Müllen. *Adv. Mater.* **2005**, *17*, 684-689.

[64] W. Hendel; Z. H. Khan; W. Schmidt. *Tetrahedron* **1986**, *42*, 1127-1134.

[65] M. Kastler; J. Schmidt; W. Pisula; D. Sebastiani; K. Müllen. *J. Am. Chem. Soc.* **2006**, *128*, 9526-9534.

[66] T. Dumslaff; B. Yang; A. Maghsoumi; G. Velpula; K. S. Mali; C. Castiglioni; S. De Feyter; M. Tommasini; A. Narita; X. Feng; K. Müllen. *J. Am. Chem. Soc.* **2016**, *138*, 4726-4729.

[67] P. T. Herwig; K. Müllen. *Adv. Mater.* **1999**, *11*, 480-483.

[68] R. Mondal; B. K. Shah; D. C. Neckers. *J. Am. Chem. Soc.* **2006**, *128*, 9612-9613.

[69] R. Mondal; C. Tönshoff; D. Khon; D. C. Neckers; H. F. Bettinger. *J. Am. Chem. Soc.* **2009**, *131*, 14281-14289.

[70] C. Tönshoff; H. F. Bettinger. *Angew. Chem. Int. Ed.* **2010**, *49*, 4125-4128.

[71] R. Zuzak; R. Dorel; M. Kolmer; M. Szymonski; S. Godlewski; A. M. Echavarren. *Angew. Chem. Int. Ed.* **2018**, *57*, 10500-10505.

[72] Y. Ni; T. Y. Gopalakrishna; H. Phan; T. S. Herng; S. Wu; Y. Han; J. Ding; J. Wu. *Angew. Chem. Int. Ed.* **2018**, *57*, 9697-9701.

[73] M. R. Ajayakumar; Y. Fu; J. Ma; F. Hennersdorf; H. Komber; J. J. Weigand; A. Alfonsov; A. A. Popov; R. Berger; J. Liu; K. Müllen; X. Feng. *J. Am. Chem. Soc.* **2018**, *140*, 6240-6244.

[74] C. Rogers; C. Chen; Z. Pedramrazi; A. A. Omrani; H.-Z. Tsai; H. S. Jung; S. Lin; M. F. Crommie; F. R. Fischer. *Angew. Chem. Int. Ed.* **2015**, *54*, 15143-15146.

[75] A. Konishi; Y. Hirao; M. Nakano; A. Shimizu; E. Botek; B. Champagne; D. Shiomi; K. Sato; T. Takui; K. Matsumoto; H. Kurata; T. Kubo. *J. Am. Chem. Soc.* **2010**, *132*, 11021-11023.

[76] A. Konishi; Y. Hirao; K. Matsumoto; H. Kurata; R. Kishi; Y. Shigeta; M. Nakano; K. Tokunaga; K. Kamada; T. Kubo. *J. Am. Chem. Soc.* **2013**, *135*, 1430-1437.

[77] J. B. Birks: Photophysics of Aromatic Molecules; Wiley-Interscience: London. 1970.

[78] J. W. Patterson. *J. Am. Chem. Soc.* **1942**, *64*, 1485-1486.

[79] R. D. Broene; F. Diederich. *Tetrahedron Lett.* **1991**, *32*, 5227-5230.

[80] Z. Sun; J. Wu. *J. Mater. Chem.* **2012**, *22*, 4151-4160.

[81] D. H. Reid. *Quarterly Reviews, Chemical Society* **1965**, *19*, 274-302.

[82] N. Pavliček; A. Mistry; Z. Majzik; N. Moll; G. Meyer; D. J. Fox; L. Gross. *Nat. Nanotechnol.* **2017**, *12*, 308-311.

[83] M. Gingras. *Chem. Soc. Rev.* **2013**, *42*, 968-1006.

[84] M. Gingras; G. Félix; R. Peresutti. *Chem. Soc. Rev.* **2013**, *42*, 1007-1050.

[85] M. Ball; Y. Zhong; Y. Wu; C. Schenck; F. Ng; M. Steigerwald; S. Xiao; C. Nuckolls. *Acc. Chem. Res.* **2015**, *48*, 267-276.

[86] J. Liu; B.-W. Li; Y.-Z. Tan; A. Giannakopoulos; C. Sanchez-Sanchez; D. Beljonne; P. Ruffieux; R. Fasel; X. Feng; K. Müllen. *J. Am. Chem. Soc.* **2015**, *137*, 6097-6103.

[87] E. Clar; J. F. Stephen. *Tetrahedron* **1965**, *21*, 467-470.

[88] S. Xiao; M. Myers; Q. Miao; S. Sanaur; K. Pang; M. L. Steigerwald; C. Nuckolls. *Angew. Chem. Int. Ed.* **2005**, *44*, 7390-7394.

[89] S. Xiao; S. J. Kang; Y. Zhong; S. Zhang; A. M. Scott; A. Moscatelli; N. J. Turro; M. L. Steigerwald; H. Li; C. Nuckolls. *Angew. Chem. Int. Ed.* **2013**, *52*, 4558-4562.

[90] T.-A. Chen; R.-S. Liu. *Org. Lett.* **2011**, *13*, 4644-4647.

[91] T.-A. Chen; R.-S. Liu. *Chem. Eur. J.* **2011**, *17*, 8023-8027.

[92] R. Berger; A. Giannakopoulos; P. Ravat; M. Wagner; D. Beljonne; X. Feng; K. Müllen. *Angew. Chem. Int. Ed.* **2014**, *53*, 10520-10524.

[93] X. Wang; F. Zhang; K. S. Schellhammer; P. Machata; F. Ortmann; G. Cuniberti; Y. Fu; J. Hunger; R. Tang; A. A. Popov; R. Berger; K. Müllen; X. Feng. *J. Am. Chem. Soc.* **2016**, *138*, 11606-11615.

[94] E. Clar; G. S. Fell; M. H. Richmond. *Tetrahedron* **1960**, *9*, 96-105.

[95] X.-Y. Wang; A. Narita; W. Zhang; X. Feng; K. Müllen. *J. Am. Chem. Soc.* **2016**, *138*, 9021-9024.

[96] X.-Y. Wang; T. Dienel; M. Di Giovannantonio; G. B. Barin; N. Kharche; O. Deniz; J. I. Urgel; R. Widmer; S. Stolz; L. H. De Lima; M. Muntwiler; M. Tommasini; V. Meunier; P. Ruffieux; X. Feng; R. Fasel; K. Müllen; A. Narita. *J. Am. Chem. Soc.* **2017**, *139*, 4671-4674.

[97] S. M. Draper; D. J. Gregg; R. Madathil. *J. Am. Chem. Soc.* **2002**, *124*, 3486-3487.

[98] C. J. Martin; B. Gil; S. D. Perera; S. M. Draper. *Chem. Commun.* **2011**, *47*, 3616-3618.

[99] B. Li; L. Zhou; D. Wu; H. Peng; K. Yan; Y. Zhou; Z. Liu. *ACS Nano* **2011**, *5*, 5957-5961.

[100] J. Wu; L. Xie; Y. Li; H. Wang; Y. Ouyang; J. Guo; H. Dai. *J. Am. Chem. Soc.* **2011**, *133*, 19668-19671.

[101] Y.-Z. Tan; B. Yang; K. Parvez; A. Narita; S. Osella; D. Beljonne; X. Feng; K. Müllen. *Nat. Commun.* **2013**, *4*, 2646.

[102] Y.-M. Liu; H. Hou; Y.-Z. Zhou; X.-J. Zhao; C. Tang; Y.-Z. Tan; K. Müllen. *Nat. Commun.* **2018**, *9*, 1901.

[103] Y.-Z. Tan; S. Osella; Y. Liu; B. Yang; D. Beljonne; X. Feng; K. Müllen. *Angew. Chem. Int. Ed.* **2015**, *54*, 2927-2931.

[104] R. Dong; M. Pfeffermann; D. Skidin; F. Wang; Y. Fu; A. Narita; M. Tommasini; F. Moresco; G. Cuniberti; R. Berger; K. Müllen; X. Feng. *J. Am. Chem. Soc.* **2017**, *139*, 2168-2171.

[105] M. D. Watson; M. G. Debije; J. M. Warman; K. Müllen. *J. Am. Chem. Soc.* **2004**, *126*, 766-771.

[106] M. Y. Han; B. Özyilmaz; Y. Zhang; P. Kim. *Phys. Rev. Lett.* **2007**, *98*, 206805.

[107] D. V. Kosynkin; A. L. Higginbotham; A. Sinitskii; J. R. Lomeda; A. Dimiev; B. K. Price; J. M. Tour. *Nature* **2009**, *458*, 872-876.

[108] A. L. Elías; A. R. Botello-Méndez; D. Meneses-Rodríguez; V. Jehová González; D. Ramírez-González; L. Ci; E. Muñoz-Sandoval; P. M. Ajayan; H. Terrones; M. Terrones. *Nano Lett.* **2010**, *10*, 366-372.

[109] L. Jiao; L. Zhang; X. Wang; G. Diankov; H. Dai. *Nature* **2009**, *458*, 877-880.

[110] L. Ma; J. Wang; F. Ding. *ChemPhysChem* **2013**, *14*, 47-54.

[111] A. Narita; X. Feng; Y. Hernandez; S. A. Jensen; M. Bonn; H. Yang; I. A. Verzhbitskiy; C. Casiraghi; M. R. Hansen; A. H. R. Koch; G. Fytas; O. Ivasenko; B. Li; K. S. Mali; T. Balandina; S. Mahesh; S. De Feyter; K. Müllen. *Nat. Chem.* **2013**, *6*, 126-132.

[112] M. G. Schwab; A. Narita; Y. Hernandez; T. Balandina; K. S. Mali; S. De Feyter; X. Feng; K. Müllen. *J. Am. Chem. Soc.* **2012**, *134*, 18169-18172.

[113] X. Yang; X. Dou; A. Rouhanipour; L. Zhi; H. J. Räder; K. Müllen. *J. Am. Chem. Soc.* **2008**, *130*, 4216-4217.

[114] J. Cai; P. Ruffieux; R. Jaafar; M. Bieri; T. Braun; S. Blankenburg; M. Muoth; A. P. Seitsonen; M. Saleh; X. Feng; K. Müllen; R. Fasel. *Nature* **2010**, *466*, 470-473.

[115] G. Z. Magda; X. Jin; I. Hagymási; P. Vancsó; Z. Osváth; P. Nemes-Incze; C. Hwang; L. P. Biró; L. Tapasztó. *Nature* **2014**, *514*, 608-611.

[116] K. Nakada; M. Fujita; G. Dresselhaus; M. S. Dresselhaus. *Phys. Rev. B* **1996**, *54*, 17954-17961.

[117] Y.-W. Son; M. L. Cohen; S. G. Louie. *Phys. Rev. Lett.* **2006**, *97*, 216803.

[118] Y.-W. Son; M. L. Cohen; S. G. Louie. *Nature* **2006**, *444*, 347-349.

[119] G. Li; K.-Y. Yoon; X. Zhong; X. Zhu; G. Dong. *Chem. Eur. J.* **2016**, *22*, 9116-9120.

[120] H. Zhang; H. Lin; K. Sun; L. Chen; Y. Zagranyarski; N. Aghdassi; S. Duhm; Q. Li; D. Zhong; Y. Li; K. Müllen; H. Fuchs; L. Chi. *J. Am. Chem. Soc.* **2015**, *137*, 4022-4025.

[121] A. Kimouche; M. M. Ervasti; R. Drost; S. Halonen; A. Harju; P. M. Joensuu; J. Sainio; P. Liljeroth. *Nat. Commun.* **2015**, *6*, 10177.

[122] L. Talirz; H. Söde; T. Dumslaff; S. Wang; J. R. Sanchez-Valencia; J. Liu; P. Shinde; C. A. Pignedoli; L. Liang; V. Meunier; N. C. Plumb; M. Shi; X. Feng; A. Narita; K. Müllen; R. Fasel; P. Ruffieux. *ACS Nano* **2017**, *11*, 1380-1388.

[123] Y.-C. Chen; D. G. de Oteyza; Z. Pedramrazi; C. Chen; F. R. Fischer; M. F. Crommie. *ACS Nano* **2013**, *7*, 6123-6128.

[124] C. Bronner; S. Stremlau; M. Gille; F. Brauße; A. Haase; S. Hecht; P. Tegeder. *Angew. Chem. Int. Ed.* **2013**, *52*, 4422-4425.

[125] Y. Zhang; Y. Zhang; G. Li; J. Lu; X. Lin; S. Du; R. Berger; X. Feng; K. Müllen; H.-J. Gao. *Appl. Phys. Lett.* **2014**, *105*, 023101.

[126] J. Cai; C. A. Pignedoli; L. Talirz; P. Ruffieux; H. Söde; L. Liang; V. Meunier; R. Berger; R. Li; X. Feng; K. Müllen; R. Fasel. *Nat. Nanotechnol.* **2014**, *9*, 896-900.

[127] G. D. Nguyen; H.-Z. Tsai; A. A. Omrani; T. Marangoni; M. Wu; D. J. Rizzo; G. F. Rodgers; R. R. Cloke; R. A. Durr; Y. Sakai; F. Liou; A. S. Aikawa; J. R. Chelikowsky; S. G. Louie; F. R. Fischer; M. F. Crommie. *Nat. Nanotechnol.* **2017**, *12*, 1077-1082.

[128] R. A. Durr; D. Haberer; Y.-L. Lee; R. Blackwell; A. M. Kalayjian; T. Marangoni; J. Ihm; S. G. Louie; F. R. Fischer. *J. Am. Chem. Soc.* **2018**, *140*, 807-813.

[129] Y.-F. Zhang; Y. Zhang; G. Li; J. Lu; Y. Que; H. Chen; R. Berger; X. Feng; K. Müllen; X. Lin; Y.-Y. Zhang; S. Du; S. T. Pantelides; H.-J. Gao. *Nano Res.* **2017**, *10*, 3377-3384.

[130] G. D. Nguyen; F. M. Toma; T. Cao; Z. Pedramrazi; C. Chen; D. J. Rizzo; T. Joshi; C. Bronner; Y.-C. Chen; M. Favaro; S. G. Louie; F. R. Fischer; M. F. Crommie. *J. Phys. Chem. C* **2016**, *120*, 2684-2687.

[131] X.-Y. Wang; J. I. Urgel; G. B. Barin; K. Eimre; M. Di Giovannantonio; A. Milani; M. Tommasini; C. A. Pignedoli; P. Ruffieux; X. Feng; R. Fasel; K. Müllen; A. Narita. *J. Am. Chem. Soc.* **2018**, *140*, 9104-9107.

[132] B. A. Bernevig; T. L. Hughes; S.-C. Zhang. *Science* **2006**, *314*, 1757-1761.

[133] M. König; S. Wiedmann; C. Brüne; A. Roth; H. Buhmann; L. W. Molenkamp; X.-L. Qi; S.-C. Zhang. *Science* **2007**, *318*, 766-770.

[134] W. P. Su; J. R. Schrieffer; A. J. Heeger. *Phys. Rev. Lett.* **1979**, *42*, 1698-1701.

[135] W. P. Su; J. R. Schrieffer; A. J. Heeger. *Phys. Rev. B* **1980**, *22*, 2099-2111.

[136] T. Cao; F. Zhao; S. G. Louie. *Phys. Rev. Lett.* **2017**, *119*, 076401.

Chapter 2. Direct C-H Borylation at the 2- and 2, 7-Positions of Pyrene Leading to Brightly Blue- and Green-Emitting Chromophores

Keywords: pyrene, heteroannulation, chromophores, fluorescence, charge transport

Toc figure

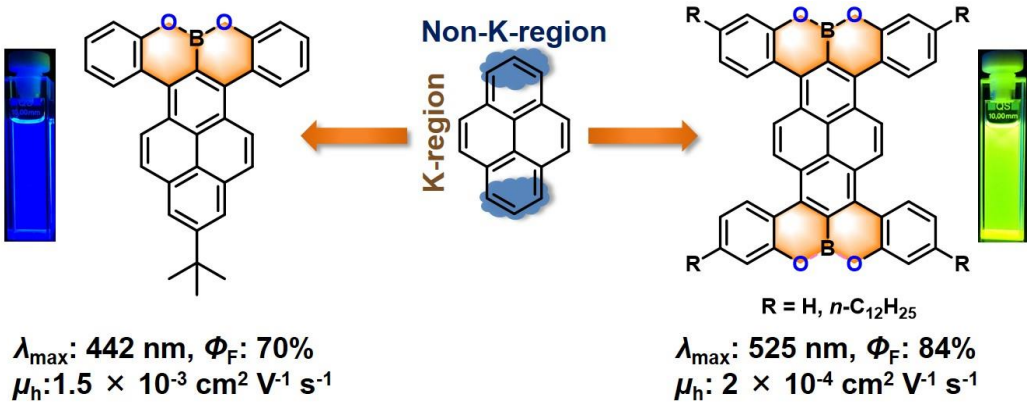

A straightforward C–H borylation at the 2- and 2,7-positions of pyrene derivatives has been demonstrated, generating a new type of non-K-region heteroannelated pyrene-based chromophores, i.e. 2-(*tert*-butyl)-10,11-dioxa-10a-boratribenzo[*a*,*f*,*l*,*m*]perylene (**1**) and 11,12,23,24-tetraoxa-11a,23a-diboratetrabenzo[*a*,*f*,*n*,*s*]terrylene (**2**). Compound **1** exhibits strong blue fluorescence (λ_{max}: 442 nm) with a quantum yield of 70%, whereas compound 2 with alkyl substituents displays green fluorescence (λ_{max}: 525 nm) with a quantum yield of 84%. Furthermore, p-type charge transport has been revealed for both compounds by organic field-effect transistors.

Published in:

Asian Journal of Organic Chemistry

Polycyclic aromatic compounds have attracted tremendous interest from both synthetic chemists and materials scientists during the past decades.[1] They are often intriguing chromophores which form the basis of industrial dyes and colorants due to the extended π-

conjugation,[2] and serve as semiconductors in electronic and optoelectronic devices, such as in organic field-effect transistors (OFETs),[3] organic light-emitting diodes (OLEDs),[4] and organic photovoltaic cells.[5] There has been a continuous demand for versatile organic materials, for example, stable blue emitters for OLEDs,[6] high-mobility semiconductors for OFETs,[7] light absorbers for solar energy conversion,[8] and radical-bearing compounds for spintronics.[9] Among various candidates, heteroatom-embedded organic π-conjugated molecules are of particular interest because of their intriguing optical, electronic, and magnetic properties.[10]

Pyrene, a classical polycyclic aromatic hydrocarbon and promising chromophore, has been frequently employed as a building block to develop novel π-extended systems.[11] It can be readily functionalized at the 1-, 3-, 6-, and 8-postions by electrophilic substitution.[12] The 4-, 5-, 9- and 10-positions (K-region) are also available for modifications through oxidation and further functionalizations (Figure 1a).[13] In contrast, the 2-and 7-positions are less reactive, which can be explained by looking at the frontier molecular orbitals of pyrene (Figure 1b,c): In its highest occupied molecular orbital (HOMO) and lowest unoccupied molecular orbital (LUMO), there is a nodal plane passing through the 2- and 7-positions; reactions at these positions are thus very difficult. Remarkably, Marder et al. have developed an Ir-catalyzed borylation at the 2- and 7-positions of pyrene,[14] providing a new entry to 2- and 2,7-substituted pyrene derivatives.[15] The π-annulation at the non-K-region (1-, 2-, 3-, and 6-, 7-, 8-postions) of pyrene has thus been achieved recently through substitution at the 2- and 7-positions followed by further cyclizations.[16]

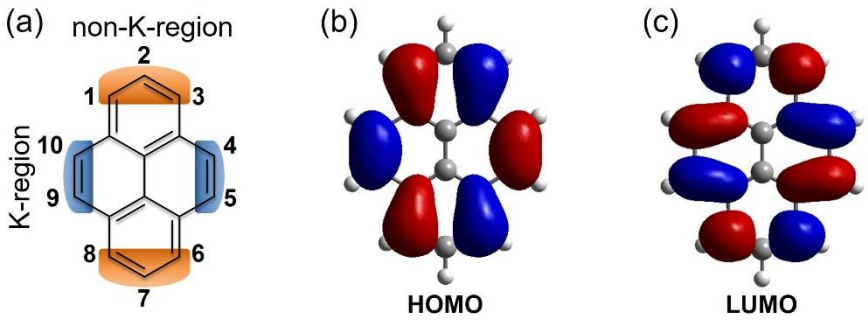

Figure 1. (a) The numbering of pyrene with its K-region and non-K-region. (b,c) HOMO and LUMO of pyrene, calculated at the B3LYP/6-31G(d) level.

Herein, we demonstrate that direct C–H borylation[17] readily occurs at the 2- and 7-positions of pyrene derivatives in the presence of BBr_3 (Scheme 1). This reactivity provides an

alternative pathway to π-extension at the non-K-region of pyrene and results in a new kind of oxaborin-annelated pyrene-based chromophores. Singly annelated 2-(*tert*-butyl)-10,11-dioxa-10a-boratribenzo[*a,f,lm*]perylene (**1**) and doubly annelated 11,12,23,24-tetraoxa-11a,23a-diboratetrabenzo[*a,f,n,s*]terrylene (**2a** without substituents and **2b** with dodecyl chains) have been obtained. Interestingly, compound **1** displays blue fluorescence with an emission maximum (λ_{max}) at 442 nm and a high quantum yield (Φ_F) of 70%, whereas **2b** shows green fluorescence (λ_{max}: 525 nm; Φ_F: 84%). Both molecules also function as p-type semiconductors in OFET devices.

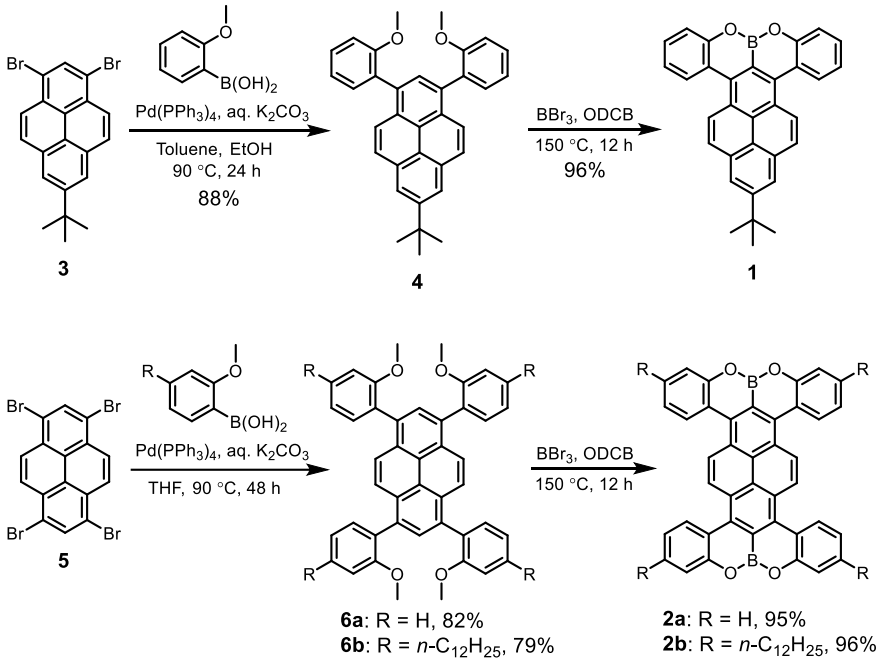

Scheme 1. Synthetic route to compounds **1** and **2a**,**b**.

The synthesis of compounds **1**, and **2a**,**b** is depicted in Scheme 1. First, 7-(*tert*-butyl)-1,3-bis(2-methoxyphenyl)pyrene (**4**) was obtained through Suzuki coupling of 1,3-dibromo-7-(*tert*-butyl)pyrene (**3**) with (2-methoxyphenyl)boronic acid in 88 % yield. Then, demethylation and subsequent direct C−H borylation were performed by heating a solution of compound **4** and BBr_3 in *o*-dichlorobenzene (ODCB) at 150 °C, furnishing compound **1** in 96% yield. In a similar approach, four-fold Suzuki coupling of 1,3,6,8-tetrabomopyrene (**5**) with (2-methoxyphenyl)boronic acid provided 1,3,6,8-tetrakis(2-methoxyphenyl)pyrene (**6a**) in 82% yield, followed by tandem demethylation-borylation of **6a** affording compound **2a** in 95 % yield. Compound **2b** with dodecyl chains was synthesized in the same manner to improve the solubility of the target compound. The chemical structures of **1** and **2b** were verified by ^{1}H, ^{13}C, and 2D NMR as well as high-resolution MALDI-TOF MS (see the Supporting

Information). However, further characterization of **2a**, except high-resolution MALDI-TOF MS, was prevented by its poor solubility.

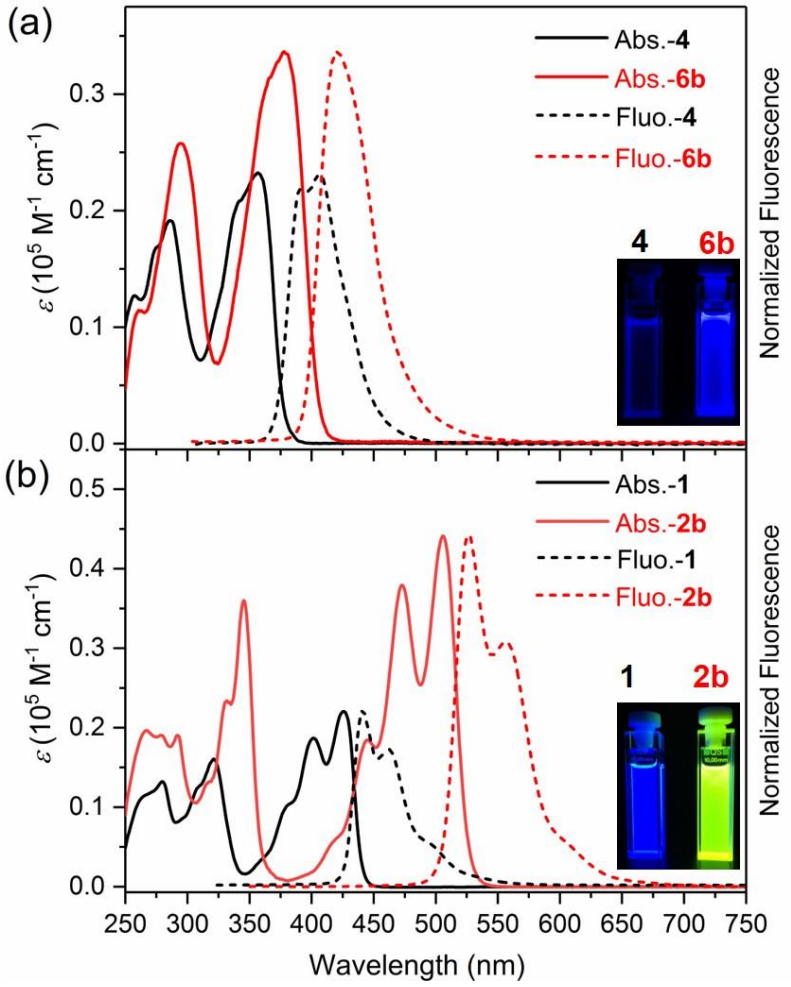

Figure 2. UV-vis absorption and fluorescence spectra of (a) **4** and **6b** in $CHCl_3$ (5×10^{-5} M and 2×10^{-5} M, respectively) and (b) **1** and **2b** in $CHCl_3$ (5×10^{-5} M and 1×10^{-5} M, respectively). Insets: pictures of (a) compounds **4** and **6b** as well as (b) compounds **1** and **2b** in $CHCl_3$ under UV light (365 nm).

The photophysical properties of compounds **1** and **2b** were investigated in $CHCl_3$ solutions to elucidate the consequence of π-annulation at the non-K-regions (Figure 2). The absorption/emission maxima of **1** (426/442 nm) and **2b** (506/525 nm) are significantly red-shifted relative to their respective precursors **4** (357/406 nm) and **6b** (378/423 nm), indicating that the cyclization effectively extends the π-conjugation. Compared with K-region π-extended pyrene derivatives, these non-K-region fused chromophores exhibit more significant red-shifts of the absorption and emission maxima upon cyclization.[18] Additionally, compared with the one-side π-extended pyrene derivative **1**, the double-side π-extended compound **2b** exhibits a

lower optical gap (2.35 eV for **2b**; 2.81 eV for **1**) and a higher maximum absorption coefficient. These observations clearly reveal that the π-annulation at the non-K-region of pyrene has a significant impact on the optical and electronic properties. The fluorescence quantum yields of compounds **1** and **2b** were measured with 9,10-diphenylanthracene and fluorescein as the respective references.[19] Notably, compound **1** displays a blue fluorescence (λ_{max}: 442 nm) with a quantum yield as high as 70%, whereas it reaches 84% for **2b** with a green fluorescence (λ_{max}: 525 nm). The Stokes shifts of **1** and **2b** are 16 and 19 nm, respectively, presumably due to the relatively rigid molecular skeletons. Both compounds are very stable under ambient conditions, having no changes in their photophysical features and in their NMR spectra after several months. The electrochemical properties of compounds **1** and **2b** were studied by cyclic voltammetry (Figure S1). With ferrocene as an external standard, the HOMO and LUMO energy levels of **1** were estimated to be –5.24 and –2.72 eV, respectively. Only the oxidative wave was observed for **2b**, whose HOMO level was determined as –5.03 eV. The LUMO level was thus calculated by the electrochemical HOMO level and the optical energy gap as –2.68 eV.

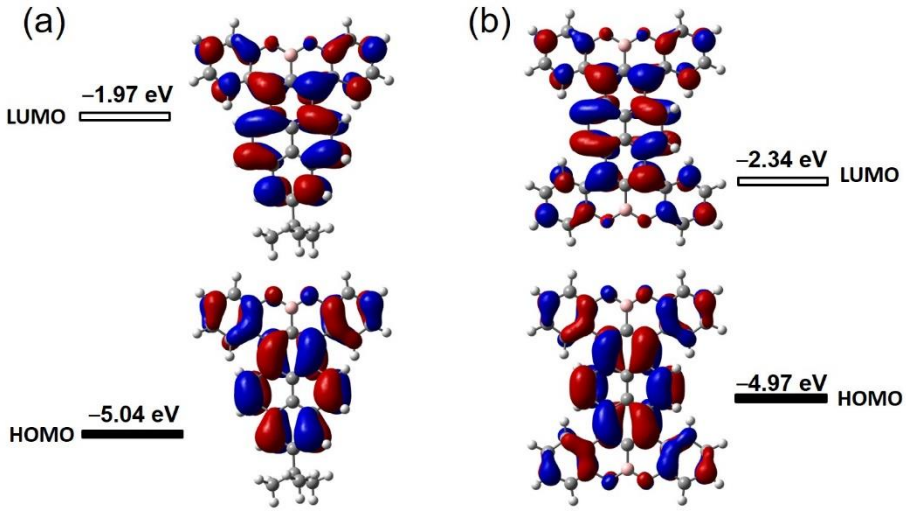

Figure 3. DFT-calculated frontier molecular orbitals and their energy levels of (a) compound **1** and (b) compound **2a** at the B3LYP/6-31G(d) level.

Density functional theory (DFT) calculations were performed to acquire more insights into the geometries and electronic properties of **1** and **2a**. As illustrated in Figure S3, the optimized geometries of both **1** and **2a** display a slightly twisted conformation because of the steric hindrance at the cove regions. Obviously, the HOMOs and LUMOs of **1** and **2a** are distributed across the entire backbones (Figure 3), revealing the effective π-extension in both

molecules. The DFT-calculated HOMO level of **2a** is higher than that of **1**, whereas the LUMO level of **2a** is lower than that of **1**, resulting in a lowered energy gap of compound **2a**. These observations indicate that π-annulation at the non-K-region of pyrene is able to modulate the HOMO and LUMO energy levels and thus the photophysical and electrochemical properties.

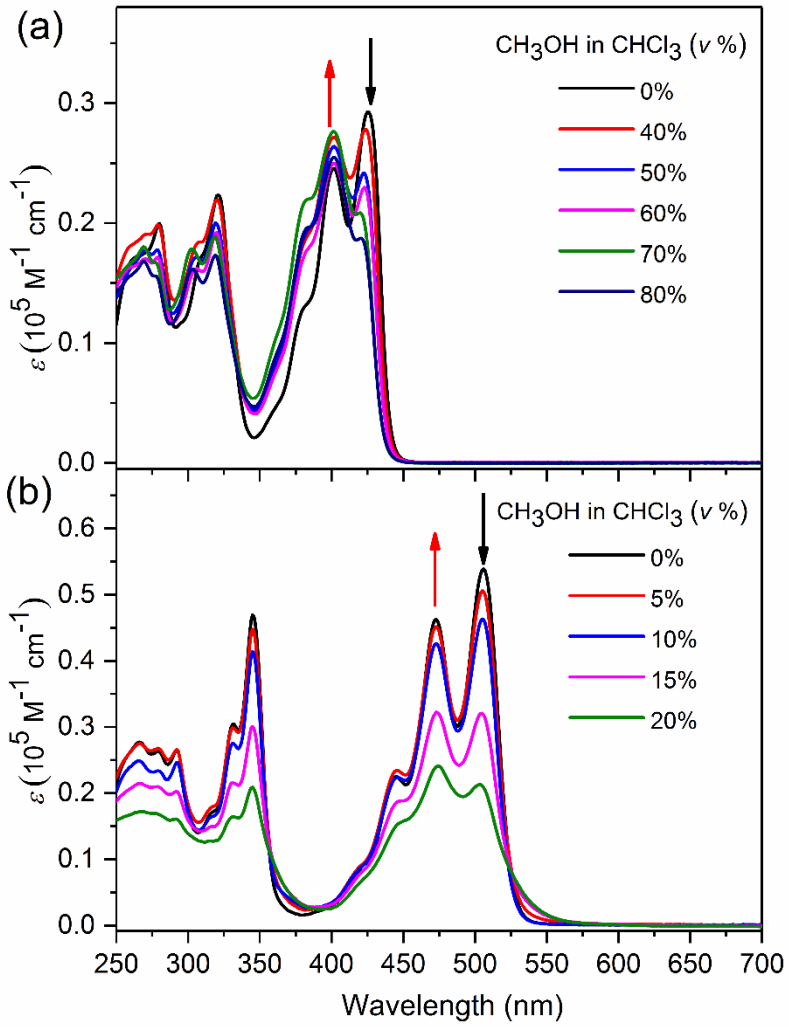

Figure 4. UV-vis absorption spectra of (a) compound **1** and (b) compound **2b** in a series of mixed solvents of $CHCl_3$ and CH_3OH. The arrows indicate the spectral changes upon increasing the amount of CH_3OH.

Temperature-dependent ^1H NMR analysis of compounds **1** and **2b** in $C_2D_2Cl_4$ (Figure S4) revealed that the aromatic protons from both molecules exhibited an upfield shift as the temperature decreased from 403 K to 298 K, indicating a strong aggregation tendency in a face-to-face manner.[10d] To further investigate the self-assembly behavior of compounds **1** and **2b**, solvent-dependent UV-vis absorption spectra in a mixed solvent of $CHCl_3/CH_3OH$ were acquired with a fixed concentration at room temperature. $CHCl_3$ is a good solvent for the

solvation of **1** and **2b**, which does not hold true for CH_3OH. As illustrated in Figure 4, compound **1** in pure $CHCl_3$ displays an absorption spectrum with well-resolved vibronic structures (Figure 4a), corresponding to a monomer-dominated absorption. Upon increasing the CH_3OH content in the mixed solvent from 30% to 80%, the aggregation starts to appear as evidenced by the spectral changes. The prominent feature is a reduction of the monomer-dominated absorption maximum at 426 nm and a relative increase of the aggregate-induced peak which is blue-shifted to 402 nm. The blue-shift of the absorption maximum is consistent with the characteristic of an H-aggregation behavior.[20] A similar trend in the solvent-dependent absorption spectra was observed for compound **2b** (Figure 4b), displaying a decreased peak intensity at 506 nm (monomer-dominated) and relatively increased peak intensity at a blue-shifted wavelength 473 nm (aggregate-dominated) upon increasing the amount of CH_3OH in the binary solvent. These features also suggest H-type aggregation of compound **2b** in the presence of a poor solvent.[20] It is however noteworthy that obvious spectral changes are already observed at a lower CH_3OH content (from 5% to 20%) for **2b** than that for **1** (starting to see the changes from 40%), suggesting a stronger π-π interaction of **2b** due to the larger π-skeleton.

The absorption spectra of compounds **1** and **2b** in drop-casted thin films were also recorded (Figure S5). Compared with their absorption spectra in $CHCl_3$ solution, both compounds in the solid state exhibit blue-shifted absorption maxima, in agreement with the aggregation behavior in solution. The fluorescence properties of both compounds in the solid state were studied in a polystyrene (PS) matrix and in a neat film. At low concentrations (<1 wt%) in PS, both compounds display monomer-dominated fluorescence, whereas at high concentrations in the PS matrix and in the neat film, they show significantly red-shifted emission maxima due to the aggregation (Figure S6). The strong intermolecular interaction observed for both compounds is believed to be interesting for self-assembly studies and favorable for charge transport.

The charge transport properties of compounds **1** and **2b** were investigated based on bottom-gate top-contact OFET devices. Heavily n-doped silicon wafers were used as the gate electrode and thermally grown SiO_2 (300 nm thick) was employed as the dielectric layer. Organic thin films were fabricated on the Si/SiO_2 substrate and gold was then deposited as the source and drain electrodes to furnish the OFET devices. To deposit the organic films, the spin-coating method was first performed for both **1** and **2b**, but only compound **2b** exhibited a homogenous film. The spin-coated film of compound **1** was discontinuous, probably caused by

the dewetting effect due to the lack of flexible alkyl chains.[22] Accordingly, dip-coating was performed for compound **1** by using a blend of compound **1** and poly(methyl methacrylate) (PMMA) in $CHCl_3$ with a weight ratio of 1 : 1 to deposit the thin film (Figure S7). In contrast, discontinuous fibres of compound **2b** were obtained by the same dip-coating process due to its low concentration caused by the limited solubility (Figure S7). Therefore, OFETs based on the dip-coated film of compound **1** exhibited a hole mobility around 1.5×10^{-3} cm^2 V^{-1} s^{-1} with an on/off ratio of 5×10^4 (Figure 5a,b), and the devices based on the spin-coated film of compound **2b** gave a hole mobility around 2×10^{-4} cm^2 V^{-1} s^{-1}, with an on/off ratio of 6×10^4 (Figure 5c,d). The device performance of these two molecules cannot be directly compared because of the different fabrication methods, but the preliminary results have demonstrated the charge transport capability for both compounds. The mobility could be improved by further optimizing the device fabrication parameters, for example, the film deposition conditions and the surface modification of the substrates, etc.

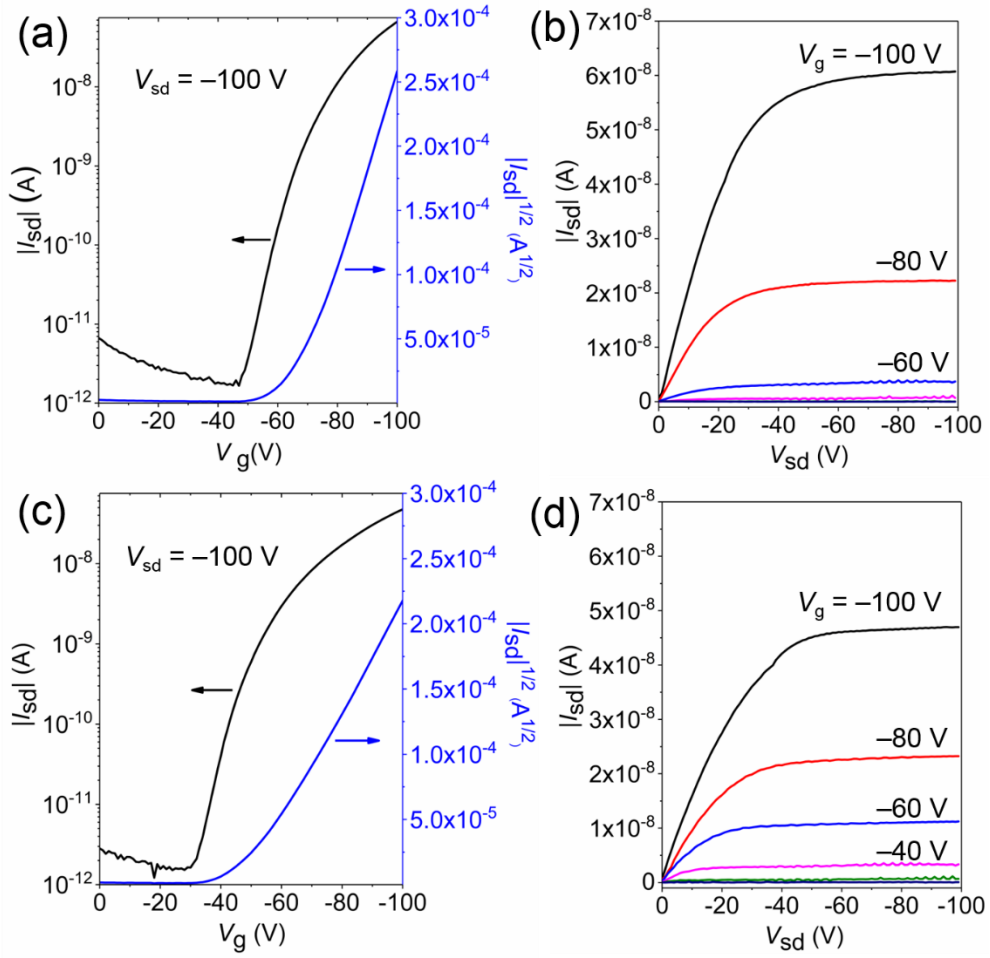

Figure 5. (a,c) Transfer and (b,d) output characteristics of the OFETs based on (a,b) dip-coated compound **1** and (c,d) spin-coated compound **2b**.

In summary, we have demonstrated that direct C–H borylation readily occurs at the 2- and 2,7-positions of pyrene, furnishing the first oxaborin-annelated pyrene derivatives in high yields. The extended π-conjugation at the non-K-region of pyrene has shown a significant impact on the optical and electronic properties. It is remarkable that strong blue fluorescence (λ_{max}: 442 nm; Φ_F: 70%) has been observed for compound **1**, which would be desirable for OLEDs as stable blue emitters. Compound **2b**, on the other hand, resembles the famous perylene diimide (PDI) dyes[23] in many ways, e.g. a similar absorption feature, bright green fluorescence (λ_{max}: 525 nm; Φ_F: 84%), and a strong self-assembly tendency in solution. It could be an interesting new chromophore for optical and supramolecular studies. Furthermore, charge transport properties of **1** and **2b** have been demonstrated by OFET devices. This work has revealed a new way of π-extension based on pyrene derivatives and provided a novel kind of materials which are promising for photonic and optoelectronic applications.

Experimental Section

General information

All commercially available chemicals were used without further purification unless otherwise noted. Column chromatography was conducted with silica gel (grain size 0.063–0.200 mm or 0.04–0.063 mm) and thin layer chromatography (TLC) was performed on silica gel-coated aluminum sheets with F254 indicator. Nuclear magnetic resonance (NMR) spectra were recorded on Bruker Avance 300 or 500 MHz spectrometer. Chemical shifts were reported in ppm. Coupling constants (*J* values) were presented in Hertz (Hz). ^{1}H NMR chemical shifts were referenced to CD_2Cl_2 (5.32 ppm) or $C_2D_2Cl_4$ (6.00 ppm). ^{13}C NMR chemical shifts were referenced to CD_2Cl_2 (53.84 ppm) or $C_2D_2Cl_4$ (73.78 ppm). Abbreviations: s = singlet, d = doublet, dd = double doublet, t = triplet, m = multiplet. High-resolution mass spectrometry (HRMS) was performed on a SYNAPT G2 Si high resolution time-of-flight (TOF) mass spectrometer (Waters Corp., Manchester, UK) by matrix-assisted laser desorption/ionization (MALDI). Melting points were measured with a Büchi B-545 apparatus. Absorption spectra were recorded on a Perkin-Elmer Lambda 900 spectrophotometer. Photoluminescence spectra were recorded on a J&MTIDAS spectrofluorometer. The quantum yield was measured with 9,10-diphenylanthracene (in toluene under air, Φ_F: 0.70) or fluorescein (in 0.1 N NaOH under air, Φ_F: 0.90) as a reference.[19] Cyclic voltammetry (CV) was performed on a WaveDriver 20 Bipotentiostat/Galvanostat (Pine Instruments Company) and measurements were carried out in

tetrahydrofuran (THF) containing 0.1 M *n*-Bu_4NPF_6 as supporting electrolyte (scan rate: 100 mV s^{-1}). A glassy carbon electrode was used as a working electrode, a platinum wire as a counter electrode and a silver wire as a reference electrode.

Synthesis of 7-(*tert*-butyl)-1,3-bis(2-methoxyphenyl)pyrene (4)

To a Schlenk tube charged with 1,3-dibromo-7-*tert*-butylpyrene (**3**) (300 mg, 0.721 mmol), (2-methoxyphenyl)boronic acid (438 mg, 2.88mmol), potassium carbonate (797 mg, 5.77 mmol) and tetrakis(triphenylphosphine)palladium(0) (83 mg, 0.072 mmol) under argon was added toluene (25 mL, degassed) and a mixture of water/ethanol (7 mL : 7 mL, degassed). The reaction mixture was stirred at 90 °C for 12 h. After cooling to room temperature, the mixture was extracted with Et_2O and washed with water. Then the organic phase was dried over $MgSO_4$. After removal of the solvent under reduced pressure, the residue was purified by column chromatography over silica gel (eluent: hexane/CH_2Cl_2 = 2 : 1) to give compound **4** as a white solid (300 mg, 88% yield). M.p.: 162.8 – 163.9 °C. ^{1}H NMR (500 MHz, $C_2D_2Cl_4$, 403 K, ppm) δ 8.22 (s, 2H), 8.01 (dd, J = 9.3, 1.4 Hz, 2H), 7.94 – 7.86 (m, 3H), 7.54 – 7.45 (m, 4H), 7.21 – 7.11 (m, 4H), 3.77 (d, J = 11.8 Hz, 6H), 1.61 (s, 9H); ^{13}C NMR (125 MHz, $C_2D_2Cl_4$, 403 K, ppm) δ 157.79, 149.05, 133.67, 132.37, 131.14, 130.72, 130.02, 128.68, 128.47, 126.67, 125.75, 124.79, 123.24, 121.78, 121.74, 120.74, 112.66, 56.01, 31.67; HRMS (MALDI) *m/z*: Calcd for $C_{34}H_{30}O_2$: 470.2246; Found: 470.2238 $[M]^+$.

Synthesis of 1,3,6,8-tetrakis(2-methoxyphenyl)pyrene (6a)

To a Schlenk tube charged with 1,3,6,8-tetrabromopyrene (**5**) (500 mg, 0.966 mmol), 2-methoxybenzeneboronic acid (1.18 g, 7.76 mmol) and tetrakis(triphenylphosphine)palladium(0) (224 mg, 0.194 mmol) under argon was added THF (45 mL, degassed) and a solution of potassium carbonate in water (8 mL, 2 M). The resulting mixture was stirred at 90 °C for 48 h. After cooling to room temperature, the reaction mixture was filtered off and washed with water, methanol and CH_2Cl_2 consecutively. The residue was then dissolved in hot 1,1,2,2-tetrachloroethane and filtered through a PTFE membrane into a filter flask containing methanol. Precipitates were thus obtained and collected by filtration to give compound **6a** as a white solid (496 mg, 82% yield). M.p.: 337.5 – 338.9 °C. ^{1}H NMR (500 MHz, $C_2D_2Cl_4$, 403 K, ppm) δ 7.96 (s, 2H), 7.87 (s, 4H), 7.50 (dd, J = 18.1, 8.5 Hz, 8H), 7.20

– 7.14 (m, 8H), 3.76 (s, 12H); ^{13}C NMR (125 MHz, $C_2D_2Cl_4$, 403 K, ppm) δ 157.79, 133.58, 132.40, 130.79, 130.30, 128.71, 128.63, 125.10, 120.67, 112.53, 55.99; HRMS (MALDI) *m/z*: Calcd for $C_{44}H_{34}O_4$: 626.2457; Found: 626.2480 $[M]^+$.

Synthesis of 1,3,6,8-tetrakis(4-dodecyl-2-methoxyphenyl)pyrene (6b)

To a Schlenk tube charged with 1,3,6,8-tetrabromopyrene (**5**) (200 mg, 0.386 mmol), (4-dodecyl-2-methoxyphenyl)boronic acid (618 mg, 1.93 mmol) and tetrakis(triphenylphosphine)palladium(0) (89 mg, 0.077 mmol) under argon was added THF (20 mL, degassed) and a solution of potassium carbonate in water (2 mL, 2 M). The reaction mixture was stirred at 90 °C for 48 h. After cooling to room temperature, the mixture was extracted with Et_2O and washed with water. Then the organic phase was dried over $MgSO_4$. After removal of the solvent under reduced pressure, the residue was purified by column chromatography over silica gel (eluent: hexane/ CH_2Cl_2 = 2 : 1) to afford compound **6b** as colorless oil (397 mg, 79% yield). ^{1}H NMR (500 MHz, $C_2D_2Cl_4$, 403 K, ppm) δ 7.93 (s, 2H), 7.87 (s, 4H), 7.39 (d, *J* = 7.5 Hz, 4H), 7.02 – 6.97 (m, 8H), 3.74 (s, 12H), 2.80 (t, *J* = 7.7 Hz, 8H), 1.84 (p, *J* = 7.3 Hz, 8H), 1.39 (s, 72H), 0.98 (t, *J* = 6.7 Hz, 12H); ^{13}C NMR (125 MHz, $C_2D_2Cl_4$, 403 K, ppm) δ 157.64, 143.75, 133.60, 132.14, 130.52, 128.70, 128.11, 125.03, 120.68, 112.84, 55.06, 35.88, 31.57, 30.85, 29.32, 29.29, 22.25, 13.52; HRMS (MALDI) *m/z*: Calcd for $C_{92}H_{130}O_4$: 1298.9969; Found: 1298.9901 $[M]^+$.

Synthesis of 2-(*tert*-butyl)-10,11-dioxa-10a-boratribenzo[*a,f,lm*]perylene (1)

To a solution of **4** (100 mg, 0.212 mmol) in anhydrous dichlorobenzene (10 mL) under argon was added BBr_3 (1.0 M in heptane, 0.32 mL, 0.32 mmol). Then the mixture was heated to 150 °C and stirred at this temperature for 12 h. After cooling to room temperature, the reaction mixture was quenched with methanol and concentrated under reduced pressure. Then the residue was purified by column chromatography over a short pad of silica gel with dichloromethane as the eluent to give compound **1** as a yellow solid (92 mg, 96% yield). M.p.: 295.6 – 296.5 °C. ^{1}H NMR (500 MHz, $C_2D_2Cl_4$, 403 K, ppm) δ 9.05 (d, *J* = 9.3 Hz, 2H), 8.74 (dd, *J* = 8.1, 1.6 Hz, 2H), 8.36 (s, 2H), 8.27 (d, *J* = 9.4 Hz, 2H), 7.66 (d, *J* = 8.2 Hz, 2H), 7.60 – 7.53 (m, 2H), 7.47 – 7.40 (m, 2H), 1.73 (s, 9H); ^{13}C NMR (125 MHz, $C_2D_2Cl_4$, 403 K, ppm) δ 152.49, 150.75, 132.46, 131.80, 129.87, 129.49, 129.05, 127.96, 125.15, 125.06, 124.52,

123.73, 122.79, 122.71, 120.35; HRMS (MALDI) *m/z*: Calcd for $C_{32}H_{23}BO_2$: 450.1791; Found: 450.1787 $[M]^+$. Element analysis calcd (%) for $C_{32}H_{23}BO_2$: C 85.35, H 5.15; found: C 85.15, H 5.09.

Synthesis of 11,12,23,24-tetraoxa-11a,23a-diboratetrabenzo[*a,f,n,s*]terrylene (2a)

To a solution of **6a** (100 mg, 0.160 mmol) in anhydrous dichlorobenzene (10 mL) under argon was added BBr_3 (1.0 M in heptane, 0.49 mL, 0.49 mmol). Then the mixture was heated to 150 °C and stirred at this temperature for 12 h. After cooling to room temperature, 20 mL of methanol was added. The precipitate was filtered and washed with methanol as well as 15 mL of CH_2Cl_2. The solid was dried under vacuum to give compound **2a** as a red solid (89 mg, 95% yield. M.p.: > 380 °C. The poor solubility of this compound prevents any NMR characterizations. HRMS (MALDI) *m/z*: Calcd for $C_{40}H_{20}B_2O_4$: 586.1548; Found: 586.1567 $[M]^+$. Element analysis calcd (%) for $C_{40}H_{20}B_2O_4$: C 81.96, H 3.44; found: C 81.75, H 3.42.

Synthesis of 2,9,14,21-tetradodecyl-11,12,23,24-tetraoxa-11a,23a-diboratetrabenzo[*a,f,n,s*]terrylene (2b)

To a solution of **6b** (150 mg, 0.115 mmol) in anhydrous dichlorobenzene (12 mL) under argon was added BBr_3 (1.0 M in heptane, 0.35 mL, 0.35 mmol). Then the mixture was heated to 150 °C and stirred at this temperature for 12 h. After cooling to room temperature, the reaction mixture was quenched with methanol and concentrated under reduced pressure. Then the residue was purified by column chromatography over a short pad of silica gel with hot chloroform as the eluent to give compound **2b** as a red solid (140 mg, 96% yield). M.p.: 146.3 – 147.8 °C. ^{1}H NMR (500 MHz, $C_2D_2Cl_4$, 403 K, ppm) δ 9.00 (s, 4H), 8.72 (d, J = 8.1 Hz, 4H), 7.51 (s, 4H), 7.33 (d, J = 8.1 Hz, 4H), 2.89 (t, J = 7.6 Hz, 8H), 1.90 (p, J = 7.5 Hz, 8H), 1.40 (s, 72H), 0.98 (t, J = 6.7 Hz, 12H); ^{13}C NMR (125 MHz, $C_2D_2Cl_4$, 403 K, ppm) δ 152.46, 144.96, 133.34, 130.04, 129.18, 124.77, 124.74, 123.00, 121.84, 119.82, 35.42, 31.58, 30.46, 29.34, 29.30, 29.27, 29.24, 29.21, 29.16, 29.11, 28.95, 22.25; HRMS (MALDI) *m/z*: Calcd for $C_{88}H_{116}B_2O_4$: 1258.9060; Found: 1258.9042 $[M]^+$. Element analysis calcd (%) for $C_{88}H_{116}B_2O_4$: C 83.92, H 9.28; found: C 83.61, H 9.15.

Device fabrication and measurement

The electrical properties were measured by fabricating bottom-gate top-contact OFET devices. Heavily n-doped silicon wafers were used as the gate electrode and thermally grown 300-nm-thick SiO_2 (capacitance: 11.0 nF cm^{-2}) was adopted as the dielectric layer. The Si/SiO_2 substrates were sonicated in acetone and 2-propanol, respectively, and then treated by an oxygen plasma. The semiconductor layer of compound **2b** was spin coated from a $CHCl_3$ solution (1 mg/mL); that of compound **1** was dip-coated by using a blend of compound **1** and PMMA in $CHCl_3$ with a weight ratio of 1 : 1. Then source and drain gold electrodes were deposited on top of the organic thin films. The characteristics of the OFETs were measured at room temperature in a glove box by using a Keithley 4200 semiconductor parameter analyzer. The charge carrier mobility was calculated in the saturated region by the equation $I_{sd} = (W/2L)C_i\,\mu(V_g - V_{th})^2$, where I_{sd} is the source/drain current in the saturated regime; W is the channel width (500 μm) and L is the channel length (25 μm); V_g and V_{th} are the gate and threshold voltage, respectively; C_i is the capacitance per unit area of the gate dielectric layer. Current on/off ratio was calculated from the I_{sd} at V_g = 0 V (I_{off}) and V_g = −100 V (I_{on}).

Acknowledgements

This work was financially supported by the Max Planck Society. [redacted] and [redacted] are grateful for a fellowship from the China Scholarship Council. [redacted] acknowledges a fellowship from the Alexander von Humboldt Foundation.

Conflict of Interest

The authors declare no conflict of interest.

Keywords: pyrene • heteroannulation • chromophores • fluorescence • charge transport

References:

[1] (a) A. Narita, X.-Y. Wang, X. Feng, K. Müllen, *Chem. Soc. Rev.* **2015**, *44*, 6616-6643; (b) Z. Sun, Q. Ye, C. Chi, J. Wu, *Chem. Soc. Rev.* **2012**, *41*, 7857-7889.

[2] (a) L. Chen, C. Li, K. Müllen, *J. Mater. Chem. C* **2014**, *2*, 1938-1956; (b) J. Fabian, H. Nakazumi, M. Matsuoka, *Chem. Rev.* **1992**, *92*, 1197-1226.

[3] (a) Y. Shirota, H. Kageyama, *Chem. Rev.* **2007**, *107*, 953-1010; (b) C. Wang, H. Dong, W. Hu, Y. Liu, D. Zhu, *Chem. Rev.* **2012**, *112*, 2208-2267.

[4] T. Yu, L. Liu, Z. Xie, Y. Ma, *Sci. China Chem.* **2015**, *58*, 907-915.

[5] (a) A. W. Hains, Z. Liang, M. A. Woodhouse, B. A. Gregg, *Chem. Rev.* **2010**, *110*, 6689-6735; (b) L. Lu, T. Zheng, Q. Wu, A. M. Schneider, D. Zhao, L. Yu, *Chem. Rev.* **2015**, *115*, 12666-12731; (c) K. A. Mazzio, C. K. Luscombe, *Chem. Soc. Rev.* **2015**, *44*, 78-90.

[6] Y. Im, S. Y. Byun, J. H. Kim, D. R. Lee, C. S. Oh, K. S. Yook, J. Y. Lee, *Adv. Funct. Mater.* **2017**, *27*, 1603007.

[7] (a) H. Sirringhaus, *Adv. Mater.* **2014**, *26*, 1319-1335; (b) X. Zhan, A. Facchetti, S. Barlow, T. J. Marks, M. A. Ratner, M. R. Wasielewski, S. R. Marder, *Adv. Mater.* **2011**, *23*, 268-284.

[8] (a) J. Roncali, P. Leriche, P. Blanchard, *Adv. Mater.* **2014**, *26*, 3821-3838; (b) C. Yan, S. Barlow, Z. Wang, H. Yan, A. K. Y. Jen, S. R. Marder, X. Zhan, *Nat. Rev. Mater.* **2018**, *3*, 18003.

[9] (a) Y. Morita, S. Suzuki, K. Sato, T. Takui, *Nat. Chem.* **2011**, *3*, 197; (b) Z. Zeng, X. Shi, C. Chi, J. T. López Navarrete, J. Casado, J. Wu, *Chem. Soc. Rev.* **2015**, *44*, 6578-6596.

[10] (a) M. Stępień, E. Gońka, M. Żyła, N. Sprutta, *Chem. Rev.* **2017**, *117*, 3479-3716; (b) W. Jiang, Y. Li, Z. Wang, *Chem. Soc. Rev.* **2013**, *42*, 6113-6127; (c) C. Dou, S. Saito, K. Matsuo, I. Hisaki, S. Yamaguchi, *Angew. Chem. Int. Ed.* **2012**, *124*, 12372-12376; (d) Y. Zhou, W.-J. Liu, Y. Ma, H. Wang, L. Qi, Y. Cao, J. Wang, J. Pei, *J. Am. Chem. Soc.* **2007**, *129*, 12386-12387; (e) S. K. Keshri, D. Asthana, S. Chorol, Y. Kumar, P. Mukhopadhyay, *Chem. Eur. J.* **2018**, *24*, 1821-1832; (f) X.-Y. Wang, M. Richter, Y. He, J. Björk, A. Riss, R. Rajesh, M. Garnica, F. Hennersdorf, J. J. Weigand, A. Narita, R. Berger, X. Feng, W. Auwärter, J. V. Barth, C.-A. Palma, K. Müllen, *Nat. Commun.* **2017**, *8*, 1948.

[11] T. M. Figueira-Duarte, K. Müllen, *Chem. Rev.* **2011**, *111*, 7260-7314.

[12] (a) S. Bernhardt, M. Kastler, V. Enkelmann, M. Baumgarten, K. Müllen, *Chem. Eur. J.* **2006**, *12*, 6117-6128; (b) M. Gingras, V. Placide, J. M. Raimundo, G. Bergamini, P. Ceroni,

V. Balzani, *Chem. Eur. J.* **2008**, *14*, 10357-10363; (c) H.-Y. Oh, C. Lee, S. Lee, *Org. Electron.* **2009**, *10*, 163-169.

[13] (a) J. Hu, D. Zhang, F. W. Harris, *J. Org. Chem.* **2005**, *70*, 707-708; (b) B. Gao, M. Wang, Y. Cheng, L. Wang, X. Jing, F. Wang, *J. Am. Chem. Soc.* **2008**, *130*, 8297-8306; (c) P. Jin, T. Song, J. Xiao, Q. Zhang, *Asian J. Org. Chem.* **2018**, DOI: 10.1002/ajoc.201800039.

[14] D. N. Coventry, A. S. Batsanov, A. E. Goeta, J. A. Howard, T. B. Marder, R. N. Perutz, *Chem. Commun.* **2005**, 2172-2174.

[15] (a) A. G. Crawford, A. D. Dwyer, Z. Liu, A. Steffen, A. Beeby, L.-O. Pålsson, D. J. Tozer, T. B. Marder, *J. Am. Chem. Soc.* **2011**, *133*, 13349-13362; (b) A. G. Crawford, Z. Liu, I. A. I. Mkhalid, M.-H. Thibault, N. Schwarz, G. Alcaraz, A. Steffen, J. C. Collings, A. S. Batsanov, J. A. K. Howard, T. B. Marder, *Chem. Eur. J.* **2012**, *18*, 5022-5035.

[16] (a) W. Yang, J. H. Monteiro, A. de Bettencourt‐Dias, V. J. Catalano, W. A. Chalifoux, *Angew. Chem. Int. Ed.* **2016**, *55*, 10427-10430; (b) L. Zou, X.-Y. Wang, K. Shi, J.-Y. Wang, J. Pei, *Org. Lett.* **2013**, *15*, 4378-4381.

[17] (a) X.-Y. Wang, A. Narita, W. Zhang, X. Feng, K. Müllen, *J. Am. Chem. Soc.* **2016**, *138*, 9021-9024; (b) X.-Y. Wang, X.-C. Wang, A. Narita, M. Wagner, X.-Y. Cao, X. Feng, K. Müllen, *J. Am. Chem. Soc.* **2016**, *138*, 12783-12786.

[18] (a) L. Zöphel, D. Beckmann, V. Enkelmann, D. Chercka, R. Rieger, K. Müllen, *Chem. Commun.* **2011**, *47*, 6960-6962; (b) L. Zöphel, V. Enkelmann, R. Rieger, K. Müllen, *Org. Lett.* **2011**, *13*, 4506-4509.

[19] K. Rurack, in *Standardization and Quality Assurance in Fluorescence Measurements I: Techniques* (Ed.: U. Resch-Genger), Springer Berlin Heidelberg, Berlin, Heidelberg, **2008**, pp. 101-145.

[20] (a) S. Ghosh, X. Q. Li, V. Stepanenko, F. Würthner, *Chem. Eur. J.* **2008**, *14*, 11343-11357; (b) Z. Chen, V. Stepanenko, V. Dehm, P. Prins, L. D. Siebbeles, J. Seibt, P. Marquetand, V. Engel, F. Würthner, *Chem. Eur. J.* **2007**, *13*, 436-449; (c) E. E. Neuteboom, S. C. Meskers, E. Meijer, R. A. Janssen, *Macromol. Chem. Phys.* **2004**, *205*, 217-222.

[21] U. Rösch, S. Yao, R. Wortmann, F. Würthner, *Angew. Chem. Int. Ed.* **2006**, *118*, 7184-7188.

[22] C. Liu, Y. Li, M. V. Lee, A. Kumatani, K. Tsukagoshi, *Phys. Chem. Chem. Phys.* **2013**, *15*, 7917-7933.

[23] (a) F. Würthner, C. R. Saha-Möller, B. Fimmel, S. Ogi, P. Leowanawat, D. Schmidt, *Chem. Rev.* **2015**, *116*, 962-1052; (b) C. Huang, S. Barlow, S. R. Marder, *J. Org. Chem.* **2011**, *76*, 2386-2407.

Supporting information

Direct C–H Borylation at the 2- and 2,7-Positions of Pyrene Leading to Brightly Blue- and Green-Emitting Chromophores

1. Synthetic Procedure

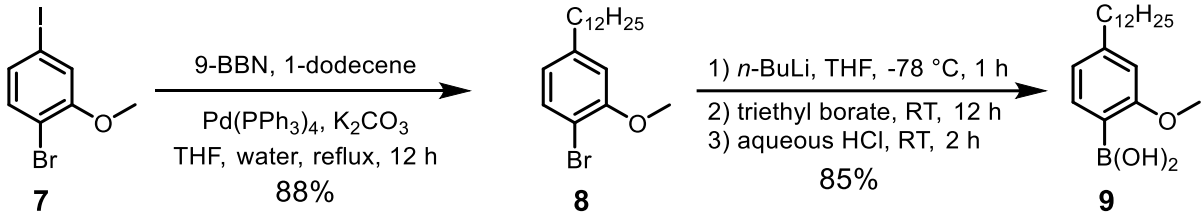

Scheme S1. Synthetic route to compound **9**.

Synthesis of 1-bromo-4-dodecyl-2-methoxybenzene (8)

To a solution of 9-borabicyclo[3.3.1]nonane (9-BBN) (10 mL, 0.50 M, 5.0 mmol) in THF in a Schlenk tube was added 1-dodecene (0.50 mL, 3.7 mmol) at room temperature under argon. After stirring at room temperature for 12 h, the mixture was transferred into another dried Schlenk tube containing 1-bromo-4-iodo-2-methoxybenzene (1.57 g, 5.00 mmol), tetrakis(triphenylphosphine)palladium(0) (289 mg, 0.250 mmol), potassium carbonate (1.38 g, 10.0 mmol), 20 mL of degassed dry THF and 3 mL of degassed water. The reaction mixture was refluxed under argon for 12 h, and then cooled down to room temperature. The mixture was poured into 1 M aqueous HCl and extracted by ethyl acetate. The combined organic layers were washed with brine and dried over $MgSO_4$. After removal of the solvent under reduced pressure, the residue was purified by flash chromatography over silica gel (eluent: hexane/CH_2Cl_2 = 5 : 1) to give compound **8** as colorless oil (1.61 g, 91 % yield). ^{1}H NMR (300 MHz, CD_2Cl_2, 298 K, ppm) δ 7.39 (d, J = 8.0 Hz, 1H), 6.75 (s, 1H), 6.67 (d, J = 8.0 Hz, 1H),

3.86 (s, 3H), 2.57 (t, J = 7.7 Hz, 2H), 1.60 (t, J = 7.5 Hz, 2H), 1.30 – 1.26 (m, 18H), 0.93 – 0.83 (m, 3H); ^{13}C NMR (75 MHz, CD_2Cl_2, 298 K, ppm) δ 156.01, 144.63, 133.06, 122.17, 108.49, 56.40, 36.17, 32.31, 31.76, 30.06, 30.03, 29.97, 29.85, 29.74, 29.62, 23.08, 14.27; HRMS (MALDI) *m/z*: Calcd for $C_{19}H_{31}BrO$: 354.1558; Found: 354.1562 $[M]^+$.

Synthesis of (4-dodecyl-2-methoxyphenyl)boronic acid (9)

To a solution of 1-bromo-4-dodecyl-2-methoxybenzene (5.00 g, 14.1 mmol) in dry THF (70 mL) under argon was added *n*-butyllithium (*n*-BuLi) (10 mL, 16 mmol, 1.6 M in hexane) dropwise at –78 °C. The reaction mixture was stirred at this temperature for 1 h, and then warmed to room temperature for another hour. The mixture was then cooled to –78 °C again. Triethyl borate was added, and then the mixture was allowed to gradually warm to room temperature. After stirring for 12 h, the reaction was quenched by adding 2 M aqueous HCl, and the mixture was stirred for 2 h at room temperature. The product was extracted with diethyl ether and the combined organic layers were washed with water and dried over $MgSO_4$. After removal of the solvent under reduced pressure, the residue was purified by flash chromatography over silica gel using CH_2Cl_2 and then ethyl acetate as the eluent to obtain compound **9** as a white solid (3.83 g, 85 % yield). M.p.: 66.3 – 67.4 °C. ^{1}H NMR (300 MHz, CD_2Cl_2, 298 K, ppm) δ 7.69 (d, J = 7.5 Hz, 1H), 6.86 (d, J = 7.5 Hz, 1H), 6.77 (s, 1H), 6.17 (s, 2H), 3.90 (s, 3H), 2.63 (t, J = 7.8 Hz, 2H), 1.60 (t, 2H), 1.27 – 1.31 (m, 18H), 0.89 (t, 3H); ^{13}C NMR (75 MHz, CD_2Cl_2, 298 K, ppm) δ 165.23, 149.17, 136.84, 129.44, 121.61, 110.67, 55.77, 36.75, 36.35, 32.33, 31.88, 31.69, 30.07, 30.05, 30.00, 29.89, 29.76, 23.09, 14.28; APCI-MS *m/z*: Calcd for $C_{19}H_{33}BO_3$: 320.3; Found: 321.3 $[M + H]^+$.

Table S1. Summary of the photophysical and electrochemical properties of **1** and **2b**.

Compound	λ_{max}^{abs}/nm	λ_{max}^{em}/nm	Φ_F	E_g^{opt}/eV	HOMO/eV	LUMO/eV	E_g^{cv}/eV
1	402, 426	442, 462	0.70	2.81	–5.24	–2.72	2.57
2b	445, 473, 506	525, 556	0.84	2.35	–5.03	–2.68[a]	N. A.

[a] Calculated from the HOMO level and the optical gap.

2. Photophysical and Electrochemical Properties

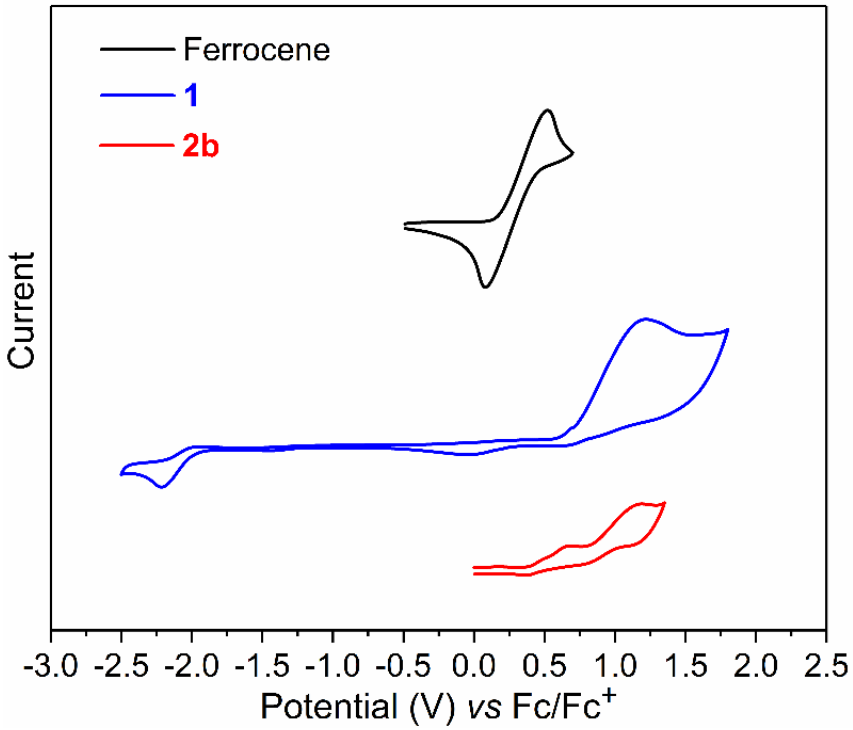

Figure S1. Cyclic voltammograms of compounds **1** and **2b** measured in THF containing 0.1 M *n*-Bu_4NPF_6 at a scan rate of 100 mV s^{-1}. Ferrocene as an external standard. A glassy carbon electrode was used as a working electrode, a platinum wire as a counter electrode and a silver wire as a reference electrode. Due to the limitedsolubility of **2b**, its reductive wave could not be clearly observed.

Fluorescence quantum yield determination

The quantum yield (Φ) of compound **1** and compound **2b** were determined by using 9,10-diphenylanthracene (in toluene under air, Φ_F: 0.70) and fluorescein (in 0.1 N NaOH under air, Φ_F: 0.90) as references, respectively. As a standard measurement, the 9,10-diphenylanthracene was dissolved in toluene (HPLC grade, refractive index η =1.497) and the fluorescein was dissolved 0.1 N NaOH (η =1.335). Compound **1** and **2b** were dissolved in chloroform (η = 1.446). All samples were measured by using UV-Vis spectrometer to obtain the absorbance intensities. Additionally, the absorbance values were kept below 0.1 in order to minimize re-absorption effects. Emission spectra were obtained after excitation at 380 nm for 9,10-diphenylanthracene and compound **1**, 452 nm for fluorescein and compound **2b**. Integrated fluorescence intensity between a fixed wavelength range (390 nm to 800 nm for

9,10-diphenylanthracene and compound **1**, 460 nm to 800 nm for fluorescein and compound **2b**) was calculated. All measurements were conducted under air condition at room temperature.

Absolute values are calculated according to the following equation:

$$\emptyset_x = \emptyset_{ST}\left(\frac{Grad_X}{Grad_{ST}}\right)\left(\frac{\eta_X^2}{\eta_{ST}^2}\right)$$

Where the subscripts ST and X denote standard and test compound respectively, Φ is the fluorescence quantum yield, *Grad* the gradient from the plot of integrated fluorescence intensity vs absorbance, and η the refractive index of the solvent.

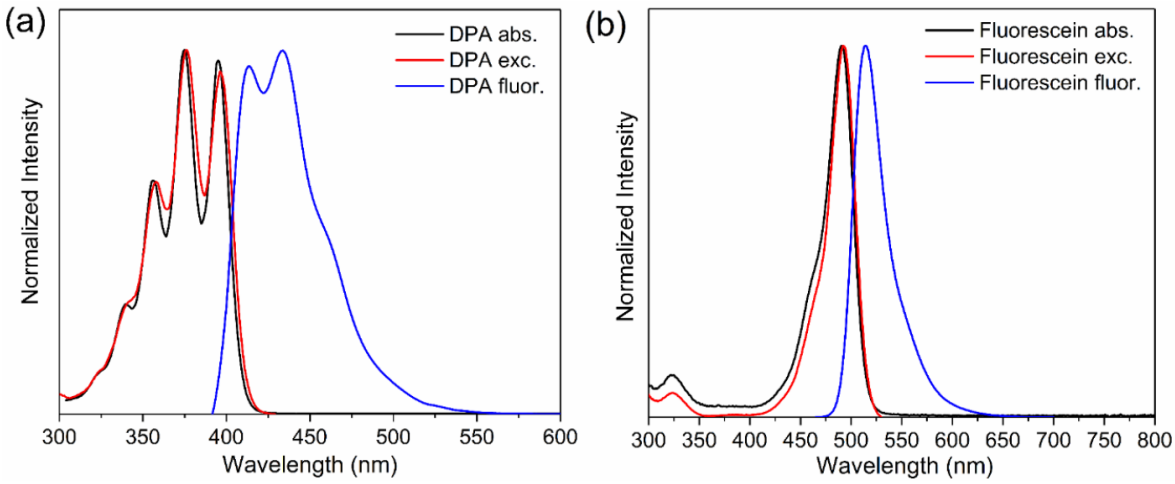

Figure S2. Absorbance, excitation and fluorescence spectra of (a) 9, 10-diphenylanthracene (DPA) in tolueneand (b) fluorescein in 0.1 N NaOH. The excitation spectrum of DPA and fluorescein was detected at 440 nm and 520 nm, respectively. The fluorescence spectrum of DPA and fluorescein was excited at 380 nm and 452 nm, respectively. All the spectra were normalized by the maximum intensity.

3. Computational Studies

DFT calculations were performed using the Gaussian 09 software package.[1] The geometries were optimized at the B3LYP/6-31G(d) level, and energies were calculated at the same level of theory.

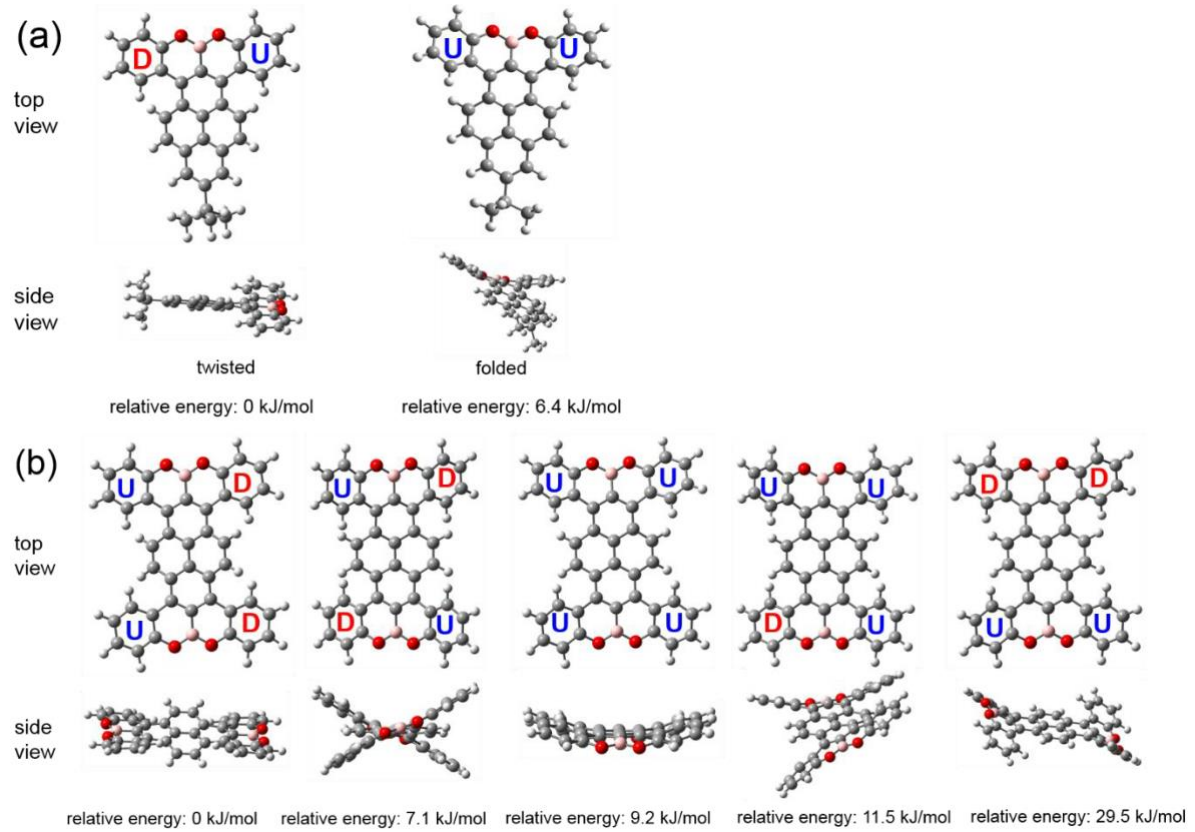

Figure S3. DFT-optimized geometries of (a) compound **1** and (b) compound **2a**. U and D were denoted as "Up" and "Down", respectively, relative to the pyrene unit which was placed on the paper plane.

Reference:

[1] M. J. T. Frisch, G. W.; Schlegel, H. B.; Scuseria, G. E.; Robb, M. A.; Cheeseman, J. R.; Scalmani, G.; Barone, V.; Mennucci, B.; Petersson, G. A.; Nakatsuji, H.; Caricato, M.; Li, X.; Hratchian, H. P.; Izmaylov, A. F.; Bloino, J.; Zheng, G.; Sonnenberg, J. L.; Hada, M.; Ehara, M.; Toyota, K.; Fukuda, R.; Hasegawa, J.; Ishida, M.; Nakajima, T.; Honda, Y.; Kitao, O.; Nakai, H.; Vreven, T.; Montgomery, Jr., J. A.; Peralta, J. E.; Ogliaro, F.; Bearpark, M.; Heyd, J. J.; Brothers, E.; Kudin, K. N.; Staroverov, V. N.; Kobayashi, R.; Normand, J.; Raghavachari, K.; Rendell, A.; Burant, J. C.; Iyengar, S. S.; Tomasi, J.; Cossi, M.;Rega, N.; Millam, N. J.; Klene, M.; Knox, J. E.; Cross, J. B.; Bakken, V.; Adamo, C.; Jaramillo, J.; Gomperts, R.; Stratmann, R. E.; Yazyev, O.; Austin, A. J.; Cammi, R.; Pomelli, C.; Ochterski, J. W.; Martin, R. L.; Morokuma, K.; Zakrzewski, V. G.; Voth, G. A.; Salvador, P.; Dannenberg, J. J.;

Dapprich, S.; Daniels, A. D.; Farkas, Ö.; Foresman, J. B.; Ortiz, J. V.; Cioslowski, J.; Fox, D. J. *Gaussian, Inc., Wallingford CT*, **2013**.

4. Aggregation Studies

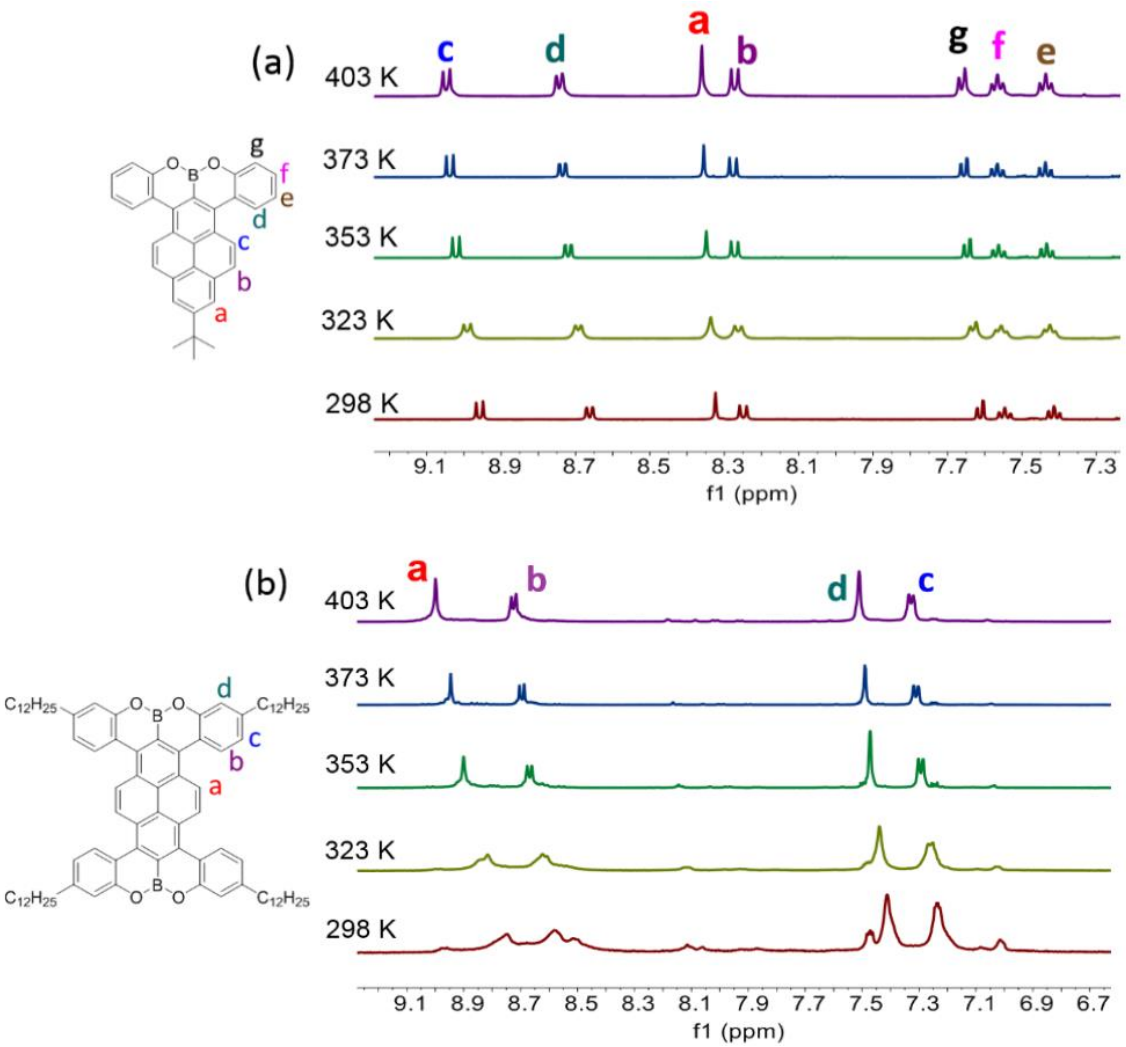

Figure S4. Temperature-dependent ^{1}H NMR spectra of (a) **1** and (b) **2b** (500 MHz, $C_2D_2Cl_4$).

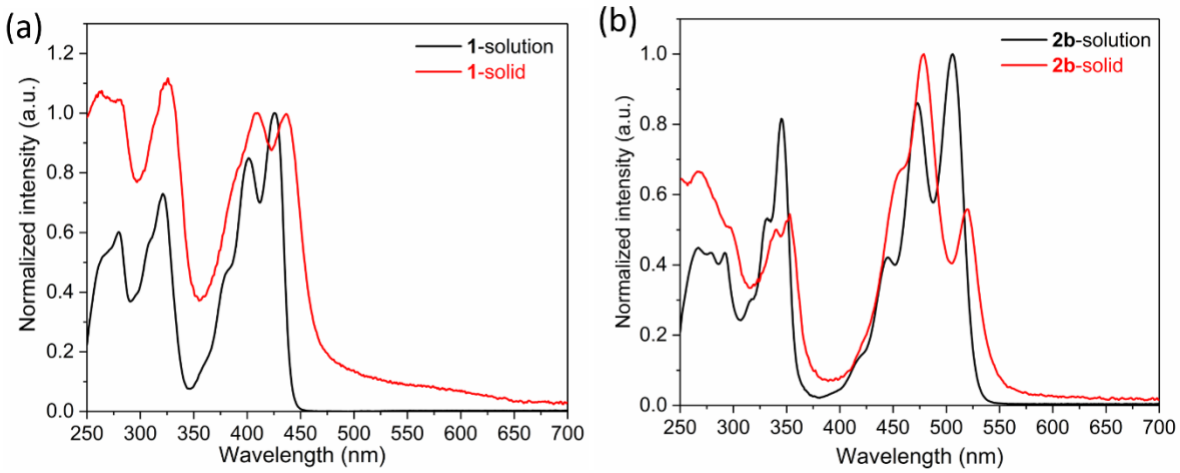

Figure S5. UV-vis absorption spectra of (a) compound **1** and (b) compound **2b** in chloroform solutions and in drop-casted films on quartz.

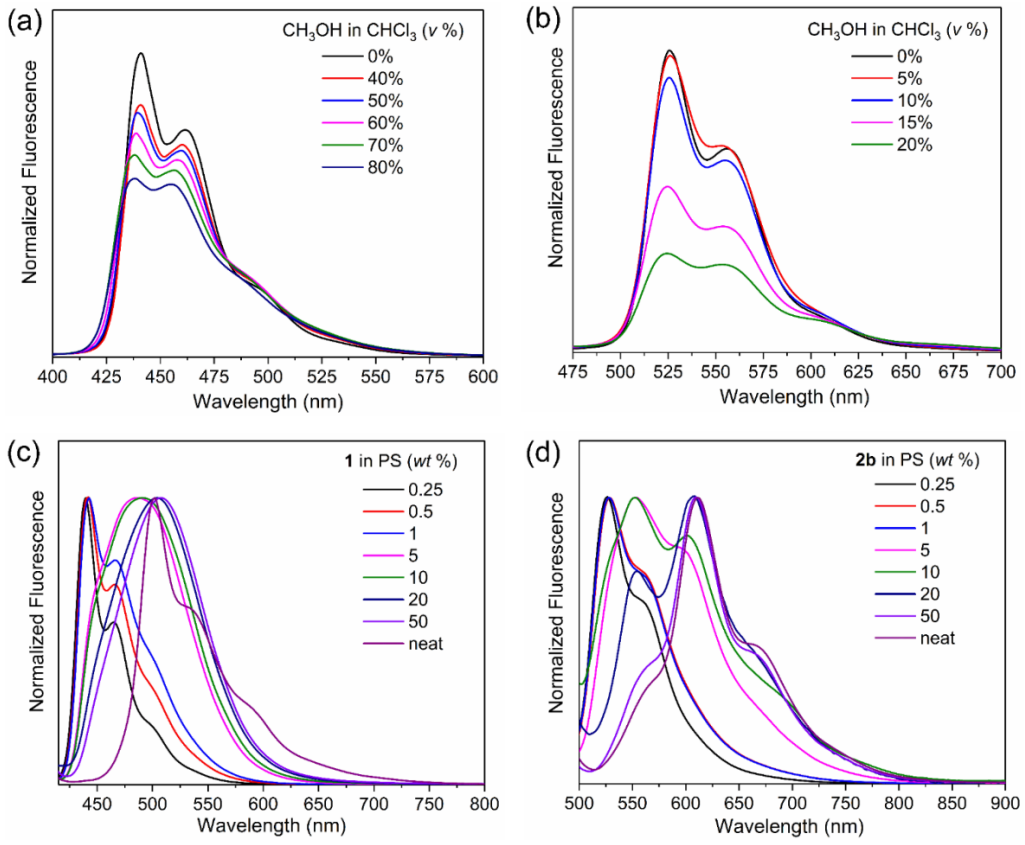

Figure S6. Fluorescence spectra of (a) compound **1** and (b) compound **2b** in a series of mixed solvents of $CHCl_3$ and CH_3OH. Fluorescence spectra of (c) compound **1** and (d) compound **2b** in PS films upon varying the concentrations from 0.25 wt% to neat film. The fluorescence spectra were normalized by the maximum intensity.

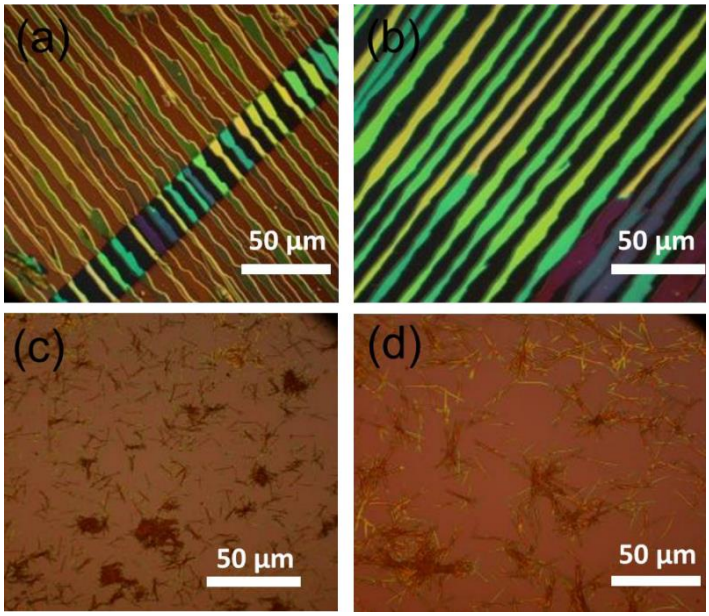

Figure S7. Polarized optical microscopy images of (a, b) compound **1** and (c, d) compound **2b** on silicon wafers by dip-coating.

5. NMR and MS Spectra

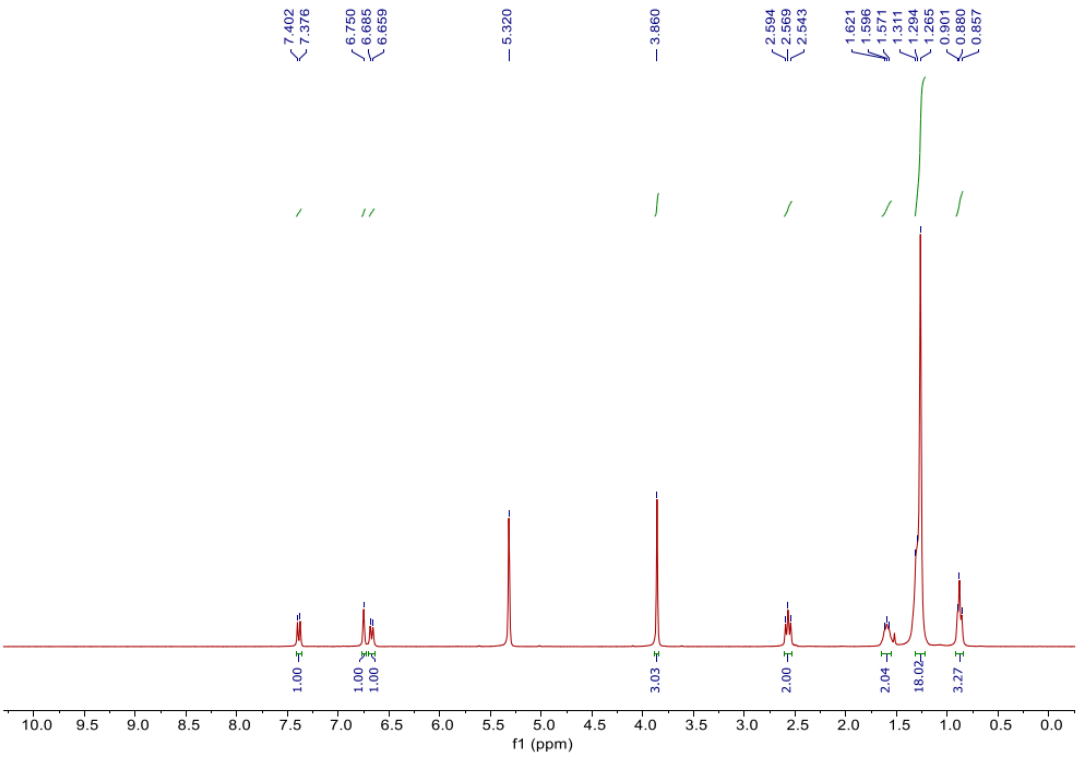

Figure S8. ^{1}H NMR spectrum of compound **8** (300 MHz, CD_2Cl_2, 298 K).

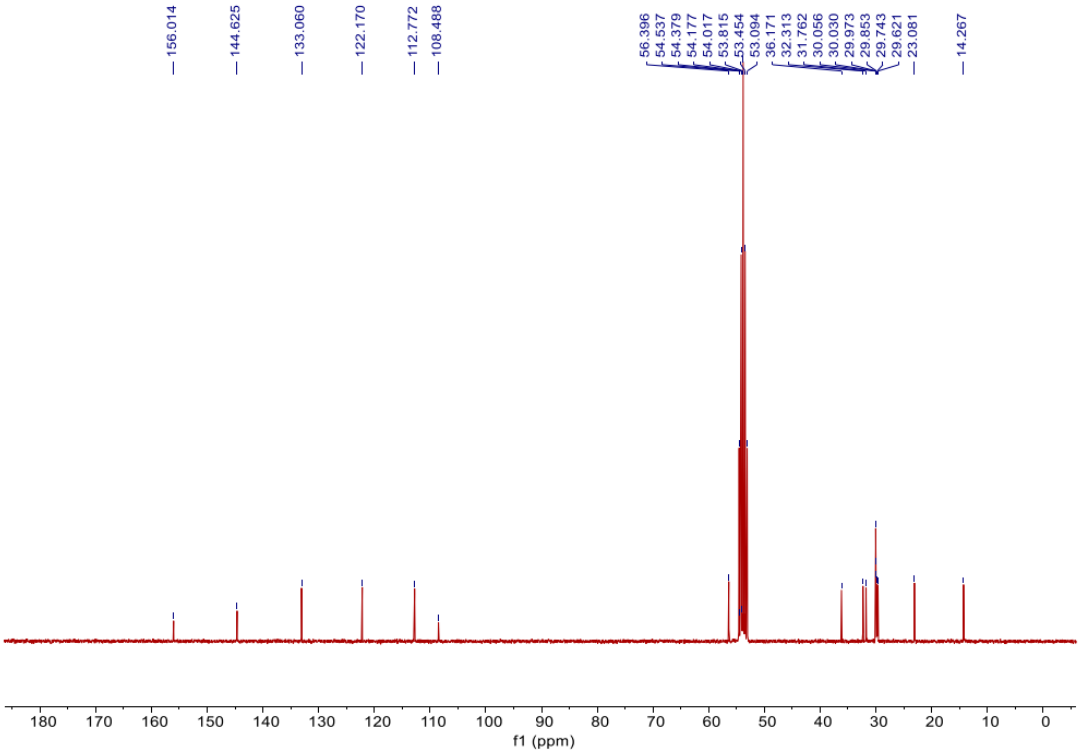

Figure S9. ^{13}C NMR spectrum of compound **8** (75 MHz, CD_2Cl_2, 298 K).

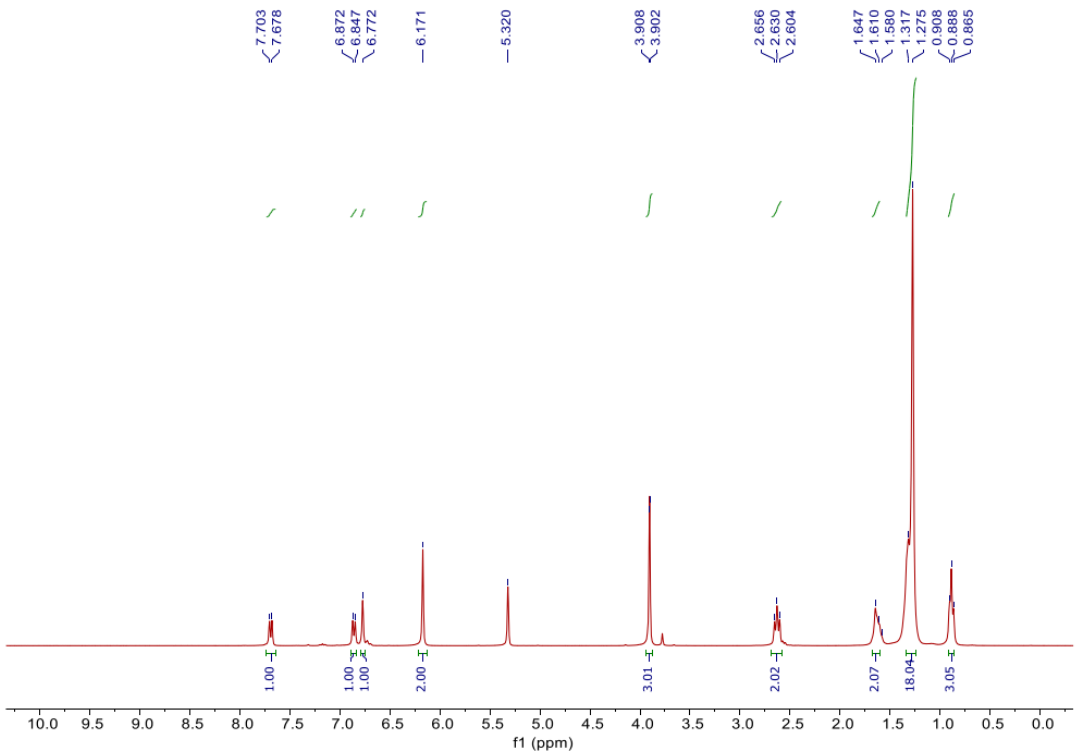

Figure S10. ^{1}H NMR spectrum of compound **9** (300 MHz, CD_2Cl_2, 298 K).

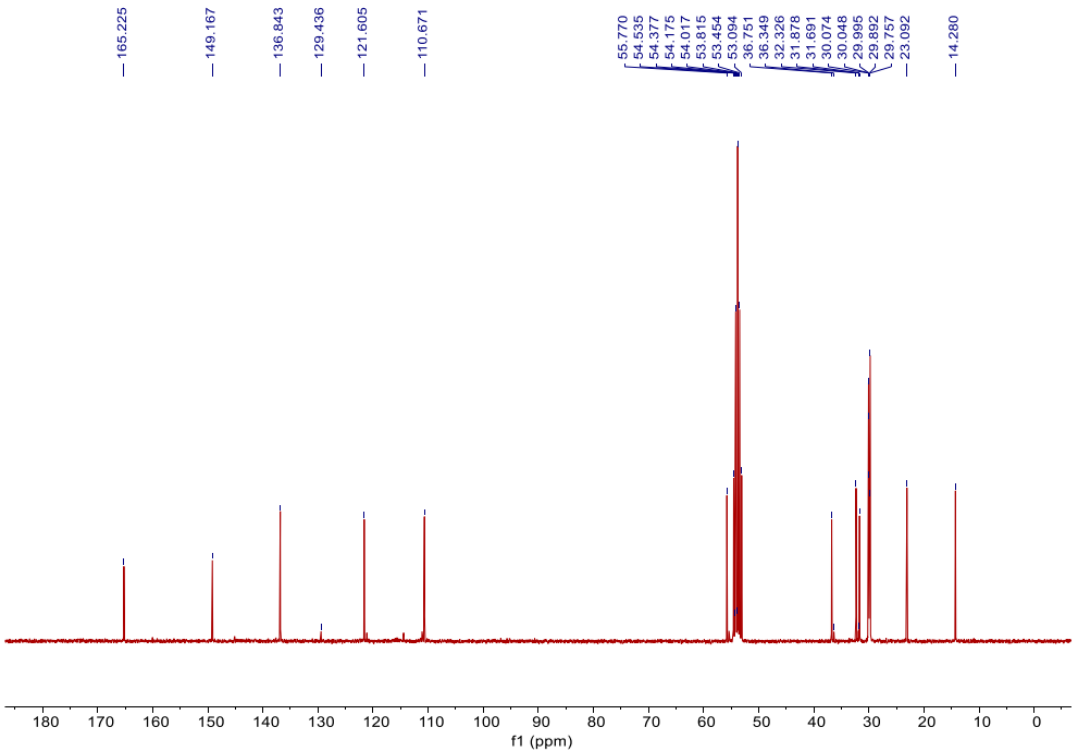

Figure S11. ^{13}C NMR spectrum of compound **9** (75 MHz, CD_2Cl_2, 298 K).

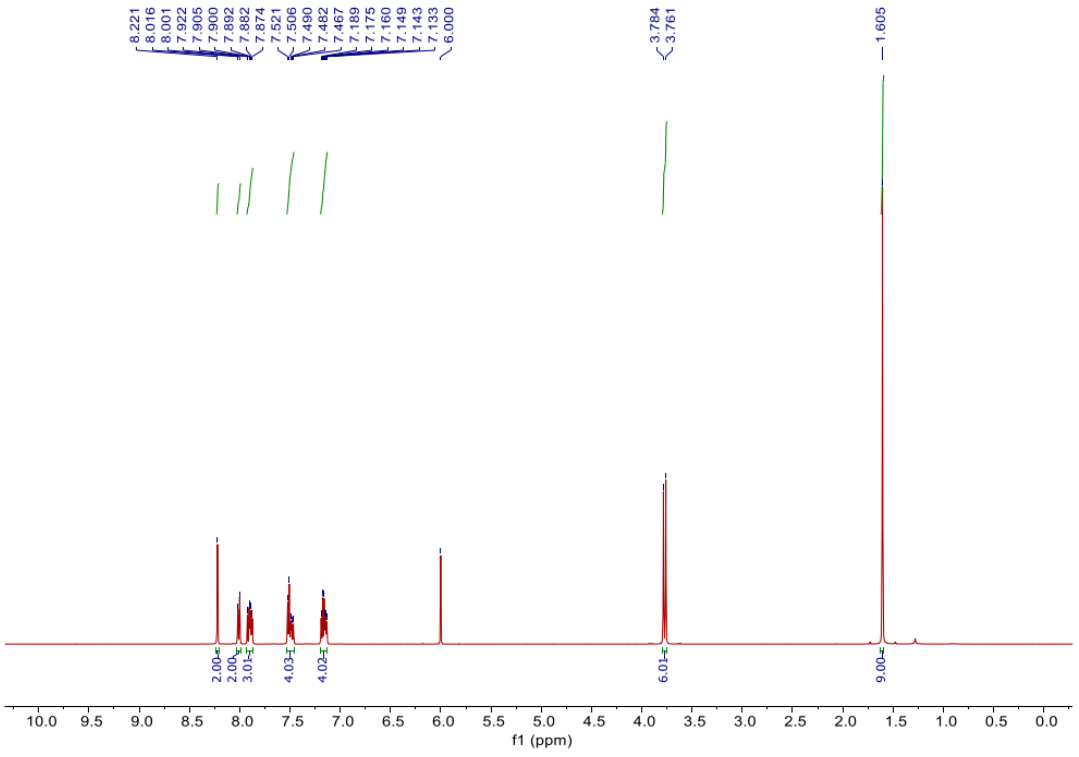

Figure S12. ^{1}H NMR spectrum of compound **4** (500 MHz, $C_2D_2Cl_4$, 403 K).

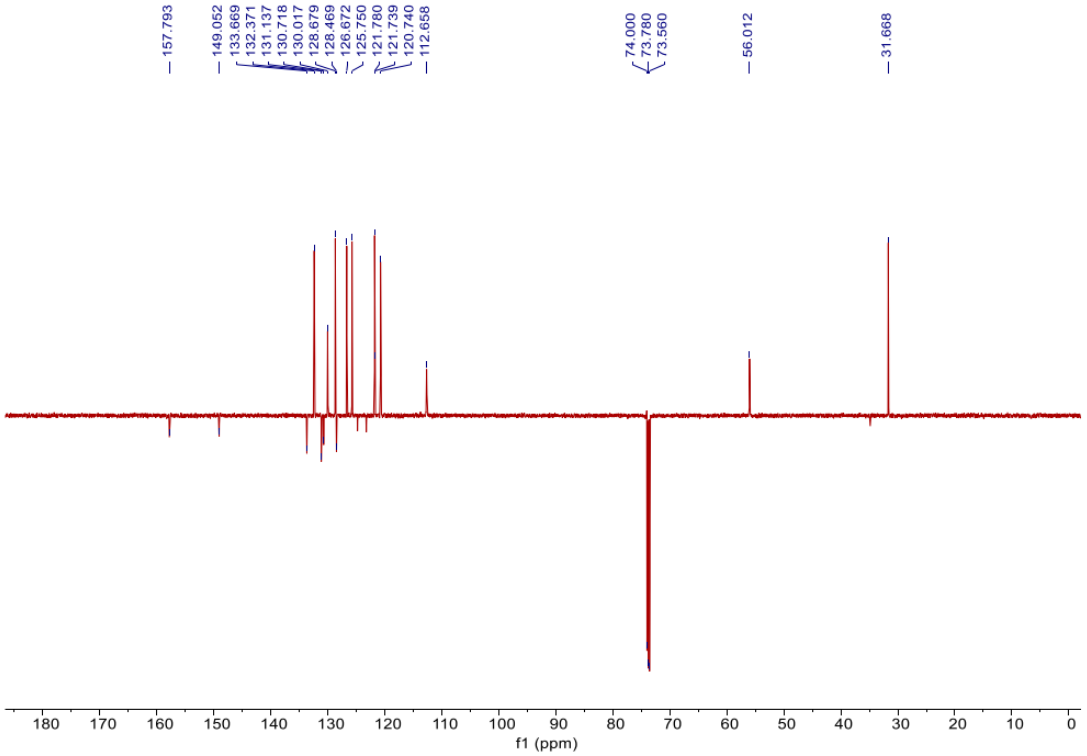

Figure S13. ^{13}C NMR spectrum of compound **4** (125 MHz, $C_2D_2Cl_4$, 403 K).

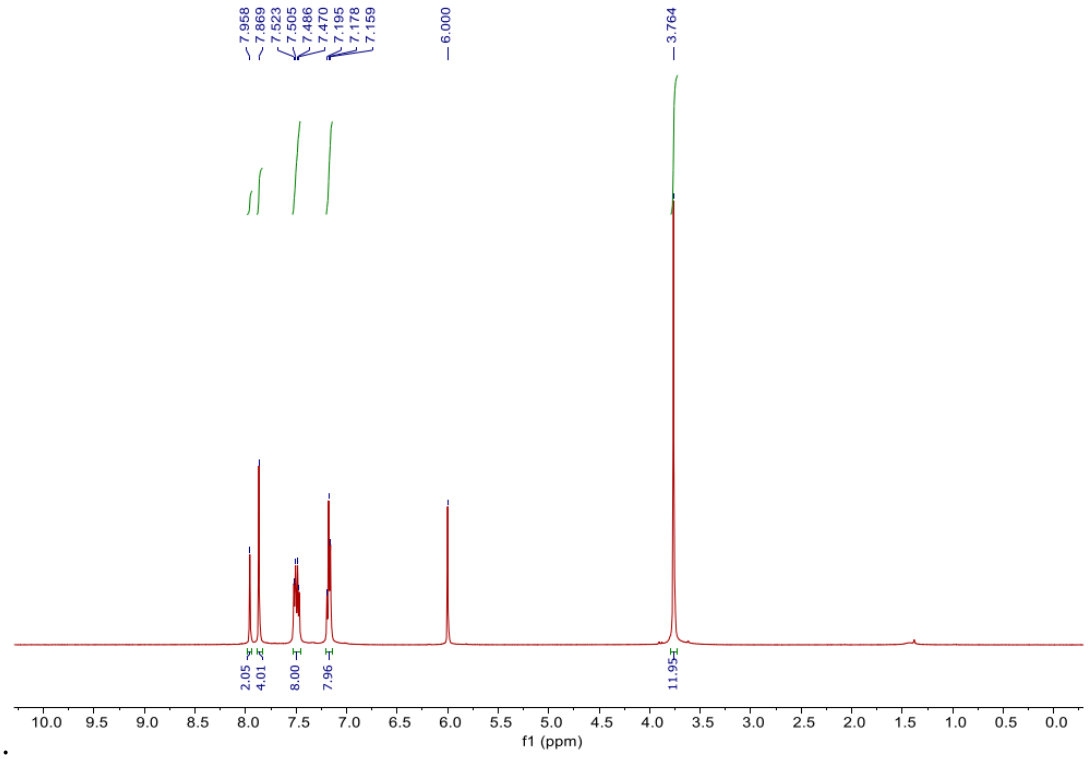

Figure S14. ^{1}H NMR spectrum of compound **6a** (500 MHz, $C_2D_2Cl_4$, 403 K).

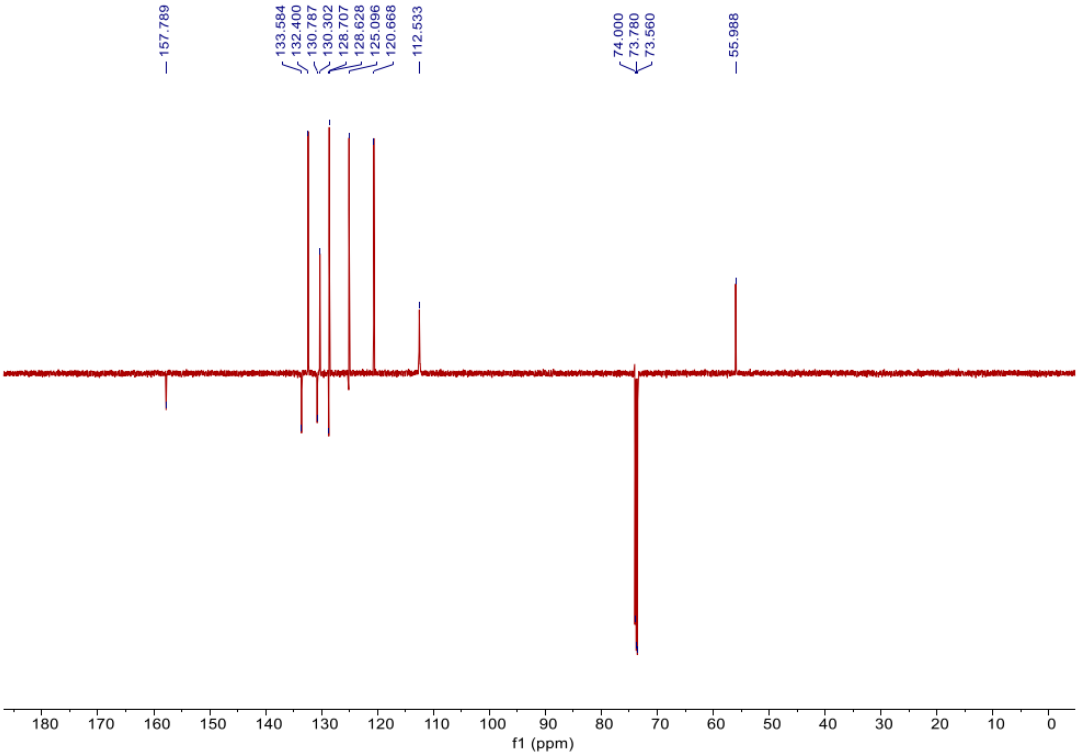

Figure S15. ^{13}C NMR spectrum of compound **6a** (125 MHz, $C_2D_2Cl_4$, 403 K).

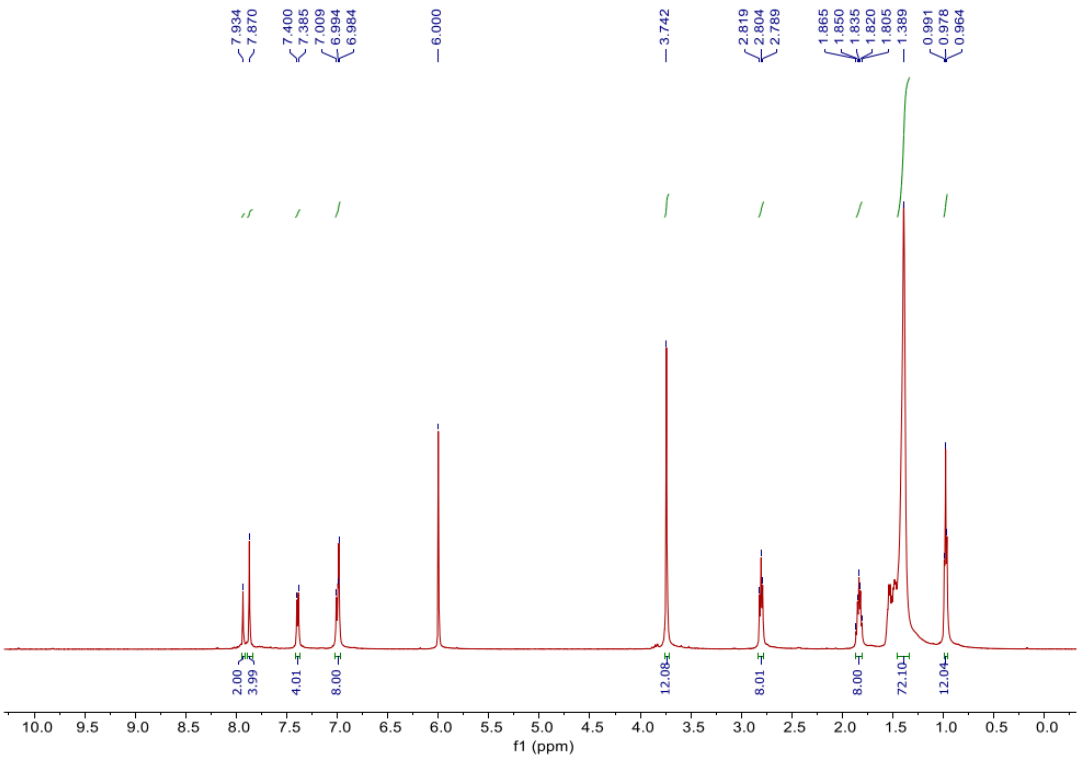

Figure S16. ^{1}H NMR spectrum of compound **6b** (500 MHz, $C_2D_2Cl_4$, 403 K).

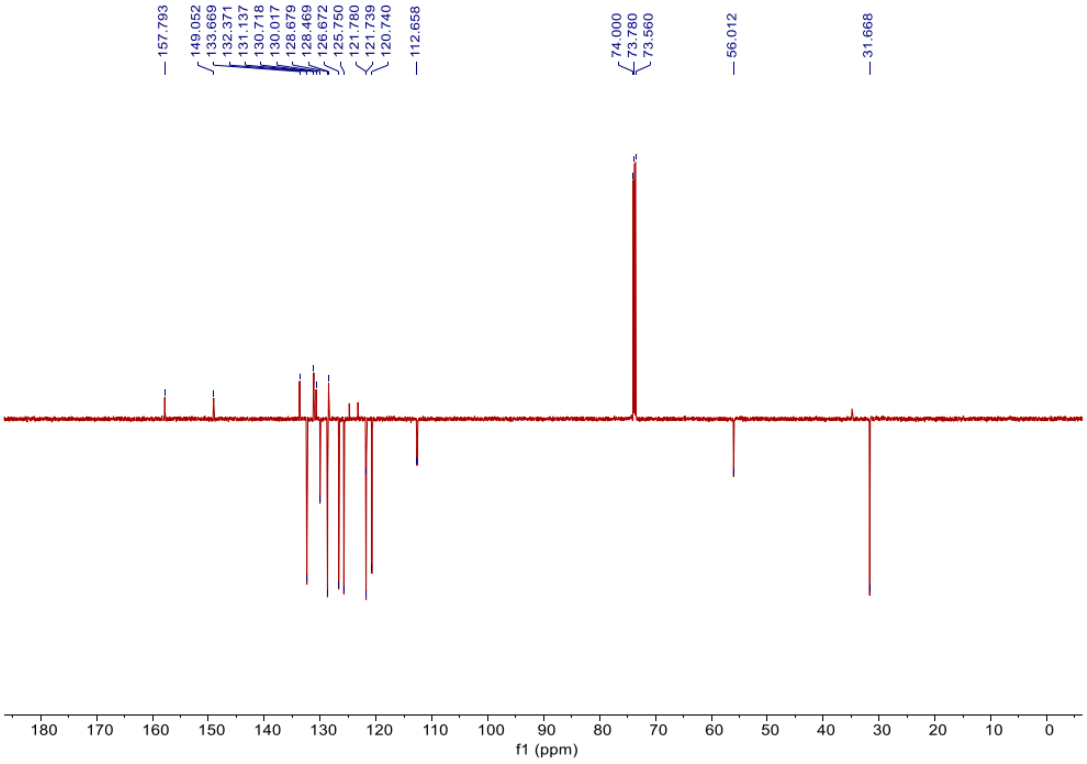

Figure S17. ^{13}C NMR spectrum of compound **6b** (125 MHz, $C_2D_2Cl_4$, 403 K).

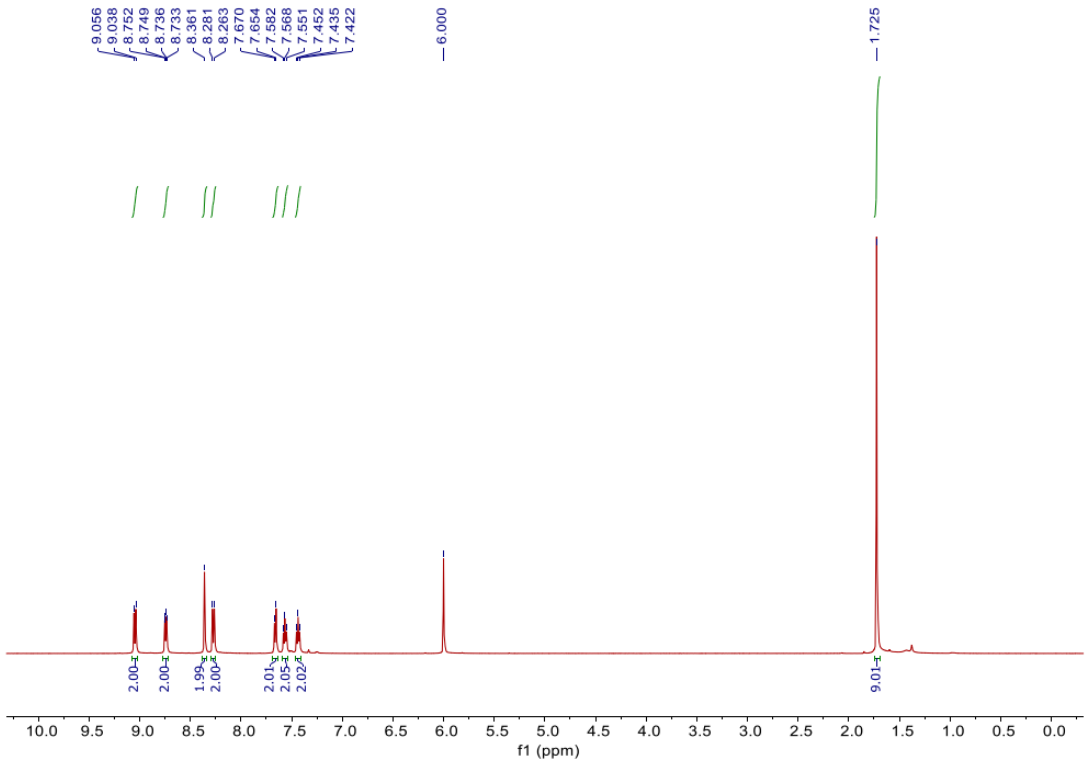

Figure S18. ^{1}H NMR spectrum of compound **1** (500 MHz, $C_2D_2Cl_4$, 403 K).

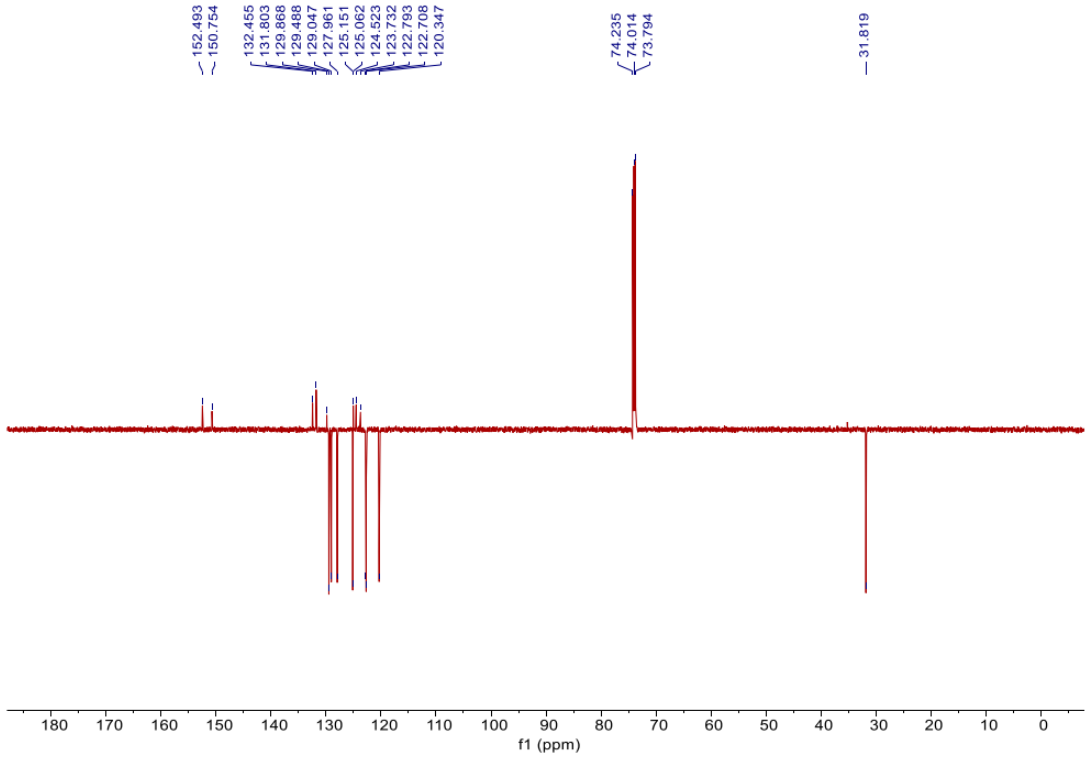

Figure S19. ^{13}C NMR spectrum of compound **1** (125 MHz, $C_2D_2Cl_4$, 403 K).

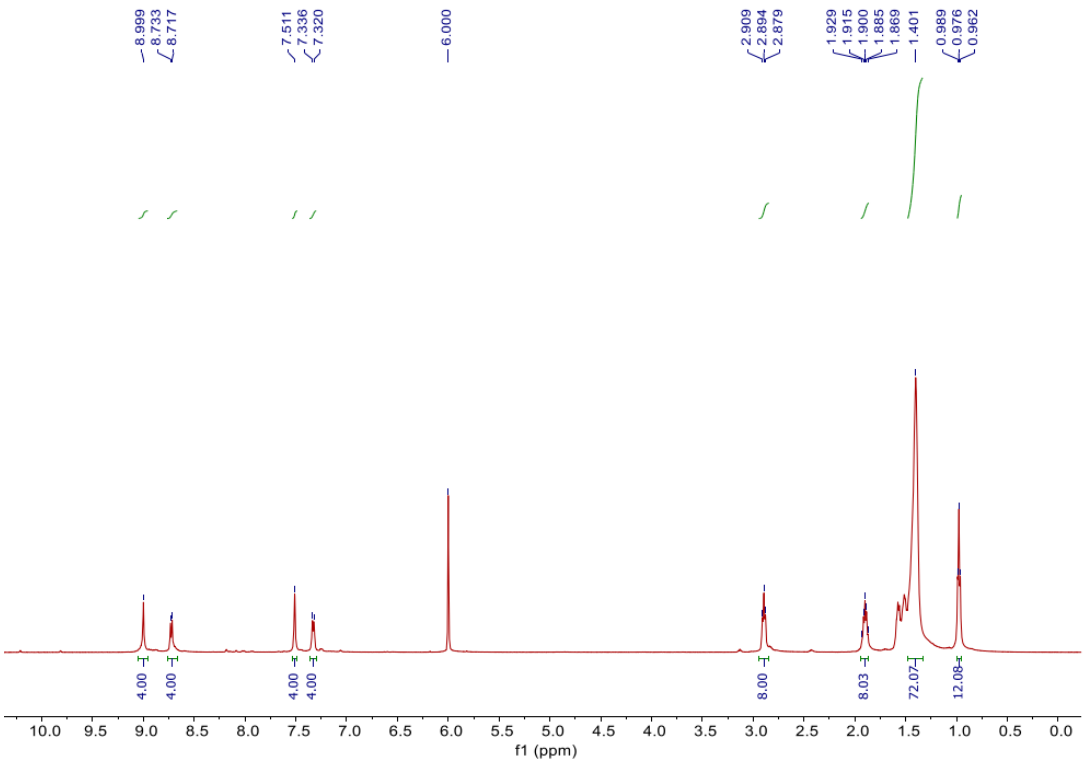

Figure S20. ^{1}H NMR spectrum of compound **2b** (500 MHz, $C_2D_2Cl_4$, 403 K).

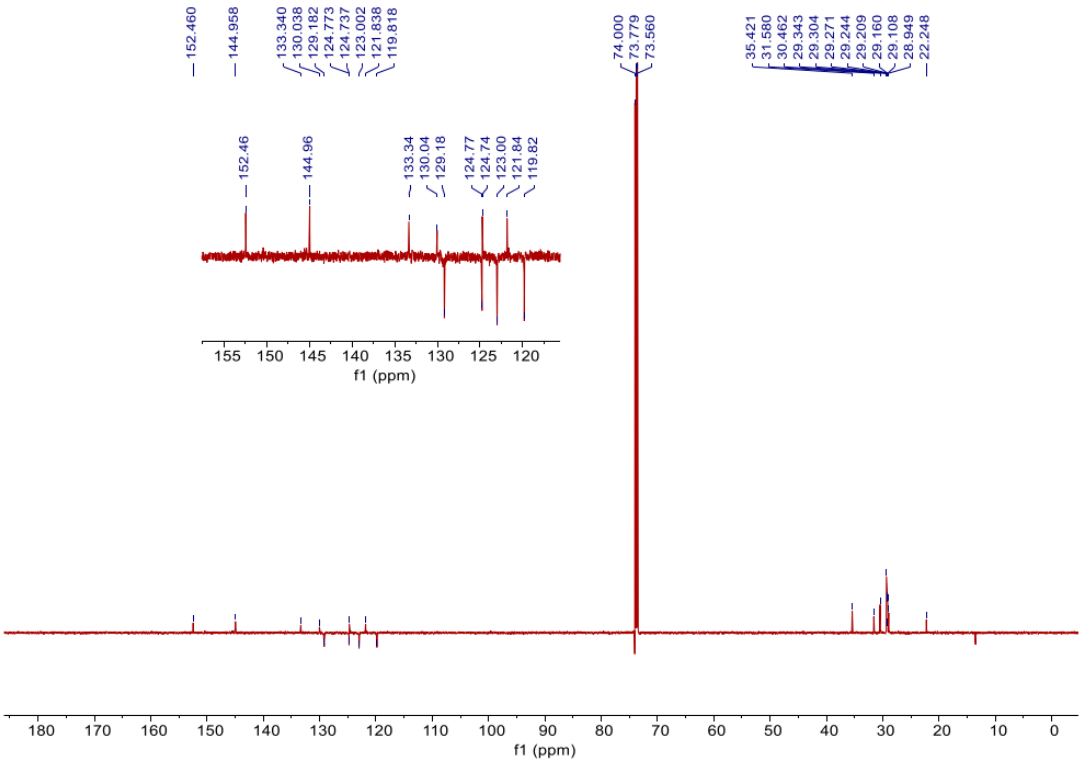

Figure S21. ^{13}C NMR spectrum of compound **2b** (125 MHz, $C_2D_2Cl_4$, 403 K).

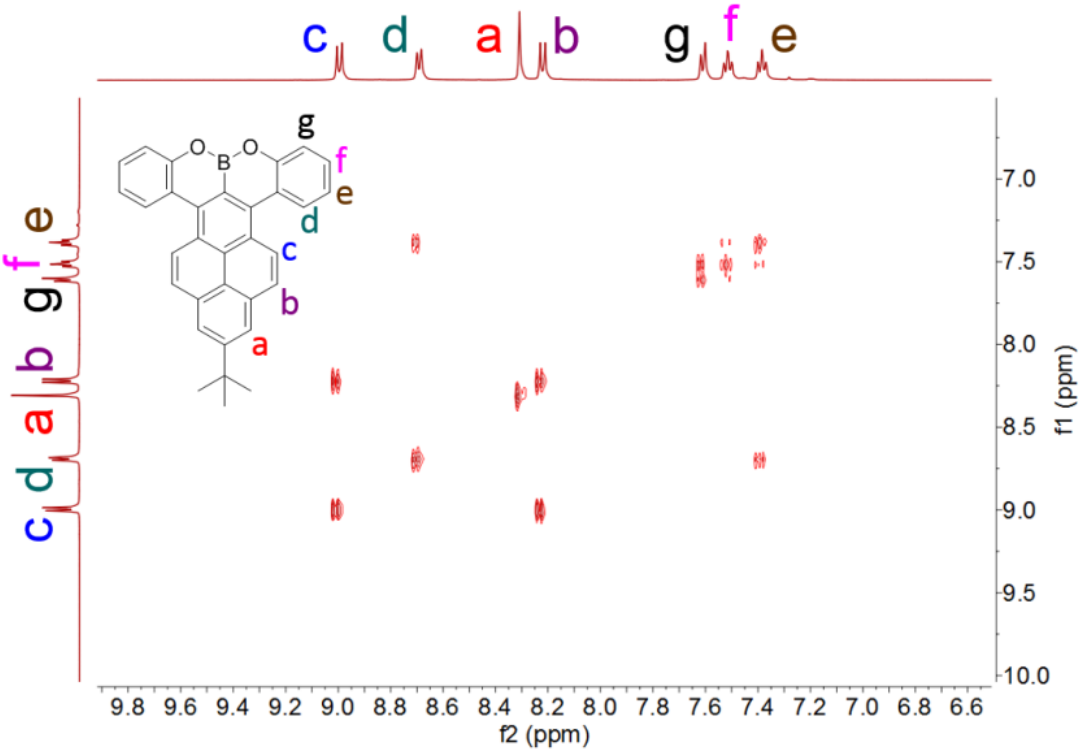

Figure S22. ^{1}H-^{1}H correlation spectroscopy (COSY) NMR spectrum of compound **1** (500 MHz, $C_2D_2Cl_4$, 403 K).

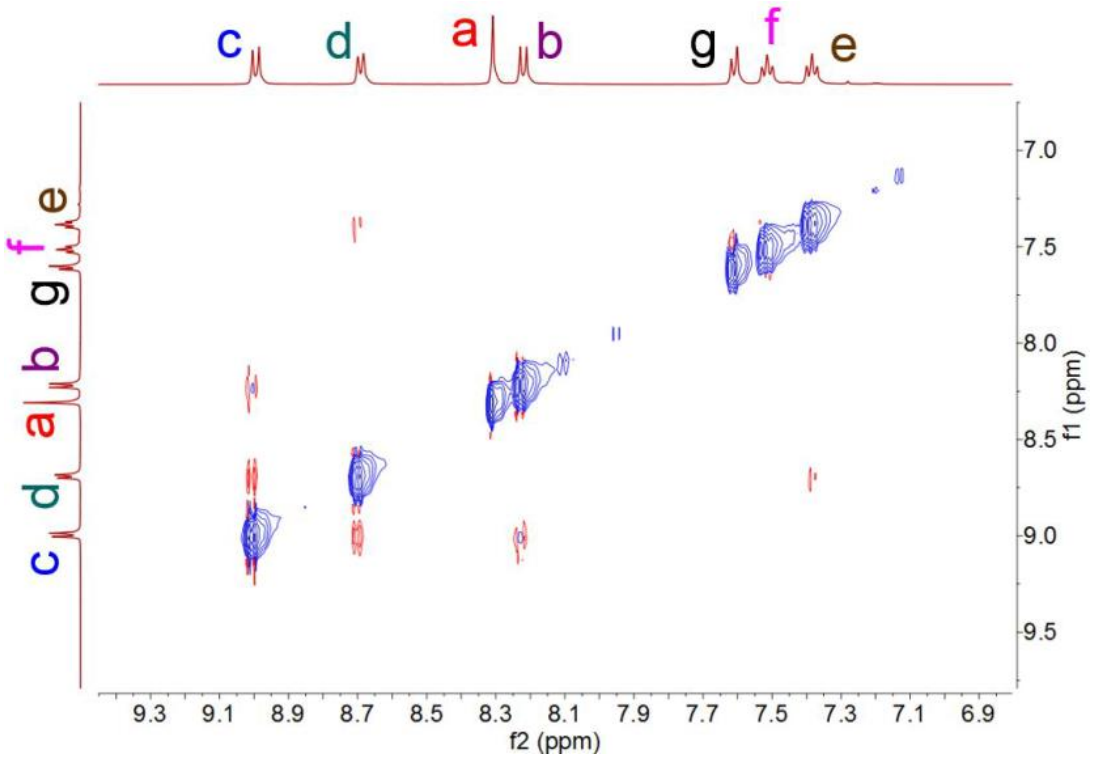

Figure S23. ^{1}H-^{1}H nuclear Overhauser effect spectroscopy (NOESY) NMR spectrum of compound **1** (500 MHz, $C_2D_2Cl_4$, 403 K).

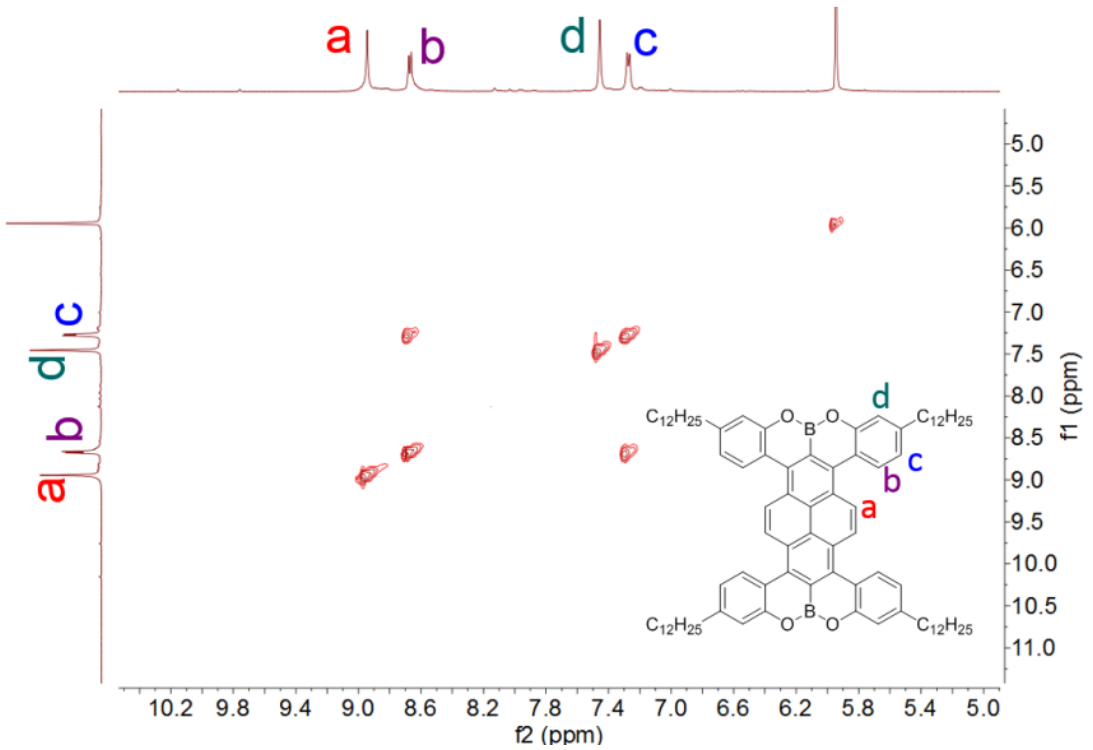

Figure S24. ^{1}H-^{1}H correlation spectroscopy (COSY) NMR spectrum of compound **2b** (500 MHz, $C_2D_2Cl_4$, 403 K).

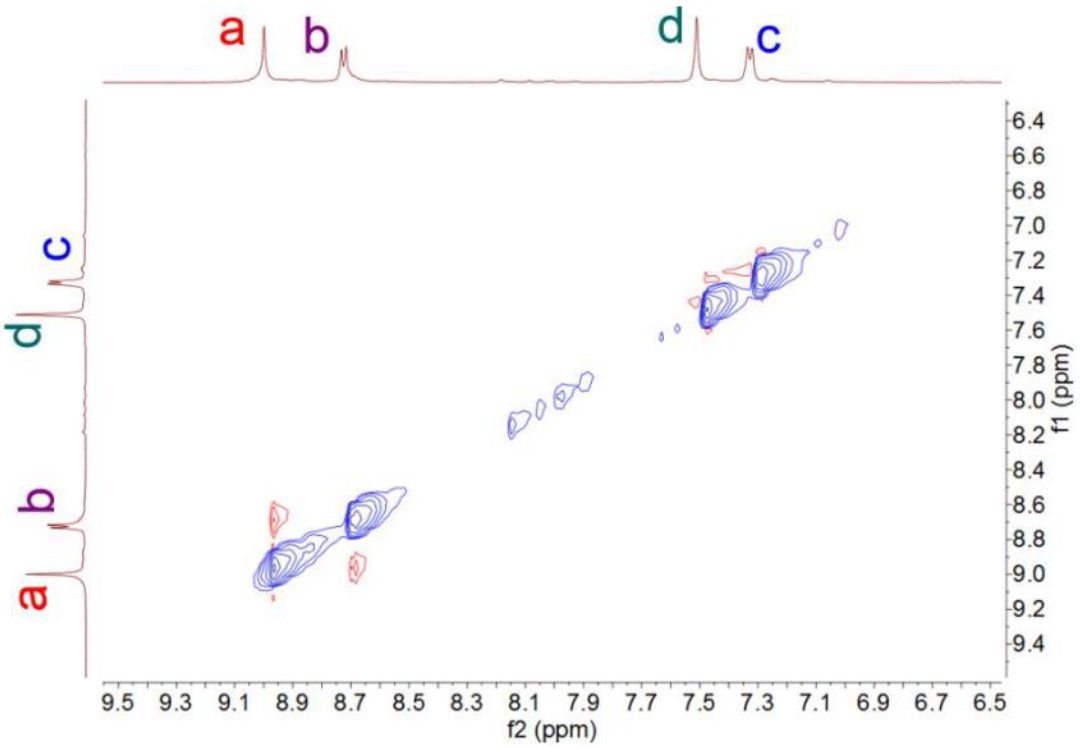

Figure S25. ^{1}H-^{1}H nuclear Overhauser effect spectroscopy (NOESY) NMR spectrum of compound **2b** (500 MHz, $C_2D_2Cl_4$, 403 K).

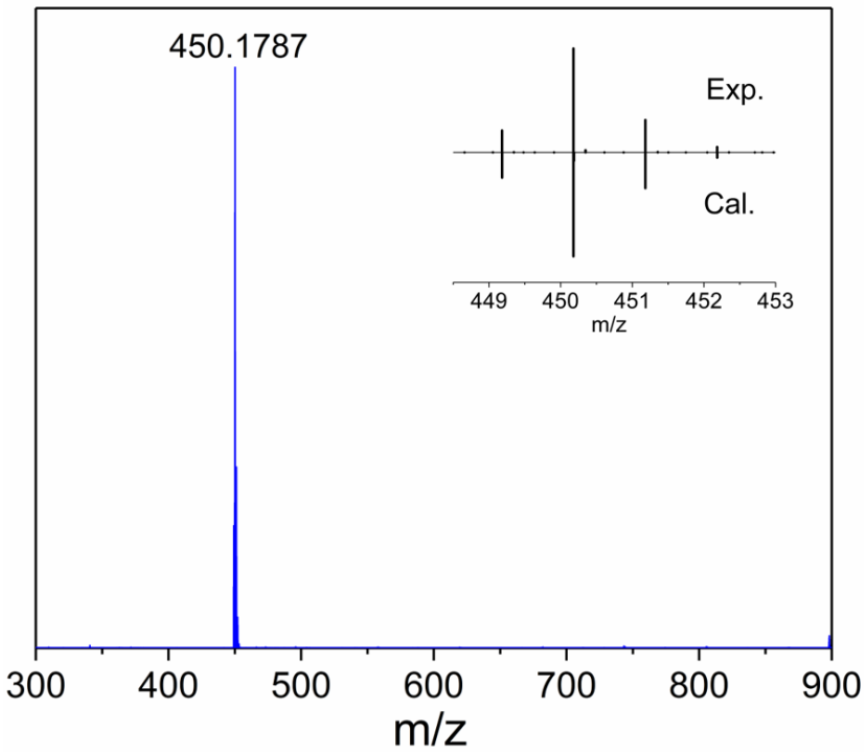

Figure S26. High-resolution MALDI-TOF MS spectrum of compound **1**. Inset displays the isotopic distribution in comparison with the simulated pattern.

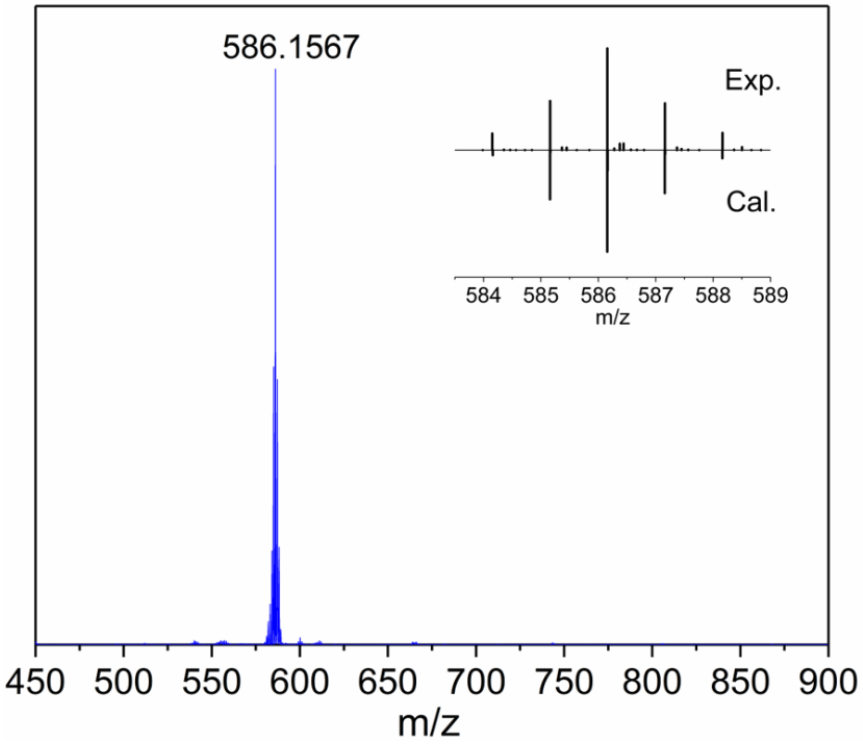

Figure S27. High-resolution MALDI-TOF mass spectrum of compound **2a**. Inset displays the isotopic distribution in comparison with the simulated pattern.

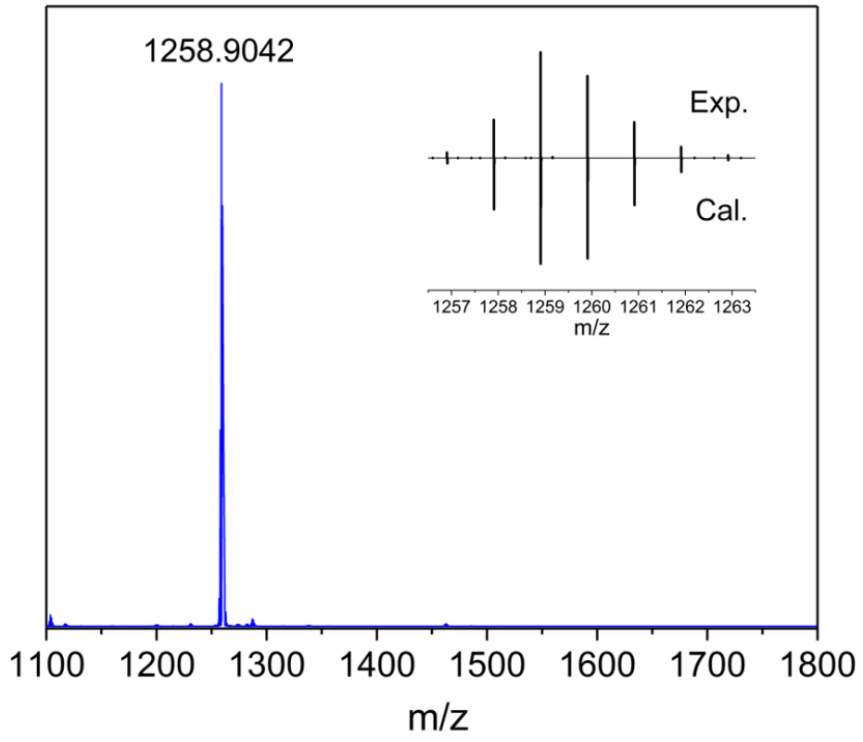

Figure S28. High-resolution MALDI-TOF MS spectrum of compound **2b**. Inset displays the isotopic distribution in comparison with the simulated pattern.

Chapter 3. Regioselective Hydrogenation of a 60-Carbon Nanographene Molecule towards a Circumbiphenyl Core

Key words: π-truncation, hydrogenation, nanographene molecule, circumbiphenyl

ToC figure

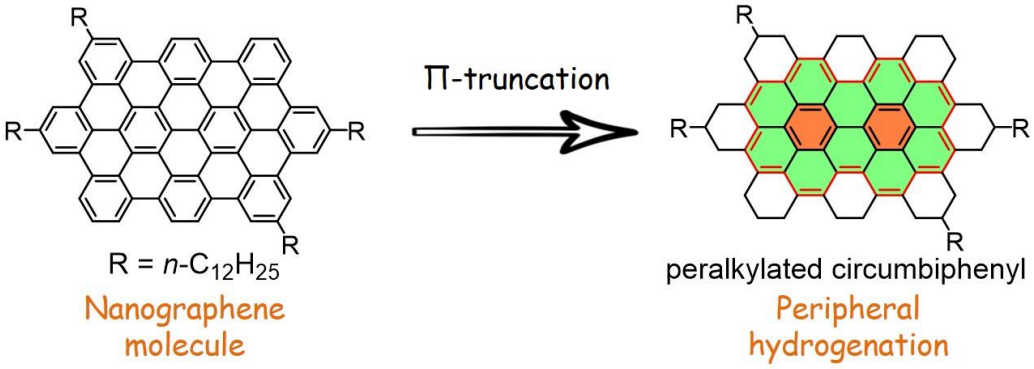

Regioselective peripheral hydrogenation of a nanographene molecule with 60 contiguous sp^2 carbons provides unprecedented access to peralkylated circumbiphenyl (**1**). Conversion to the circumbiphenyl core structure was unambiguously validated by MALDI-TOF mass spectrometry, NMR, FTIR, and Raman spectroscopy. UV-vis absorption spectra and DFT calculations demonstrated the significant change of the optoelectronic properties upon peripheral hydrogenation. Stimulated emission from **1**, observed via ultrafast transient absorption measurements, indicates potential as an optical gain material.

Published in:

Journal of the American Chemical Society

Reprinted with permission from (*J. Am. Chem. Soc.***2019**, *141*, 104230-4234), copyright (2019) American Chemical Society.

Large polycyclic aromatic hydrocarbons (PAHs),[1] i.e., with size >1 nm, can be regarded as nanographene molecules, and have attracted attention for their unique optical, electronic, and magnetic properties.[2] These properties are critically dependent on their aromatic core

structure, motivating development of novel synthetic pathways to a variety of distinct aromatic frameworks.[3] Conventional synthetic strategies towards nanographene molecules are mostly based on π-expansion, mainly through planarization of tailor-made oligoarylene precursors, e.g., by oxidative cyclodehydrogenation,[4] photochemical cyclization,[5] and/or flash vacuum pyrolysis.[6] π-expansion of smaller PAH structures also provides access to larger PAHs, for example through Diels–Alder cycloaddition[7] or a sequence of arylation and cyclization at the periphery.[8]

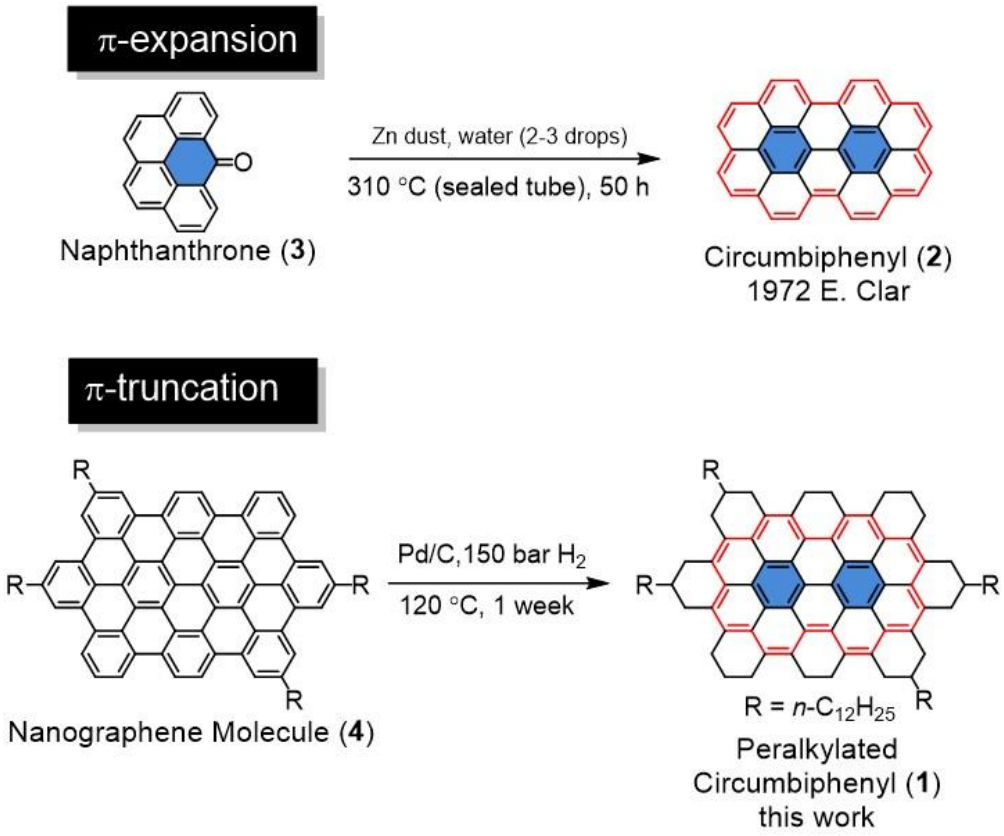

Figure 1. "π-Expansion" towards circumbiphenyl **2** by E. Clar and the post-synthetic "π-truncation" to peralkylated circumbiphenyl **1**.

Alternatively, it is possible to modify the aromatic structures of PAHs by "shrinking" the π-conjugated cores, for example through peripheral hydrogenation. We have previously reported that peripheral hydrogenation of hexa-*peri*-hexabenzocoronene (HBC) selectively leads to peralkylated coronenes.[9] More recently, Shionoya et al. described a catalytic reductive C-C bond cleavage of a corannulene derivative, leading to a benzo[*ghi*]fluoranthene structure.[10] On the other hand, "π-truncation" of aromatic structures has been applied to fullerene, with the formation of a hoop-shaped cyclic benzenoid compound by Nakamura et al. as one of the most elegant examples.[11] Nevertheless, compared with the π-expansion procedure, the "π-truncation"

strategy is underdeveloped. We have been particularly interested in peripheral hydrogenation to produce new PAH or nanographene structures other than known skeletons such as coronene. However, hydrogenation of nanographene molecules larger than HBC has remained elusive.

Circumbiphenyl (**2**) is a PAH consisting of a biphenyl core encircled by an annulene ring (Figure 1). The parent **2** was accidentally obtained by E. Clar nearly half a century ago during his attempts to synthesize tetrabenzoperopyrene by reductive condensation of naphthanthrone (**3**).[12] However, this first reported synthetic approach yielded a complex mixture and required multi-step separation processes to isolate **2**. In 2013, Nuckolls et al. reported a synthesis of a contorted octabenzocircumbiphenyl.[13] However, a straightforward and efficient synthesis of the pristine aromatic structure of circumbiphenyl has never been achieved.

Herein, we report an efficient synthesis of peralkylated circumbiphenyl **1** through "π-truncation", namely by regioselective hydrogenation of a nanographene molecule **4** with 60 sp^2 carbons (Figure 1). Standard spectroscopic characterization corroborates the successful formation of the circumbiphenyl core. UV-vis absorption spectroscopy combined with DFT calculations demonstrate the modulating effect of peripheral hydrogenation on electronic properties, while ultrafast spectroscopy highlights the presence of optical gain. This work offers possibilities not only for acquiring new or unobtainable aromatic structures but also for tuning (opto-)electronic properties of PAHs.

The synthesis of peralkylated circumbiphenyl **1** is outlined in Figure 1. The hydrogenation of nanographene molecule **4**, which was prepared following reported procedures,[14] was carried out with Pd/C in dry tetrahydrofuran (THF). The reaction mixture was pressurized to 150 bar H_2 and stirred at 120 °C in an autoclave for 1 week to complete the reaction. At a lower pressure of 120 bar and the same temperature of 120 °C, the hydrogenation needed 2 weeks for completion. These conditions are indeed much harsher than those used for the previous hydrogenation of HBC with six dodecyl chains (55-65 bar, 60 °C, 12 h).[9] After cooling, the catalyst was removed by passing through a short pad of silica gel with THF as eluent, and the crude product was obtained as yellowish brown powder in 30% yield.

High-resolution MALDI-TOF MS analyses of **4** and the hydrogenation product revealed exact mass of m/z = 1414.9216 and 1437.0945, respectively, in agreement with the formation of **1** ($C_{108}H_{140}$) possessing 22 more hydrogen atoms than **4** ($C_{108}H_{118}$) (Figure 2). The isotopic distribution observed for **1** perfectly matched the simulated pattern, validating the successful hydrogenation of **4**. Compound **1** was soluble even in *n*-hexane (0.65 mg/mL), in

which **4** showed little solubility. Both the room-temperature and high-temperature ^{1}H NMR spectra of **1** revealed the disappearance of signals from protons attached to aromatic systems and appearance of new signals in the aliphatic region, indicating the peripheral hydrogenation of **4**. 2D NMR analyses of **1** could distinguish different aliphatic proton signals originating from >CH-, –CH_2- and -CH_3. (NMR spectra see Figure S1-S6 in the Supporting Information). However, accurate assignment of each proton signal of **1** was hampered by the existence of multiple diastereotopic peripheral protons and ^{1}H signal overlap. Compound **1** might consist of multiple stereoisomers, depending on the relative orientations of the four alkyl chains, which is under further investigation in our laboratory.

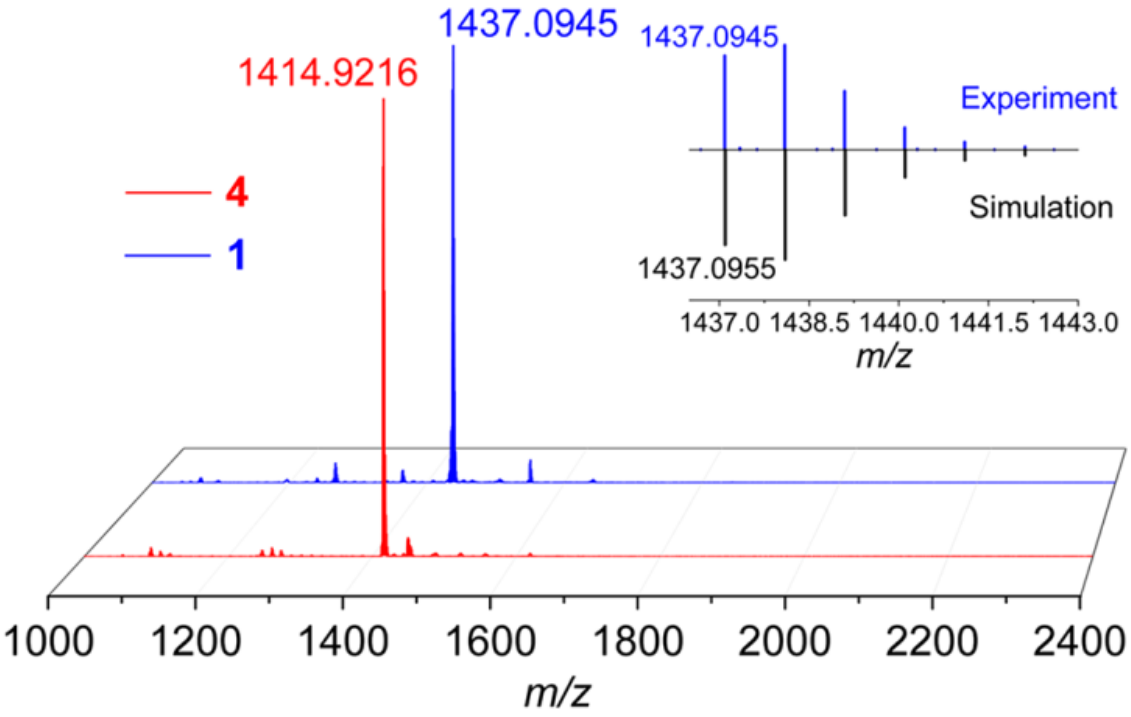

Figure 2. High-resolution MALDI-TOF MS spectrum of **1** and **4**; inset: the corresponding experimental and simulated isotopic distributions of **1**.

FT-IR spectroscopic analysis of **1** and **4** demonstrates the disappearance of aromatic C−H stretching bands at around 3073 cm^{-1},[15] as well as the fingerprint aromatic C-H bending bands between 730 and 860 cm^{-1}, corroborating peripheral hydrogenation (Figure 3, for full spectra, see Figure S7). Additionally, appearance of bands at 1080 cm^{-1} and 465 cm^{-1} from the saturated C-C stretching vibrations and out-of-plane bending, respectively, verifies the hydrogenated periphery of **1**.[16] In Raman spectra (Figure S8), the ratios between D and G bands, I(D)/I(G) for **4** and **1** are 0.50 and 0.56, respectively, in accordance with the fact that I(D)/I(G) varies inversely with the extension of the π-conjugation.[17]

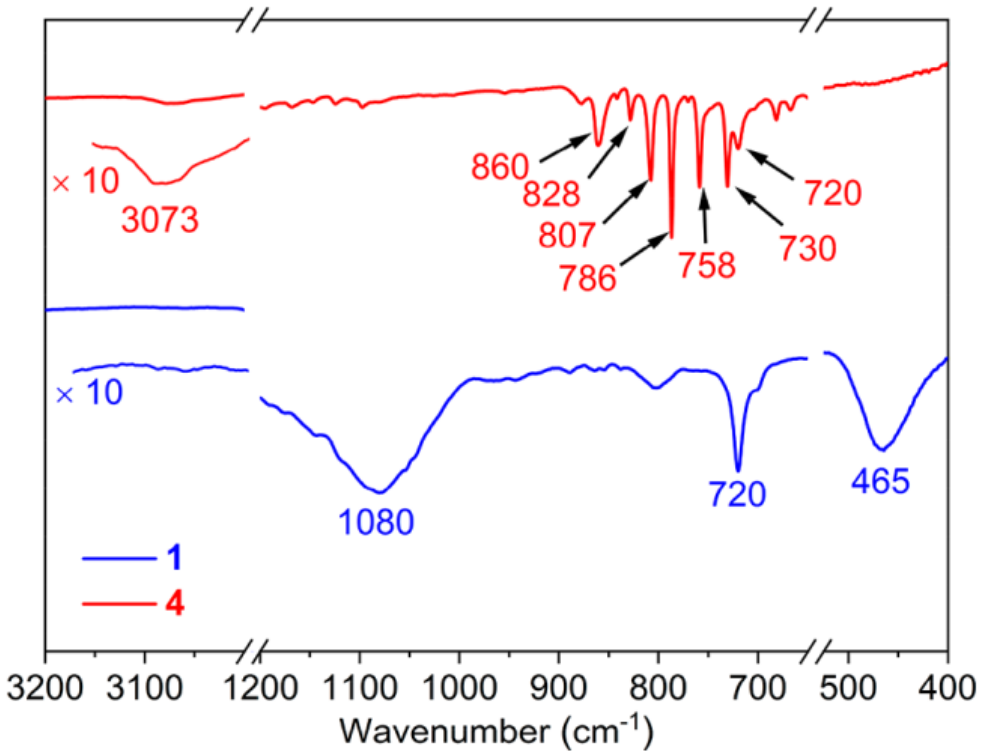

Figure 3. Representative FTIR spectra regions of **1** (blue line) and **4** (red line) measured on powder samples.

In contrast to the broad optical spectra of **4**, which could be ascribed to the presence of aggregates,[18] those of **1** (THF solution, see Figure 4a) reveal well-resolved vibronic structures, indicating a significant improvement of solubility after peripheral hydrogenation, suppressing the aggregation.[19] The absorption maximum of **1** (λ_{max} = 381 nm) exhibits a significant blue-shift with respect to **4** (λ_{max} = 411 nm), indicating truncation of the π-skeleton. Notably, the absorption profile of peralkylated circumbiphenyl **1** perfectly matches that of the parent circumbiphenyl **2** (absorption maximum: 364 nm) reported by E. Clar,[12] with a red-shift of the absorption maximum by 17 nm. Peralkylated circumbiphenyl **1** displays a green fluorescence with the emission maximum at 512 nm. The fluorescence quantum yield Φ_F of **1** was measured as 12% using 9,10-diphenylanyhracene (in toluene under air, Φ_F: 70%) as reference.[20] Compound **4** exhibits a broad fluorescence peaking at 700 nm. The broad peak originates from aggregation, as revealed by concentration-dependent fluorescence studies, whereas the emission maximum of the monomer is at 555 nm (Figure S9). The weak fluorescence of **4** hindered the determination of its fluorescence quantum yield.

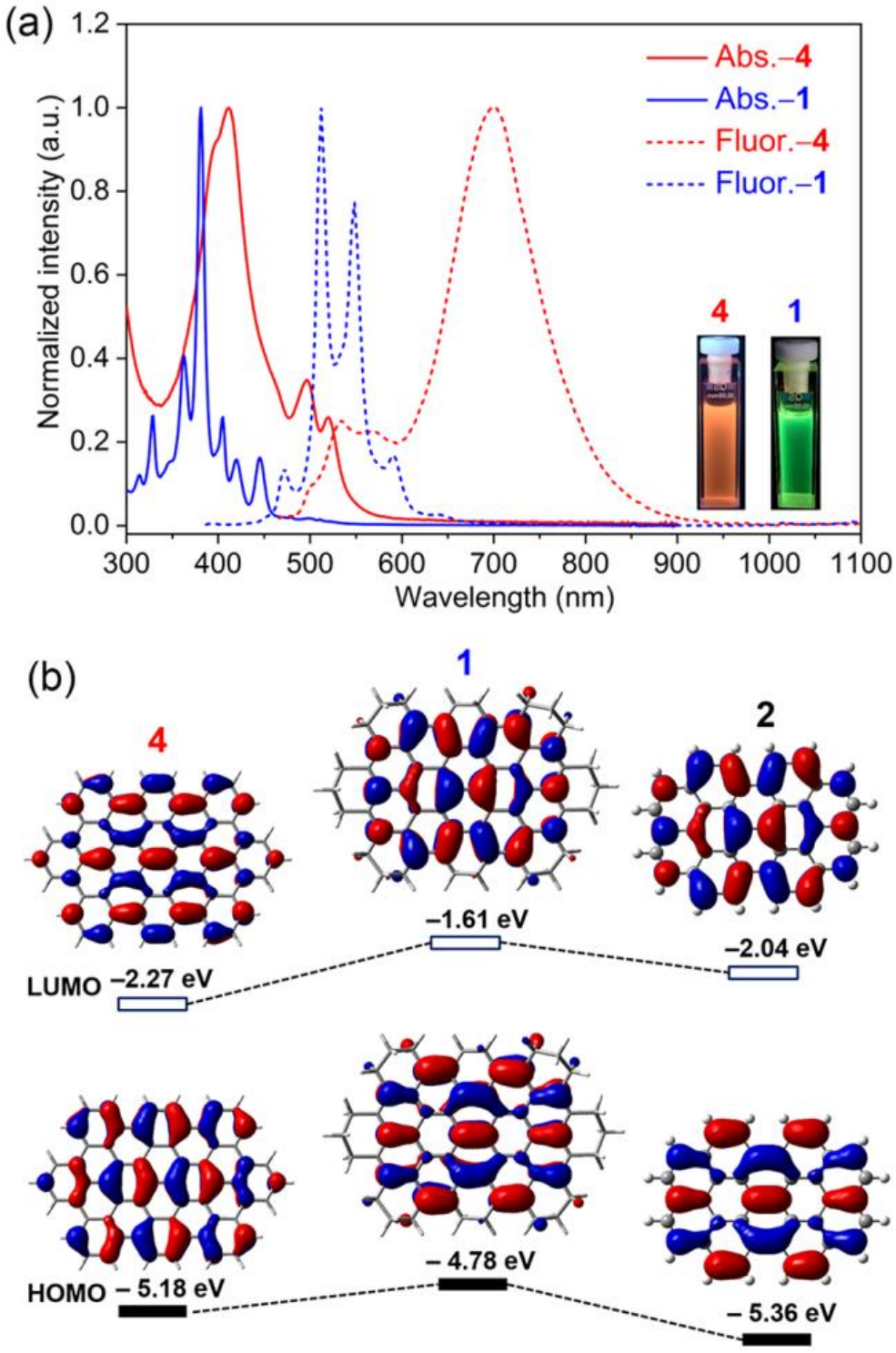

Figure 4. (a) Normalized UV-vis absorption and fluorescence spectra (excited at the absorption maxima) of **1** and **4** in THF solution (2×10^{-5} M); inset: emission of **1** and **4** under 365 nm wavelength of UV lamp; (b) Frontier molecular orbitals and energy diagrams of **1**, **2** and **4** at the B3LYP/6–311G(d) level. For simplicity of computation, dodecyl chains of **1** and **4** were removed.

DFT calculations were performed to compare the electronic properties of pristine **4**, peripheral hydrogenated **1** and parent circumbiphenyl **2** (Figure 4b). The HOMO and LUMO energy levels of **4** are calculated to be −5.18 eV and −2.27 eV, respectively, with a HOMO-LUMO gap of 2.91 eV. Peripheral hydrogenation results in a higher lying HOMO (−4.78 eV) and LUMO energy levels (−1.61 eV) of **1**, with an energy gap of 3.17 eV which is by 0.26 eV greater than that of **4**. These observations are in accordance with the UV-vis experiment, indicating the ability of electronic tuning of PAHs through peripheral hydrogenation. Besides, the DFT-calculated HOMO and LUMO of peralkylated circumbiphenyl **1** reveal the same orbital distribution pattern as that of **2**. In addition, the HOMO-LUMO gap of **1** is smaller than that of **2** (3.32 eV), in line with the red-shifted onset of absorption of **1**.

Ultrafast transient absorption (TA) spectroscopy (see the supporting information) discloses the effect of peripheral hydrogenation on the excited state photodynamics of the molecules. Figure 5 presents the TA spectra for **1** and **4** excited at the low-energy absorption edge (470 nm). Interestingly, whereas for **4** we can distinguish two photobleaching (PB) peaks (500 nm and 530 nm) and a broad photoinduced absorption (PA) from 600 nm to 750 nm, **1** exhibits a sharp positive band at 500 nm that can be attributed to stimulated emission (SE), as it overlaps with one of the multiple well-resolved fluorescence peaks and cannot be connected to ground state absorption. Note that the other potential SE signals (550 nm and 600 nm) are overlapped with the strong and broad PA in the mid-visible, which is typical for conjugated systems.[21] The reason why **1** displays SE likely lies in its improved solubility brought about by selective peripheral substitution, as we have recently reported that intermolecular interactions in nanographenes lead to the formation of aggregates with charge-transfer character, in which charge generation quenches SE and gain.[22] The TA dynamics (probe at 500 nm, Figure 5b) show a longer lifetime for **1** ($\tau_1 = 0.4 \pm 0.04$ ps; $\tau_2 = 420 \pm 20$ ps) than **4** ($\tau_1 = 0.1 \pm 0.01$ ps ; $\tau_2 = 120 \pm 15$ ps), a result that can also correlate with the poorer solubility of **4** with respect to the hydrogenated molecule. In general, these findings highlight the potential of peralkylated circumbiphenyl **1** for applications in photonics and optoelectronics.

In summary, we have presented hydrogenation as a "π-truncation" strategy leading to the first peralkylated circumbiphneyl **1**. MALDI-TOF MS, 1D and 2D NMR combined with FT-IR and Raman results provided an explicit structure proof of the regiospecific peripheral hydrogenation of nanographene molecule **4**, leading to a peralkylated circumbiphenyl core. Moreover, investigation of **1** by ultrafast transient absorption measurements revealed stimulated emission, which was absent for **4** before the hydrogenation, pointing toward the

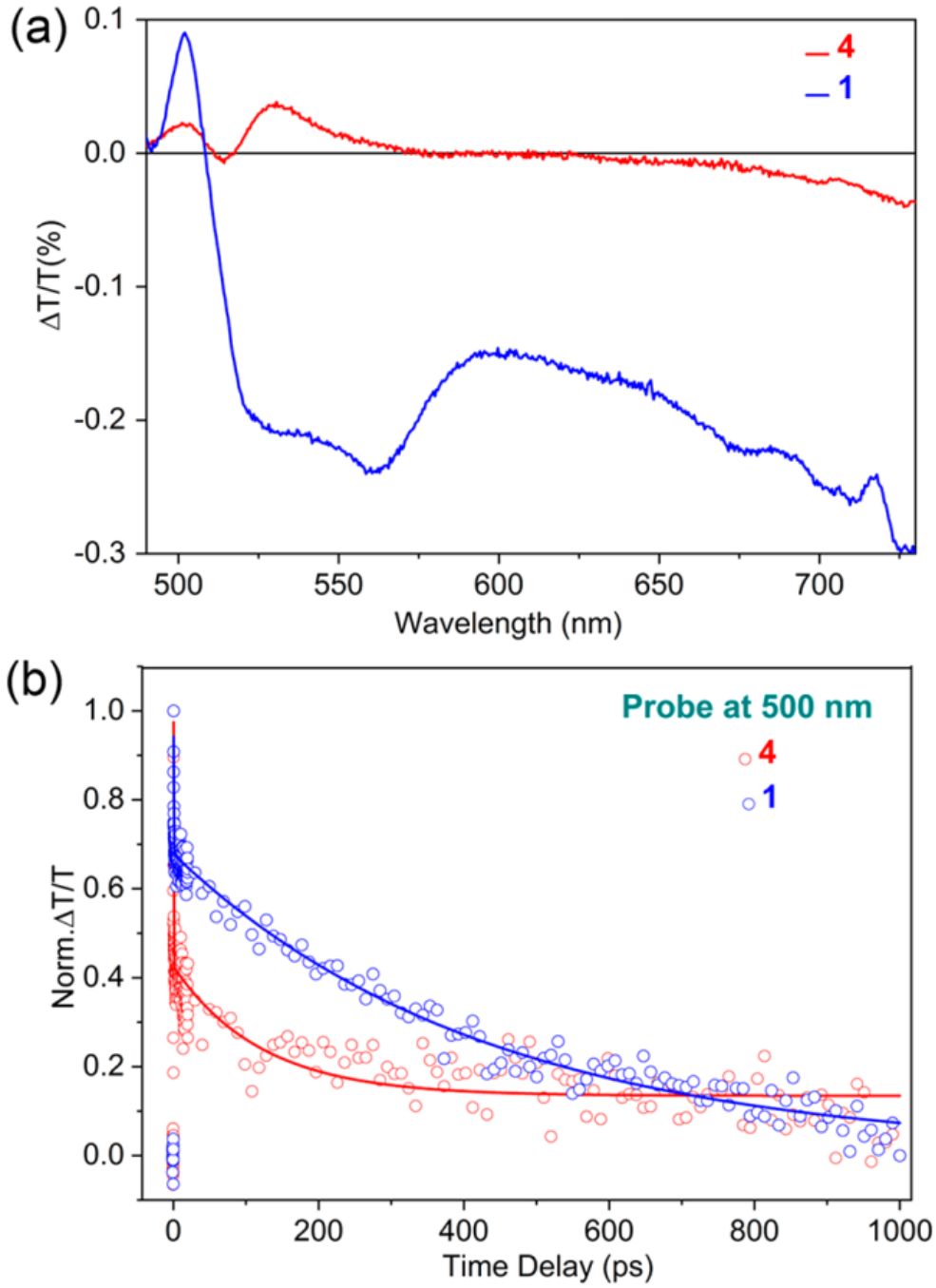

Figure 5. (a) Femtosecond transient absorption spectra of **1** and **4** in THF solution at 1 fs pump-probe delay obtained by exciting at 470 nm and probing with a broadband probe light. (b) Transient dynamics for **1** and **4** at a probe wavelength of 500 nm. The solid blue and red lines represent the bi-exponential best-fit curves for **1** and **4**, respectively.

possible application of such hydrogenated nanographene molecules as optical gain materials, for example to develop an organic laser. Considering the directness and efficiency of π-truncation, this strategy could serve as a general approach to other unique aromatic structures

not available by π-expansion, providing new candidates for (opto-)electronic devices and supramolecular chemistry.

ASSOCIATED CONTENT

Supporting Information

The Supporting Information is available free of charge on the ACS Publications website.

Materials and methods, synthetic procedure, NMR, Raman, FT-IR spectroscopy and photoluminescence spectroscopy, transient absorption information (PDF)

Notes

The authors declare no competing financial interests.

ACKNOWLEDGMENT

This work was financially supported by Max Planck Society and the European Union's Horizon 2020 research and innovation programme under Marie-Curie ITN project "iSwitch" (GA No.642196) and under Graphene Flagship (785219 GrapheneCore 2). [redacted] is grateful for the scholarship from China Council Scholarship (CSC).

REFERENCES

[1] J. C. Fetzer: *Large (C>=)24) Polycyclic Aromatic Hydrocarbons*; John Wiley & Sons: New York, 2000.

[2] (a) Z. Sun; Q. Ye; C. Chi; J. Wu. *Chem. Soc. Rev.* **2012**, *41*, 7857-7889. *Chem. Soc. Rev.* **2012,** *41* (23), 7857-7889; (b) A. Narita; X.-Y. Wang; X. Feng; K. Mullen. *Chem. Soc. Rev.* **2015**, *44*, 6616-6643. *Chem. Soc. Rev.* **2015,** *44* (18), 6616-6643; (c) X.-Y. Wang; A. Narita; K. Müllen. *Nat. Rev. Chem.* **2017,** *2*, 0100.

[3] L. Chen; Y. Hernandez; X. Feng; K. Müllen. *Angew. Chem. Int. Ed.* **2012,** *51* (31), 7640-7654.

[4] X. Feng; W. Pisula; K. J. P. Müllen; A. Chemistry. *Pure Appl. Chem.* **2009**, *81*, 2203-2224.

[5] (a) S. Xiao; M. Myers; Q. Miao; S. Sanaur; K. Pang; M. L. Steigerwald; C. Nuckolls. *Angew. Chem. Int. Ed.* **2005**, *44*, 7390-7394; (b) C.-Y. Chiu; B. Kim; A. A. Gorodetsky; W. Sattler; S. Wei; A. Sattler; M. Steigerwald; C. Nuckolls. *Chem. Sci.* **2011**, *2*, 1480-1486; (c) M. Daigle; A. Picard-Lafond; E. Soligo; J.-F. Morin. *Angew. Chem. Int. Ed.* **2016,** *128* (6), 2082-2087.

[6] (a) L. T. Scott; P.-C. Cheng; M. M. Hashemi; M. S. Bratcher; D. T. Meyer; H. B. Warren. *J. Am. Chem. Soc.* **1997,** *119*, 10963-10968; (b) L. T. Scott; E. A. Jackson; Q. Zhang; B. D. Steinberg; M. Bancu; B. Li. *J. Am. Chem. Soc.* **2012**, *134*, 107-110; (c) L. T. Scott; M. M. Boorum; B. J. McMahon; S. Hagen; J. Mack; J. Blank; H. Wegner; A. de Meijere. *Science* **2002**, *295*, 1500.

[7] (a) E. Clar; M. Zander. *J. Chem. Soc.* **1957**, 4616-4619.; (b) E. H. Fort; P. M. Donovan; L. T. Scott. *J. Am. Chem. Soc.* **2009**, *131*, 16006-16007; (c) E. H. Fort; L. T. Scott. *Tetrahedron Lett.* **2011**, *52*, 2051-2053; (d) A. Konishi; Y. Hirao; K. Matsumoto; H. Kurata; T. Kubo. *Chem. Lett.* **2013**, *42*, 592-594; (e) J. Li; C. Jiao; K.-W. Huang; J. Wu. *Chem. Eur. J.* **2011**, *17*, 14672-14680; (f) B. Schuler; S. Collazos; L. Gross; G. Meyer; D. Pérez; E. Guitián; D. Peña. *Angew. Chem. Int. Ed.* **2014**, *126*, 9150-9152.

[8] (a) Q. Zhang; K. Kawasumi; Y. Segawa; K. Itami; L. T. Scott. *J. Am. Chem. Soc.* **2012**, *134*, 15664-15667; (b) K. Kawasumi; Q. Zhang; Y. Segawa; L. T. Scott; K. Itami. *Nat. Chem.* **2013**, *5*, 739.

[9] M. D. Watson; M. G. Debije; J. M. Warman; K. Müllen. *J. Am. Chem. Soc.* **2004**, *126*, 766-771.

[10] S. Tashiro; M. Yamada; M. Shionoya. *Angew. Chem. Int. Ed.* **2015**, *54*, 5351-5354.

[11] Y. Matsuo; K. Tahara; M. Sawamura; E. J. J. o. t. A. C. S. Nakamura. *J. Am. Chem. Soc.* **2004**, *126*, 8725-8734.

[12] E. Clar; C. C. Mackay. *Tetrahedron* **1972**, *28*, 6041-6047.

[13] S. Xiao; S. J. Kang; Y. Wu; S. Ahn; J. B. Kim; Y.-L. Loo; T. Siegrist; M. L. Steigerwald; H. Li; C. Nuckolls. *Chem. Sci.* **2013**, *4*, 2018-2023.

[14] V. S. Iyer; K. Yoshimura; V. Enkelmann; R. Epsch; J. P. Rabe; K. Müllen. *Angew. Chem. Int. Ed.* **1998**, *37*, 2696-2699.

[15] D. M. Hudgins; S. A. Sandford. *J. Phys. Chem. A* **1998**, *102*, 344-352.

[16] J. Wei; X. Jia; J. Yu; X. Shi; C. Zhang; Z. Chen. *Chem. Commun.* **2009**, 4714-4716.

[17] (a) J. Wu; Ž. Tomović; V. Enkelmann; K. Müllen. *J. Org. Chem.* **2004**, *69*, 5179-5186; (b) C. Casiraghi; A. C. Ferrari; J. Robertson. *Phys. Rev. B* **2005**, *72*, 085401.

[18] M. Kastler; W. Pisula; D. Wasserfallen; T. Pakula; K. Müllen. *J. Am. Chem. Soc.* **2005**, *127*, 4286-4296.

[19] D. Wasserfallen; M. Kastler; W. Pisula; W. A. Hofer; Y. Fogel; Z. Wang; K. Müllen. *J. Am. Chem. Soc.* **2006**, *128*, 1334-1339.

[20] K. Rurack: In Standardization and Quality Assurance in Fluorescence Measurements I: Techniques; Resch-Genger, U., Ed. Springer: Berlin-Heidelberg, **2008**.

[21] J. Cabanillas-Gonzalez; G. Grancini; G. Lanzani. *Adv. Mater.* **2011**, *23*, 5468-5485.

[22] (a) G. M. Paternò; Q. Chen; X.-Y. Wang; J. Liu; S. G. Motti; A. Petrozza; X. Feng; G. Lanzani; K. Müllen; A. Narita; F. Scotognella. *Angew. Chem. Int. Ed.* **2017**, *129*, 6857-6861.; (b) G. M. Paternò; L. Nicoli; Q. Chen; K. Müllen; A. Narita; G. Lanzani; F. Scotognella. *J. Phys. Chem. C* **2018**, *122*, 25007-25013.

Supporting information

Regioselective Hydrogenation of a 60-Carbon Nanographene Molecule towards a Circumbiphenyl Core

1. Experimental section

Materials and Methods. All commercially available chemicals were used without further purification unless otherwise stated. Absorption spectra were recorded on a Perkin-Elmer Lambda 900 spectrophotometer at room temperature. Photoluminescence spectra were recorded on a J&MTIDAS spectrofluorometer. The quantum yield was measured with 9,10-diphenylanthracene (in toluene under air, ΦF: 70%) as reference. High-resolution mass spectrometry (HRMS) was performed on a SYNAPT G2 Si high resolution time-of-flight (TOF) mass spectrometer (Waters Corp., Manchester, UK) by matrix-assisted laser desorption/ionization (MALDI) with 7,7,8,8-tetracyanoquinodimethane (TCNQ) as matrix. The micro-FTIR measurements were carried out through a diamond anvil cell (transmission mode) with a Nicolet Nexus FT-IR spectrometer coupled with a Thermo Electron Continuμm IR microscope. Raman spectra were measured with a Bruker RFS 100/S Raman spectrometer excited by 488 nm laser. Melting points were measured with a Büchi B-545 apparatus. DFT calculations were performed using the Gaussian 09 software package.[1] The geometries were optimized at the B3LYP/6-311G(d) level, and energies were calculated at the same level of theory.

Nuclear Magnetic Resonance (NMR) spectra were recorded with a 5 mm PATXI ^{1}H-^{13}C/^{15}N/D z-gradient on the 850 MHz spectrometer with a Bruker Avance III system. High temperature NMR was recorded on Bruker Avance 500 MHz spectrometer.

For quantitative ^{1}H NMR measurements 512 transients were used with a 9.0 μs long 90° pulse and a 13600 Hz (16 ppm) spectral width together with a recycling delay of 8 s. The

^{13}C NMR (214 MHz) measurements were obtained with a J-modulated spin-echo for ^{13}C-nuclei coupled to ^{1}H to determine the number of attached protons with decoupling during acquisition. The used 90° pulse was 12.0 μs long for carbon with a relaxation delay of 2 s. The proton and carbon spectra were conducted in $C_2D_2Cl_4$ and the spectra were referenced with the residual $C_2D\mathbf{H}Cl_4$ at 5.98 ppm ($\delta(^1H)$). The carbon spectra were referenced with the carbon signal of the solvent $\mathbf{C}_2D_2Cl_4$ at 74.19 ppm.

For the 2D NOESY experiments a spectroscopic width of 11900 Hz (14ppm) in both dimensions (f1 and f2) was used and the relaxation delay was 2.0 s. The mixing time used in the 2D NOESY was kept at 300ms. The spectroscopic widths of the homo-nuclear 2D COSY experiments were typically 11900 Hz in both dimensions (f1 and f2) with a relaxation delay of 2.0 s. The 2D correlation between proton and carbon used ^{1}H-^{13}C-HSQC (heteronuclear single quant correlation) edited[2] pulse program via double inept transfer for sensitivity improvement and with decoupling during acquisition via trim pulses in the inept transfer and with multiplicity editing during the selection step. $^{1}J_{CH}$ = 145 Hz was used for optimizing observable intensities of cross peaks from multiple bond ^{1}H-^{13}C correlation.

Transient absorption experiments were performed with a home-built setup powered by an amplified Ti:sapphire laser (Coherent Libra) emitting 100-fs, 4-mJ pulses at 800 nm and 1 kHz repetition rate. The pump pulses were generated by an optical parametric amplifier, while the broadband probe pulses were obtained by white-light continuum generation in a sapphire plate. Pump and probe pulses were non-collinearly overlapped on the sample and the transmitted probe spectrum was measured by an optical multichannel analyzer working at the full 1-kHz laser repetition rate. The pump pulse was chopped at 500 Hz and the differential transmission (ΔT/T) spectra were calculated for pairs of consecutive pulses and averaged over 300 pulse pairs.

Hydrogenation of nanographene molecule 4. Nanographene molecule **4** (100 mg, 0.07 mmol) and Pd/C (10% Pd, 100 mg) was placed in an autoclave ("limbo" 350 bar/350 °C/100 mL autoclave system, Brüchi AG), and 50 mL of degassed dry THF was added. The autoclave was sealed and pressurized to 150 bar H_2, and then the pressure was slowly and carefully released. This process was repeated for 3 times. The reaction mixture was then stirred at 150 bar H_2 and 120 °C for 1 week. After cooling down the system to a room temperature, the reaction mixture was passed through a short pad of silica gel with THF as eluent. After removing the solvent under reduced pressure, peralkylated circumbiphenyl **1** was obtained as yellowish brown

powder (30 mg, 30% yield). M.p.: 201.1 – 202.3 °C. ^{1}H NMR (850 MHz, $C_2D_2Cl_2/CS_2$, 298 K, ppm) δ 4.27 – 3.65 (m, 20H), 3.56 – 3.45 (m, 2H), 3.39 – 2.99 (m, 7H); 2.73 – 2.67 (m, 1H), 2.57 – 2.48 (m, 4H), 2.41 – 2.28 (m, 1H), 2.07 – 2.01 (m, 1H), 1.88 – 1.82 (m, 4H), 1.81 – 1.74 (m, 8H), 1.48 – 1.44 (m, 8H), 1.34 – 1.28 (m, 60H), 0.97 – 0.81 (m, 24H) ^{13}C NMR (214 MHz, $C_2D_2Cl_2/CS_2$, 298 K, ppm) δ 130.15, 130.00, 129.92, 129.81, 129.76, 129.58, 129.52, 129.34, 129.29, 125.63, 125.04, 122.70, 122.56, 121.11, 120.90, 120.18, 120.11, 120.04, 118.95, 37.14, 36.99, 36.93, 35.15, 35.11, 34.85, 34.83, 34.55, 34.37, 32.34, 30.61, 30.57, 30.32, 30.19, 30.13, 29.82, 29.06, 27.90, 26.59, 24.23, 23.25, 14.62, HRMS (MALDI) *m/z*: Calcd for $C_{108}H_{140}$: 1437.0955; Found: 1437.0945 $[M]^+$.

2. NMR spectra

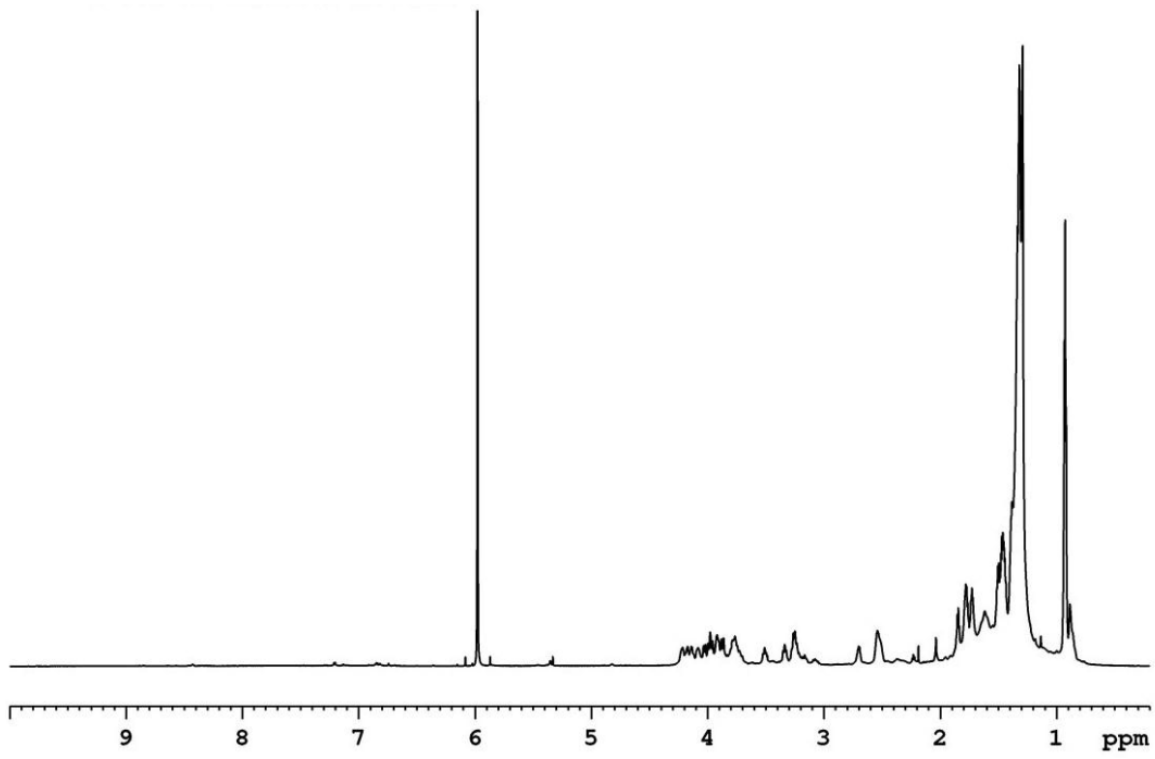

Figure S1. ^{1}H NMR at 850 MHz at 298 K of compound **1** in $C_2D_2Cl_4/CS_2$.

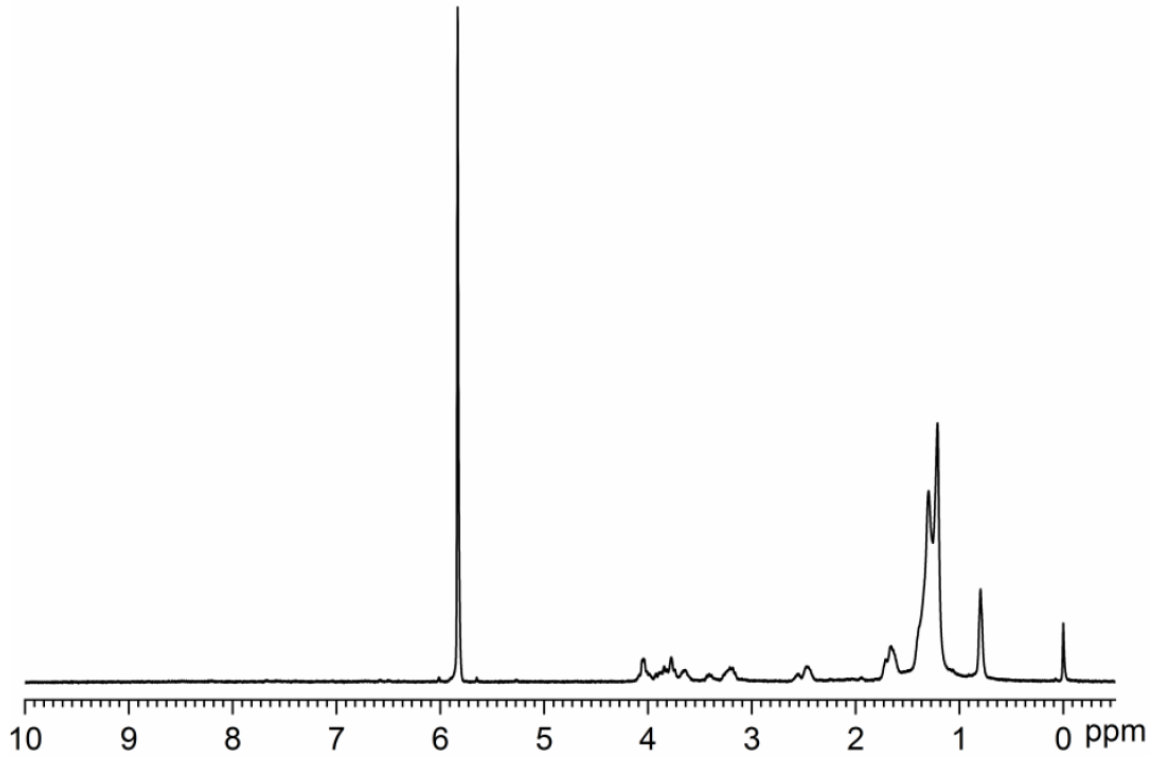

Figure S2. ^{1}H NMR at 500 MHz at 413 K of compound **1** in $C_2D_2Cl_4$.

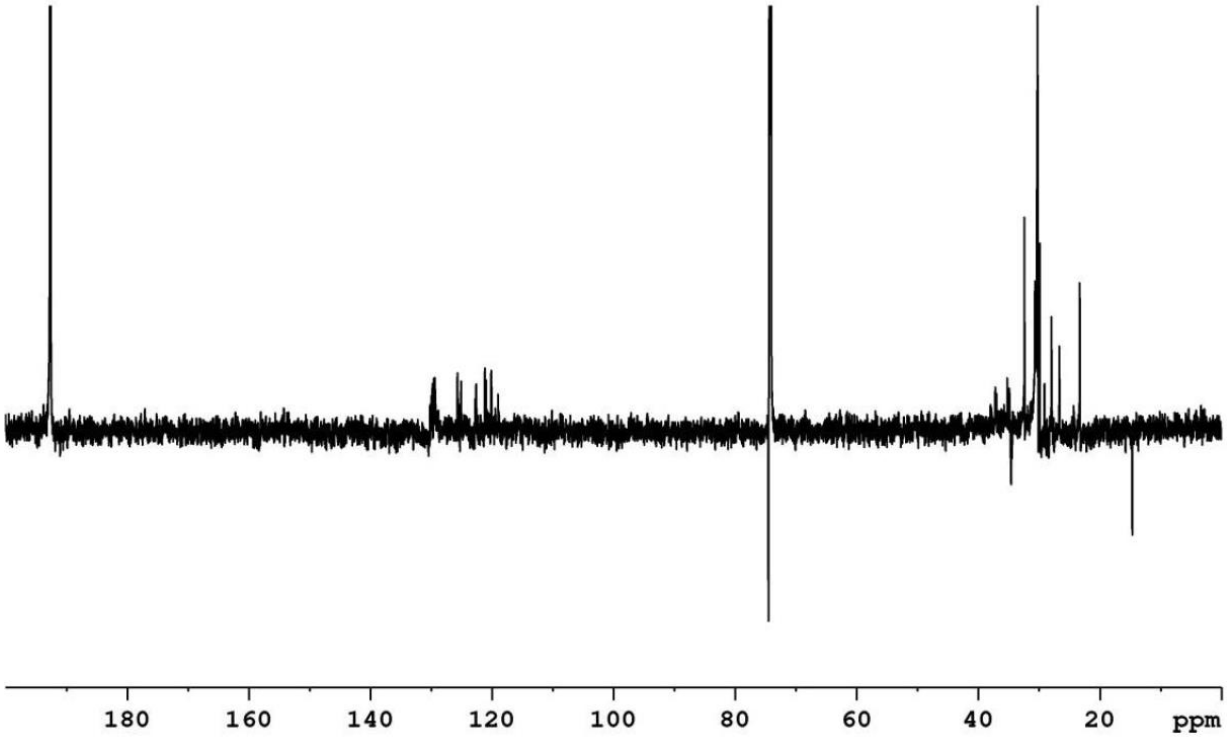

Figure S3. ^{13}C NMR (jmod: attached proton test) at 214 MHz at 298 K of compound **1** in $C_2D_2Cl_4/CS_2$ (**up** C and CH_2 and **down** CH and CH_3).

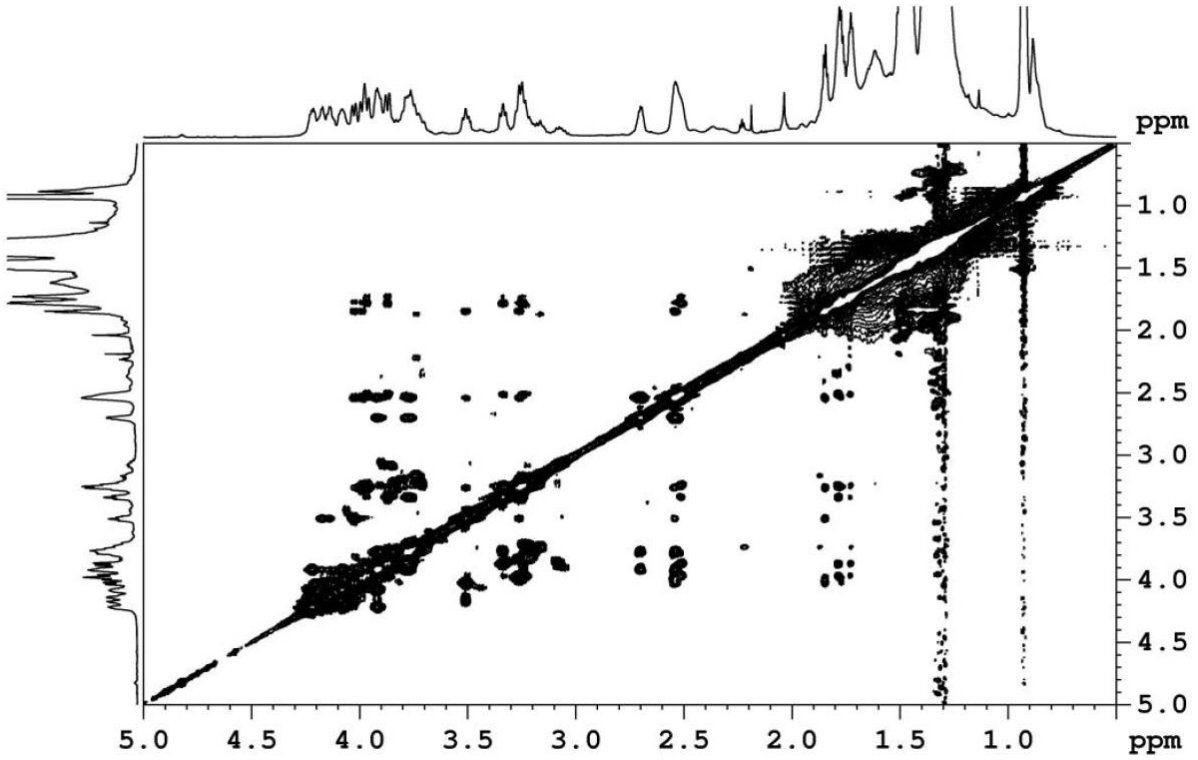

Figure S4. 2D NOESY NMR at 850 MHz at 298 K of compound **1** in $C_2D_2Cl_4/CS_2$.

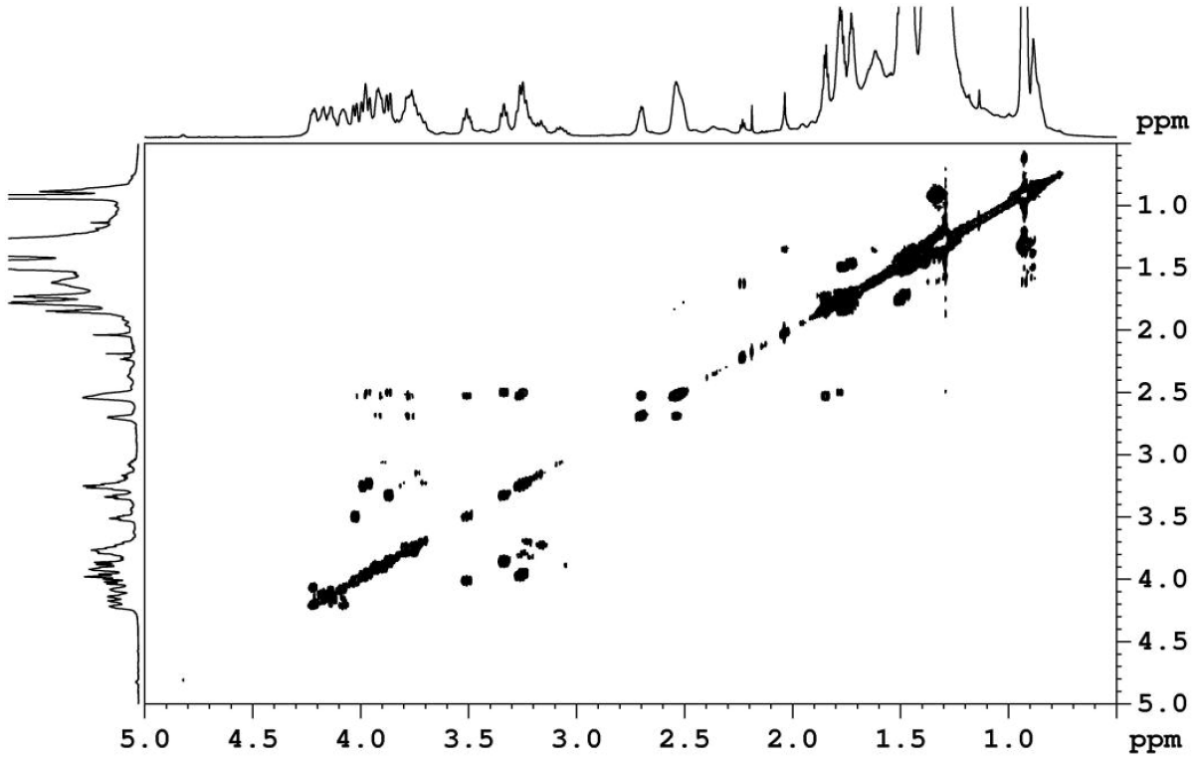

Figure S5. 2D COSY NMR at 850 MHz at 298 K of compound **1** in $C_2D_2Cl_4/CS_2$.

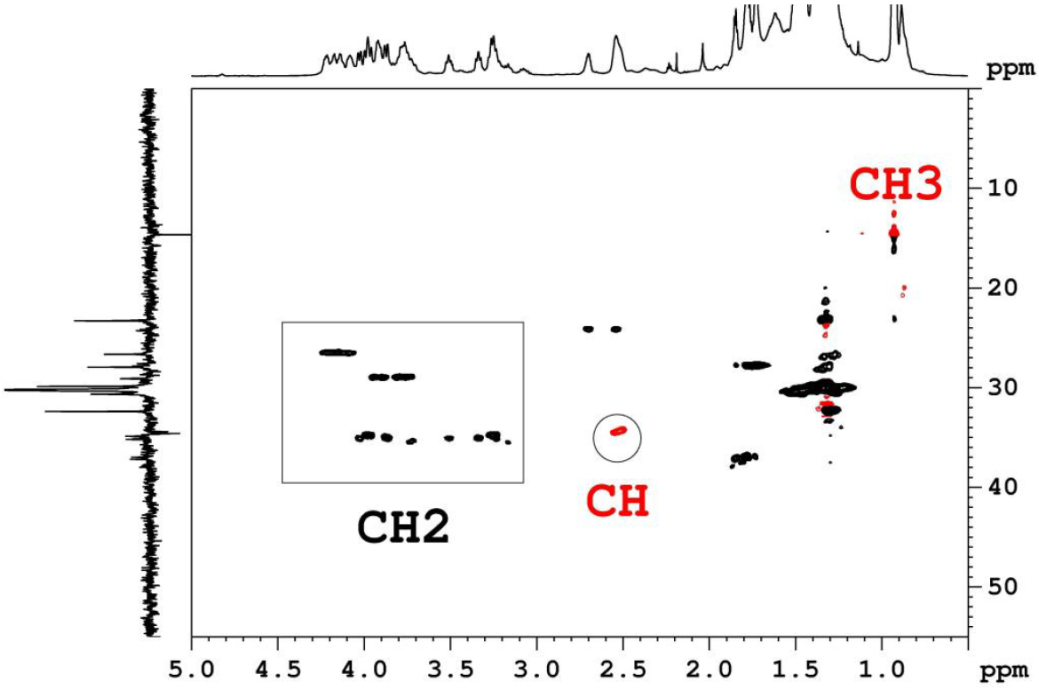

Figure S6. 2D ^{1}H-^{13}C HSQCed NMR at 850 MHz at 298 K of compound **1** in $C_2D_2Cl_4/CS_2$ (signals in **red** (CH and CH_3) in **black** CH_2).

3. FT-IR and Raman spectra

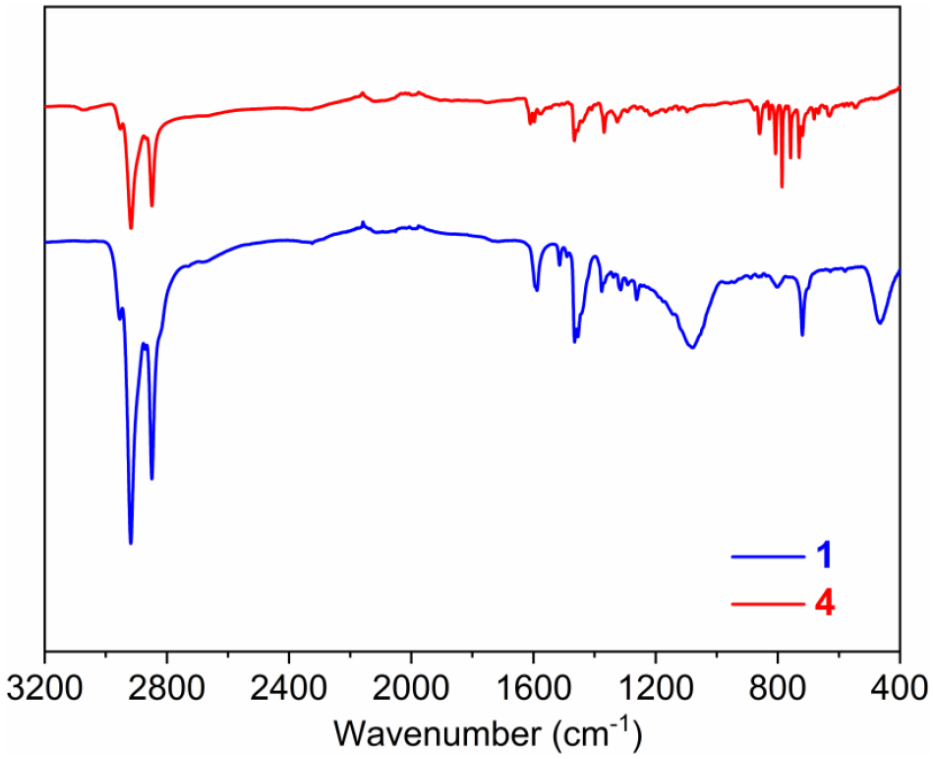

Figure S7. Full region of FT-IR spectra of **1** and **4**.

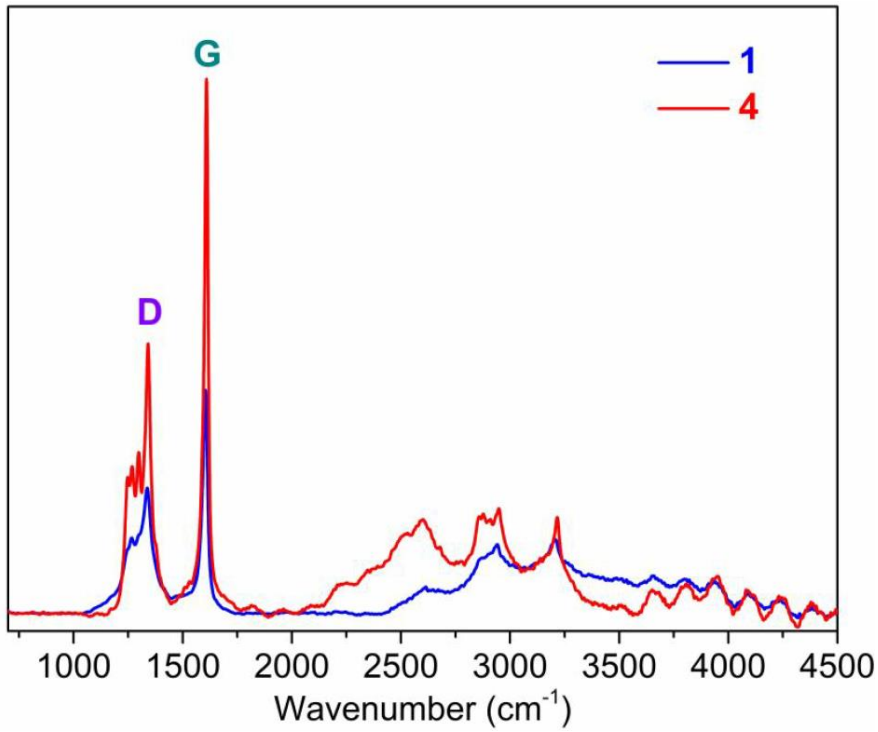

Figure S8. Raman spectra of **1** and **4** recorded with 488 nm excitation laser wavelength.

4. Concentration-dependent fluorescence spectra

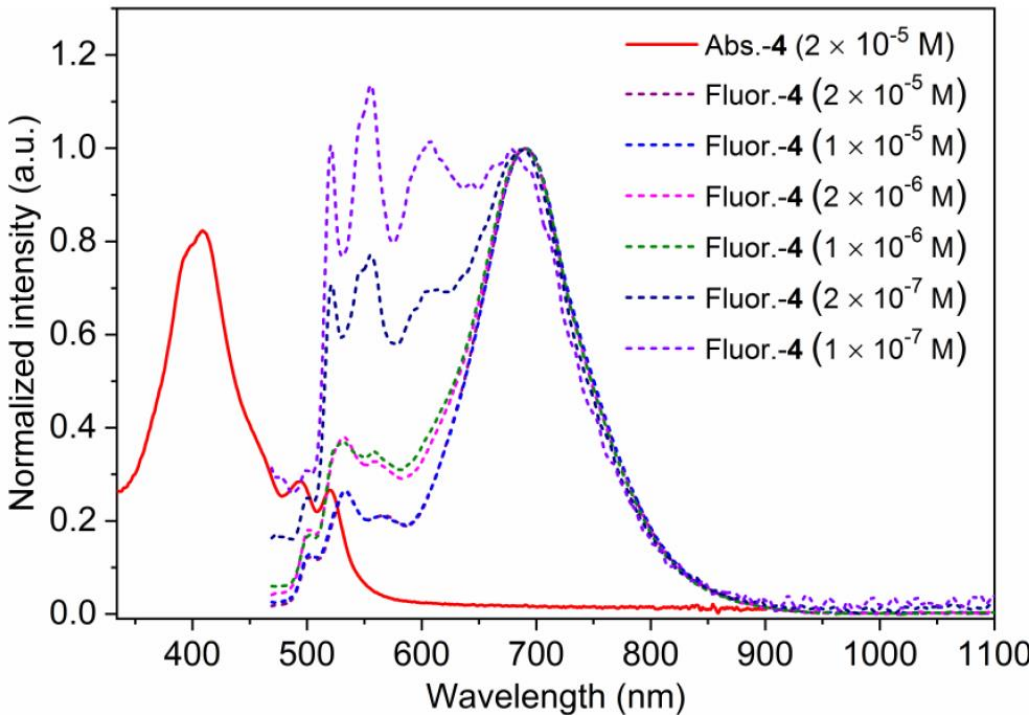

Figure S9. UV-vis spectrum and concentration-dependent fluorescence spectra of compound **4**.

5. Supplementary transient absorption information

In a typical TA experiment, a pump pulse populates the excited states while a broadband probe pulse investigates both the differential transmission ($\frac{T_{pump\ ON} - T_{pump\ OFF}}{T_{pump\ OFF}} = \frac{\Delta T}{T}$) and the lifetime of those states. When the probe is in resonance with the S_0-S_1 transition, its transmission will be enhanced by the pump-induced ground state depletion ($\Delta T/T > 0$). For this reason, such a positive transient signal overlapping with ground state absorption is called photobleaching (PB). On the other hand, the probe transmission decreases when it is in resonance with excited states absorption (S_1-S_n), and the resultant negative feature is called photoinduced absorption (PA). Finally, when the probe pulse is in resonance with the S_1-S_0 transition it will cause stimulate emission (SE) of a second photon, and the transient band associated with such an effect will be positive and, in general, overlapping with the emission spectrum.

References:

[1] M. J. T. Frisch, G. W.; Schlegel, H. B.; Scuseria, G. E.; Robb, M. A.; Cheeseman, J. R.; Scalmani, G.; Barone, V.; Mennucci, B.; Petersson, G. A.; Nakatsuji, H.; Caricato, M.; Li, X.; Hratchian, H. P.; Izmaylov, A. F.; Bloino, J.; Zheng, G.; Sonnenberg, J. L.; Hada, M.; Ehara, M.; Toyota, K.; Fukuda, R.; Hasegawa, J.; Ishida, M.; Nakajima, T.; Honda, Y.; Kitao, O.; Nakai, H.; Vreven, T.; Montgomery, Jr., J. A.; Peralta, J. E.; Ogliaro, F.; Bearpark, M.; Heyd, J. J.; Brothers, E.; Kudin, K. N.; Staroverov, V. N.; Kobayashi, R.; Normand, J.; Raghavachari, K.; Rendell, A.; Burant, J. C.; Iyengar, S. S.; Tomasi, J.; Cossi, M.;Rega, N.; Millam, N. J.; Klene, M.; Knox, J. E.; Cross, J. B.; Bakken, V.; Adamo, C.; Jaramillo, J.; Gomperts, R.; Stratmann, R. E.; Yazyev, O.; Austin, A. J.; Cammi, R.; Pomelli, C.; Ochterski, J. W.; Martin, R. L.; Morokuma, K.; Zakrzewski, V. G.; Voth, G. A.; Salvador, P.; Dannenberg, J. J.; Dapprich, S.; Daniels, A. D.; Farkas, Ö.; Foresman, J. B.; Ortiz, J. V.; Cioslowski, J.; Fox, D. J. *Gaussian, Inc., Wallingford CT,* **2013**.

[2] (a) A. G. Palmer; J. Cavanagh; P. E. Wright; M. Rance. *J. Magn. Reson.* **1991**, *93*, 151-170; (b) L. Kay; P. Keifer; T. Saarinen. *J. Am. Chem. Soc.* **1992**, *114*, 10663-10665; (c) J. Schleucher;

M. Schwendinger; M. Sattler; P. Schmidt; O. Schedletzky; S. J. Glaser; O. W. Sørensen; C. Griesinger. *J. Biomol. NMR* **1994**, *4*, 301-306; (d) W. Willker; D. Leibfritz; R. Kerssebaum; W. Bermel. *Magn. Reson. Chem.* **1993**, *31*, 287-292.

Chapter 4. Engineering of Robust Topological Quantum Phases in Graphene Nanoribbons

Keywords: on-surface synthesis, dependent band-gap, Majorana fermions, state, polyacetylene, superconductor, insulator, solitons, width, edge

ToC figure

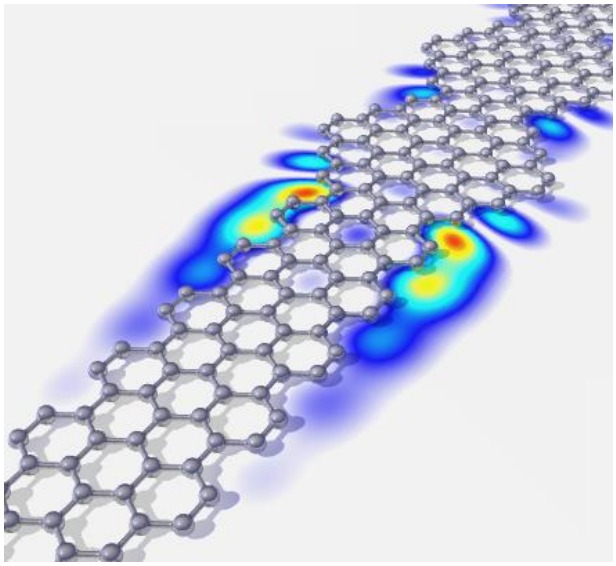

Published in:

Nature

Boundaries between distinct topological phases of matter support robust, yet exotic quantum states such as spin-momentum locked transport channels or Majorana fermions.[1-3]The perspective to use such states in spintronic devices or as Qubits in quantum information technology is a strong driver of current research in condensed matter physics.[4-6] The understanding of topological properties of quantum states has seen early success in explaining the conductivity of doped *trans*-polyacetylene (*trans*-PA) in terms of dispersionless soliton states.[7-9] In their seminal paper Su, Schrieffer and Heeger (SSH) described the occurrence of these exotic quantum states using a one-dimensional Tight Binding (TB) model.[10,11] Because

the SSH model describes chiral topological insulators, charge fractionalization, and spin-charge separation in one-dimension (1D), numerous efforts have been made to realize the SSH-Hamiltonian in cold atom, photonic, and acoustic experimental configurations.[12-14] It is, however desirable to rationally engineer topological electronic phases into stable and processable materials to exploit the corresponding quantum states. Here we present a flexible strategy based on atomically precise graphene nanoribbons (GNR) to design robust nanomaterials exhibiting valence electronic structures described by the SSH-Hamiltonian.[15-17] We demonstrate the controlled periodic coupling of topological boundary states[18] at junctions of armchair GNRs to create quasi-1D trivial and non-trivial electronic quantum phases. This strategy has the potential to tune the bandwidth of the topological electronic bands close to the energy scale of proximity-induced spin-orbit coupling[19] or superconductivity,[20] and may allow the realization of Kitaev like Hamiltonians[3] and Majorana type end states.[21]

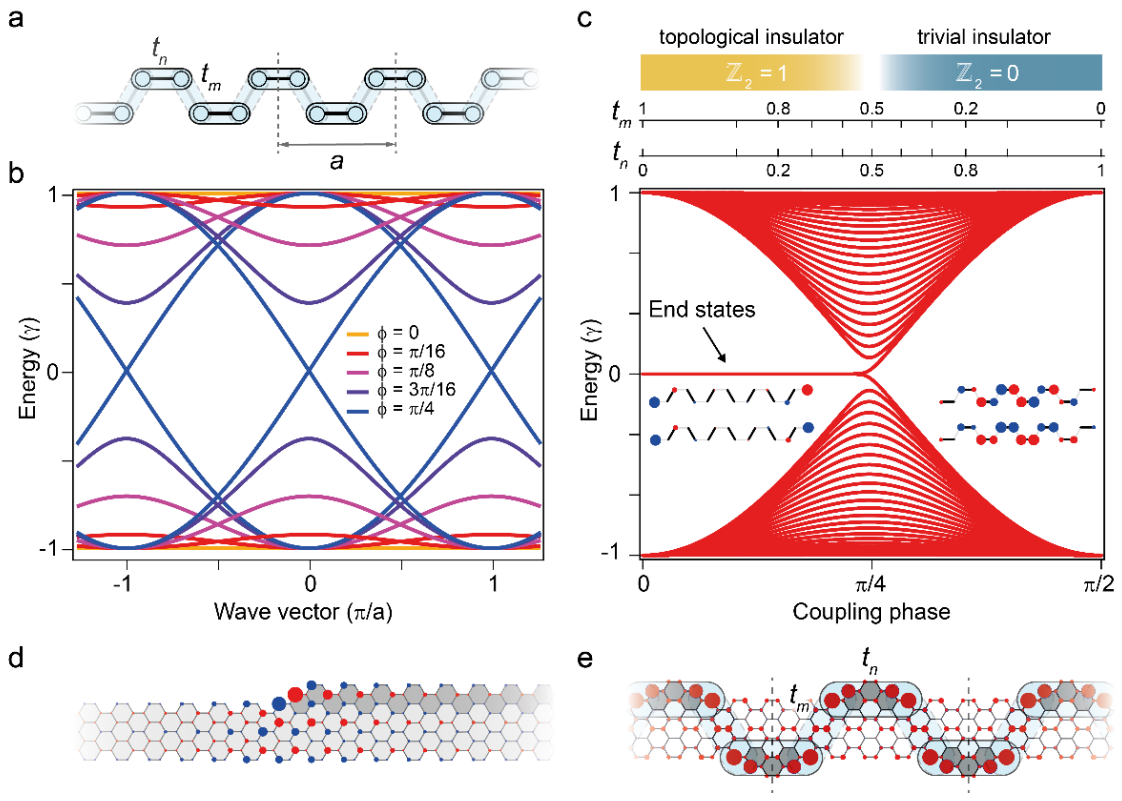

Figure 1 | The SSH model and its realization in edge-extended graphene nanoribbons. a, Schematic representation of the dimerized *cis*-PA like SSH chain with illustration of the intra-cell coupling t_n and inter-cell coupling t_m within and between dimers, respectively. **b**, Dispersion relation $E(k)$ of the SSH chain displayed in **a** as a function of the phase factor ϕ which governs the coupling strengths t_n and t_m (see text). **c**, Energy level diagram as a function of ϕ for a finite SSH chain of 25 dimers, revealing topological zero energy modes for

$\phi < \frac{\pi}{4}$ (that is, $t_n < t_m$). The inset in **c** displays the wave functions of the frontier orbitals (that is, closest to E = 0 eV) for a short 8 dimer chain with localized end state character for $\phi < \frac{\pi}{4}$ and extended bulk like character for $\phi > \frac{\pi}{4}$. **d**, Wave function of the N to $(N+2)$-AGNR boundary state at an isolated smooth 7-AGNR to 9-AGNR junction. Marker size in **d** denotes wave function amplitude and color (blue-red) parity. **e**, Schematic representation of the frontier orbitals (marker size denotes charge density) of a 7-AGNR with staggered edge extensions leading to short 9-AGNR segments. The corresponding 7- to 9-AGNR boundary states couple within the 9-AGNR segments (t_n) and across the 7-AGNR backbone (t_m), in analogy to the *cis*-SSH chain illustrated in **a**.

The fundamental features of the SSH model which describes a 1D chain of dimerized, coupled, and spinless fermion states are summarized in Fig. 1. Conceptually, its basic elements are an ensemble of equivalent fermion states $|\psi_i\rangle$ at each site i of the chain, an intra-cell coupling t_n between two such states within the same dimer, and an inter-cell coupling t_m between states of neighboring dimers (Fig. 1a). The corresponding spinor-based Hamiltonian $H(k) = d_x(k)\sigma_x + d_y(k)\sigma_y$ (with $d_x(k) = t_n + t_m \cos(k)$; $d_y(k) = t_n + t_m \sin(k)$) leads to the energy spectrum $E(k) = \pm\sqrt{t_n^2 + t_m^2 + 2t_n t_m \cos(k)}$ [11]. This dispersion relation yields three extremal phases: (*i*) An intra-cell decoupled, insulating phase with $E(k) = \pm t_m$ for $t_n = 0$ and $t_m \neq 0$; (*ii*) a metallic phase with $E(\pi) = 0t_n$ and $E(0) = \pm 2t_n$ for equal coupling strengths $t_n = t_m \neq 0$; and (*iii*) an inter-cell decoupled, insulating phase with $E(k) = \pm t_n$ for $t_n \neq 0$ and $t_m = 0$.

These three extremal solutions of the SSH chain can be smoothly connected by introducing a phase factor $\phi \in [0, \pi/2]$ governing the strength of t_n and t_m via $t_n = \gamma \cdot sin^2(\phi)$ and $t_m = \gamma \cdot cos^2(\phi)$, where γ denotes the bandwidth. The corresponding series of band structures (BS) $E(k, \phi)$ in Fig. 1b reveals non-dispersive BSs (orange) for the two insulating chain configurations at $\phi = 0$ and $\phi = \frac{\pi}{2}$, while for $\phi = \frac{\pi}{4}$ (blue) a gapless metallic phase is found. That the smooth transition between two insulating phases can only occur by closing the gap is a clear evidence of their distinct topological class. This class can be assigned using the winding number of $\vec{r}(k, \phi) = (d_x(k, \phi), d_y(k, \phi))$ around the origin as a $\mathbb{Z}_2$ topological invariant,[11] which is $\mathbb{Z}_2 = 1$ for $\phi < \frac{\pi}{4}$ and $t_n < t_m$, making the corresponding phases topologically non-trivial, and topologically trivial with $\mathbb{Z}_2 = 0$ for $\phi > \frac{\pi}{4}$ and $t_n > t_m$. However, the winding number cannot be directly determined in experiments. Fortunately, the

bulk-boundary correspondence, i.e. the relation between the bulk winding number and the existence or absence of boundary states, offers a convenient experimental approach to determine a topological class. In the energy spectrum of a finite SSH chain of 25 dimers (Fig. 1c) the topologically non-trivial phases for $\phi < \frac{\pi}{4}$ can readily be distinguished from the trivial ones with $\phi > \frac{\pi}{4}$ by the presence of two degenerate zero energy states localized at the chain ends.

Specifically designed graphene nanoribbons (GNRs) provide the platform to realize a novel class of robust solid state nanomaterials which can flexibly encompass all three aforementioned quantum phases of the SSH chain. The atomically precise structural control required to rationally engineer the corresponding electronic structures can be achieved by on-surface synthesis.[22] Since the first successful bottom-up synthesis of GNRs by polymerization of dedicated molecular precursors.[15] a wide variety of GNRs exhibiting different width, chirality, edge structure and chemical doping has been realized.[16,17] The chemical robustness of GNRs allows their handling under ambient conditions[23] and their integration into high-performance electronic nanodevices,[24] promising a technological exploitation of GNR based topological quantum phases.[12]

The ability to flexibly engineer SSH-like topological quantum phases in GNRs requires a suitable electronic state representing $|\psi_i\rangle$. We identify such a state in the zero energy boundary state at the junction of two armchair graphene nanoribbons (N-AGNR) of different width. Here N denotes the number of transverse carbon atom rows.[15] The boundary state we are considering here is itself of topological origin.[18] To understand this, we consider that N-AGNRs can be classified into three families according to their electronic properties. For $N = 3p$ and $N = 3p + 1$ (p integer) the corresponding AGNRs exhibit a gapped electronic structure, whereas for $N = 3p + 2$ a gapless (that is metallic) behavior is observed at the TB level of theory.[25] At a smooth junction of a gapped N-AGNR with $N = 3p + 1$ and a gapped $N = 3p + 3$ AGNR (that is, with two additional rows of carbon atoms) (Fig. S1-S4), a zero energy boundary state occurs due to the gapless $N = 3p + 2$ intermediate (Fig. S5-S9). This situation is analogous to PA, where the smooth transition from one bond alternation pattern to the complementary one can only proceed via closure of the gap, leading to a zero energy soliton state.[8,11] The wave function of the corresponding boundary state at a 7-AGNR / 9-AGNR junction is displayed in Fig. 1d. Creating a periodic sequence of such boundary states along

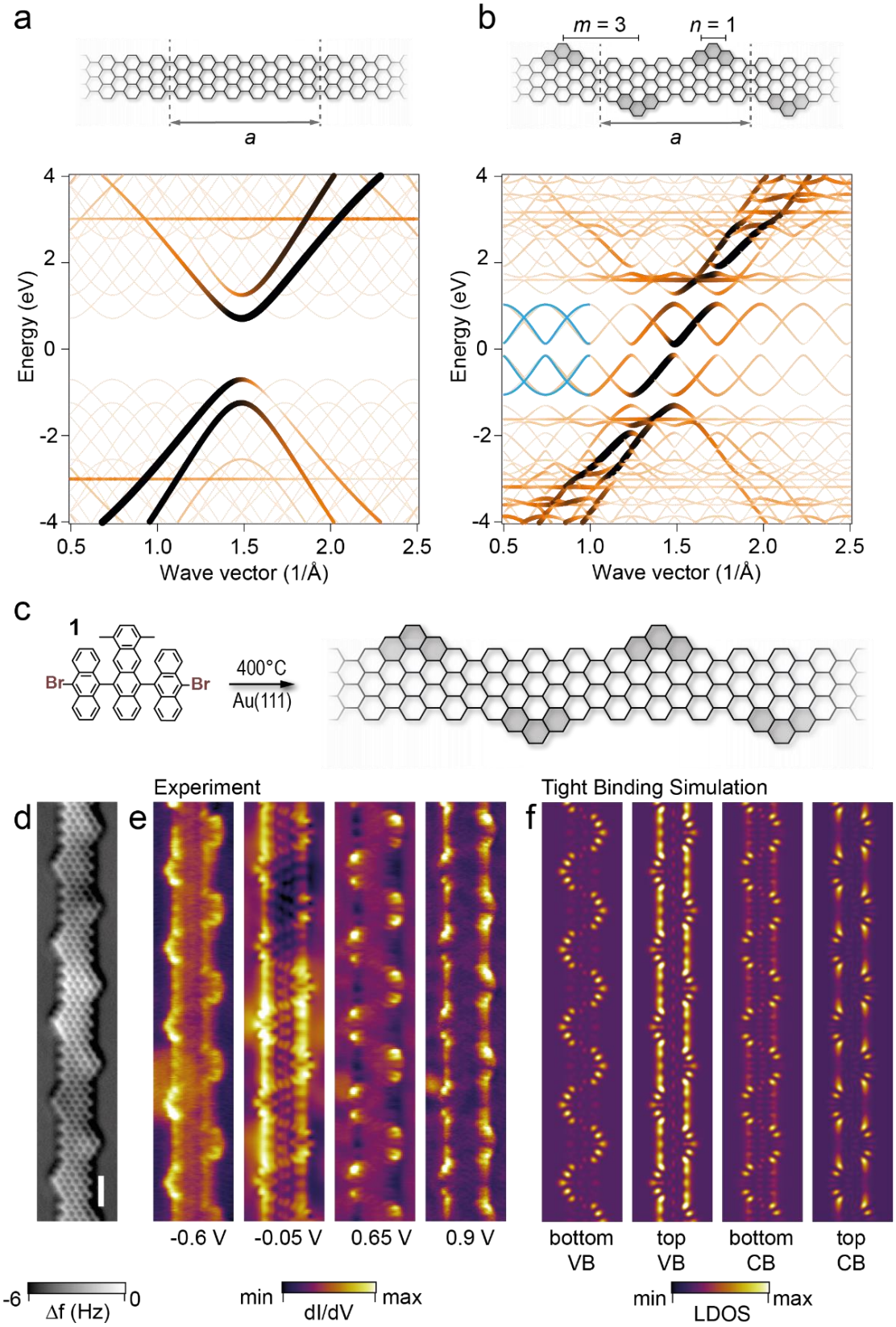

Figure 2 | Electronic structure of the staggered edge-extended 7-AGNR-$S(1,3)$ nanoribbon. **a**,**b**, Structural models and TB band structure diagrams for the pristine 7-AGNR backbone **a** and the staggered 7-AGNR-$S(1,3)$ (with γ_0 = 3 eV). **b**. Marker size and color

(black to yellow) denote the magnitude of $\left|\langle\vec{k}|\psi_n(k)\rangle\right|$ i.e. the projection of the electronic states onto free electron states (Brillouin zone unfolding). Solid blue lines in **b** denote the analytical bands of the *cis*-SSH chain. **c**, Schematic representation of the on-surface synthesis route from monomer **1** to the 7-AGNR-$S(1,3)$. **d**, Constant-height nc-AFM image (with CO functionalized tip) of the frequency shift Δf of a 7-AGNR-$S(1,3)$ segment on Au(111). **e**, Series of constant-current dI/dV maps of the GNR shown in **d** at selected energies close to E_F (which corresponds to 0 V sample bias). The set-point currents are 300 pA (U = −0.6 V), 600 pA (U = −0.05 V), 800 pA (U = 0.65 V) and 1 nA (U = 0.9 V). **f**, Sequence of TB derived constant-height charge density maps at the VB and CB extrema (at −1 eV, −0.2 eV, +0.2 and +1.0 eV from bottom VB to top CB). The 1 nm scale bar in (**e**) applies to all maps **d-f**.

and across the N-AGNR backbone, by local extension to a finite $(N+2)$-AGNR segment (Fig. 1e), produces an effective solid-state analogue of a *cis*-SSH chain. Here, the index n denotes the length of the $(N+2)$-AGNR segment and m corresponds to the separation between the opposite segments across the backbone. The resulting staggered (S) ribbon structure is labeled N-AGNR-$S(n,m)$. Thereby, the structure shown in Fig. 1e and Fig. 2b with $N=7$, $n=1$ and $m=3$ is denoted as 7-AGNR-$S(1,3)$ (see Fig. S1-S4 for details). In terms of the SSH Hamiltonian, n is directly related to the intra-cell coupling t_n while m determines the inter-cell coupling t_m.

The tight-binding bulk band structure of the staggered 7-AGNR-$S(1,3)$ is compared to the band structure of the pristine 7-AGNR backbone in Fig. 2. The appearance of four dispersive bands around the Fermi energy of the 7-AGNR backbone structure is readily observed (see also Fig. S10 and S11). These bands are in excellent agreement with the zone-folded SSH energy spectrum $E(k)$ (blue solid lines in Fig. 2b) with $t_n = 0.45\ eV$ and $t_m = 0.59\ eV$.

We have conceived a synthetic design to experimentally realize the staggered 7-AGNR-$S(1,3)$ structure by using 6,11-bis(10-bromoanthracen-9-yl)-1,4-dimethyltetracene (BADMT, monomer **1**) as precursor monomer. The methyl groups can form zigzag edges bridging smoothly the 7- and 9-AGNR segments via cyclization with the neighboring aromatic rings, forming the intermediate 8-AGNR structure. The corresponding on-surface synthesis route (Fig. 2c) consists of the sublimation of monomer **1** onto a clean Au(111) surface, subsequent thermal precursor activation (dehalogenation) and polymerization at 200 °C, and finally cyclodehydrogenation of the polymer at 400 °C. A constant-height non-contact atomic

force microcopy (nc-AFM) image of the resulting structure is shown in Fig. 2d. The chemical stability of this GNR has been investigated by Raman spectroscopy (Fig. S27), and no spectral changes were detected after 5 days under ambient conditions, consistent with the high stability of the pristine backbone 7-AGNR.[23]

STS investigation reveals that the 2.4 eV band gap of the pristine 7-AGNR on Au(111)[26,27] is drastically reduced to 0.65 ± 0.1 eV for the 7-AGNR-$S(1,3)$. Constant current dI/dV maps of the main spectroscopic features around the gap (Fig. 2e) can be reliably assigned to bottom and top of the valence band (VB) and conduction band (CB), respectively, by comparison with TB simulations (Fig. 2f). The experimentally observed total bandwidth ΔE_{exp} = 1.6 eV (VB minimum to CB maximum, see Fig. S15 and Fig. S17) is in good agreement with the one found from the TB calculations $\Delta E_{\mathrm{TB}} = 2\sqrt{t_n^2 + t_m^2 + 2t_n t_m} = 2.08\,eV$ with $t_n = 0.45\,eV$ and $t_m = 0.59\,eV$. From Density functional theory (DFT, Fig. S12) we deduce $\Delta E_{\mathrm{DFT}} = 1.95\,eV$ with $t_n = 0.37\,eV$ and $t_m = 0.60\,eV$. The symmetry of $E(k)$ with regard to exchange of t_n and t_m does not allow to determine which coupling term prevails and it remains open whether the 7-AGNR-$S(1,3)$ structure belongs to the topologically non-trivial ($\mathbb{Z}_2 = 1$ with $t_m > t_n$) or the topologically trivial class ($\mathbb{Z}_2 = 0$ with $t_m < t_n$).

To clarify this question we exploit the bulk-boundary correspondence[11] and check for the presence of end states at the termini of the N-AGNR-$S(n,m)$ nanoribbon family. There is, however, a complication arising from the concomitant presence of zigzag termini related end states of the N-AGNR backbone.[28] Both types of end states have topological origins but of different nature. As detailed in the Supplementary Materials (Fig. S18-S20), these two states can interact and hybridize such that the SSH end state is no longer present at zero energy. To prevent this, the terminus of the N-AGNR-$S(n,m)$ needs to be extended by a sufficiently long segment of the pristine N-AGNR backbone, as illustrated in Fig. 3a,b. The resulting local density of states (LDOS) at the end of the N-AGNR-$S(n,m)$ segment (indicated by the arrows) as a function of m is shown in Fig. 3a and 3b for the 7-AGNR-$S(1,m)$ and 7-AGNR-$S(3,m)$ nanoribbon families, respectively.

The $(m = 1)$ 7-AGNR-$S(1,1)$ exhibits a zero energy end state, indicating that it belongs to the topologically non-trivial phase ($\phi < \frac{\pi}{4}$) with $t_n < t_m$. Increasing m decreases t_m while t_n remains approximately constant ($n = 1 = const.$). For $m = 2$ the LDOS shows a closing of the gap corresponding to $t_n \approx t_m$ ($\phi \approx \frac{\pi}{4}$), thus marking the metallic intermediate

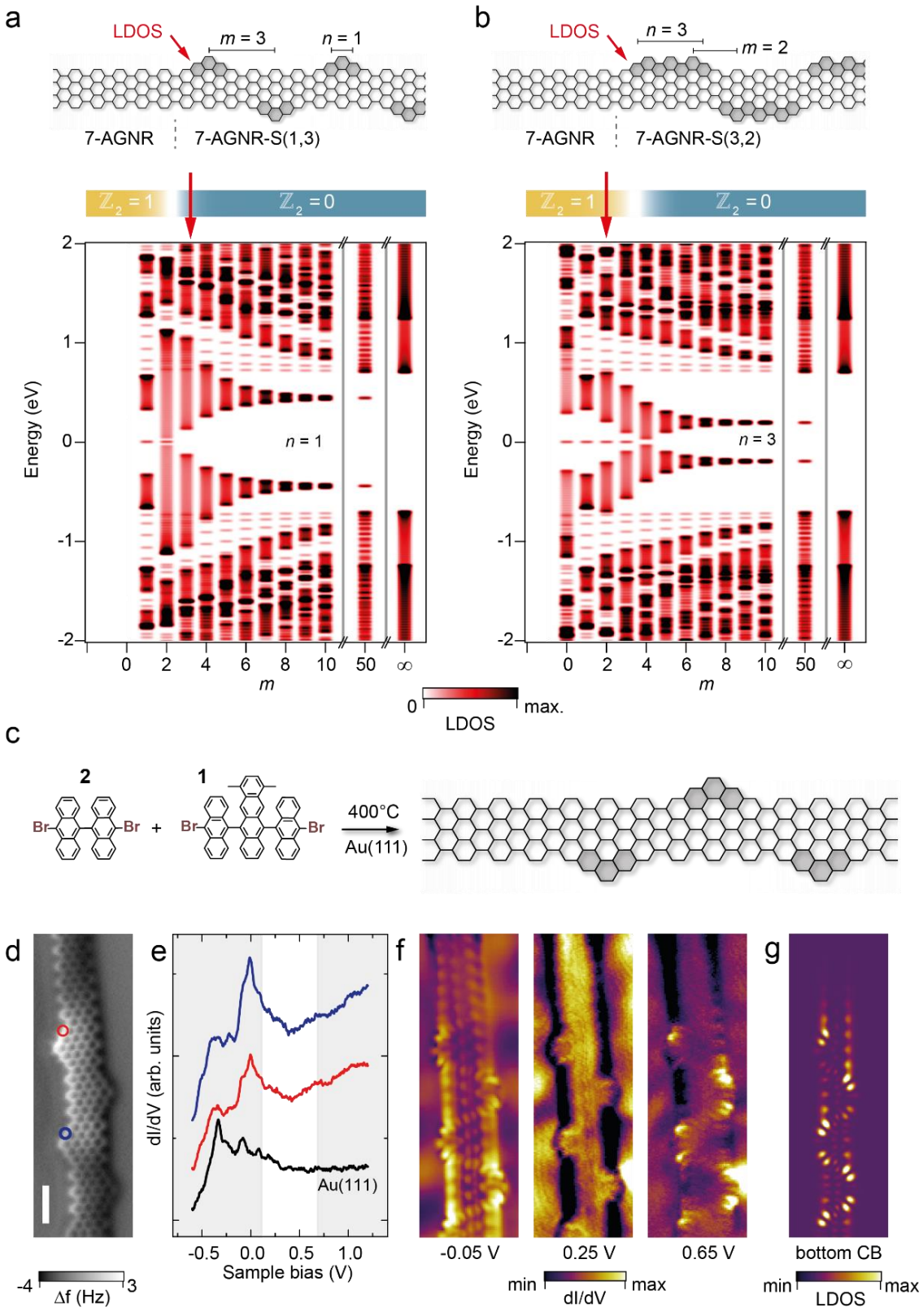

Figure 3 | Bulk-boundary correspondence for the staggered edge-extended 7-AGNR-$S(n,m)$ nanoribbon family. a,**b**, LDOS plots for the 7-AGNR backbone extended 7-AGNR-$S(1,m)$ **a** and 7-AGNR-$S(3,m)$ **b** nanoribbon families, evaluated at the end of the 7-AGNR-

$S(n,m)$ segment (see LDOS-labeled red arrows). The 7-AGNR-$S(1,3)$, whose structural model is depicted in **a**, exhibits no zero energy end state (LDOS indicated by red arrow) and thus belongs to the topologically trivial $\mathbb{Z}_2 = 0$ class. Conversely, the 7-AGNR-$S(3,2)$ structure (model in **b**, LDOS indicated by red arrow) reveals zero energy end states and thus belongs to the topologically non-trivial $\mathbb{Z}_2 = 1$ class. **c**, Synthetic pathway to the 7-AGNR backbone extended 7-AGNR-$S(1,3)$ nanoribbon using **1** and **2** as precursor molecules. **d**, Constant-height nc-AFM frequency shift (Δf) image of a 7-AGNR-$S(1,3)$ segment (acquired with CO functionalized tip). **e**, STS dI/dV spectra taken at positions indicated by the markers of the corresponding color in **e**. **f**, Experimental constant-current dI/dV maps at the top of the VB (−0.05 V, I = 200 pA), in the gap (+0.25 V, I = 500 pA) and at the bottom of the CB (+0.65 V, I = 500 pA) of the 7-AGNR-$S(1,3)$ shown in **e**. **g**, TB simulated charge density map of the bottom of the CB, computed for the experimental structure **d**. The 1 nm scale bar in **d** applies also to panel **f** and **g**.

separating the non-trivial 7-AGNR-$S(1,1)$ from the trivial 7-AGNR-$S(1,3)$ which shows a gap again but with no zero energy end states. For $n = 3$ (Fig. 3b) t_n is reduced and the non-trivial to trivial transition with $t_n \approx t_m$ should occur at larger m (that is, smaller t_m) than in the $n = 1$ case. As can be seen from Fig. 3b, zero-energy end states occur indeed for $m = 1$, 2 and 3, indicating that, according to the TB calculations, the experimentally realized 7-AGNR-$S(1,3)$ belongs to the topologically trivial $\mathbb{Z}_2 = 0$ class.

To verify this finding experimentally, the synthetic route shown in Fig. 2 was modified to allow the required extension of the staggered nanoribbon structure with a pristine 7-AGNR backbone segment. This is realized by sequential deposition of monomer **1** for the 7-AGNR-$S(1,3)$ and dibromo-bianthryl (DBBA, monomer **2**) for the 7-AGNR (Fig. 3c, Fig. S25). Differential conductance dI/dV spectroscopy at the end of the SSH GNR segment (red curve and marker in Fig. 3d,e) and at the internal SSH chain site (blue) shows nearly identical spectra with no indication of an end state. This is further corroborated by dI/dV mapping at selected energies around E = 0 eV (Fig. 3f). At U = −0.05 V the onset of the spatially extended VB states of the 7-AGNR-$S(1,3)$ can be seen; at U = 0.25 V we are in the gap with no particular features, and at +0.65 V the bottom of the CB can be observed, in good agreement with the TB charge density simulation of the lowest energy CB state of the 7-AGNR – 7-AGNR-$S(1,3)$ heterostructure (Fig. 3g). The experiment therefore confirms the TB prediction that the 7-AGNR-$S(1,3)$ is topologically trivial with $\mathbb{Z}_2 = 0$.

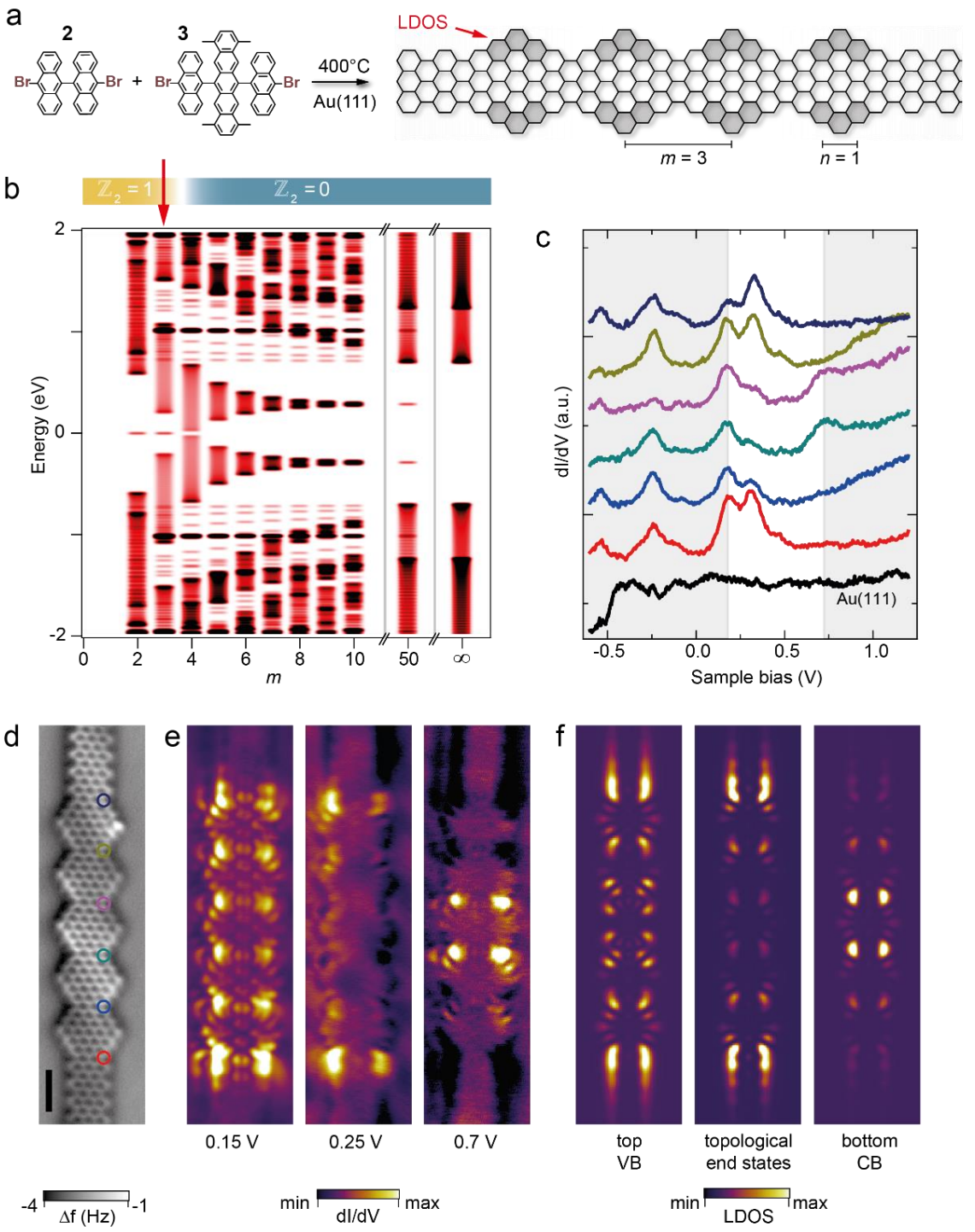

Figure 4 | Non-trivial topological ($\mathbb{Z}_2 = 1$) phase of the inline edge-extended 7-AGNR-$I(1,3)$ structure. a, On-surface synthesis route to the 7-AGNR backbone extended 7-AGNR-$I(1,3)$ nanoribbon. **b**, LDOS plots evaluated at the end of the 7-AGNR-$I(1,m)$ segment (see arrow in **a**) as a function of inter-segment spacing m, revealing the $\mathbb{Z}_2 = 1$ to $\mathbb{Z}_2 = 0$ transition at $m = 4$ with nearly complete gap closure and disappearance of the zero energy states for $m > 3$. **d**, Constant-height nc-AFM frequency shift (Δf) image of a 5 unit 7-AGNR-$I(1,3)$

segment with 7-AGNR extensions at both ends. **c**, d*I*/d*V* spectra (-0.6 V and 100 pA set-point before opening feedback loop) taken at the locations indicated by the markers of corresponding color in **d**. **e**, Experimental d*I*/d*V* maps of the main spectroscopic features at +0.15 V, +0.25 V and +0.7 V (all with I = 500 pA). **f**, TB simulated charge density maps at the top of the VB, at E = 0 eV, and at the bottom of the CB, computed for the experimental structure **d**.

The staggered N-AGNR-$S(n,m)$ exhibits boundary states only for nanoribbon widths $N = 3p + 1$ (p integer) and provides an electronic *cis*-PA analogue. If instead of an asymmetric N- to $(N+2)$-AGNR junction an axially symmetric N- to $(N+4)$-AGNR junction is considered, as illustrated in Fig. 4a, the resulting "inline" edge-extended GNR will yield zero energy boundary states for all backbone widths N (Fig. S6). Similar to the staggered structure, the $(N+4)$ segment length is denoted by n and the segment spacing by m, and the inline "I" structure is thus labeled N-AGNR-$I(n,m)$. The structure shown in Fig. 4a is therefore a 7-AGNR-$I(1,3)$. The LDOS series for the 7-AGNR-$I(1,m)$ family in Fig. 4b reveals topological end states for m = 2 and m = 3 with the non-trivial to trivial phase transition between m = 3 ($\mathbb{Z}_2 = 1$) and m=4 ($\mathbb{Z}_2 = 0$). The bulk BS for the 7-AGNR-$I(1,3)$ exhibits two *trans*-PA like bands with t_n = 0.45 eV and t_m = 0.65 eV (Fig. S11), which is very similar to 7-AGNR-$S(1,3)$. Topological phase diagrams for the 7-AGNR-$S(n,m)$ and -$I(n,m)$ structures are given in Fig. S14 for $n \in [1,9]$ and $m \in [1,9]$.

The synthetic route to the 7-AGNR extended 7-AGNR-$I(1,3)$ inline structure is analogous to the one for the staggered structure, but using 6,13-bis(10-bromoanthracen-9-yl)-1,4,8,11-tetramethylpentacene (BATMP, monomer **3**) as the precursor molecule. Fig. 4d presents the nc-AFM image of a 5 unit 7-AGNR-$I(1,3)$ that is extended by 7-AGNR segments at both ends. d*I*/d*V* spectra recorded at the 7-AGNR / 7-AGNR-$I(1,3)$ junction (dark blue and red in Fig. 4c and 4d) reveal a state at approximately 0.25 V that is only present at the chain ends, as confirmed by d*I*/d*V* mapping (Fig. 4e). Comparison with TB calculations (Fig. 4f) reveals that the extended state at 0.15 V can be assigned to the top of the VB, the 4 lobe state at +0.7 V in the center of the chain to the CB minimum, and that the state at +0.25 V is indeed the expected topologically non-trivial bulk-boundary end state (see Fig. S26 for a high-resolution d*I*/d*V* map). This state is not observed at exactly 0 V due to charge doping of the nanoribbon by the substrate, which is well known to occur for low bandgap GNRs on Au(111)[29,30] and its non-mid-gap position might be due to substrate dependent many-body energy renormalization.[31] Altogether, this analysis shows that, in contrast to the staggered

trivial 7-AGNR-$S(1,3)$, the inline edge-extended 7-AGNR-$I(1,3)$ belongs to the topologically non-trivial $\mathbb{Z}_2 = 1$ class and hosts topological end states.

For our discussion we have chosen the topological invariant related to the winding number of the SSH model ($\mathbb{Z}_2$) as identifier of the topological class. Alternatively, the Zak phase of all occupied bands can also be used, yielding the topological invariant $\mathbb{Z}_2'$[18], which is $\mathbb{Z}_2' = 1 - \mathbb{Z}_2$ for the structures considered here (see Fig. S13).

The presence of short zigzag edge segments in the structure families discussed here suggests the possibility of magnetic ordering.[32] For the 7-AGNR-$S(1,3)$ and 7-AGNR-$I(1,3)$ structures the relatively strong coupling suppresses magnetic ordering, but the formation of antiferromagnetic spin-chains is expected for structures with larger n and m (Fig. S21-S23). A more direct effect of the (n,m) dependent coupling strength is that the band gap can be tuned over a wide range without changing the ribbon width (Fig. S14).

References:

[1] M. Z. Hasan and C. L. Kane. *Rev. Mod. Phys.* **2010**, *82*, 3045–3067.

[2] M. König, S. Wiedmann, C. Brüne, A. Roth, H. Buhmann, L. W. Molenkamp, X.-L. Qi, S.-C. Zhang. *Science* **2007**, *318*, 766–770.

[3] A. Y. Kitaev. *Phys. Usp.* **2001**, *44*, 131–136.

[4] B. Bradlyn, L. Elcoro, J. Cano, M. G. Vergniory, Z. Wang, C. Felser, M. I. Aroyo, B. A. Bernevig. *Nature* **2017**, *547*, 298–305.

[5] E. K. de Vries, A. M. Kamerbeek, N. Koirala, M. Brahlek, M. Salehi, S. Oh, B. J. van Wees, and T. Banerjee. *Phys. Rev. B* **2015**, *92*, 201102.

[6] V. Mourik1, K. Zuo1, S. M. Frolov, S. R. Plissard, E. P. A. M. Bakkers, L. P. Kouwenhoven. *Science* **2012**, *336*, 1003–1007.

[7] C. K. Chiang, C. R. Fincher, Jr., Y. W. Park, A. J. Heeger, H. Shirakawa, E. J. Louis, S. C. Gau, and Alan G. MacDiarmid. *Phys. Rev. Lett.* **1977**, *39*, 1098–1101.

[8] W. P. Su, J. R. Schrieffer, and A. J. Heeger. *Phys. Rev.B* **1980**, *22*, 2099–2111.

[9] Longuet-Higgins, H. C. & Salem, F. R. S. L. The alternation of bond lengths in long conjugated chain molecules. *Proc. R. Soc. Lond. A* **1959**, *251*, 172–183.

[10] W. P. Su, J. R. Schrieffer, and A. J. Heeger. *Phys. Rev. Lett.* **1979**, *42*, 1698–1701.

[11] J. K. Asbóth, L. Oroszlány. and O. Pályi. Lecture Notes in Physics Vol. 919 (Springer, Cham, 2016).

[12] E. J. Meier, F. A. An and B. Gadway. *Nat. Commun.* **2016**, *7*, 13986.

[13] W. Tan, Y. Sun, H. Chen and S.-Q. Shen. *Sci. Rep.* **2015**, *4*, 3842.

[14] B. G. Chen, N. Upadhyaya, and V. Vitelli. *Proc. Natl Acad. Sci. USA* **2014**, *111*, 13004–13009.

[15] J. Cai, P. Ruffieux, R. Jaafar, M. Bieri, T. Braun, S. Blankenburg, M. Muoth, A. P. Seitsonen, M. Saleh, X. Feng, K. Müllen and R. Fasel. *Nature* **2010**, *466*, 470–473.

[16] G. D. Nguyen, H.-Z. Tsai, A. A. Omrani, T. Marangoni, M. Wu, D. J. Rizzo, G. F. Rodgers, R. R. Cloke, R. A. Durr, Y. Sakai, F. Liou, A. S. Aikawa, J. R. Chelikowsky, S. G. Louie, F. R. Fischer and M. F. Crommie. *Nat. Nanotechnol.* **2017**, *12*, 1077–1082.

[17] L. Talirz, P. Ruffieux and R. Fasel. *Adv. Mater.* **2016**, *28*, 6222–6231.

[18] T. Cao, F. Zhao and S. G. Louie. *Phys. Rev. Lett.* **2017**, *119*, 076401.

[19] Z. Wang, D.–K. Ki, H. Chen, H. Berger, A. H. MacDonald and A. F. Morpurgo. *Nat. Commun.* **2015**, *6*, 8339.

[20] M. V. Feigel'man, M. A. Skvortsov and K. S. Tikhonov. *Solid State Commun.* **2009**, *149*, 1101–1105.

[21] S. Nadj-Perge1, I. K. Drozdov1, J. Li, H. Chen, S. Jeon, J. Seo, A. H. MacDonald, B. A. Bernevig, A. Yazdani. *Science* **2014**, *346*, 602–607.

[22] Q. Shen, H.-Y. Gao and H. Fuchs. *Nano Today* **2017**, *13*, 77–96.

[23] A. Fairbrother, J.-R. Sanchez-Valencia, B. Lauber, I. Shorubalko, P. Ruffieux, T. Hintermann and R. Fasel. *Nanoscale* **2017**, *9*, 2785–2792.

[24] J. P. Llinas, A. Fairbrother, G. B. Barin, W. Shi, K. Lee, S. Wu, B. Y. Choi, R. Braganza, J. Lear, N. Kau, W. Choi, C. Chen, Z. Pedramrazi, T. Dumslaff, A. Narita, X. Feng, K. Müllen,

F. Fischer, A. Zettl, P. Ruffieux, E. Yablonovitch, M. Crommie, R. Fasel and J. Bokor. *Nat. Commun*. 2017, **8**, 633.

[25] K. Wakabayashi1, K.Sasaki1, T.Nakanishi and T. Enoki. *Sci. Technol. Adv. Mater.* **2010**, *11*, 054504.

[26] H. Söde, L. Talirz, O. Gröning, C. A. Pignedoli, R. Berger, X.Feng, K. Müllen, R. Fasel, and P. Ruffieux. *Phys. Rev. B* **2015**, *91*, 045429.

[27] O. Deniz, C. Sánchez-Sánchez, T. Dumslaff, X. Feng, A. Narita, K. Müllen, N. Kharche, V. Meunier, R. Fasel, P. Ruffieux. *Nano Lett.* **2017**, *17*, 2197–2203.

[28] S.Wang, L. Talirz, C. A. Pignedoli, X. Feng, K. Müllen, R. Fasel and P. Ruffieux. *Nat. Commun.* **2016**, *7*, 11507.

[29] A. Kimouche, M. M. Ervasti, R. Drost, S. Halonen, A. Harju, P. M. Joensuu, J. Sainio and P. Liljeroth. *Nat. Commun.* **2015**, *6*, 10177.

[30] N. Merino-Díez, A. Garcia-Lekue, E. Carbonell-Sanromà, J. Li, M. Corso, L. Colazzo, F. Sedona, D. Sánchez-Portal, J. I. Pascual, D. G. de Oteyza. *ACS Nano* **2017**, *11*, 11661–11668.

[31] N. Kharche and V. Meunier. *J. Phys. Chem. Lett.* **2016**, *7*, 1526–1533.

[32] M. Fujita, K. Wakabayashi, K. Nakada and K. Kusakabe. *J. Phys. Soc. Jpn* **1996**, *65*, 1920–1923.

Acknowledgements This work was supported by the Swiss National Science Foundation, the Office of Naval Research BRC Program, European Union's Horizon 2020 research and innovation program (GrapheneCore1 696656), and the NCCR MARVEL. C.A.P. thanks the Swiss Supercomputing Center (CSCS) for computational support. [redacted] is grateful for the fellowship from the China Scholarship Council. [redacted] thanks [redacted], [redacted] and [redacted] for fruitful discussions.

Reviewer information Nature thanks [redacted] and the other anonymous reviewer(s) for their contribution to the peer review of this work.

Author contributions [redacted] and [redacted] conceived and supervised this work. [redacted] and [redacted] designed and synthesized the molecular precursors. [redacted] performed the on-surface synthesis and SPM characterization. [redacted] did the Raman analysis, [redacted] and

[redacted] performed the corresponding simulations. [redacted] did the DFT calculations. [redacted] developed the conceptual framework, performed the TB calculations and wrote the manuscript, with contributions from all co-authors. [redacted] and [redacted] made the figures, with contributions from other co-authors.

Competing interests The authors declare no competing interests.

Additional information

Supplementary information is available for this paper at https://doi.org/ 10.1038/s41586-018-0375-9.

Reprints and permissions information is available at http://www.nature.com/ reprints.

Correspondence and requests for materials should be addressed to [redacted]

Publisher's note: Springer Nature remains neutral with regard to jurisdictional claims in published maps and institutional affiliations.

Methods

Tight Binding calculations of electronic structure. The calculations of the electronic structure are based on the nearest-neighbor hopping Tight Binding (TB) Hamiltonian considering the $2p_z$ orbital of the carbon atoms only:

$$H = \sum_i \varepsilon_i c_i^\dagger c_i - \sum_{<i,j>} \gamma_0 c_i^\dagger c_j \qquad (1)$$

Here $c_i^\dagger$ and c_i denote the usual creation and annihilation operators on site i. $\langle i,j\rangle$ denotes the summation over nearest-neighbour sites, the on-site energies ε_i are all set to zero, and the nearest-neighbour hopping parameter is chosen to be γ_0=3 eV.

Band structures (BS) are calculated by taking into account the wave-vector dependent complex Bloch phase factors in the TB Hamiltonian. Unfolding of the BS into the extended Brillouin zone is achieved by projection of the wave functions of energy $E_n(\vec{k}_\parallel)$ on plane waves $\left|\langle \vec{k}_\parallel + \vec{k}_\perp | \psi_n(\vec{k}_\parallel)\rangle\right|$. The corresponding weight is displayed by marker size and color. Here $\vec{k}_\parallel$ and $\vec{k}_\perp$ denote the wave vectors parallel and perpendicular to the GNR axis,

respectively. The perpendicular wave vector $\vec{k}_\perp$ for the projection is chosen non-zero in order to cut through the Dirac point of the parent graphene structure at $\vec{k}_\perp = 2\pi/3a$ and $\vec{k}_\parallel = 2\pi/\sqrt{3}a$ with a=2.44 Å being the length of the graphene basis vector.

Wave functions are reconstructed from the TB Eigenvectors $\alpha_{i,n}$ of energy E_n by summing up the C $2p_z$ Slater type orbitals with ξ = 1.625/a_u over the atomic sites i of the structure.

$$\psi_n(\vec{r}) = \sum_i \alpha_{i,n} \cdot z \cdot \exp(-\xi|\vec{r} - \vec{r}_i|) \qquad (2)$$

STS-mapping simulations are achieved in first approximation by displaying the charge density of the considered states in the energy interval $[\varepsilon_1, \varepsilon_2]$ at constant height z_0 according to:

$$LDOS(x, y, z_0) = \sum_n |\psi_n(\vec{r})|^2 \qquad \text{for all } n \text{ with } E_n \in [\varepsilon_1, \varepsilon_2] \qquad (3)$$

The results of the BS calculations for the 7-AGNR-*S(1,3)* and 7-AGNR-*I(1,3)* structures are compared to DFT calculations in supplementary Fig. 12.

Molecular precursor and nanoribbon synthesis. The chemical synthesis of the monomers **1** (BADMT), **2** (BATMP) and **3** (DBBA) is detailed in the Supplementary Information together with details of the on-surface synthesis of the corresponding GNRs (Supplementary Scheme 1, Supplementary Figs. 28–38, 24–26).

STM/STS and nc-AFM characterization. A commercial low-temperature STM/AFM system (Scienta Omicron) with a base pressure below 1×10^{-10} mbar was used for sample preparation and characterization under ultrahigh-vacuum conditions. STM images and differential conductance d*I*/d*V* maps were recorded in constant-current mode unless noted otherwise. Constant-height tunnelling current and nc-AFM frequency shift images were recorded with a CO-functionalized tip attached to a quartz tuning fork sensor (resonance frequency 23.5 kHz). d*I*/d*V* spectra were recorded using the lock-in technique (U_{rms} = 20 mV at 680 Hz modulation). All data shown were acquired at a sample temperature of 5 K.

Data availability. The datasets generated and/or analysed during the current study are available from the corresponding author on reasonable request.

Code availability. The tight-binding calculations were performed using a custom-made code on the WaveMetrics IGOR Pro platform. Details of this tight-binding code can be obtained from the corresponding author on reasonable request.

Supporting information

Engineering of Robust Topological Quantum Phases in Graphene Nanoribbons

1. Structure classification and nomenclature

The atomic structure of the graphene nanoribbons (GNRs) discussed in this work is based on an armchair GNR (AGNR) backbone having N rows of carbon atoms in the transverse direction (N-AGNR). This N-AGNR backbone is locally asymmetrically extended to a (N + 2)-AGNR or symmetrically extended to a (N + 4)-AGNR, as illustrated in Fig. S1. These edge extensions produce boundary regions at the junction with the N-AGNR backbone.

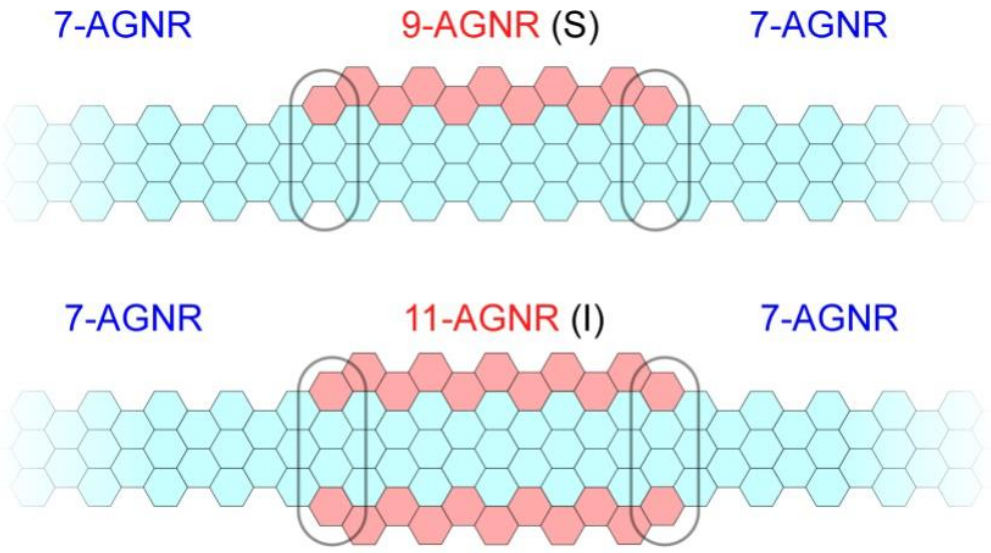

Figure S1. Schematic representation of the structural elements of the asymmetric (N + 2)-AGNR (top) and the symmetric (N + 4)-AGNR (bottom) segments on the N-AGNR backbone. The displayed structures are exemplary for a N = 7 backbone (7-AGNR). The left and right junction regions between the 7-AGNR backbone and the 9- or 11-AGNR segments, respectively, are highlighted by ovals.

The periodic arrangement of these basic segments on the N-AGNR backbone yields non-trivial, edge extended AGNR structures. The two specific structures of interest in the context of this work are the so-called "staggered" (S-type, based on asymmetric $N + 2$ segments) and the "inline" (I-type, based on axially symmetric $N + 4$ segments) structures that are discussed in detail below.

1.1. The staggered ("*S*"-type) structure

For the staggered S-structure the segment length is denoted by the integer $n \geqslant 1$, which refers to the number of units constituting the ($N + 2$)-AGNR segment (Fig. S2a).

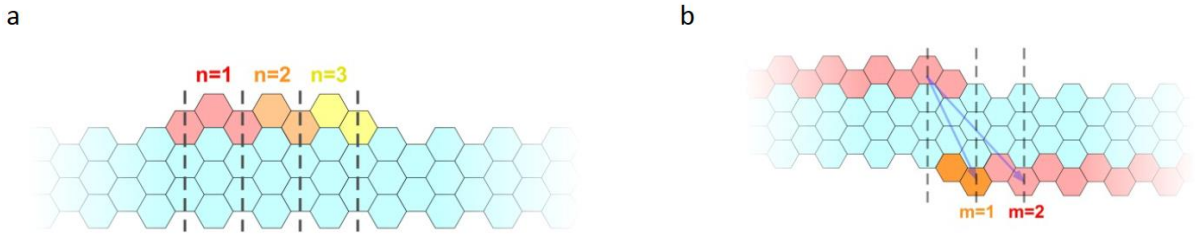

Figure S2. **a**, Schematics of edge extension producing a ($N + 2$)-AGNR segment structure (reddish to yellow color) on a N-AGNR backbone (light blue color). The length of the ($N + 2$)-AGNR segment is denoted by index n. **b**, Schematic illustration of the inter-edge separation m of two ($N + 2$) segments.

In order to realize the periodically staggered structure of interest, the edge extensions producing the ($N + 2$) segments are alternatingly placed at opposite edges of the N-AGNR backbone. The separation of the segments is denoted by index m, which denotes the axial distance of the left hand terminus of the lower edge segment with respect to the right hand terminus of the upper edge segment (Fig. S2b). The same separation applies for the left hand terminus of the upper edge segment with respect to the right hand terminus of the lower edge segment.

The index m denotes the axial displacement in terms of unit cells of the backbone (a_0 = 3*a_c=3*1.41 Å = 4.23 Å). Although m can be smaller than 1 we do not consider such structures because the resulting segment overlap will yield local ($N + 4$)-AGNR structures.

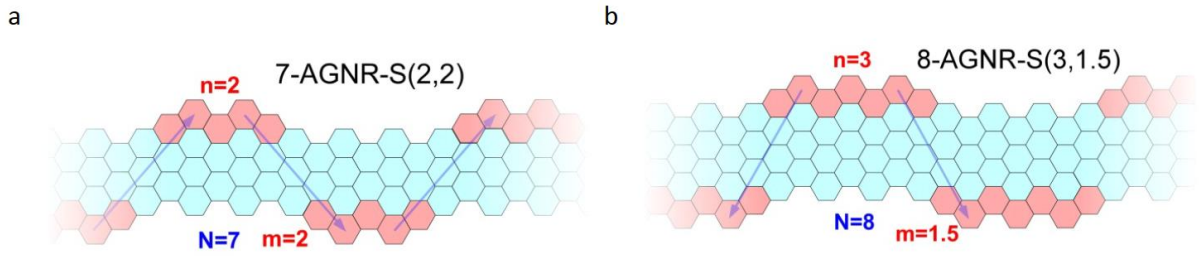

Figure S3. Examples of staggered edge-extended AGNRS: **a**, N = 7, n = 2 and m = 2 ("7-AGNR-(2,2)"); and **b**, N = 8, n = 3 and m = 1.5 ("8-AGNR-S(3,1.5)").

The resulting staggered edge-extended GNR structures are denoted as N-AGNR-(n, m), with:

N: Width of the backbone, counting the number of transverse rows of carbon atoms.

S: Identifier for "**S**taggered"

n: (N + 2) segment length, starting with $n \geqslant 1$

m: Across the ribbon (N + 2) segment spacing, with $m \geqslant 1$ (N odd $\rightarrow$ m integer, N even $\rightarrow$ m half integer)

1.2. The inline "*I*"-type structure

In addition to the staggered (S) structure, the inline (I) arrangement of two (N + 2) aligned segments across the N-AGNR backbone is possible. N, n and m retain the meaning used to describe the S-structures with the index m denoting the separation of the segments along the same edge as well as across the backbone. In contrast to the S-structure, the N-AGNR backbone of the I-structure is locally extended to a finite length (N + 4)-AGNR segment with N being odd.

The nomenclature for this inline arrangement is N-AGNR-(n, m), with:

N: Number of transverse rows of carbon atoms in the backbone N, must be odd.

I: Identifier for "**I**nline"

n: (N + 4) segment length, starting with ($n \geqslant 1$)

m: Across the ribbon (N + 4) segment spacing ($m \geqslant 2$)

Figure S4 shows schematically a 7-AGNR-(2,3) (**a**) and a 7-AGNR-I(1,4) (**b**) structures.

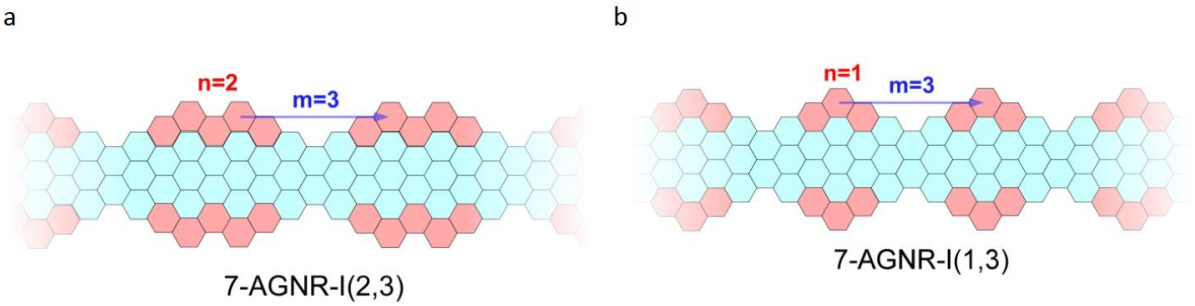

Figure S4. Examples of inline edge-extended AGNRs: **a**, 7-AGNR-(2,3), and **b**, 7-AGNR-I(1,3).

2. Electronic properties of the *S* and *I* edge-extended AGNR structures

The specific electronic properties of the S- and I-structures are rooted in the particular electronic character of their parent N-AGNR.

2.1. The *N*-AGNR backbone structure

The N-AGNRs can be classified according to their electronic character in 3 families:[1] Two semiconducting families with $N = 3p$ or $N = 3p + 1$ and a metallic family with $N = 3p + 2$, with $p \geqslant 0$ integer. These families can be well distinguished by the evolution of their energy gap with increasing ribbon width N, as displayed in Fig. S5 (from Tight-Binding (TB) calculations with the nearest-neighbor hopping $\gamma_0 = 3$ eV).

The sequence of semiconducting and metallic properties of AGNRs as a function of ribbon width N can be regarded as a discrete topological phase diagram, where the metallic structures represent the boundaries separating one topological family of semiconducting N-AGNRs (e.g., $N = 3p$ or $N = 3p + 1$) from the next one (e.g. $N = 3p^*$ or $N = 3p^* + 1$ with $p^* = p + 1$). In this context the junctions formed between the N-AGNR backbone and the edge-extended N + 2 segments of the S-structure (or the N + 4 segments of the I-structure) can be regarded as "smooth" electronic transition regions within the same topological class if the

transition can proceed without closing the gap (i.e., there is no intermediate metallic N-AGNR). On the other hand, the transition is considered to be across topological classes if it cannot proceed without closing the gap, i.e., if there is a metallic N-AGNR intermediate. Although a gap closure is not always required it is a hallmark of a topological phase transition.[2] The topological nature of AGNRs and the occurrence of boundary states have been discussed recently by Louie et al.[3]

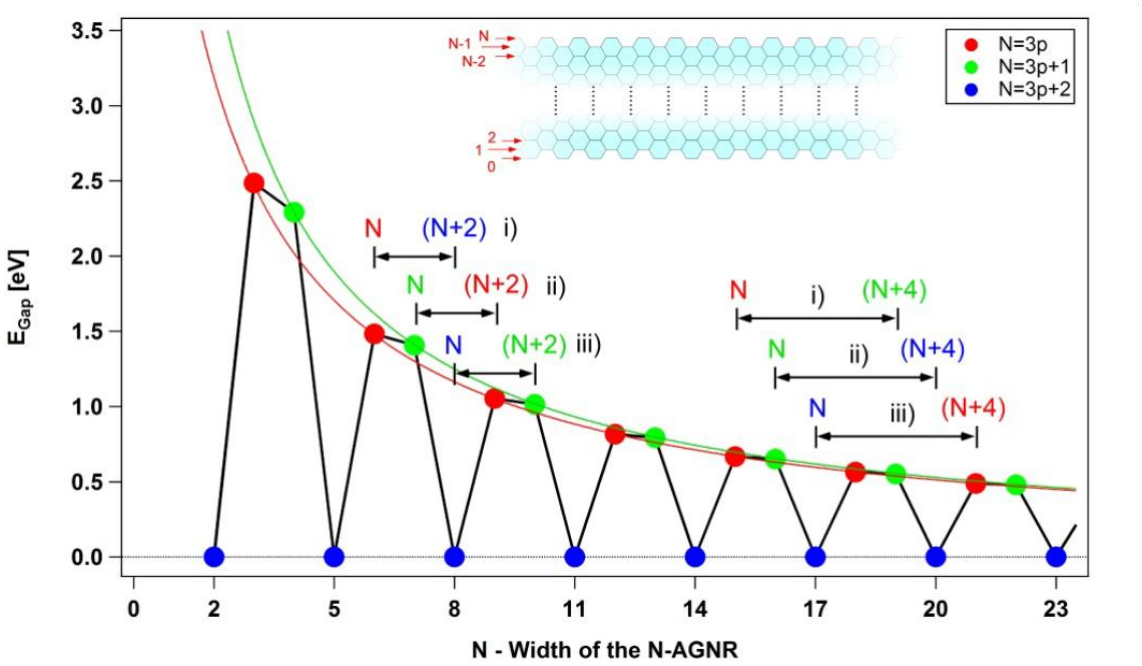

Figure S5. Dependence of the N-AGNR nearest-neighbor TB energy gap on ribbon width N. The electronic family is denoted by the marker color. The three electronically different types of junctions i) – iii) for the staggered $N/(N + 2)$ (Fig. S3) and the inline $N/(N + 4)$ (Fig. S4) structures are indicated.

As we will see, this result has consequences on the appearance of topologically protected zero-energy (E = 0) boundary states, as discussed in the following.

2.2. Boundary states at the *S*- and *I*-segment junctions and their on-segment interaction

Considering a N-AGNR backbone with a single edge-extended segment (as shown in Fig.S1) one realizes that the junctions between the N-AGNR backbone and the $(N + 2)$- respectively $(N + 4)$-AGNR segments mark the transition from one electronic structure type to

another. Accordingly, as a function of the width N of the backbone N-AGNR we can identify three different junction types:

For the staggered edge extensions (S-structure):

i) $N = 3p$ $(sc) \rightarrow (N + 2) = 3p + 2$ (met)

ii) $N = 3p + 1$ $(sc) \rightarrow (N + 2) = 3p + 3 = 3p*$ (sc with $p^* = p + 1$)

iii) $N = 3p + 2$ $(met) \rightarrow (N + 2) = 3p + 4 = 3p* + 1$ (sc with $p^* = p + 1$)

For the inline edge extensions (II structure):

i) $N = 3p$ $(sc) \rightarrow N + 4 = 3p + 4 = 3p* + 1$ (sc with $p^* = p + 1$)

ii) $N = 3p + 1$ $(sc) \rightarrow N + 4 = 3p + 5 = 3p* + 2$ (met with $p^* = p + 1$)

iii) $N = 3p + 2$ $(met) \rightarrow N + 4 = 3p + 6 = 3p*$ (sc with $p^* = p + 2$)

where "*sc*" and "*met*" indicate the semiconducting and metallic nature of the corresponding ribbon structure, respectively.

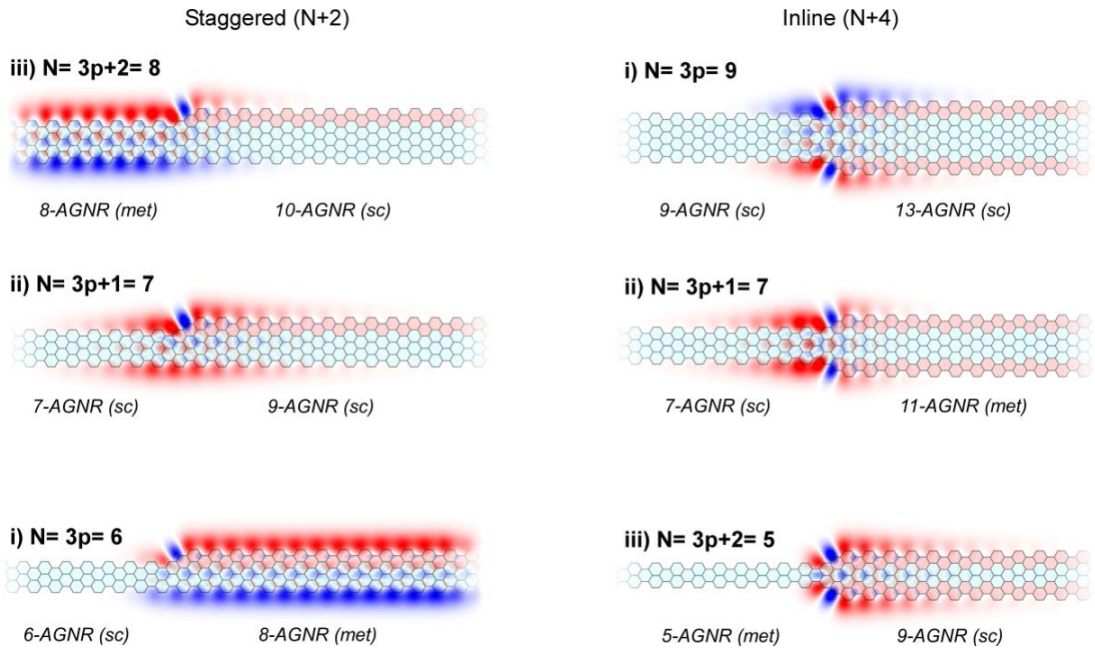

Figure S6. Catalogue of highest occupied molecular orbital (HOMO, i.e. closed to E = 0) TB wave functions (color denoting the parity) for the six possible junction types i) to iii) for the staggered $N \rightarrow (N + 2)$-AGNR and the inline $N \rightarrow (N + 4)$-AGNR junctions.

It can be seen from Fig. S6 that the different junction types yield different types of low energy states. In the staggered case only junction type ii) with $N = 3p + 1$ yields a zero-energy state localized at the junction. In the two other cases i) and iii) the states closest to E = 0 are the metallic states of either the backbone (for $N = 3p + 2$) or of the metallic $(N + 2)$-segment (for $N = 3p$). In contrast the inline $(N + 4)$ structure exhibits localized junction states for all three cases i)-iii).

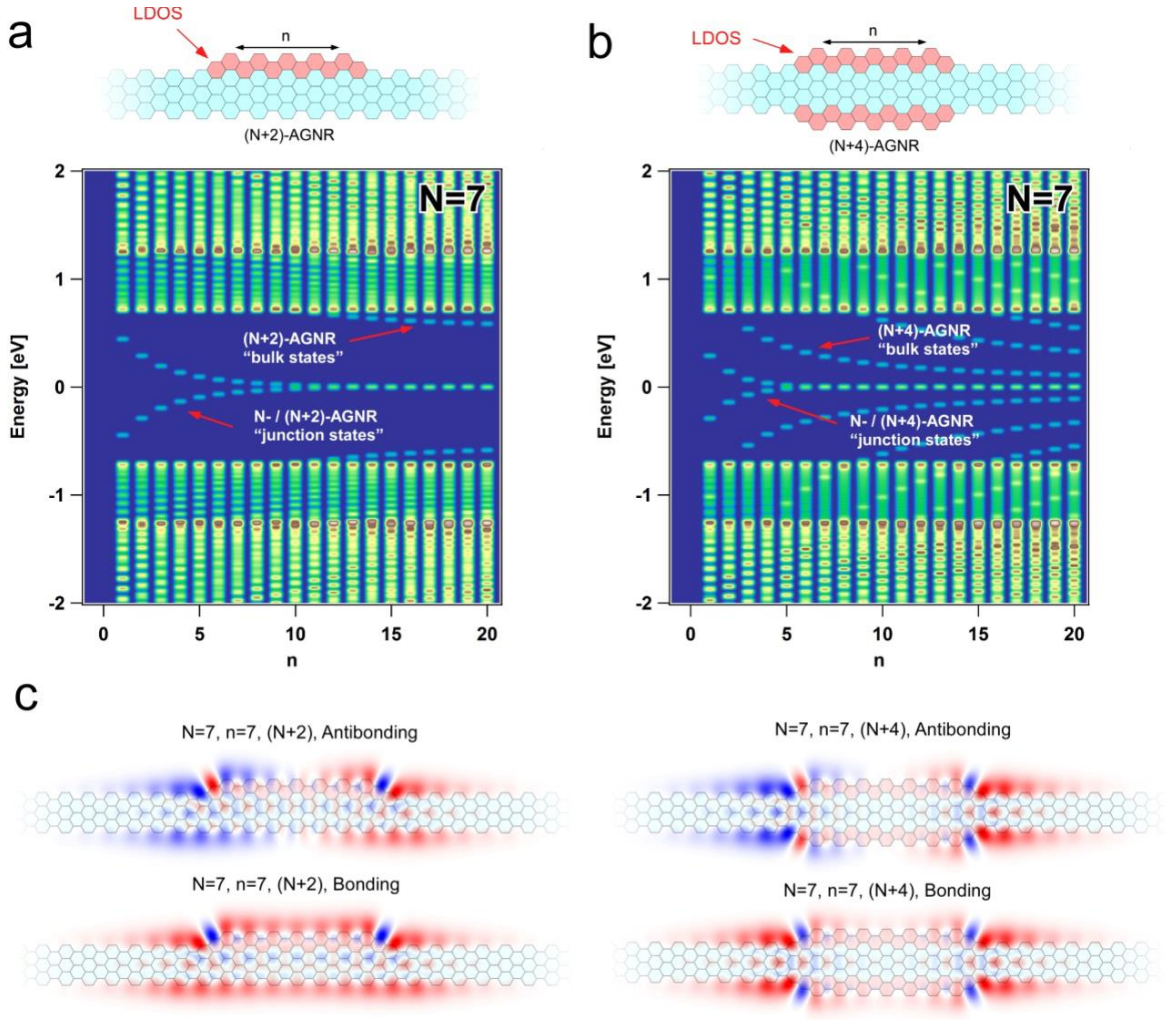

Figure S7. Local density of states (LDOS) maps (DOS at the segment boundary) for **a**, an isolated 9-AGNR and **b**, an isolated 11-AGNR segment of varying length n within a 7-AGNR backbone. **c**, Wave function plots for the bonding and anti-bonding hybrid states for $n = 7$ in the two cases.

If the segment length n is reduced to finite values, the junction states at the left and right ends of the edge-extended segment can no longer be regarded as isolated because they can interact with each other. In fact, a segment of finite length n can be viewed as the intra-cell

dimer of the SSH model. Depending on segment length n, the boundary states at either end (left $|L\rangle$ and right $|R\rangle$) will hybridize to form bonding and antibonding hybrid states with energy $E = \pm t_n$ where $t_n = \langle L|H|R\rangle$ (H denoting the Hamiltonian of the system). The energy splitting t_n will generally decrease (exponentially for large n) with n as shown in Fig. S7.

The interaction of the $|L\rangle$ (left) and $|R\rangle$ (right) boundary states does not only depend on segment length n but also on backbone width N as can be seen from the LDOS maps of Fig. S8.

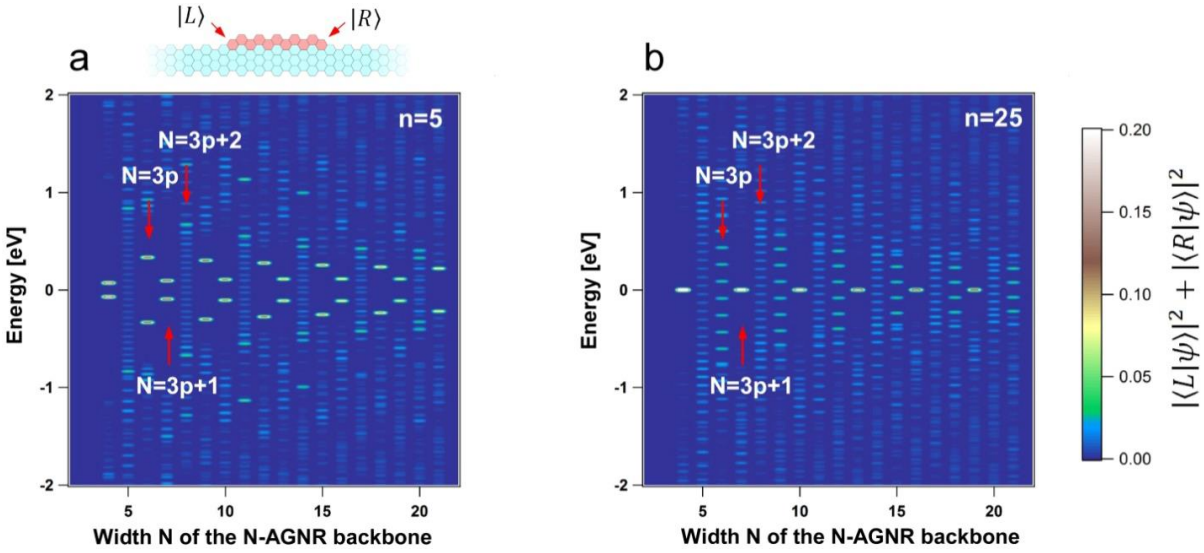

Figure S8. LDOS maps (DOS at the segment boundaries) for an isolated (N + 2)-AGNR segment within a N-AGNR backbone for backbone widths N = 4, 5, … , 21. **a**, Short segment length n = 5. **b**, Long segment length n = 25.

The three junction types i) - iii) discussed above can be well distinguished in the energy level spectra for different values of N (Fig. S8a). For the case iii) with $N = 3p + 2$ the N-AGNR backbone is metallic and no states with particularly strong weight at the junction can be discerned. The situation is different for the cases i) with $N = 3p$ and ii) with $N = 3p + 1$, where two low-energy states localized in the junction region (i.e. with high amplitude in the LDOS) can clearly be observed. If the N + 2 segment length is increased from n = 5 to n = 25 (Fig. S8b), localized states remain only in the case ii) with $N = 3p + 1$. In the limit of $nn \longrightarrow \infty$ this junction state collapses to $E \cong 0$ with 2-fold degeneracy.

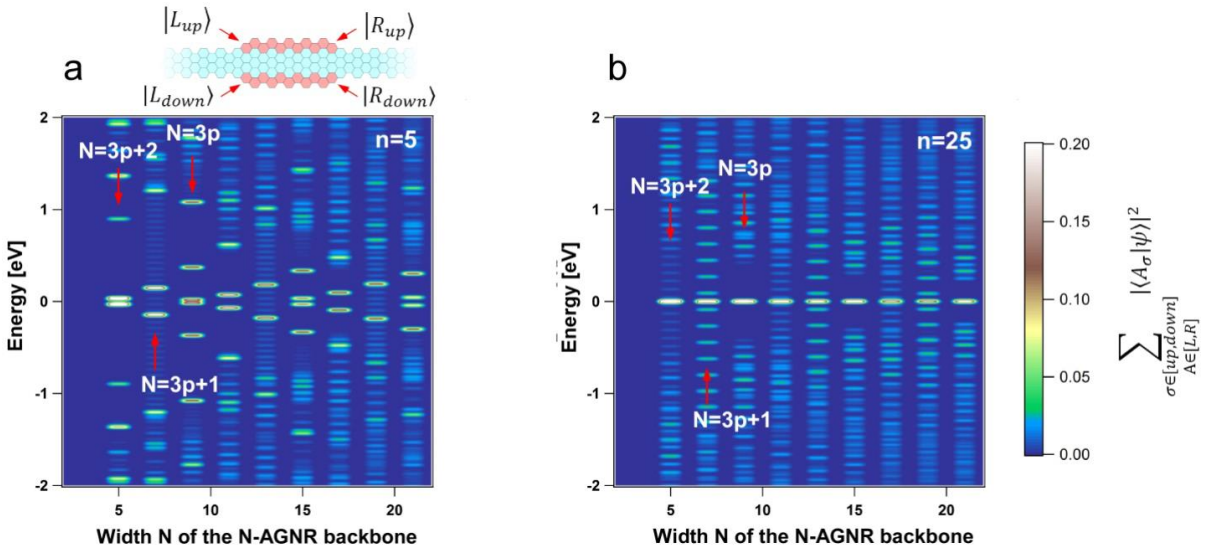

Figure S9. LDOS maps (DOS at the segment boundaries) for an isolated (N + 4)-AGNR segment within a N-AGNR backbone for backbone widths N = 5, 7, … , 21. **a**, Short segment length n = 5. **b**, Long segment length n = 25. The color scale displays the summed square of the wave function amplitude on the center atoms of the four zigzag kink sites.

In the case of the inline edge-extended (N + 4)-AGNR segment again all three cases i) - iii) can be well distinguished in the sequence of energy level spectra for increasing backbone width N (Fig. S9). For the short segment length n = 5, states localized at the junctions are observed in all cases. If the segment length is increased to n = 25 (Fig. S9b) a 2-fold degenerate zero-energy state appears for all backbone widths N, and not just for $N = 3p + 1$ as in the case of the S-type structure.

This behavior can be understood when looking at the staggered N-AGNR / (N + 2)-AGNR and the inline N-AGNR / (N + 4)-AGNR junctions as regions of gradual increase of AGNR width, i.e. by considering the (N + 1) and the (N + 1), (N + 2) and (N + 3) intermediate widths for the two cases, respectively (Fig. S6). For the staggered structure only the $N = 3p + 1$ case (case ii) in Fig. S6) features a metallic (N + 1) = $3p$ + 2 intermediate. In this case we can understand the junction as connecting two insulating/semiconducting AGNR segments via closure of the gap. Accordingly, we have the appearance of a topologically protected zero-energy state at the junction, very much like for the soliton case of polyacetylene.[4] For the inline structure there is always an intermediate width with metallic properties between the N-AGNR and the (N + 4)-AGNR segments, and we will thus find a topologically protected zero-energy state at the junction for all AGNR backbone widths N.

2.3. Periodic coupling of junction states

For small n and m the junction states interact with each other and split in energy. Furthermore, the junction states can hybridize with the metallic N-AGNR backbone for case iii) or the metallic (N + 2) segment in case i) of the staggered N-AGNR-(n, m).

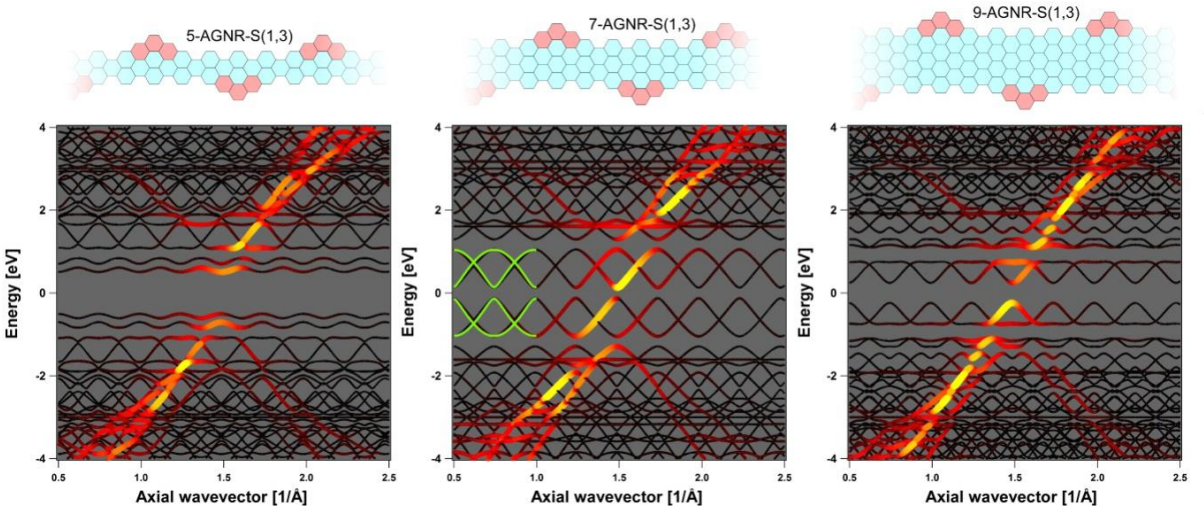

Figure S10. Band structure calculations for the staggered edge-extended 5-AGNR-(1,3) (left), 7-AGNR-S(1,3) (middle) and 9-AGNR-S(1,3) (right), representing the cases iii), ii) and i), respectively. The green solid curves in the panel 7-AGNR-S(1,3) denote the fit with the analytical solution of the *cis*-PA structure.

The impact of hybridization can clearly be observed in Fig. S10. Only the case where N = 7 (i.e. N = 3p + 1 with p = 2) shows nearly undistorted *cis*-PA like bands around E = 0. In the case N = 5 (i.e. N = 3p + 2) no such band can be identified, and for N = 9 (i.e. N = 3p with p = 3) the PA like bands hybridize at about +/- 0.8 eV with the valence and conduction band states of the backbone AGNR.

For the I-type structures shown in Fig. S11 the *trans*-PA like bands (highlighted in light green) near E = 0 show little tendency of hybridization.

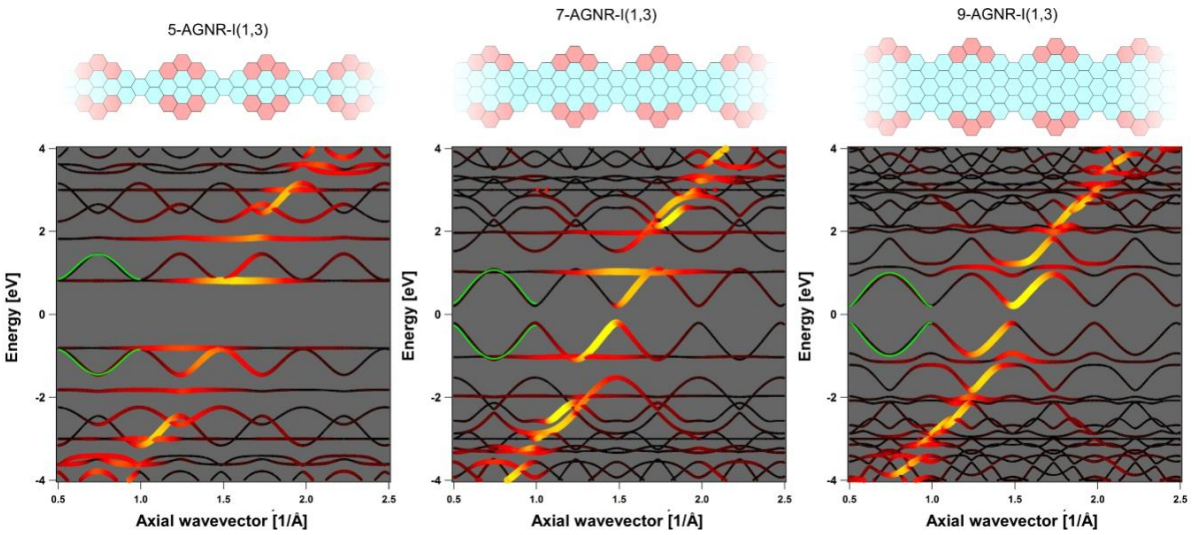

Figure S11. Band structure calculations for the inline edge-extended 5-AGNR-(1,3) (left), 7-AGNR-*I*(1,3) (middle) and 9-AGNR-*I*(1,3) (right), representing the cases iii), ii) and i), respectively. As in Fig. S10 the solid green curves denote the fits with the analytical solution for the *trans*-PA structure.

2.4. Comparison of Tight-Binding (TB) and Density Functional Theory (DFT) band structures

In Fig. S12 we compare the band structures obtained from TB with the ones from DFT. Very good agreement is observed for the frontier bands around the Fermi energy E_F (dashed line).

The DFT simulations were performed with the plane wave code quantum espresso.[5] The generalized gradient a*pp*roximation within the PBE[6] parameterization was used for the exchange correlation functional. Ultrasoft pseudopotentials from the Standard Solid State Pseudopotentials accuracy library[7] were employed to model the ionic potentials. A cutoff of 50 Ry (400 Ry) was used for the plane wave expansion of the wave function (charge density). For the convergence of the wave function a grid of 10 / 17 k-points was used to sample the 1D Brillouin zone for the 7-AGNR-*S*(1,3) / 7-AGNR-*I*(1,3) ribbons, respectively. The unit cell of the 7-AGNR-(1,3) / 7-AGNR-*I*(1,3) ribbon contained 120 / 66 atoms corresponding to a length of 25.75 A / 12.86 A, respectively. The simulation cell contained 15 Å of vacuum in the non-periodic directions to minimize interactions among periodic replica of the system. The

thickness of the vacuum region, the sampling of the BZ, and the cutoff ensure convergence for the computed band structures. The atomic positions of the ribbon and the cell dimension along the ribbon axis were optimized until fall orces were lower than 0.002 eV/Å and the pressure in the cell was negligible. The DFT band structures shown in Fig. S12 are aligned to the vacuum level, which was computed from the average electrostatic potential in the vacuum region. All calculations were performed through a Jupiter based GUI for the AiiDA platform.[8]

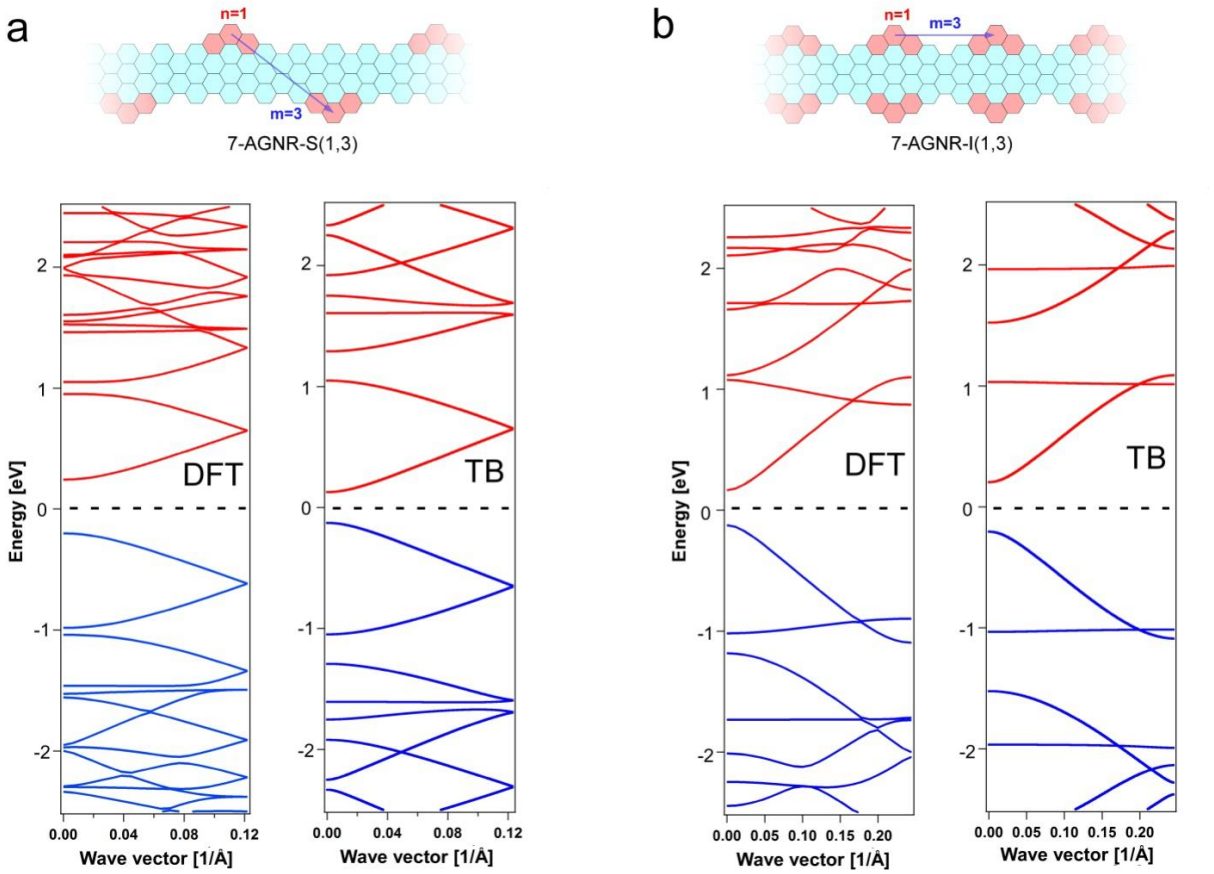

Figure S12. Comparison of the DFT bands close to E_F (dotted line) with the nearest neighbor TB bands calculated with γ_0 = 3 eV. a, The staggered edge-extended 7-AGNR-*S*(1,3). b, The inline edge-extended 7-AGNR-*I*(1,3).

2.5. SSH $\mathbb{Z}_2$ and Zak phase related $\mathbb{Z}_2'$ topological invariants

In our principal discussion, we have chosen to classify the topology of our GNR structures by the winding number 0 or 1 of the SSH Hamiltonian that describes the frontier bands (i.e. closest to the charge neutrality point). We have labeled this SSH related topological

invariant as $\mathbb{Z}_2$. In this picture the role of the 7-AGNR backbone is reduced to a bystanding host structure. However, in analogy to the treatment of Cao, Zhao and Louie,[3] we can also attribute a {0,1} topological invariant to these structures using the Zak phases (γ_n) including all the occupied bands and not just the frontier ones. With the Zak phase being the integral of the Berry connection $\langle\left\langle \mu_{kn} \middle| \frac{\partial \mu_{kn}}{\partial k} \right\rangle\rangle$ in the first Brillouin zone:[3]

$$\gamma_n = i\frac{2\pi}{a}\int_{-\pi/a}^{\pi/a} dk \left\langle u_{kn} \middle| \frac{\partial u_{kn}}{\partial k} \right\rangle$$

Here the parameter a denotes the size of the unit cell and u_{kn} the periodic part of the electron Bloch wave function of the nth band. With $\mathbb{Z}_2'$ given by the relation$(-1)^{\mathbb{Z}_2'} = e^{i\sum_n \gamma_n}$, summing over all occupied bands n. The value of $\mathbb{Z}_2$ as well as $\mathbb{Z}_2'$ depends on the choice of the unit cell as shown in Fig. S13.

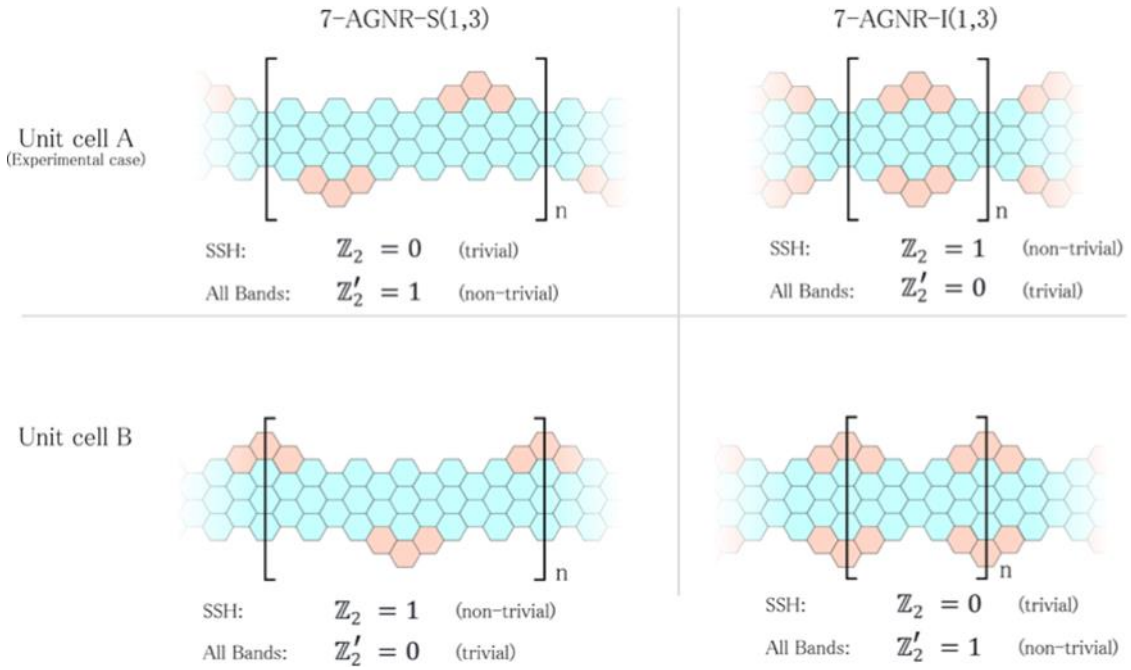

Figure S13. Topological character of the 7-AGNR-(1,3) and 7-AGNR-*I*(1,3) depending on the choice of the unit cell.

The relation between the two topological invariants for the A type unit cell (which is the one realized in the experiments) is:

$\mathbb{Z}_2' = 1 - \mathbb{Z}_2$ if m is odd

and

$\mathbb{Z}_2' = \mathbb{Z}_2$ if m is even.

Figure S14 shows the topological phase diagram (according to $\mathbb{Z}_2$) of the 7-AGNR-$S(n, m)$ and 7-AGNR-$I(n, m)$ structure family on a TB level of theory with γ_0 = 3 eV.

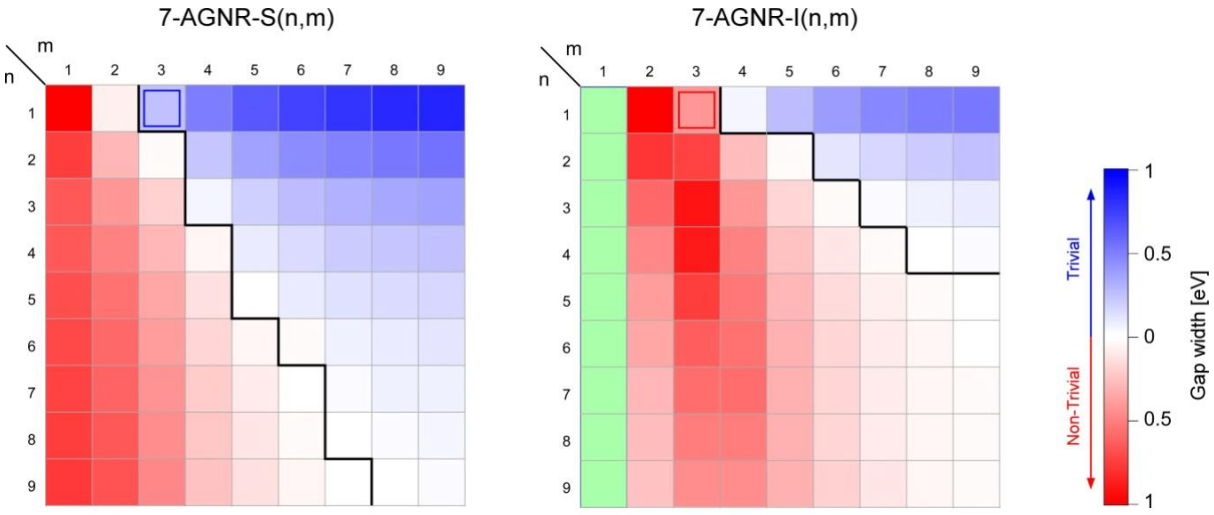

Figure S14. SSH $\mathbb{Z}_2$ topological phase diagram calculated from TB of the 7-AGNR-(n, m) and 7-AGNR-(n, m) structure family. The color scale encodes the band gap of the SSH bands (white-blue for $\mathbb{Z}_2$ = 0 and white-red for $\mathbb{Z}_2$ = 1). The experimentally realized structures (1,3) are highlighted by squares. The solid black line denotes the topological $\mathbb{Z}_2$ phase boundary in both diagrams.

The gap displayed in Fig. S14 is related to SSH coupling strengths t_n and t_m by the relation $E_{\text{gap}} = 2|t_n - t_m|$ such that the column $(n, 9)$ reflects in first approximation $2t_n$ (for n<6 where $t_n \gg t_m$). Similarly, the row $(9, m)$ reflects $2t_m$ (for m<6 where $t_m \gg t_n$).

3. Scanning Tunneling Spectroscopy (STS) of the GNR structures

In the case of the 7-AGNR-(1,3) the dI/dV spectra using a metallic tip are rather featureless except for the strong valence band maximum. In order to identify the band onsets,

we typically use a sequence of constant current tunneling spectroscopy maps (CITS), which show states associated with the bands with higher contrast.

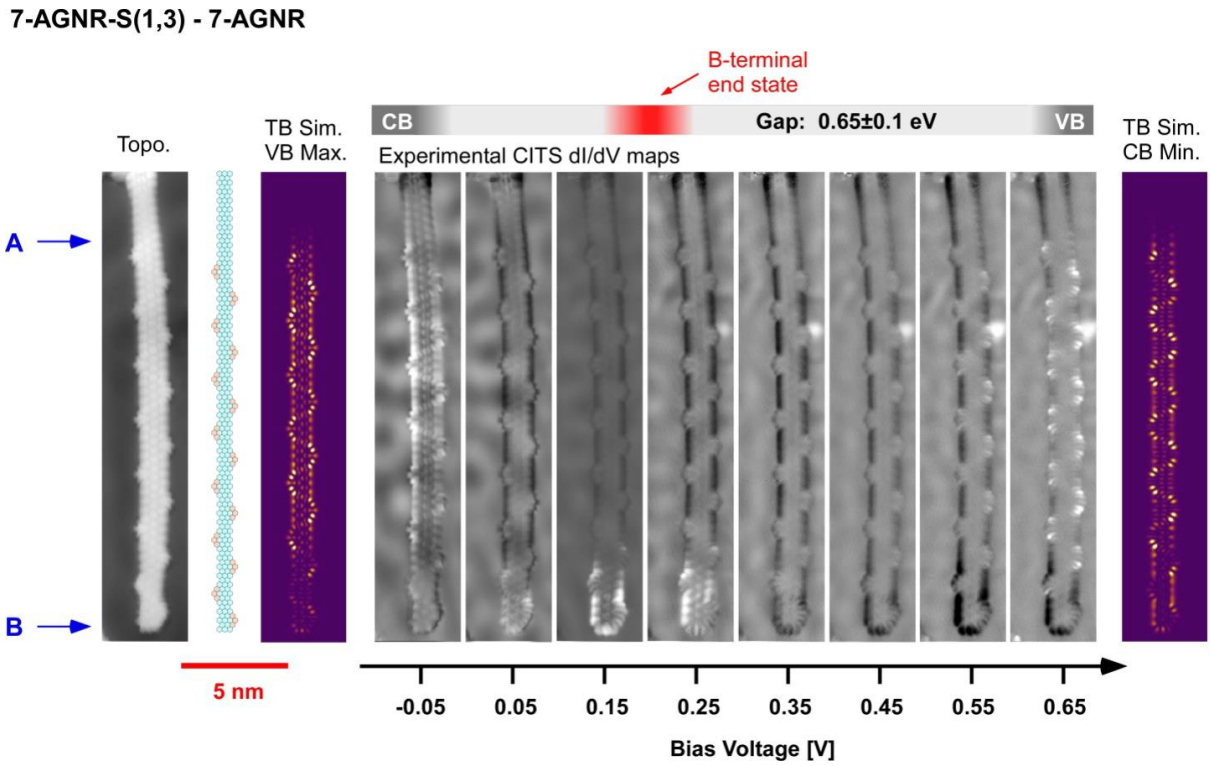

Figure S15. Sequence of CITS maps revealing the band gap of the 7-AGNR-*S*(1,3) together with TB LDOS simulations of the valence band maximum (VB Max.) and conduction band minimum (CB Min.) respectively. The extent of the energy gap and the position of the localized state are given schematically in the top part of the figure.

Figure S15 shows the presence of an end state at the terminal of the pristine 7-AGNR-(1,3) (B site at 0.15-0.25 V bias). In contrast there is no localized state visible at the junction between the 7-AGNR-(1,3) and the 7-AGNR. Complementary to the discussion in the main text of the paper, this can be understood by the non-trivial $\mathbb{Z}_2^{Zak}$ invariant of the 7-AGNR-(1,3) structure, which interfaced to the ($\mathbb{Z}_2^{Zak}$ trivial) vacuum at B will yield an end state. At the A junction however the $\mathbb{Z}_2^{Zak}$ non-trivial 7-AGNR-(1,3) meets the likewise non-trivial 7-AGNR and resulting in an absent interface state.

The corresponding CITS sequence for the 7-AGNR-(1,3) is exhibited in Fig. S16 displaying the end state of the 7-AGNR at 0.05 V, the VB Max. at 0.15 V, the SSH end state at 0.25 V and CB Min. at 0.65 V.

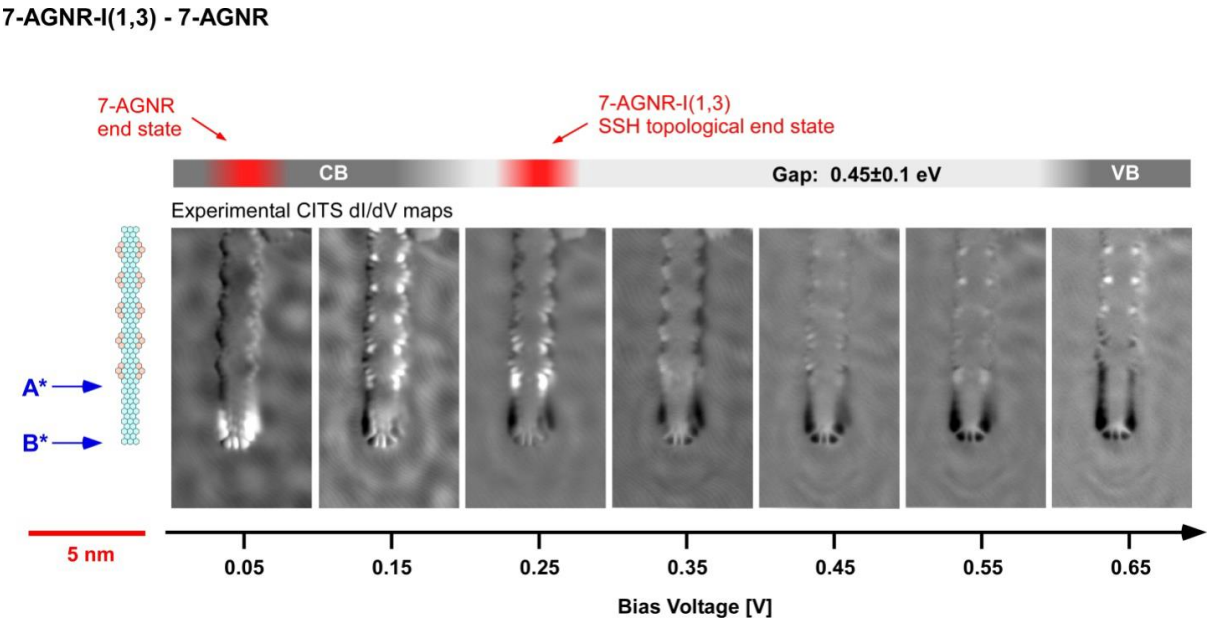

Figure S16. Sequence of CITS maps revealing the band gap of the 7-AGNR-(1,3) anagloge to Fig. S15

As indicated in the main text and as can also be seen in Fig. S16, the location of the SSH topological end states is not exactly at E = 0 and is also not in the middle of the gap. Whereas the upshift in energy can be attributed to charge transfer with the substrate, the non-mid-gap position cannot be explained by this effect. However, one needs to keep in mind that all the calculations we are considering here do not take into account the metallic substrate, which can significantly renormalize the energy positions of the electronic states of GNR. This is due to many-body interactions such as the image charge potential energy (as mentioned in the main text). The image charge correction tends to lower the energy of a given electron state and depends on the details of the spatial extend of its wave function. We therefore assume that the renormalization of the localized end states is stronger than the one of the extended band. Accordingly we expect this effect to be a probable origin of the asymmetric position of the 7-AGNR-*I*(1,3) topological end state on the gap of the SSH bands.

Whereas the d*I*/d*V* spectra of the 7-AGNR-(1,3) are generally rather featureless, under specific tip conditions the band edges can also be clearly discerned in the d*I*/d*V* spectrum. The spectra in figure S17 for the 7-AGNR-(1,3) have been measure with a tip that has been conditioned on an NaCl island and picked up a NaCl cluster or individual Na or Cl atom. As can be seen in comparison with the DFT derived DOS (compare with Fig. S12a) we find a good correspondence between gap energy and the bandwidth of the SSH like band. However these

imaging conditions are not generally reproducible and accordingly we have systematically used the CITS mapping with a metallic tip for the band edge determination.

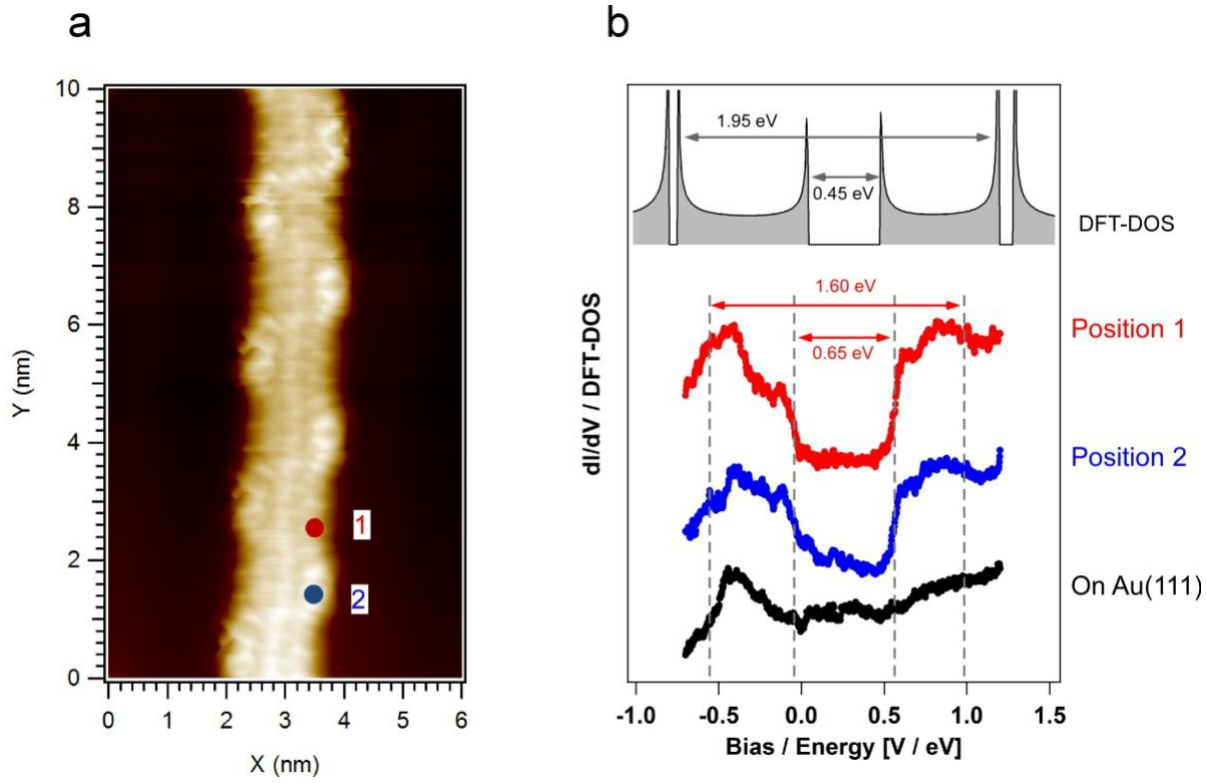

Figure S17. **a**, STM topography image with a NaCl conditioned tip of the pristine 7-AGNR-*S*(1,3). **b**, DFT calculated DOS of the 7-AGNR-*S*(1,3) and STS d*I*/d*V* spectra at selected positions on the GNR edge together with the reference on Au(111), also measured with the NaCl functionalized tip.

4. Conservation of the topological end states in finite *S* and *I* edge-extended AGNR structures

The terminus of a *N*-AGNR-(n, m) can host two kinds of zero-energy states: A topological end state originating from the segment boundary states, and the zigzag end state of the N-AGNR backbone (Fig. S21a).[11] Therefore, the E = 0 states occurring at the ends of non-trivial *N*-AGNR-*S*(n, m) and *N*-AGNR-*I*(n, m) structures need to be protected from hybridization with the zigzag end states of the backbone *N*-AGNR. Figure S18 shows the end of a 7-AGNR-(1,1) structure (a topologically non-trivial insulator) that is longitudinally extended by 8 units (Fig. S18a) or 2 units (Fig. S18b) of the backbone 7-AGNR.

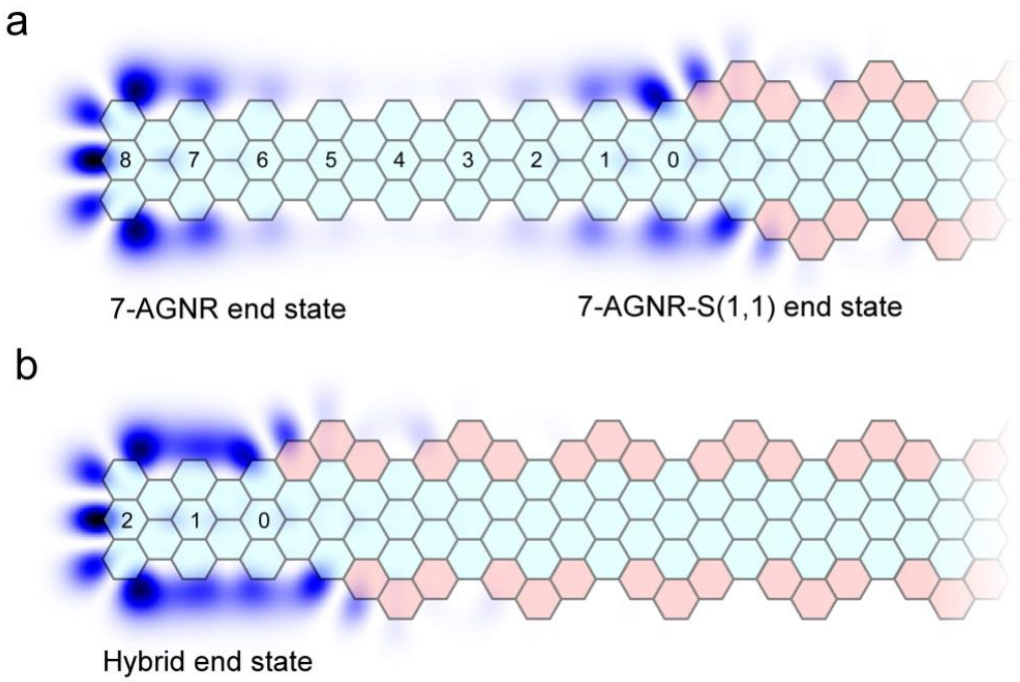

Figure S18. **a**, 7-AGNR-$S(1,1)$ structure with terminus longitudinally extended by 8 units of the 7-AGNR backbone. The charge density of the frontier orbitals close to E = 0 are overlaid to the structural drawing. **b**, Same as (a) but for a shorter end extension of only 2 backbone units.

Fig. S18a reveals that the zigzag end state of the 7-AGNR backbone and the topological end state of the 7-AGNR-$S(1,1)$ show only marginal (if any) orbital overlap for reasonably long backbone extension (8 units). The situation is different if the backbone extension length is reduced to 2, as shown in Fig. S18b. In this case the two end states overlap strongly and split in energy. For the inline N-AGNR-(n, m) structures the situation is analogous.

The dependence on backbone extension length of the hybridization between the backbone end state and the end state of topologically non-trivial staggered and inline AGNRs is illustrated in Fig. S19 for a 7-AGNR-(1,1) and a 7-AGNR-$I(1,3)$. For both hybrid structures it can be observed, that a backbone extension exceeding 7 or 8 7-AGNR units effectively suppresses hybridization of the two different end states. For backbone extensions less than 5 7-AGNR units, however, a sizeable bonding and anti-bonding splitting of the zero-energy end states is observed. In the case of the experimentally realized 7-AGNR-(1,3) structure the end states are completely suppressed for backbone extensions shorter than 2 units.

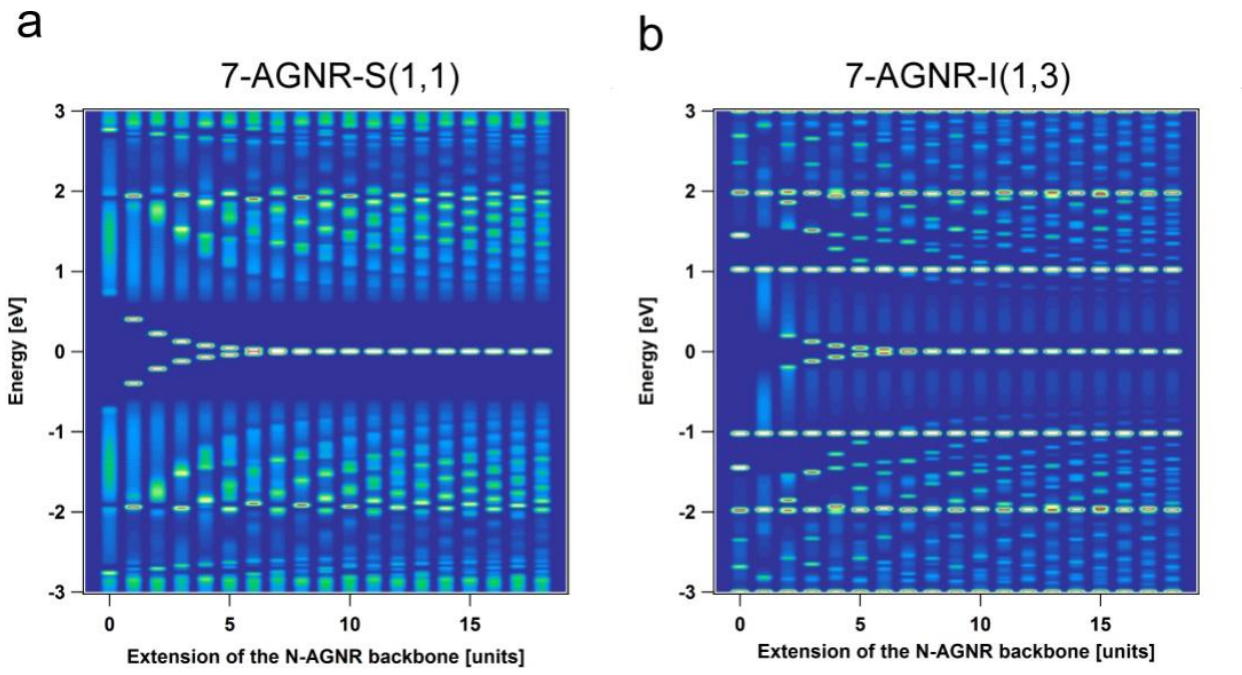

Figure S19. LDOS at the junction end state as a function of the length of the backbone extension in (terms of 7-AGNR unit cells) for **a**, the 7-AGNR-(1,1) and **b**, the 7-AGNR-*I*(1,3).

In the case of a topologically trivial structure such as the experimentally realized 7-AGNR-(1,3), only the zigzag backbone end state is present. Due to particle-hole symmetry, it remains at E = 0 independent of the length of the backbone extension. This can clearly be seen in Fig. S20a where the LDOS at the short zigzag 7-AGNR terminus is plotted as a function of the backbone extension length. Even in the absence of any backbone extension the zero-energy state persists and can be observed experimentally, as is confirmed in Fig. S20b.

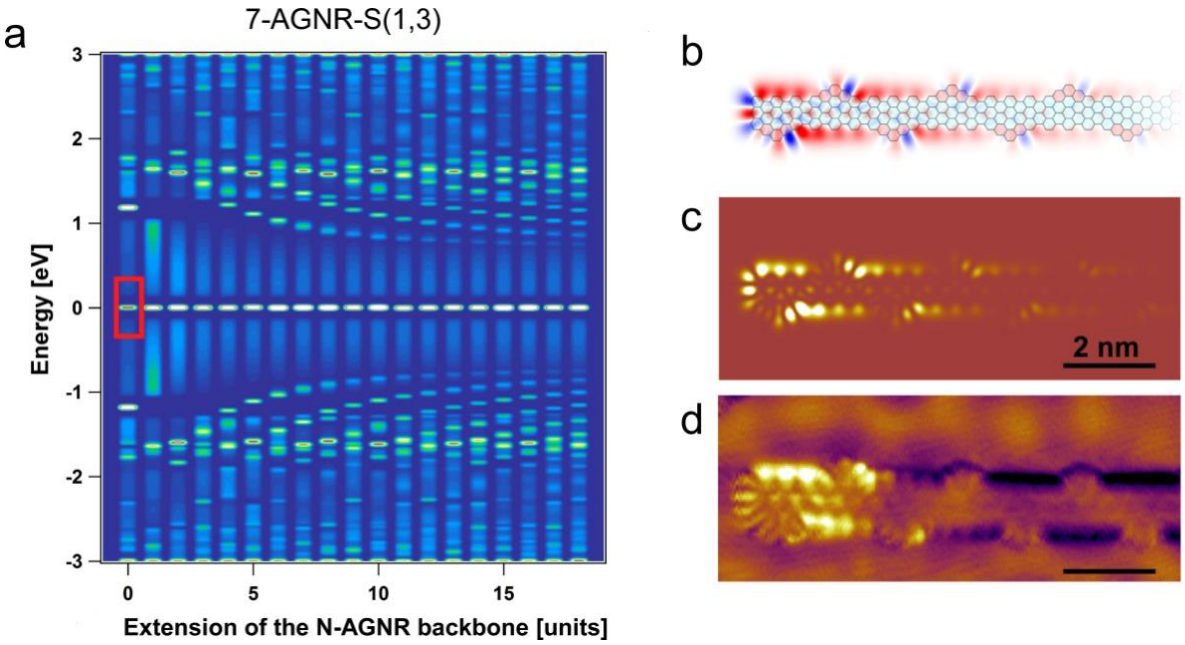

Figure S20. **a**, LDOS map of the 7-AGNR-*S*(1,3) structure at the zigzag terminus as a function of 7-AGNR backbone extension length. **b**, Wave function map of the E = 0 state for a 7-AGNR-*S*(1,3) (without backbone extension), and **c**, corresponding TB-STS simulation of the E = 0 state (marked by red rectangle in a)). **d**, Experimental d*I*/d*V* map acquired from a corresponding 7-AGNR-*S*(1,3) end segment at +0.15 eV (500 pA).

5. Magnetic properties of the edge-extended AGNRs

The zigzag edge structure at the boundary of the N-AGNR backbone and the edge-extended ribbon segments suggests the possibility of magnetic ordering of the corresponding boundary states. To explore this, Mean-Field Hubbard Tight-Binding (MFH-TB) calculations were carried out in the single-band scheme by considering only the nearest-neighbor hopping parameter γ_0 = 3 eV in the tight binding term of the Hamiltonian, and an on-site Coulomb repulsion $U = 1 * \gamma_0$.[9,10] Half filling, i.e. charge neutrality, was assumed for all calculations. The iterative self-consistent solution of the Hubbard Hamiltonian was initiated with a weak antiferromagnetic (AFM) bias on the zigzag edges of 0.05 μB per atom in all cases.

The localized nature of the spin-degenerate zero-energy junction states implies that they can be susceptible to Hubbard type splitting due to Coulombic electron-electron interaction. This energy splitting, which is the analogue of the opening of the Hubbard gap in regular zigzag edge GNRs, is accompanied with spin polarization of the corresponding states.[9] The effect is also analogous to the spin polarization occurring at the short zigzag ends of *N*-AGNRs for $N \geqslant 7$.[11]

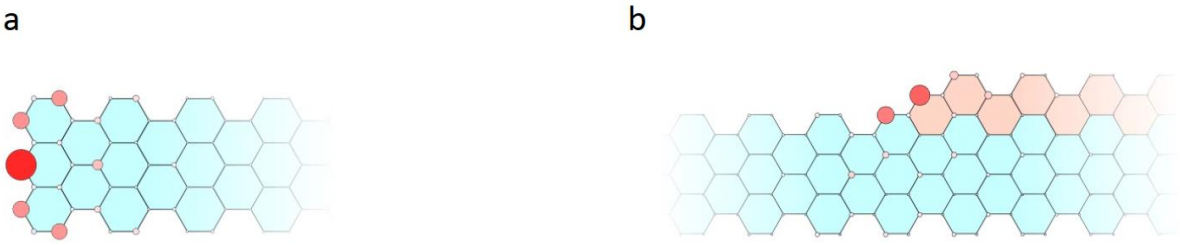

Figure S21. Spin polarization at **a**, the short zigzag end of a 7-AGNR, and **b**, at the 7-ANGR / 9-AGNR junction. Marker size denotes the absolute value of the spin polarization $|n_{i,\uparrow} - n_{i,\downarrow}|$

and marker color the relative value of the spin imbalance $\mu_i = \mu_i = n_{i,\uparrow} - n_{i,\downarrow}$ (red -1/3 μB to blue +1/3 μB).

For the two examples shown in Fig. S21 the maximum spin polarization occurs at the center of the 3 atom short zigzag edges and amounts to $|\mu_{max}| = 0.28\ \mu_B$ and $|\mu_{max}| = 0.20\ \mu_B$ for the pristine 7-AGNR end state (Fig. S21a) and the 7-AGNR – 9-AGNR boundary state (Fig. S21b), respectively. The total absolute spin anisotropy $\mu_{tot} = \sum|n_{i,\uparrow} - n_{i,\downarrow}|$ is $\mu_{tot} = 1.64\ \mu_B$ and $\mu_{tot} = 1.73\ \mu_B$ for the two cases. Here $n_{i,\uparrow}$ denotes the spin-up density on the atomic site i of the structure. The Hubbard energy splitting of the up- and down-spin localized state is 0.129 γ_0 and 0.070 γ_0, respectively.

This Hubbard type spin dependent energy splitting and the associated spin polarization of the boundary state is strongly suppressed upon hybridization with neighboring boundary states or metallic states. One should thus only expect sizeable spin polarization and energy splitting for $N = 3p + 1$ and large n and m.

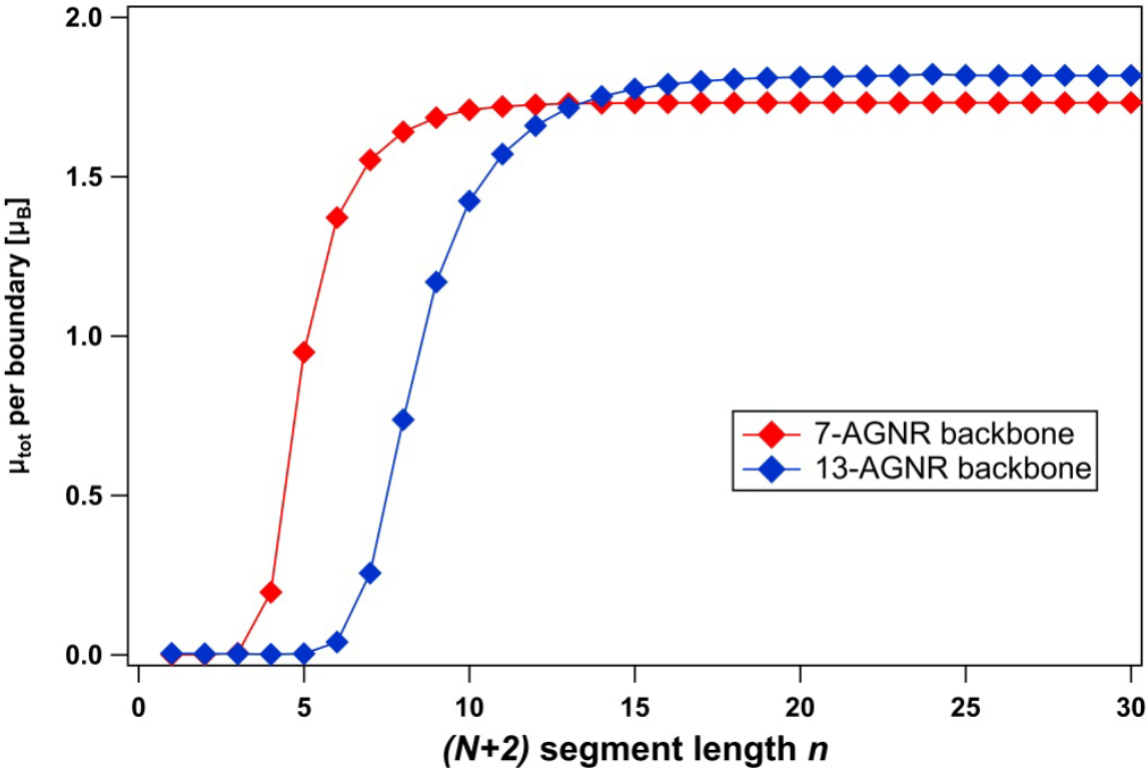

Figure S22. Total absolute magnetization μtot per N-AGNR / (N + 2)-AGNR boundary state as a function of segment length n with $m \sim \infty$ for a 7-AGNR (red) and a 13-AGNR backbone (blue).

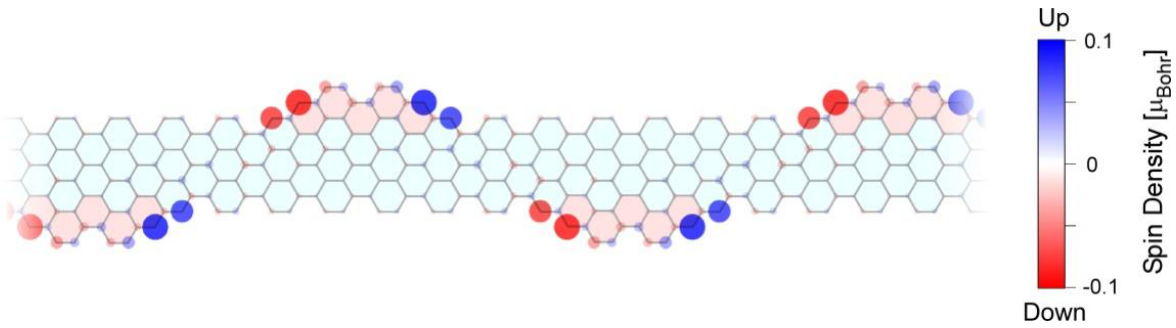

Figure S23. Spin polarization expressed by the spin-density ($n_\uparrow - n_\downarrow$) for the 7-AGNR-(2,4) with $U_C = 1.6 * \gamma_0$. Marker color and size denote the magnitude ($n_\uparrow - n_\downarrow$) and absolute magnitude ($|n_\uparrow - n_\downarrow|$) of the spin polarization.

Fig. S22 reveals that the interaction of the left and right boundary state for short (i.e. $n < 4$) edge-extended ($N + 2$)-AGNR segments is so strong that the Hubbard splitting is effectively suppressed, as evidenced by suppression of the spin polarization (for an on-site Coulomb repulsion chosen as $U_C = 1 * \gamma_0 = 3$ eV). This means that the experimentally realized structures ($n = 1$) are essentially non-magnetic, also if values of U_C up to $2\gamma_0$ are considered. For structures of larger n and m (i.e. smaller t_n and t_m), however, the system will exhibit spin polarization. Figure S23 shows the spin polarization of a 7-AGNR-(2,4) revealing formation of a staggered, antiferromagnetic spin chain for a high, yet not unrealistic[12] value of $U_C = 1.6 * \gamma_0$.

5. On-surface synthesis

Synthesis of the 7-AGNR-(1,3) and 7-AGNR-*I*(1,3) nanoribbon structures has been realized by means of dehalogenative aryl-aryl coupling and subsequent cyclodehydrogenation of the precursor monomers **1** and **3** (for details see section 7. "Precursor synthesis"), respectively, on a Au(111) surface under ultrahigh-vacuum conditions. The on-surface synthesis strategy is analogous to the one described by Cai et al.[13] for the synthesis of 7-AGNRs, but complemented by the use of methyl groups that undergo cyclization with the neighboring aromatic rings to form smooth zigzag edges.

Au(111) single crystal substrates were cleaned by standard argon ion sputtering and annealing cycles. Molecular precursors were sublimated using a homemade six-fold evaporator,

which allows sublimation of two molecules sequentially or at the same time. The deposition flux was around 2Å/min as determined by a quartz crystal microbalance.

7-AGNR-(1,3) nanoribbons were synthesized via a multiple step annealing process to achieve high-quality samples. The molecular precursor (monomer **1**, 6,11-bis(10-bromoanthracene-9-yl)-1,4-dimethyltetracene, BADMT) was deposited on a clean Au(111) substrate held at room temperature. Subsequently, the sample was annealed at 200° C, 250° C, 280° C and 400° C for 10 minutes at each temperature. This procedure results in the stepwise monomer activation (i.e., radical formation by dehalogenation), polymerization of the radical intermediates, and subsequent cylcodehydrogenation to form the fully conjugated AGNR structure. GNRs of lengths up to 60 nm with excellent quality could be grown on Au(111), as is illustrated in Fig S24.

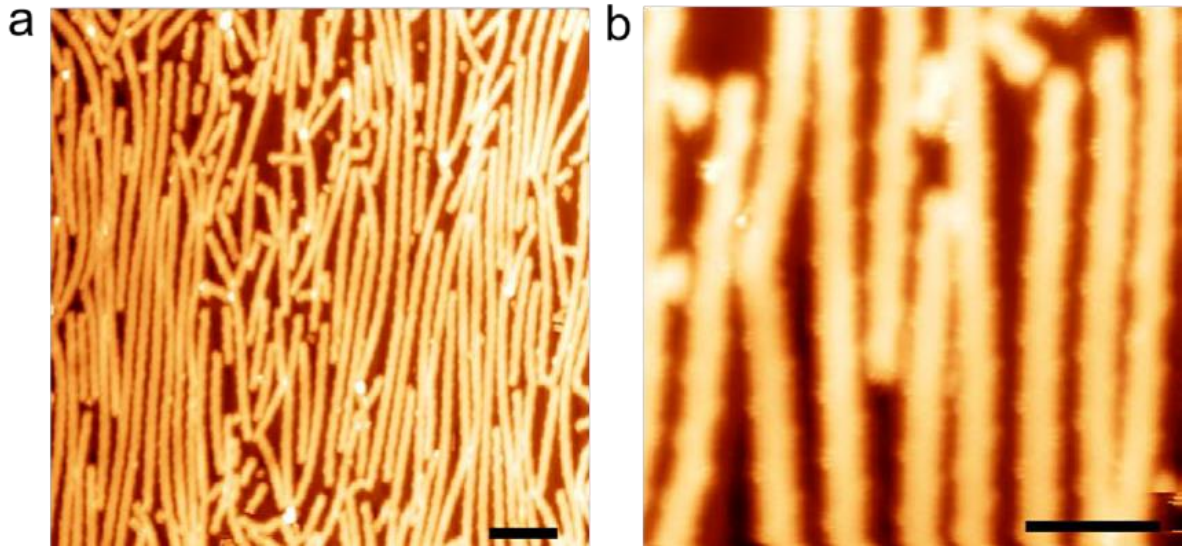

Figure S24. **a**, Large scale constant current STM image of 7-AGNR-*S*(1,3) ribbons grown on Au(111). Scale bar: 10 nm. **b**, Zoomed-in constant current STM image of 7-AGNR-*S*(1,3) ribbons. Scale bar: 5 nm.

Fig. S24 and Fig. S25 reveal that the alternating sequence of the dimethyltetracene units which leads to the staggered 7-AGNR-(1,3) structure is perfect. This indicates a very high conformational selectivity in the precursor coupling process, details of which will be discussed elsewhere.[14]

On-surface synthesis of backbone extended 7-AGNR / 7-AGNR-(1,3) heterostructures was achieved via sequential deposition of monomer **1** and monomer **2** (10,10'-dibromo-9,9'-bianthryl, DBBA). In a first step, monomer 1 was deposited on the Au(111) substrate held at

room temperature, followed by an annealing step at 150° C for 10 minutes. In a second step, monomer **2** was deposited onto the sample held at 150° C, followed by annealing steps at 200° C, 250° C, and 400° C for 10 minutes at each temperature. With this recipe, the 7-AGNR segments always locate at the termini of heterostructures, as seen in Fig. S25.

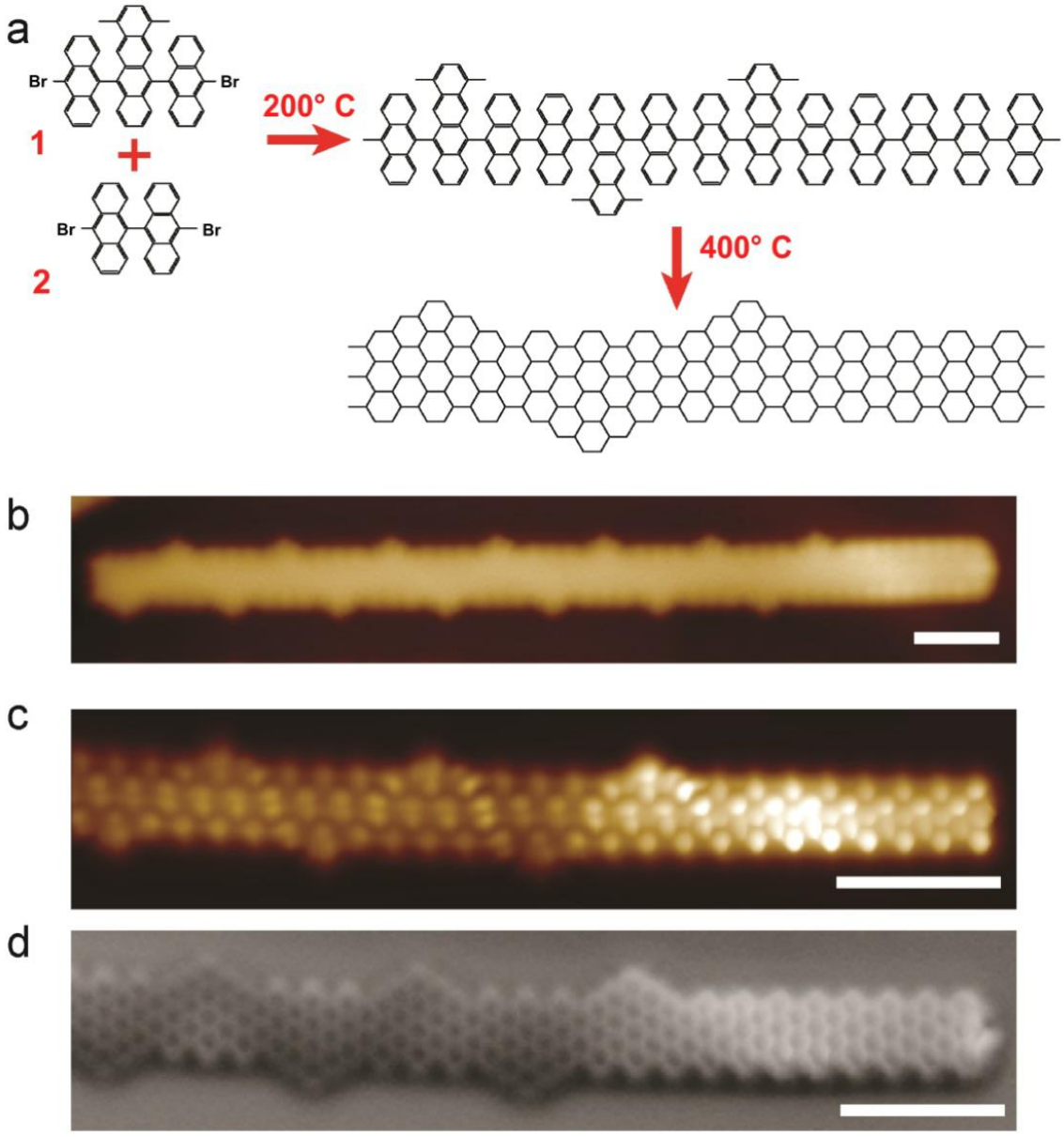

Figure S25. **a**, Schematic representation of the synthetic pathway to the backbone extended 7-AGNR – 7-AGNR-*S*(1,3) heterostructure. **b**, Constant-current STM image (−1.5 V / 10 pA) of a single 7-AGNR-*S*(1,3) ribbon whose right terminus is extended by a short 7-AGNR backbone segment. **c** and **d**, constant-height nc-AFM images of the tunneling current at 10 mV (c) and the frequency shift (d) of the hybrid structure in **b**. The scale bar is 2 nm in all panels.

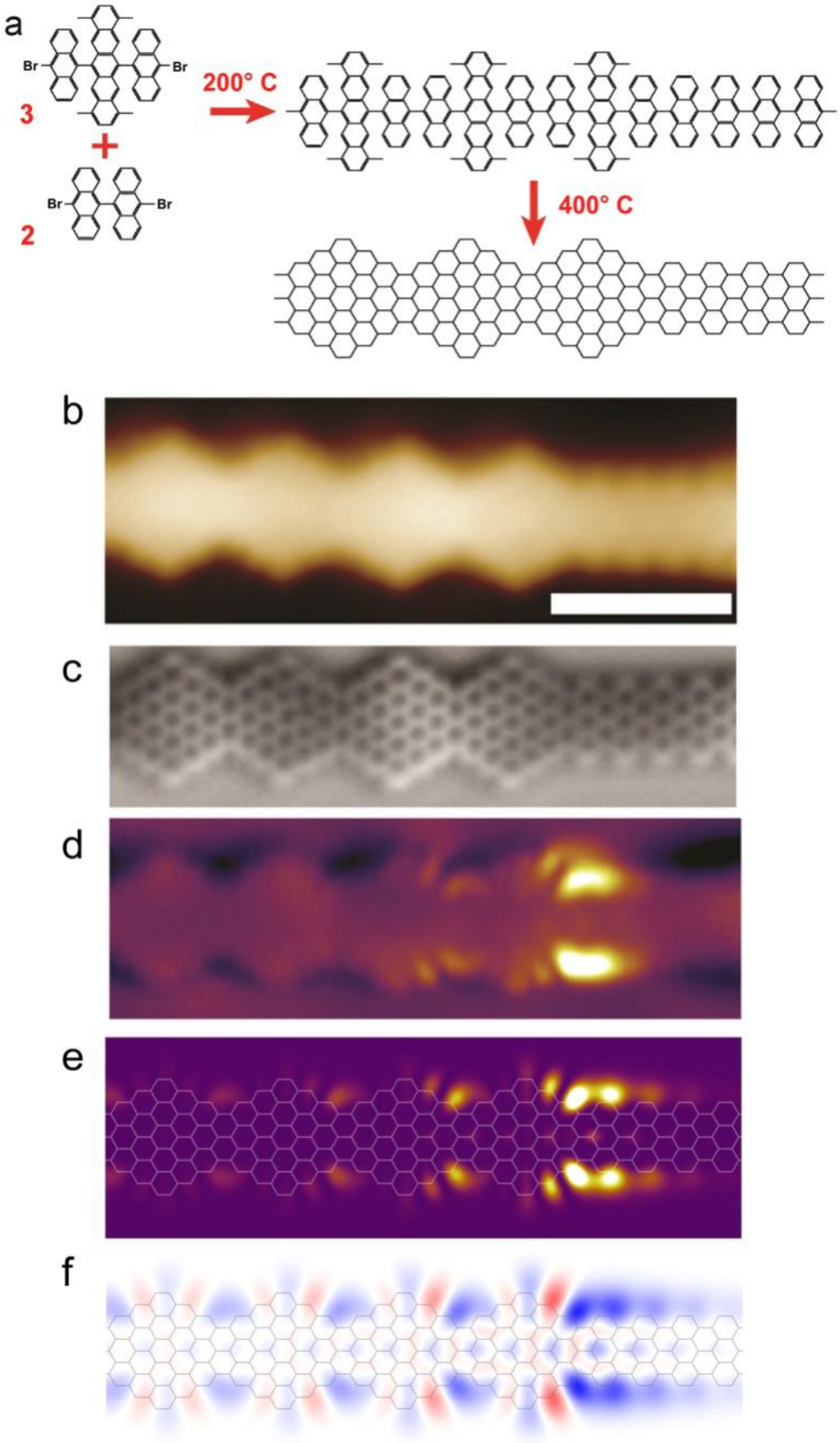
a
Br
Br
3
+
Br
Br
2
200° C
400° C
b
c
d
e
f

Figure S26. **a**, Schematic representation of the synthetic pathway for the backbone extended 7-AGNR – 7-AGNR-*I*(1,3) heterostructure. **b**, Constant-current STM image (10 mV / 50 pA) of a single 7-AGNR-*I*(1,3) ribbon whose right terminus is extended by a 7-AGNR backbone segment. **c**, Constant-height frequency shift nc-AFM image of the heterostructure shown in (a). **d**, Constant-current STS d*I*/d*V* map (at +0.25 V / 500 pA) of the topological end state. **e**, TB computed charge density map of the topological end state superimposed on a structural model. **f**, Wave function map associated with (e). The scale bar is 2 nm.

7-AGNR / 7-AGNR-(1,3) heterostructures were synthesized using the same recipe than the one described above for 7-AGNR / 7-AGNR-*S*(1,3) heterostructures, but with the precursor monomers **2** and **3** (6,13-bis(10-bromoanthracene-9-yl)-1,4,8,11-tetramethylpentacene, BATMP) (Fig. 26a). High resolution STM and nc-AFM images of a resulting heterostructure are shown in Figs. S26b and S26c, respectively. A high-resolution STS d*I*/d*V* map acquired at +0.15 V clearly reveals the topological end state at the terminus of the 7-AGNR-(1,3) (Fig. S26d). The corresponding TB simulation of the end state charge density (Fig. S26e) and the corresponding end state wave function (Fig. S26f) show excellent agreement with experimental data.

6. Raman characterization

Experimental Raman data from a sample of 7-AGNR-*S*(1,3) grown on Au(111) were obtained under ambient conditions using a Raman Bruker Senterra spectrometer (3 × 60 seconds, 2 mW) with an incident wavelength of 532 nm.

Raman modeling of the 7-AGNR-(1,3) was conducted with a combination of density functional theory (DFT) based calculations to determine the normal modes of the structure and of a bond-polarization model for the determination of Raman intensities. The DFT calculations were performed with the VASP package[15] using projector-augmented-wave (PAW) pseudopotentials, the Perdew−Burke−Ernzerhof (PBE) exchange-correlation functional [6] and a plane-wave cutoff energy of 400 eV. Prior to building the dynamical matrix for the calculation of phonons, all the atomic positions were relaxed until residual forces were below 0.001 eV/Å. Phonon calculations were performed utilizing the Phonopy package, written by

Atsushi Togo.[16] From the atomic positions and phonon normal mode information, non-resonant Raman spectrum intensities were calculated using an empirical bond-polarization model.[17]

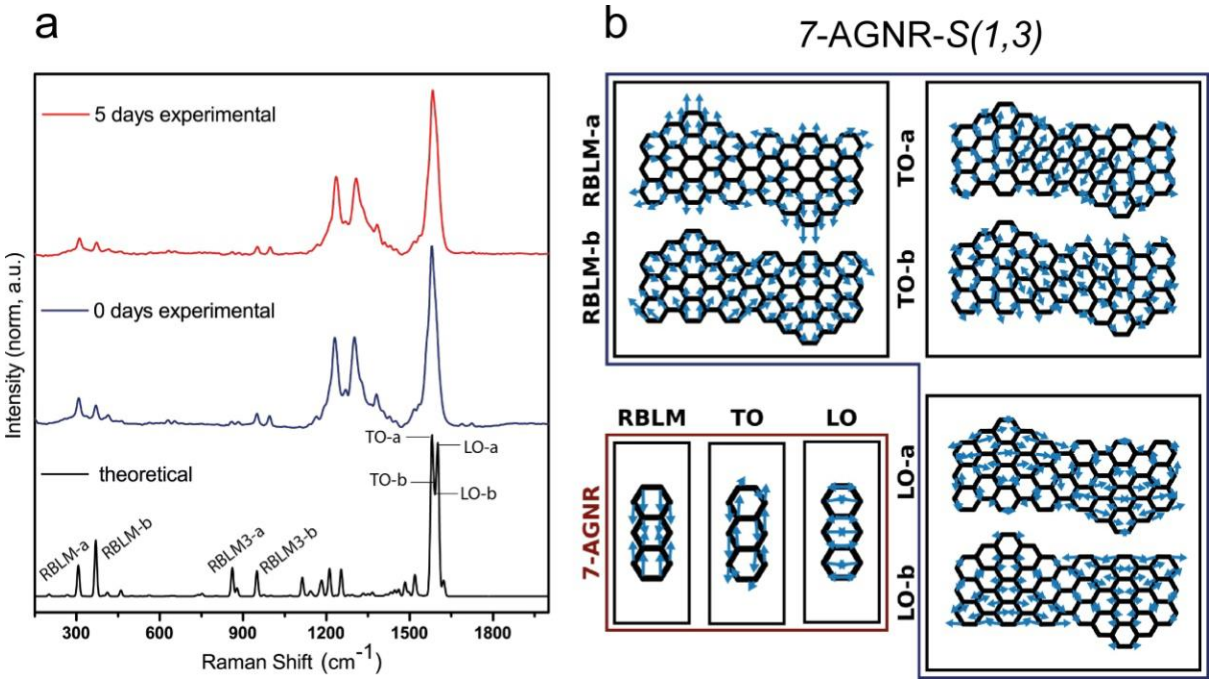

Figure S27. Raman analysis of the staggered edge-extended 7-AGNR-(1,3) ribbon structure. a, Comparison of DFT simulated spectrum (black curve) and experimental Raman spectra taken directly after growth (blue curve) and after 5 days in air (red curve). Both experimental and simulated spectra show multiple radial breathing like modes (RBLM) centered at about 300 cm^{-1} (experiment: 308 and 370 cm^{-1}; DFT: 307 and 370 cm^{-1}, labeled RBLM-a and RBLM-b) and a multitude of TO and LO mode analogues. These are located around 1580 cm^{-1} (experiment) and at 1579, 1587, 1595, and 1603 cm^{-1} (DFT) and labeled TO-a, TO-b, LO-a, and LO-b, respectively. These rich features are unique fingerprints of GNRs with non-trivial edge structure. The good agreement between experimental and theoretical data underlines the quality of the sample. A 5-day stability study proves the robustness of the 7-AGNR-(1,3) under ambient conditions, with no significant changes in the main Raman modes ("5-day experimental", measured under the same conditions as "0-day experimental"). b, Phonon mode schematics of selected Raman-active modes for the staggered edge-extended 7-AGNR-*S*(1,3) as well as for the pristine 7-AGNR for comparison.

7. Precursor synthesis

General: Column chromatography was conducted with silica gel (grain size 0.063–0.200 mm or 0.04–0.063 mm) and thin layer chromatography (TLC) was performed on silica gel-coated aluminum sheets with F254 indicator. Nuclear Magnetic Resonance (NMR) spectra were recorded on a Bruker Avance 300 MHz spectrometer. Chemical shifts were reported in ppm. Coupling constants (*J* values) are reported in Hertz. ^{1}H NMR chemical shifts were referenced to $C_2D_2Cl_4$ (6.00 ppm). ^{13}C NMR chemical shifts were referenced to $C_2D_2Cl_4$ (73.78 ppm). Abbreviations: s = singlet, d = doublet, dd = double doublet, t = triplet, m = multiplet. High-resolution mass spectrometry (HRMS) was performed on a SYNAPT G2 Si high-resolution time-of-flight mass spectrometer (Waters Corp., Manchester, UK) by matrix-assisted laser desorption/ionization (MALDI). Melting points were measured with a Büchi B-545 apparatus.

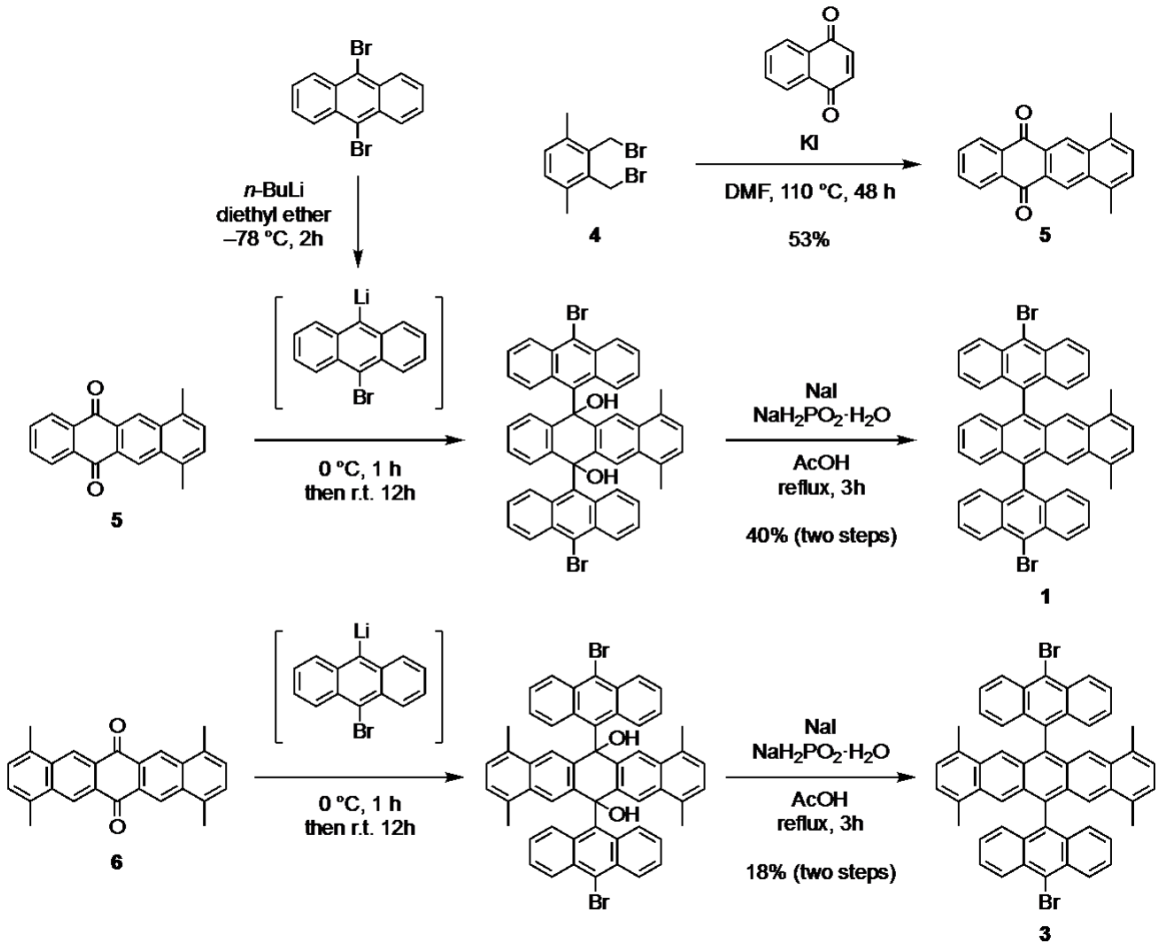

Scheme S1. Synthesis of monomers **1** and **3**.

Materials: All commercially available chemicals were purchased from TCI, Aldrich, Acros, Merck, and other commercial suppliers and used without further purification unless otherwise noted. Monomer **2** (10,10'-dibromo-9,9'-bianthryl) was synthesized according to our previous report [13]. 2,3-Bis(bromomethyl)-1,4-dimethylbenzene (**4**) and 1,4,8,11-tetramethyl-6,13-pentacenedione (**6**) were prepared following reported procedures.[18,19]

Synthesis of monomers 1 and 3

Monomers **1** and **3** were synthesized as shown in Scheme S1. 7,10-Dimethyltetracene-5,12-dione (**5**) was initially prepared through Diels–Alder cycloaddition of 1,4-napthoquinone and an *o*-quinodimethane in-situ generated from 2,3-bis(bromomethyl)-1,4-dimethylbenzene (**4**) through iodide-induced debromination.[18] Subsequently, **5** was reacted with 10-bromo-9-anthracenyllithium generated by mono-lithiation of 9,10-dibromoanthracene, followed by dehydroxylation with sodium iodide/sodium hypophosphite monohydrate to give monomer **1** in 40% yield over two steps. Synthesis of monomer **3** was conducted in a similar manner, through the reaction of 1,4,8,11-tetramethyl-6,13-pentacenedione (**6**)[19] with 10-bromo-9-anthracenyllithium, followed by the dehydroxylation to afford monomer **3** in 18% yield over two steps.

7,10-dimethyltetracene-5,12-dione (5)

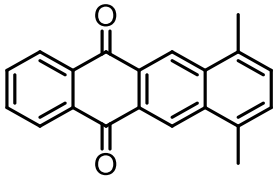

A mixture of 2,3-bis(bromomethyl)-1,4-dimethylbenzene (**4**) (3.00 g, 10.3 mmol), 1,4-naphthoquinone (1.62 g, 10.3 mmol) and KI (17.1 g, 103 mmol) in dry dimethylformamide (DMF) (50 mL) was stirred at 110 °C for 48 h. The reaction mixture was cooled to room temperature and then 100 mL of water was added. After filtration, the resulting precipitates were intensively washed with water, ethanol, ethyl acetate and hexane to obtain the title compound as an orange-yellow solid (1.54 g, 53% yield). M.p.: 273.4–274.6 °C. ^{1}H NMR (300 MHz, $C_2D_2Cl_4$, 298 K, ppm) δ 8.89 (d, J = 1.3 Hz, 2H), 8.32 (ddd, J = 5.9, 3.3, 1.3 Hz, 2H), 7.81 (ddd, J = 5.9, 3.3, 1.3 Hz, 2H), 7.36 (d, J = 1.3 Hz, 2H), 2.75 (d, J = 1.3 Hz, 6H); ^{13}C

NMR (75 MHz, $C_2D_2Cl_4$, 298 K, ppm) δ 183.09, 135.23, 134.73, 134.35, 134.27, 130.22, 128.70, 127.37, 126.28, 19.48. HRMS (MALDI-TOF, positive) *m/z*: Calcd for $C_{20}H_{14}O_2$: 286.0994; Found: 286.0989 $[M]^+$.

6,11-bis(10-bromoanthracen-9-yl)-1,4-dimethyltetracene (1)

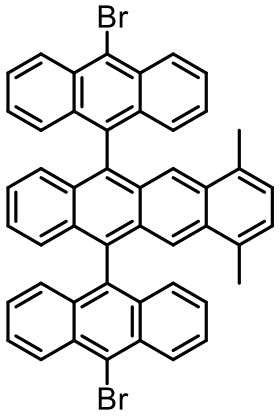

To a suspension of 9,10-dibromoanthracene (1.01 g, 3.00 mmol) in dry diethyl ether (30 mL) was added a solution of *n*-Butyllithium (*n*-BuLi) (1.5 mL, 2.4 mmol, 1.6 M in hexanes) dropwise at –78 °C. The reaction mixture was stirred for 2 h under argon to obtain an orange solution of 10-bromo-9-anthracenyllithium. To a suspension of 7,10-dimethyltetracene-5,12-dione (**7**) (258 mg, 0.900 mmol) in 20 mL of dry diethyl ether was added at 0 °C the separately prepared solution of 10-bromo-9-anthracenyllithium via a double-tipped needle under argon. The reaction mixture was stirred for 1 h at this temperature, and then allowed to gradually warm to room temperature. After stirring for 12 h, the reaction was quenched by adding 3 mL of glacial acetic acid. The precipitates were then collected by filtration and washed with diethyl ether. To the resulting crude material placed in a 100-mL round-bottom flask was added glacial acetic acid (45 mL), NaI (1.35 g, 9.00 mmol) and $NaH_2PO_2 \cdot H_2O$ (1.43 g, 13.5 mmol). The reaction mixture was refluxed for 3 h under the exclusion of light. After cooling down to room temperature, the precipitates were collected by filtration, and then washed with water and methanol to afford analytically pure monomer **1** as an orange solid (288 mg, 40% yield). For the on-surface experiments, further purification was performed by recrystallization through slow diffusion of degassed methanol into a degassed solution of **1** in dichloromethane under argon, which was repeated 8 times. M.p.: >315 °C. ^{1}H NMR (300 MHz, $C_2D_2Cl_4$, 298 K, ppm) δ 8.80 (d, J = 9.1 Hz, 4H), 7.99 (s, 2H), 7.71 – 7.67 (m, 4H), 7.39 (d, J = 8.8 Hz, 4H), 7.33 (dt,

J = 9.9, 4.6 Hz, 4H), 7.22 (d, *J* = 8.1 Hz, 2H), 7.09 (d, *J* = 8.2 Hz, 2H), 6.91 (s, 2H), 2.01 (s, 6H); ^{13}C NMR (75 MHz, $C_2D_2Cl_4$, 298 K, ppm) δ 132.48, 130.53, 128.14, 127.46, 127.16, 126.55, 125.85, 125.66, 123.18, 19.15. HRMS (MALDI-TOF, positive) *m/z*: Calcd for $C_{48}H_{30}Br_2$: 764.0714; Found: 764.0705 $[M]^+$.

6,13-bis(10-bromoanthracen-9-yl)-1,4,8,11-tetramethylpentacene (3)

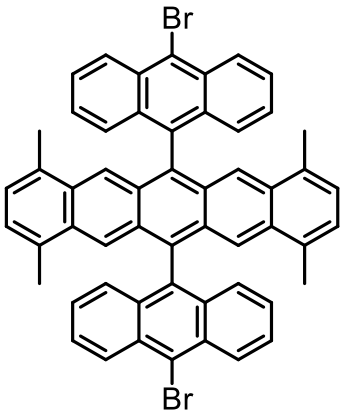

To a suspension of 9,10-dibromoanthracene (300 mg, 0.893 mmol) in dry diethyl ether (20 mL) was added a solution of *n*-BuLi (0.45 ml, 0.72 mmol, 1.6 M in hexanes) dropwise at –78 °C. The reaction mixture was stirred for 2 h under argon to obtain an orange solution of 10-bromo-9-anthracenyllithium. To a suspension of 1,4,8,11-tetramethyl-6,13-pentacenedione (**6**) (97.6 mg, 0.268 mmol) in 10 mL of dry diethyl ether was added at 0 °C the separately prepared solution of 10-bromo-9-anthracenyllithium via a double-tipped needle under argon. The reaction mixture was stirred for 1 h at this temperature, and then allowed to gradually warm to room temperature. After stirring for 12 h, the reaction was quenched by adding 5 mL of glacial acetic acid. The precipitates were then collected by filtration and washed with diethyl ether. To the resulting crude material placed in a 100-mL round-bottom flask was added glacial acetic acid (30 mL), NaI (405 mg. 2.70 mmol) and $NaH_2PO_2 \cdot H_2O$ (429 mg. 4.05 mmol). The reaction mixture was refluxed for 3 h under the exclusion of light. After cooling down to room temperature, the precipitates were collected by filtration, and then washed with water and methanol to afford analytically pure monomer **3** as a dark blue solid (140 mg, 18% yield). For the on-surface experiments, further purification was performed by recrystallization through slow diffusion of degassed methanol into a degassed solution of **3** in chloroform under argon, which was repeated 7 times. M.p.: >315 °C. ^{1}H NMR (300 MHz, $C_2D_2Cl_4$, 298 K, ppm) δ 8.82

(d, *J* = 8.9 Hz, 2H), 7.98 (s, 2H), 7.68 (t, *J* = 7.8 Hz, 2H), 7.38 (d, *J* = 8.8 Hz, 2H), 7.29 (t, *J* = 7.7 Hz, 2H), 6.85 (s, 2H), 1.99 (s, 6H); ^{13}C NMR (75 MHz, $C_2D_2Cl_4$, 298 K, ppm) δ 132.50, 130.52, 128.09, 127.65, 127.40, 126.51, 125.56, 123.04, 19.12. HRMS (MALDI-TOF, positive) *m/z*: Calcd for $C_{54}H_{36}Br_2$: 842.1184; Found: 842.1197 $[M]^+$.

Single crystal X-ray diffraction analysis

The single crystal of **1** suitable for X-ray analysis was obtained by slow diffusion of degassed methanol into a degassed solution of **1** in dichloromethane under argon and exclusion of light.

Crystal data

formula	$C_{48}H_{30}Br_2$
molecular weight	766.54 $gmol^{-1}$
absorption	μ = 2.049 mm^{-1} correction with 7 crystal faces
transmission	Tmin = 0.7275, Tmax = 0.9053
crystal size	0.06 x 0.06 x 0.24 mm^3 brown needle
space group	P 2_1/n (monoclinic)
lattice parameters	a = 9.0127(6)Å
(calculate from	b = 23.8476(11)Å ß = 93.029(6)°
14422 reflections with	c = 18.7144(13)Å
2.2° < θ < 28.1°)	V = 4016.7(4)Å^3 z = 4 F(000) = 1552
temperature	-80°C
density	d_{xray} = 1.268 gcm^{-3}

data collection

diffractometer	STOE IPDS 2T
radiation	Mo-K_α Graphitmonochromator
Scan – type	ω scans
Scan – width	1°
scan range	2° ≤ θ < 28°
	-11 ≤ h ≤ 9 -31 ≤ k ≤ 27 -24 ≤ l ≤ 24
number of reflections:	
measured	22569
unique	9881 (R_{int} = 0.0688)
observed	4323 (|F|/σ(F) > 4.0)

data correction, structure solution and refinement

corrections	Lorentz and polarisation correction.
Structure solution	Program: SIR-2004 (Direct methods)
refinement	Program: SHELXL-2014 (full matrix). 454 refined parameters, weighting scheme: $w = 1/[\sigma^2(F_o^2) + (0.1088*P)^2]$ with $(Max(F_o^2,0)+2*F_c^2)/3$. H-atoms at calculated

	positions and refined with isotropic displacement parameters, non H- atoms refined anisotropically.
R-values	wR2 = 0.22 (R1 = 0.0687 for observed reflections, 0.1593 for all reflections)
goodness of fit	S = 0.943
maximum deviation of parameters	0.001 * e.s.d
maximum peak height in diff. Fourier synthesis	0.65, -0.89 eÅ^{-3}
remark	structure contains two molecule CH_2Cl_2 which are completely disordered – SQUEEZE was used

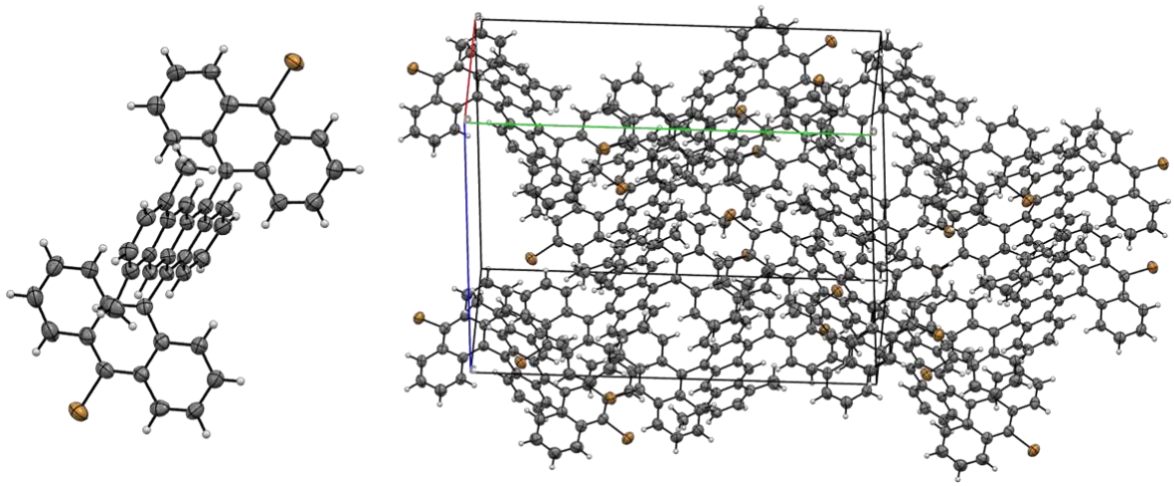

Figure S28. X-ray single-crystal analysis of **1** (ORTEP drawings with thermal ellipsoids set at 50% probability). Bromine atoms are labelled in brown.

The single crystal of **3** suitable for X-ray analysis was obtained by slow diffusion of degassed methanol into a degassed solution of **3** in chloroform under argon and exclusion of light .

Crystal data

formula	$C_{54}H_{36}Br_2$, 1($CHCl_3$)		
molecular weight	1083.38 gmol^{-1}		
absorption	μ = 2.129 mm^{-1} correction with six crystal faces		
transmission	T_{min} = 0.480, T_{max} = 0.934		
crystal size	0.04 x 0.05 x 0.64 mm^3 brown needle		
space group	P -1 (triclinic)		
lattice parameters	a = 8.4370(6)Å	α = 113.069(5)°	
(calculate from	b = 12.4974(8)Å	ß = 103.666(5)°	
7729 reflections with	c = 13.0211(8)Å	γ = 101.311(6)°	
2.6° < θ < 28.4°)	V = 1161.63(14)Å^3	z = 1	F(000) = 546
temperature	-80°C		
density	d_{xray} = 1.549 gcm^{-3}		

data collection	
diffractometer	STOE IPDS 2T
radiation	Mo-K_α Graphitmonochromator
Scan – type	ω scans
Scan – width	1°
scan range	$2° \leq \theta < 28°$ $-11 \leq h \leq 10 \quad -16 \leq k \leq 16 \quad -17 \leq l \leq 17$
number of reflections:	
measured	11053
unique	5729 ($R_{int} = 0.0448$)
observed	3711 ($\|F\|/\sigma(F) > 4.0$)
data correction, structure solution and refinement	
corrections	Lorentz and polarisation correction.
Structure solution	Program: SIR-2004 (Direct methods)
refinement	Program: SHELXL-2014 (full matrix). 291 refined parameters, weighting scheme: $w = 1/[\sigma^2(F_o^2) + (0.0477*P)^2+3.26*P]$ with $(Max(F_o^2,0)+2*F_c^2)/3$. H-atoms at calculated positions and refined with isotropic displacement parameters, non H- atoms refined anisotropically.
R-values	wR2 = 0.1483 (R1 = 0.0576 for observed reflections, 0.1064 for all reflections)
goodness of fit	S = 1.034
maximum deviation of parameters	0.001 * e.s.d
maximum peak height in diff. Fourier synthesis	0.51, -0.55 $eÅ^{-3}$
remark	crystal contains two molecules of solvents per main molecule,which has Ci symmetry

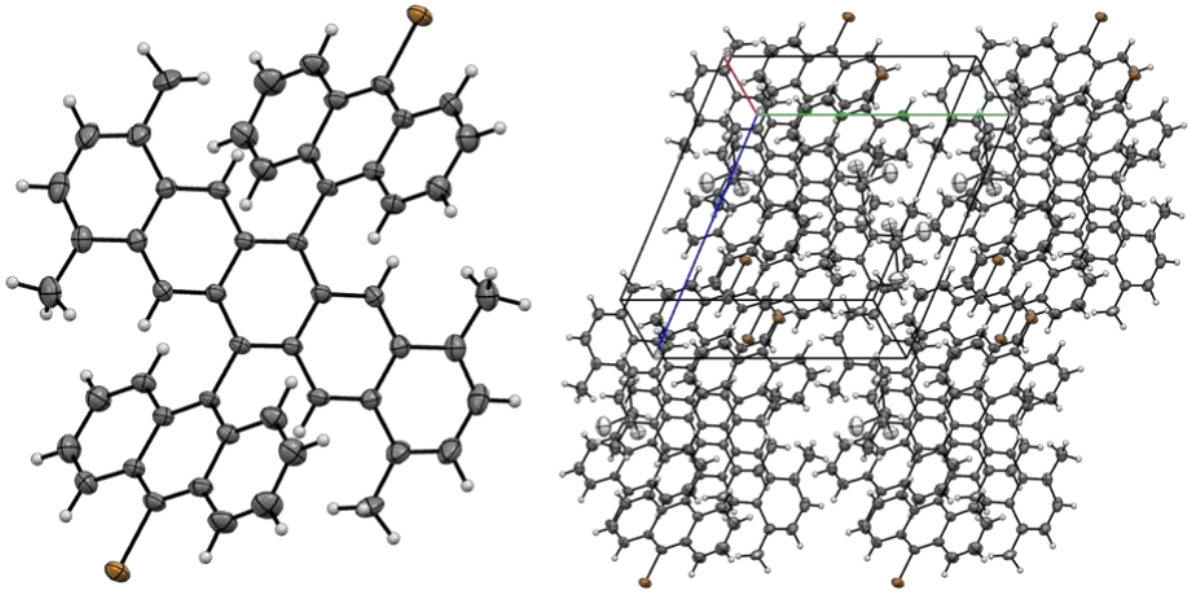

Figure S29. X-ray single-crystal analysis of **3** (ORTEP drawings with thermal ellipsoids set at 50% probability). Solvent molecules ($CHCl_3$) are omitted for clarity. Bromine atoms are labelled in brown.

NMR and mass spectra

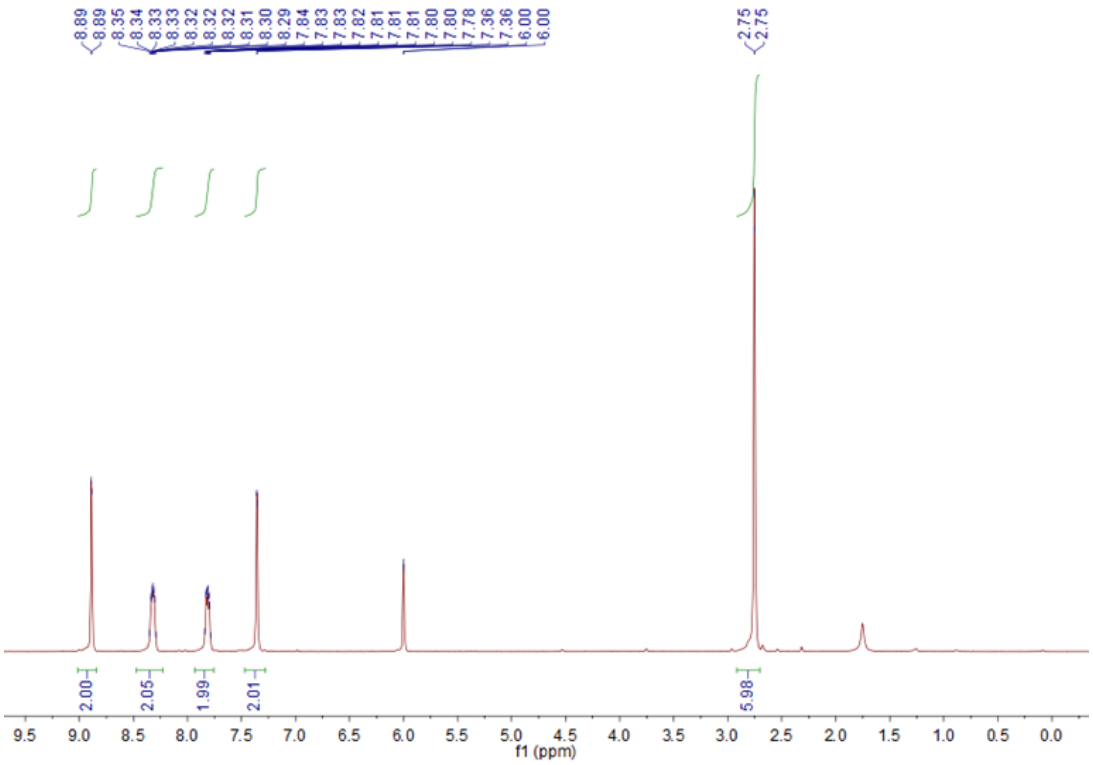

Figure S23. ^1H NMR spectrum of **5** (300 MHz, $C_2D_2Cl_4$, 298 K).

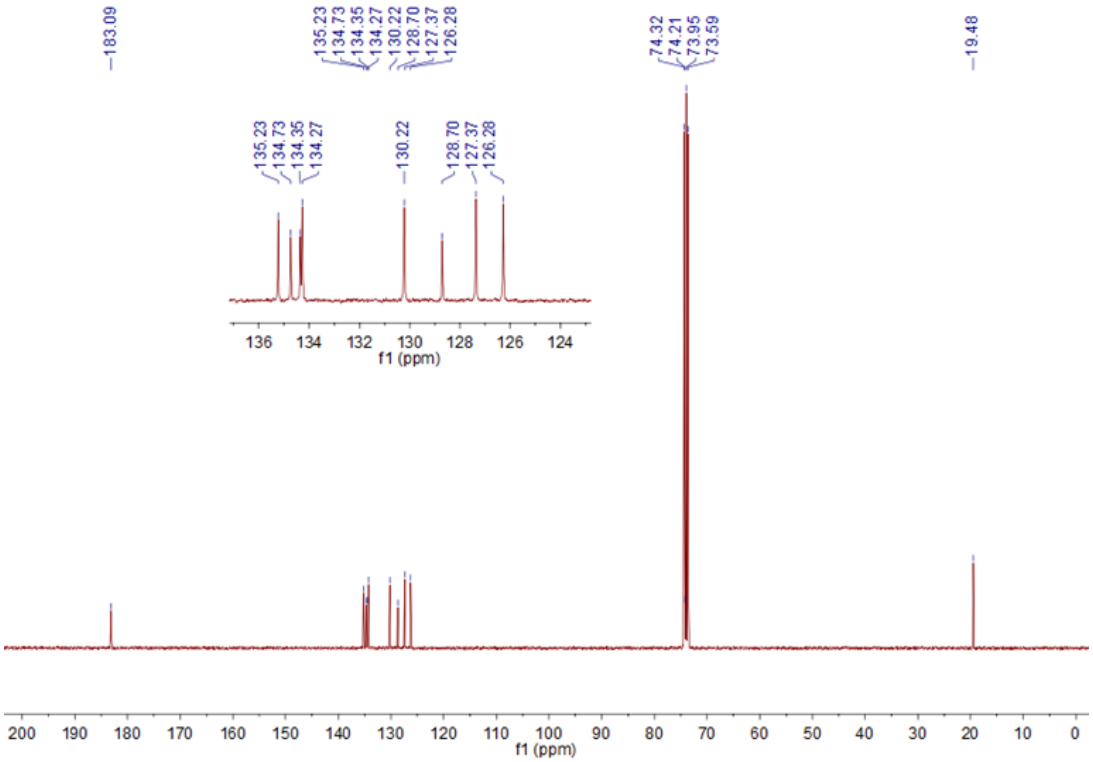

Figure S24.[13]C NMR spectrum of **5** (75 MHz, $C_2D_2Cl_4$, 298 K).

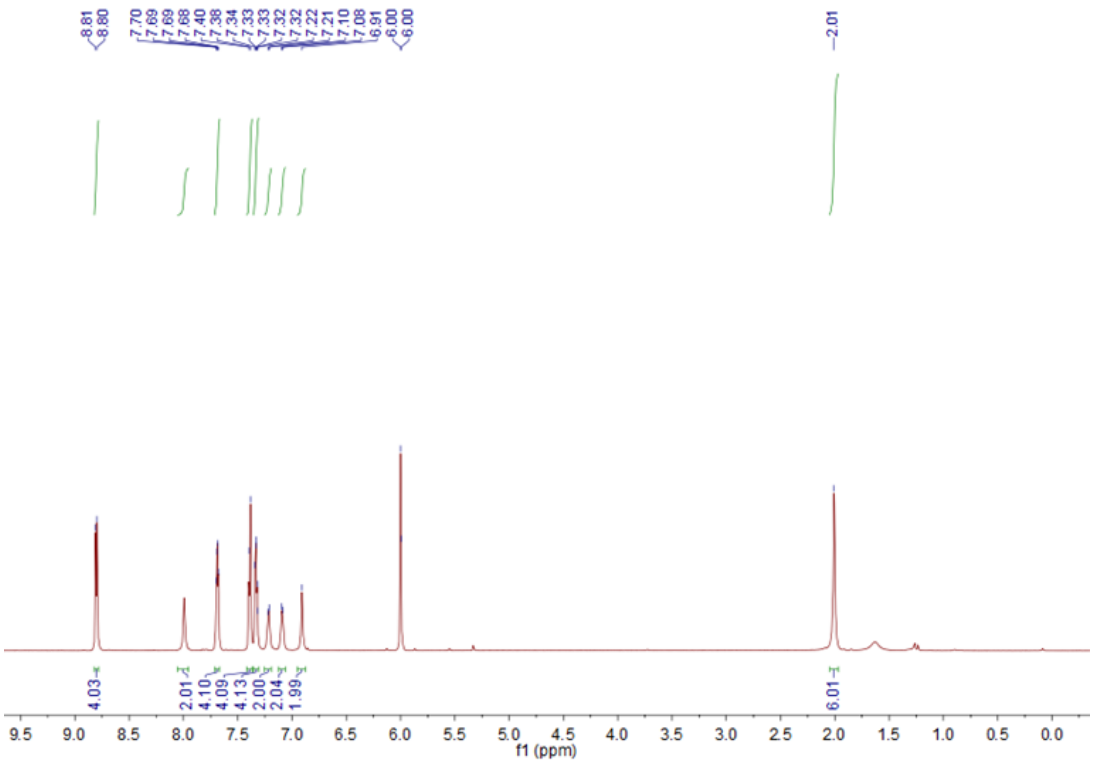

Figure S25. [1]H NMR spectrum of monomer **1** (300 MHz, $C_2D_2Cl_4$, 298 K).

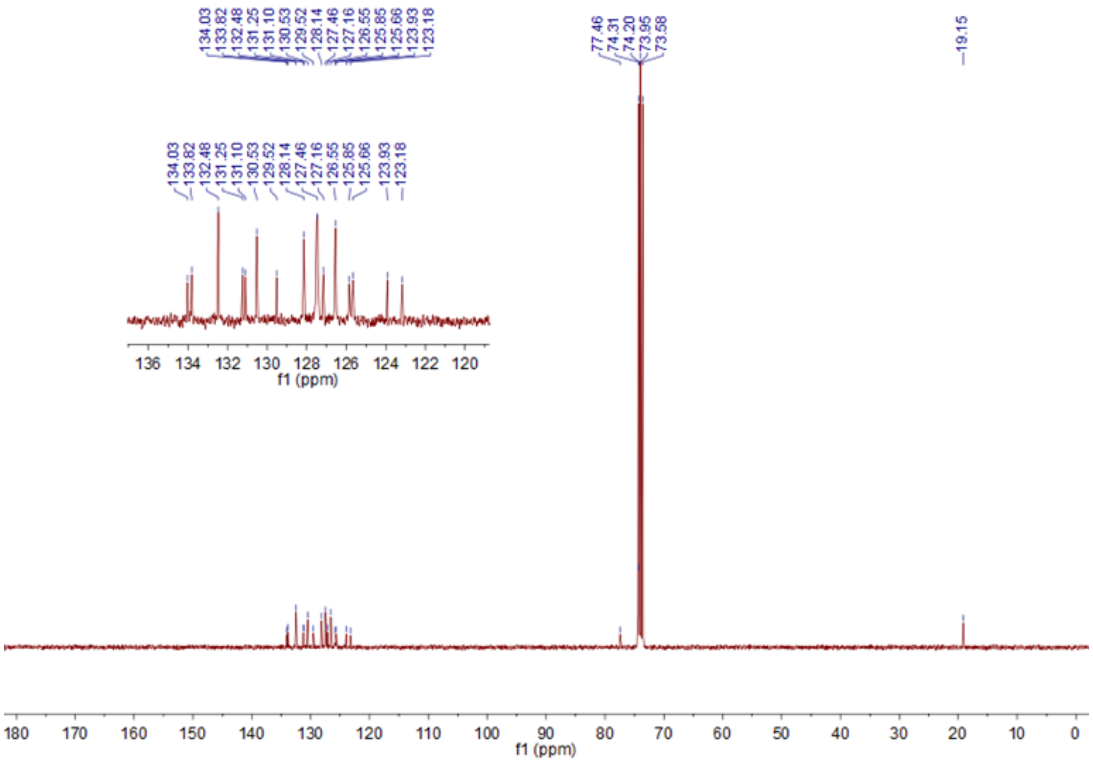

Figure S26.[13]C NMR spectrum of monomer **1** (75 MHz, $C_2D_2Cl_4$, 298 K).

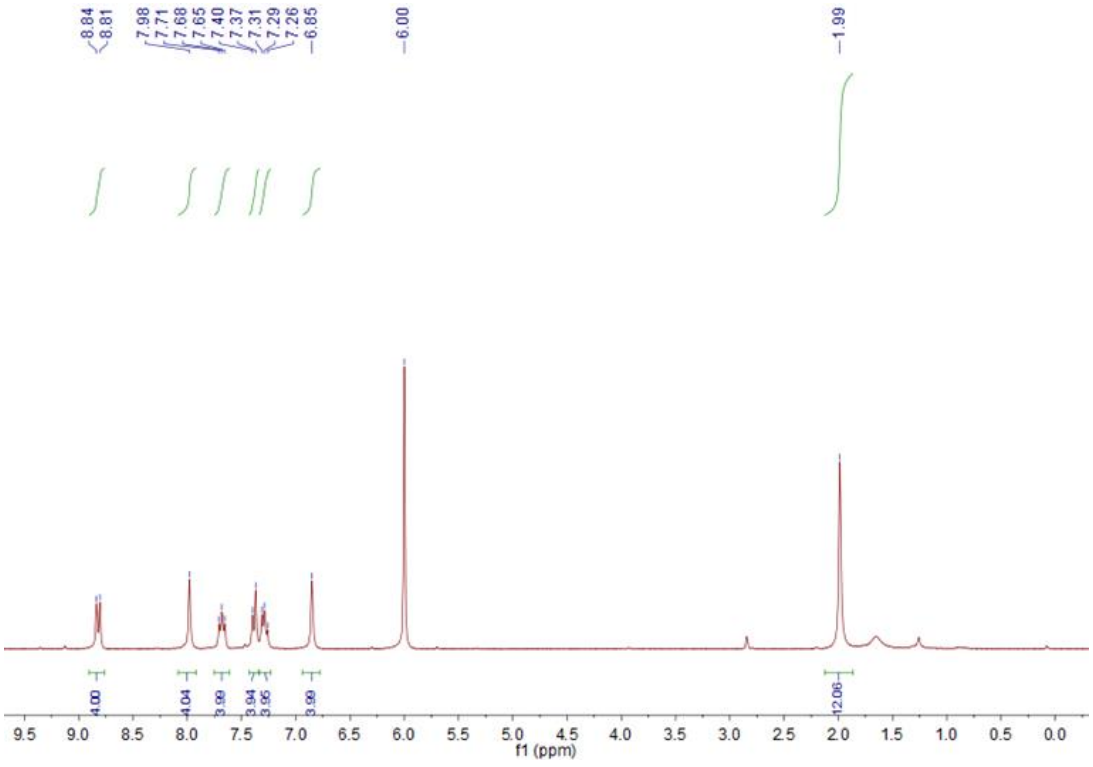

Figure S27. [1]H NMR spectrum of monomer **3** (300 MHz, $C_2D_2Cl_4$, 298 K).

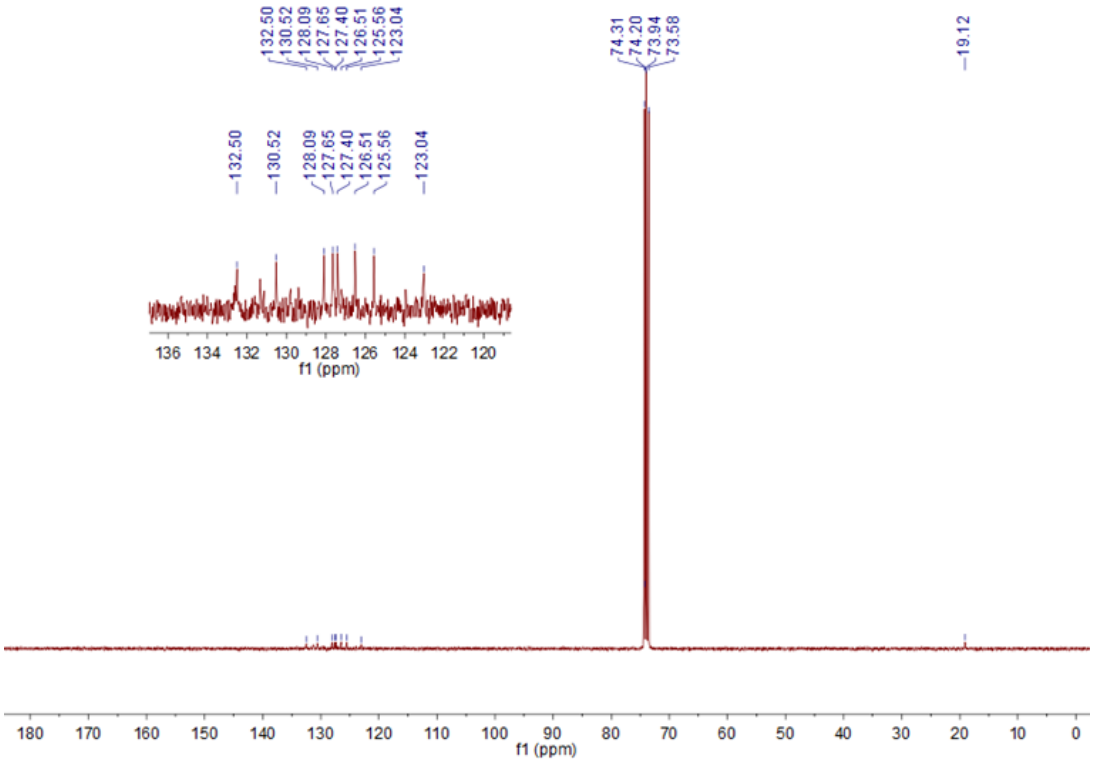

Figure S28.[13]C NMR spectrum of monomer **3** (75 MHz, $C_2D_2Cl_4$, 298 K).

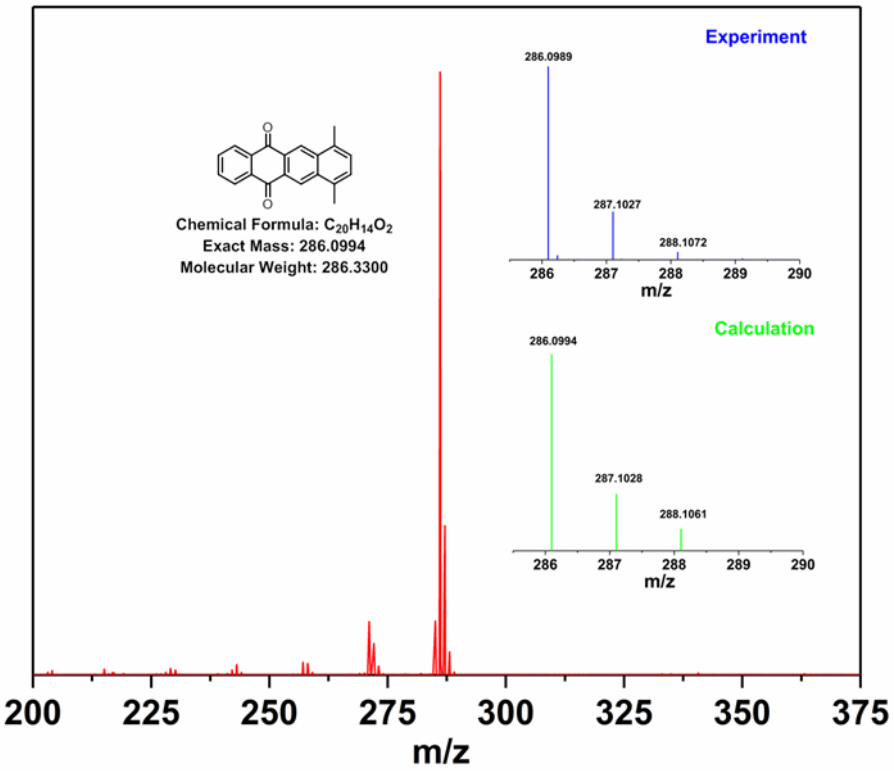

Figure S29. High-resolution MALDI-TOF mass spectrum of **7**. Inset displays the isotopic distribution in comparison to the simulated pattern.

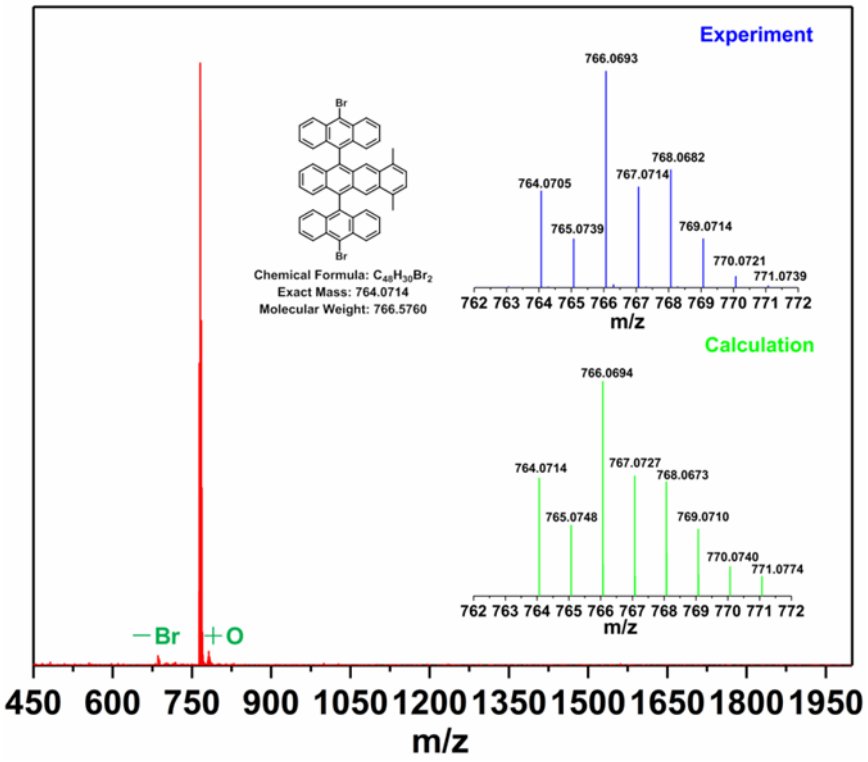

Figure S30. High-resolution MALDI-TOF mass spectrum of monomer **1**. Two small signals from $[M–Br]^+$ and $[M + O]^+$ were also detected most probably due to debromination and oxidation, respectively, under the measurement condition or during sample preparation. Inset displays the isotopic distribution in comparison to the simulated pattern.

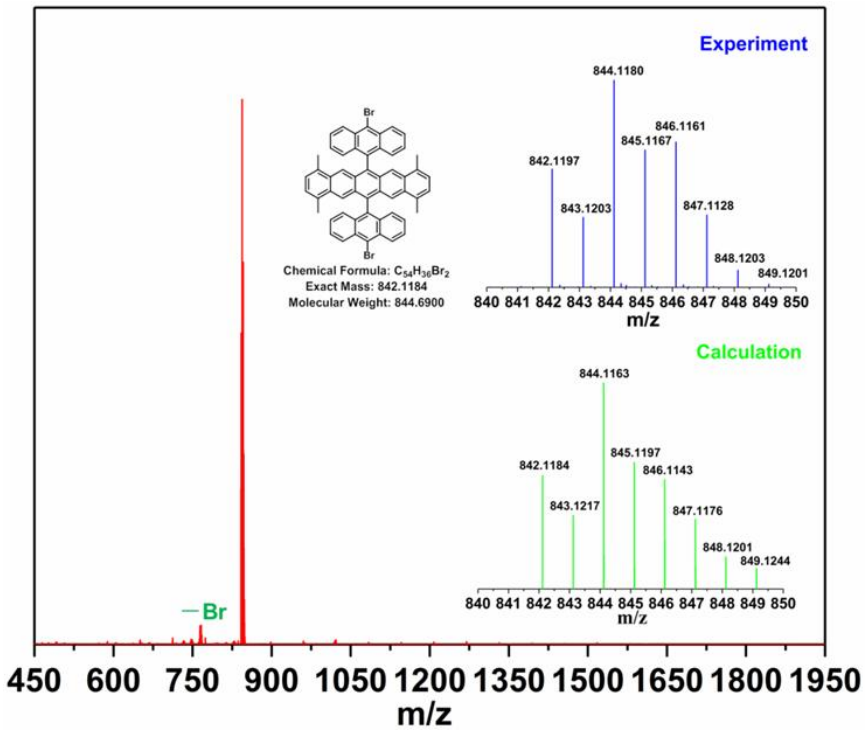

Figure S31. High-resolution MALDI-TOF mass spectrum of monomer **3**. A small signal from $[M–Br]^+$ was also detected most probably due to debromination under the measurement condition. Inset displays the isotopic distribution in comparison to the simulated pattern.

References

[1] K. Wakabayashi, K. Sasaki, T. Nakanishi and T. Enoki. *Sci. Technol. Adv. Mater.* **2010**, *11*, 054504.

[2] M. Ezawa, Y. Tanaka and N. Nagaosa. *Sci. Rep.* **2013**, *3*, 2790.

[3] T. Cao, F. Zhao and S. G. Louie. *Phys. Rev. Lett.* **2017**, *119*, 076401.

[4] W. Su, J. R. Schrieffer and A. J. Heeger. *Phys. Rev. Lett.* **1979**, *42*, 1698–1701.

[5] P. Giannozzi1, S. Baroni, N. Bonini, M. Calandra, R. Car, C. Cavazzoni, D. Ceresoli, G. L Chiarotti, M. Cococcioni, I. Dabo, A. D. Corso, S. de Gironcoli, S. Fabris, G. Fratesi, R.Gebauer, U. Gerstmann, C. Gougoussis, A. Kokalj, M. Lazzeri, L. Martin-Samos, N. Marzari, F. Mauri, R. Mazzarello, S. Paolini, A. Pasquarello, L. Paulatto, C. Sbraccia, S. Scandolo1, G. Sclauzero, A. P. Seitsonen, A. Smogunov, P. Umari and R. M Wentzcovitch. *J. Phys.: Condens. Matt*er **2009**, *21*, 395502.

[6] J. P. Perdew, K. Burke and M. Ernzerhof. *Phys. Rev. Lett.* **1996**, ***77***, 3865–3868.

[7] I. E. Castelli, I.E., et al. http://materialscloud.org/sssp, in preparation (2018).

[8] G. Pizzi, A. Cepellotti, R. Sabatini, N. Marzari and B. Kozinsky. *Comput. Mater. Sci.* **2016**, *111*, 218–230.

[9] A. Yamashiro, Y. Shimoi, K. Harigaya and K. Wakabayashi. *Phys. Rev. B* 2003, *68*, 193410.

[10] O. V. Yazyev. *Phys. Rev. Lett.* **2008**, *101*, 037203.

[11] S. Wang, L. Talirz, C. A. Pignedoli, X. Feng, K. Müllen, R. Fasel and P. Ruffieux. *Nature Commun.* **2016**, ***7***, 11507.

[12] P. P. Shinde, O. Gröning, S. Wang, P. Ruffieux, C. A.Pignedoli, R. Fasel, D. Passerone. *Carbon* **2017**, *124*, 123.

[13] J. Cai, P. Ruffieux, R. Jaafar, M. Bieri, T. Braun, S. Blankenburg, M. Muoth, A. P. Seitsonen, M. Saleh, X. Feng, K. Müllen and R. Fasel. *Nature* **2010**, *466*, 470–473.

[14] S. Wang et al. Molecular steric hindrance induced selectivity of on-surface reaction paths. To be published (2018).

[15] G. Kresse, J. Furthmüller. *Comput. Mater. Sci.* **1996**, *6*, 15−50.

[16] A Togo, A. and I. Tanaka. *Scr. Mater.* **2015**, *108*, 1–5.

[17] S. Guha, J. Menéndez, J. B. Page, and G. B. Adams. *Phys. Rev. B* **1996**, *53*, 13106–13114.

[18] C. Kitamura, T. Naito, A. Yoneda, T. Kawase and T. Komatsu. *Chem Lett.* **2010**, *39*, 771-773.

[19] G. R. Llorente., M.-B. Dufourg-Madec, D J. Crouch, R. G. Pritchard, S. Ogier and S. G. Yeates. *Chem. Comm.* **2009**, 3059-3061.

Chapter 5 Summary and future outlook

For both PAHs and GNRs, size and edge structure serve as two crucial ingredients in modulation of electronic properties. According to this motif, a serious of PAHs and GNRs with different peripheral structures have been fabricated via bottom-up strategies. Intriguing properties have been revealed by combination of various techniques, such as transient absorption spectroscopy and scanning probe techniques. Most importantly, those works unequivocally revealed a tight connection between edge structure and property in PAHs and GNRs.

In chapter 2, a tandem demethylation-electrophilic borylation method was developed to furnish the first oxaborin-annelated pyrene derivatives, featuring OBO-doped peripheries. The extended π-conjugation at the non-K-region of pyrene with multiple heteroatoms showed a significant impact on both the optical and electronic properties, as well as self-assembly behaviour in solution. The favourable fluorescence property makes the oxaborin-annelated pyrene derivatives an interesting new chromophore for optical studies. Furthermore, charge transport measurements illustrated p-type semiconducting behaviour.

Heteroatom-doping of PAHs and GNRs provides numerous opportunities to tune molecular properties and raises many challenges in synthesis. Thus, the development of novel and efficient synthetic methods has always been urgently needed, including precise and concentration-controllable doping strategies. Besides, there is an inadequate development in the research of catalytic activity of PAHs and GNRs featuring edge doped or basal plane doped structures. Moreover, as mentioned before, the full zigzag GNRs carry spin-polarized states which makes them unlikely to exist under ambient conditions, its application in devices is thus inevitably hindered. The demonstration of stabilization effects of heteroatoms in PAHs with zigzag periphery may provide new ideas for achieving a heteroatom-doped full zigzag GNRs. In general, examples of PAHs and GNRs with heteroatom-doped peripheral structures are still scarce, and there is much space to explore new structures and properties.

In chapter 3, a "π-truncation" strategy, namely, regioselective hydrogenation, was developed as an efficient synthesis of peralkylated circumbiphenyl possessing unique peripheral structure. Moreover, investigations of this peralkylated circumbiphenyl by ultrafast transient absorption measurements revealed a stimulated emission, which was not observed in PAHs featuring full armchair periphery before "π-truncation". Comparing with the

conventional approach towards PAHs, the elegance and efficiency of π-truncation offered an "opposite" direction to other unique aromatic structures, providing promising candidates for electronic devices and supramolecular chemistry.

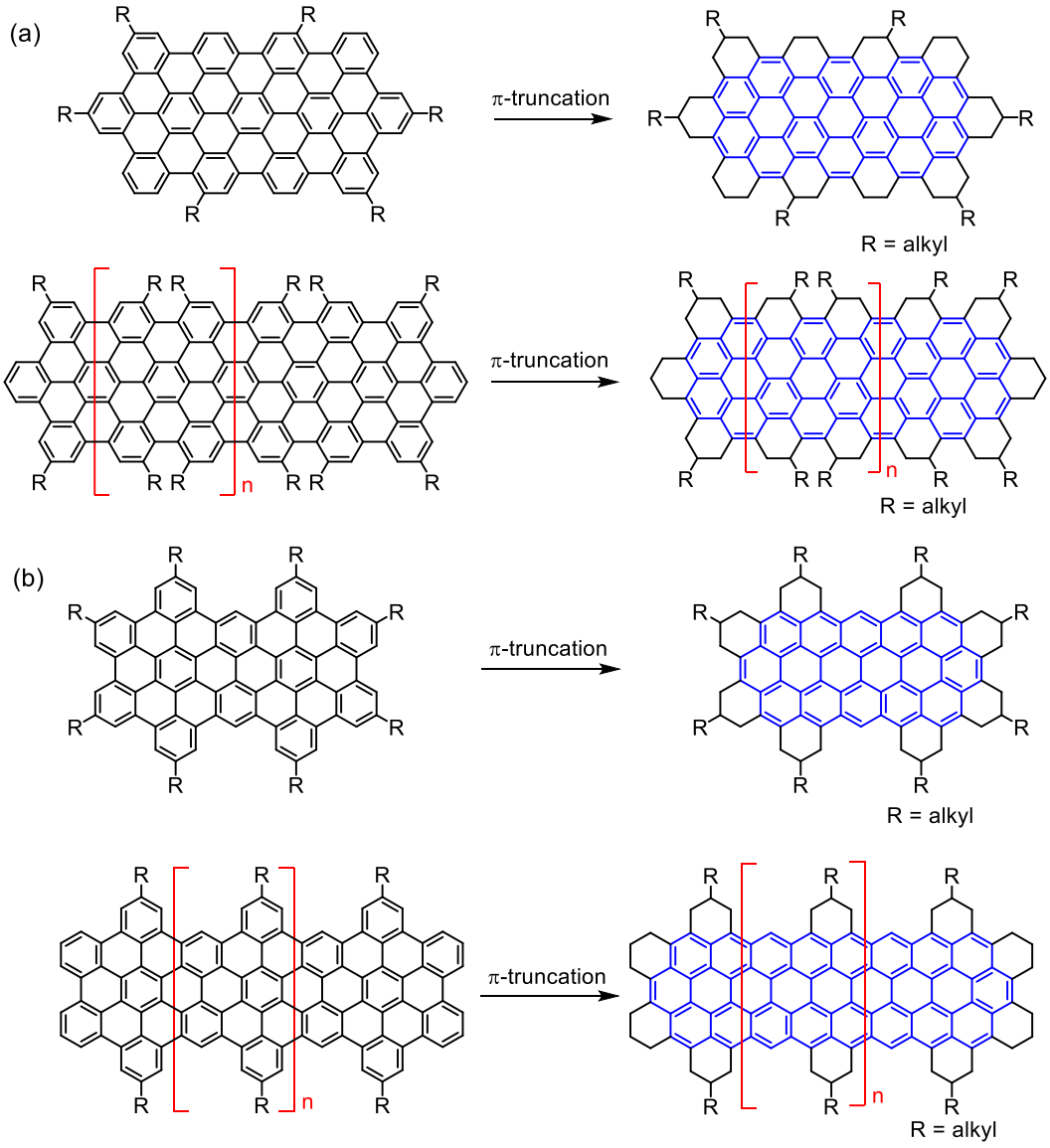

Up to now, there are few reports on larger PAHs and GNRs with functionalized peripheral structures. The reason might be ascribed to the lack of appropriate synthetic methods. The "π-truncation" concept developed in chapter 3 could provide a powerful toolbox for PAH and GNR functionalization. The development of PAHs has already provided a huge reservoir for "π-truncation". 7-AGNRs is the first synthetic example with atomically precise structure, while it only succeeded in on-surface synthesis, solution processable 7-AGNRs is still not available. Thus, the "π-truncation" method provides an alternative way to 7-AGNRs, as shown above. 9-AGNRs, which had already been synthesized in a large scale in solution, could be

used as starting material to the desired 7-AGNRs. As a model compound, a larger PAH with 78 sp^2 carbon, has been tested, and the preliminary results verified the regioselective hydrogenation, leading to an aromatic core with alkylated periphery.

While PAHs with zigzag-edged structure display distinct electronic properties, their accessibility is always hampered because of their poor stability. Peripheral hydrogenation provides a promising approach just by rationally pick starting materials from the sample reservoir, as shown above. Alkyl chains could not only offer sufficient protection to those reactive zigzag sites but also enhance the solubility. Besides, we could apply this kind of hydrogenation to GNRs to obtain full zigzag GNRs in solution. The "π-truncation" strategy could provide fresh ideas to the research field of PAHs and GNRs.

In chapter 4, topological phases in 1D systems have been first realized. Starting with rationally designed precursor molecules, combining with on-surface synthesis, GNRs with regularly alternating zones constituted from periodically arranged zigzag segments have been fabricated. A combination of nc-AFM, STM and STS characterizations visualized the desired structures clearly and revealed the electronic properties with atomic-scale spatial resolution. A very robust and localized quantum state was created at the interface of different GNRs in a synthesis-driven approach. Such topological phases hold great potential for the implementation of nanotransistors in the future, serving as a fundamental step towards nanoelectronics.

According to the SSH model elucidated in chapter 4, topological phases in 1D GNRs can be successfully tuned from trivial insulator to non-trivial insulator by structural variation, where chemical design plays an indispensable role. Considering the flexibility of design, GNRs with topological phases will be an extremely promising research direction in the future. GNRs with various edge structures and widths can be achieved via tailor-made precursor molecules, and thus different GNRs possessing topological phases can be brought to reality. More importantly, further possibilities in applications can be imagined, for example in the field of spintronics and quantum informatics. Besides, when we push the limit of GNRs to GNRs with topological metallic phases, which is a long-pursued goal among both physicists and materials scientists, then an even more fascinating scenario lies just ahead. Last but not least, all those visions remain fancy bubbles without synthetic chemistry to rationally designed structures with atomic precision.

Acknowledgements

Four years which passes just like in an instant. Standing at this point, scenes of the past leap before my eyes. Along all the way of my PhD study at Max Planck Institute for Polymer Research, I have gained a lot from different people, without whom this work would not be possible. With utmost sincerity, I would like to express my deepest acknowledgements to these persons.

First and foremost, I would like to sincerely acknowledge my supervisor, [redacted], who provided me the precious opportunity to work on one of the most interesting and exciting topics of today in such a prestigious group. I am also deeply grateful to you continuous support on this work as well as your trust, patience and belief to me. Your encouraging words and constructive suggestions always guide me through the hard moment of research. During the four-year work with you, your passion and insightful perspectives as well as critical thinking on scientific research deeply impressed me, which will be influential for my future careers.

I would also cordially thank my project leader [redacted], who always be there and helps me out. The discussion with you is always exciting and fruitful, your suggestions is always valuable, and your significant support for the research is crucial for the accomplishment of this dissertation. Moreover, besides the scientific work, I would like to express my sincere appreciation to you for your personal support and assistance.

I would like to extend my acknowledgement to all my colleagues in [redacted] for their great support and help in both aspects of my research and life. My acknowledgement also goes to my collaboration partners inside and outside of Max Planck Institute for Polymer Research for their great efforts into the collaboration projects and exciting results.

I am grateful to my former colleagues, [redacted] and [redacted], who helped me a lot on the hydrogenation system when I started the hydrogenation project at the very beginning.

I would like to also thank my former office members, [redacted], who gave me a lot of help on my life when I first came to Germany. We shared plenty of enjoyed moments on Christmas markets and cycling tours.

I would like to acknowledge [redacted] for our cheerful collaboration in the project of heteroatom-doped PAHs as well as two impressive reviews on nanographenes. Many thanks also extend to [redacted], for your valuable suggestions and help on my experiments.

My sincere thanks also go to [redacted] for your fruitful discussion and collaboration on surface-assisted synthesis of GNRs with topological phase.

[redacted] for your detailed introduction and explanation of all the lab stuff at my earliest day in Max Planck Institute for Polymer Research and always willing to help me out in my daily life, which made me get into the right track quickly.

[redacted] for your help in measurement of NMR.

[redacted] for measurement of the MALDI-TOF MS spectra.

[redacted] for single crystal X-ray diffraction analysis.

All technicians in [redacted] for keeping our lab and office always in order, offering great convenience for my research.

Great acknowledgements belong to the members of [redacted] for your kind help, inspirations, friendship and unforgettable moment together during my PhD study in Mainz: [redacted]

Last but not the least, I would like to thank my parents for supporting me materially and spiritually throughout my life. You are my warmest harbour, letting me pursue my dreams without any fears. Special thanks to my beloved girlfriend for her continuous support and understanding along the way.

Many thanks also to everybody I might have unintentionally forgotten to mention here.

List of Publications and Patents

1. O. Gröning,[1] S. Wang,[1] **X. Yao**[1] **(co-first author)**, C. A. Pignedoli, G. B. Barin, C. Daniels, A. Cupo, V. Meunier, X. Feng, A. Narita, K. Müllen, P. Ruffieux, R. Fasel. Engineering of Robust Topological Quantum Phases in Graphene Nanoribbons. *Nature* **2018**, *560*, 204-208.

2. **X. Yao**, K. Zhang, K. Müllen, X. -Y. Wang. Direct C−H Borylation at the 2-and 2, 7-Positions of Pyrene Leading to Brightly Blue-and Green-Emitting Chromophores *Asian J. Chem.* **2018**, *7*, 2233-2238.

3. X.-Y. Wang, **X. Yao**, K. Müllen. Novel Fluorescent Pyrene Derivatives, Methods for Preparing the Same, and Uses thereof. Patent number: EP18195866.1

4. **X. Yao**, X. -Y. Wang, C. Simpson, G. M. Paternò, M. Guizzardi, M. Wagner, G. Cerullo, F. Scotognella, M. Watson, A. Narita, K. Müllen. Regioselective Hydrogenation of a 60-Carbon Nanographene Molecule towards a Circumbiphenyl Core. *J. Am. Chem. Soc.* **2019**,*141*, 4230-4234.

5. X. -Y. Wang, **X. Yao**, K. Müllen. Polycyclic Aromatic Hydrocarbons in the Graphene Era. *Sci. China: Chem.* **2019**, *62*, 1099−1144. (review paper)

6. X. -Y. Wang, **X. Yao**, A. Narita, Klaus Müllen. Heteroato-Doped Nanographenes with Structural Precision. *Acc. Chem. Res.* **2019**, DOI: 10.1021/acs.accounts.9b00322. (review paper)

7. **X. Yao**, W. Yu, X. Xin, F. Chen, Q. Fu. Amphiphilic, Ultralight, and Multifunctional Nanofibrillated Cellulose/Graphene Aerogel Achieved by Cation-Induced Gelation and Chemical Reduction. *Nanoscale* **2015**, ***7***, 3959-3964.

8. **X. Yao**, X. Qi, Y. He, D. Tan, F. Chen, Q. Fu. Simultaneous Reinforcing and Toughening of Polyurethane via Grafting on the Surface of Microfibrillated Cellulose. *ACS Appl. Mater. Interfaces* **2014**, *6*, 2497-2507.

9. X. Qi, **X. Yao**, S. Deng, T. Zhou, Q. Fu. Water-Induced Shape Memory Effect of Graphene Oxide Reinforced Polyvinyl Alcohol Nanocomposites. *J. Mater. Chem. A* **2014**, *2***,** 2240-2249.